Atomic Electronics With Silicon Dangling Bonds: Error Correction, Logical Gates, and Electrostatic Environment

by

Taleana Huff

A thesis submitted in partial fulfillment of the requirements for the degree of

Doctor of Philosophy

Department of Physics
University of Alberta

© Taleana Huff, 2020

Abstract

With the potential to unleash a new basis for electronics that are more energy efficient, faster, and at the ultimate scale in size density, single atoms as building blocks for miniature circuity have long been a technological holy grail. Preventing significant development have been various roadblocks such as practical operation temperatures, limited error correction ability, lack of homogeneity of device properties, and the ability of atomic patterns to be electrically isolated from the substrate they are put on. Here, we solve these issues and put forth a platform based on the atomically precise patterning of dangling bonds on a hydrogen-terminated silicon substrate. These dangling bonds exhibit electronic band gap states that allow them to fundamentally act as atomically-sized quantum dots, with their gap nature substantially electrically isolating them from mixing with bulk properties. They are structurally stable up to room temperature, with strong evidence supporting their function as binary logic elements at these temperatures too, unlike prior atomic logic approaches. In this work we present three key advancements for this emerging technology. The first is a reliable method of error correction for dangling bond structures. While great strides have been made over the last decade to improve fabrication of dangling bond arrays through the atomically-precise removal of surface hydrogen atoms, a complimentary

way to correct errantly patterned ones was lacking. We demonstrate a methodology wherein a scanning probe tip is reliably functionalized with a single hydrogen atom at the apex, which can then be brought into spatial proximity of a dangling bond. At a key distance, a silicon-hydrogen covalent bond is induced mechanically, erasing the dangling bond with no damage to tip or sample. This erasure technique enabled the second important advancement of construction and actuation of binary atomic logic elements made of dangling bonds. In these demonstrations, paired dangling bonds (two) are occupied by one moveable electron to form a binary electronic building block. Clever geometric arrangement of many of these blocks, combined with control over the spatial arrangement of electrons within using local electrostatic fields, allowed for demonstration of low-power binary operation of a wire and logical OR gate at the atomic scale. Finally, the third key advancement, as a prerequisite for unimpaired operation of atomic binary circuitry, involved examination of the electrostatic landscape of the surface through development of a new technique employing a dangling bond as a moveable electrostatic point-probe. Irregularities in the local electrostatic environment on length scales comparable to our device sizes are looked for, which could impact their correct operation. Additionally, model fits on the dangling bond point-probe acquired data allowed extraction of important surface parameters, such as the dielectric constant and screening length, giving a basis to explore tolerance ranges for atomic-logic operation. For all presented experiments, the powerful single-electron sensitivity of non-contact atomic force microscopy (AFM) is employed, with the ensembles examined using a variety of AFM spectroscopic techniques. With these results combined together, we put forward dangling bonds

on hydrogen-terminated silicon as an attractive medium for atomic electronics, with higher functionality immediately within reach.

Preface

This thesis is an original work by Taleana R. Huff. Three of the chapters within, however, are centered around three papers published as part of a collaborative effort with others.

Chapters 1, 2, 6 are all original writing and work.

Chapter 3 focuses on the published paper "Atomic White-Out: Enabling Atomic Circuitry Through Mechanically Induced Bonding of Single Hydrogen Atoms to a Silicon Surface". Huff, T. R., Labidi, H., Rashidi, M., Koleini, M., Achal, R., Salomons, M. H., & Wolkow, R. A. (2017). ACS Nano, 11(9), 8636-8642. For this paper I experimentally observed the primary dangling bond erasure result in AFM first, figured out how to perform the erasure methodology deterministically, collected the raw data for all figures in the main part of the manuscript, contributed to analysis of the results, assisted with making figures, and co-wrote the manuscript. H.L. mentored me, equally helped to write the manuscript and make figures, collected data, and contributed to analysis. M.R. commented on the manuscript and contributed to analysis. M.K. made the 3D ball and stick diagrams for the figures and commented on the manuscript. R.A commented on the manuscript and contributed to analysis. M.H.S commented on the manuscript, helped with analysis, and assisted with AFM qPlus sensor creation. R.A.W was the supervisory author and was involved in commenting on, analyzing, and refining the manuscript.

Chapter 4 contains the paper "Binary Atomic Silicon Logic". Huff, T., Labidi, H., Rashidi, M., Livadaru, L., Dienel, T., Achal, R., Vine, W., Pitters, J., & Wolkow, R. A. (2018). Nature Electronics, 1(12), 636. For this paper I showed that AFM could resolve electron position in dangling bond structures, co-designed and performed

the experiments, co-wrote the paper, analyzed results, and made or finalized the figures. H.L., M.R., T.D., R.A. and W.V. contributed to designing and performing the experiments and analyzing the data. R.A.W., T.D., L.L., W.V. and M.R. co-wrote the paper. L.L and M.R. performed the theoretical modeling. J.P. and R.A. contributed to the interpretation and discussion of the results. R.A.W. conceived of and supervised the project. All authors discussed the results and commented on the manuscript.

Chapter 5 is the paper "Electrostatic Landscape of a Hydrogen-Terminated Silicon Surface Probed by a Moveable Quantum Dot" by Huff, T. R., Dienel, T., Rashidi, M., Achal, R., Livadaru, L., Croshaw, J., & Wolkow, R. A. (2019). ACS Nano. 13(9), 10566-10575. As part of this work I performed all the published experiments, contributed to methodology conceptualization, performed the theoretical fits, wrote the fit code, made all the figures, and largely wrote, edited, and revised the manuscript. T.D., M.R., R.A., and J.C. also performed experiments. M.R., and R.A.W. were integral to conceptualizing the methodology. All authors contributed to writing, editing, commenting, and refinements for the figures. L.L. performed the TIBB calculations. L.L. and M.R., assisted with refining and performing the theoretical fits. R.A.W. supervised the project, including valuable comments, analysis, and writing.

Any additional analysis in the appendix sections that follow Chapters 3-5 is all original work done by myself. All figures are original unless otherwise indicated in the figure caption.

Dedication

Dedicated to
the memory of my dad,
Clinton A. D. Huff

Acknowledgments

A thesis is supposed to be about individual discoveries contributed to the body human knowledge, but I would not have been able to complete this work without the support and guidance of others.

To my mom Debra Huff, while we were not given the easiest lot in life you did everything you could to make sure I never felt it. You worked two jobs for many of my teenage years to enable me to pursue my dream of getting a doctorate in something I loved and for this I can never fully express my gratitude. Love you mom.

To my brother Tarlin Huff, thanks for always being supportive of my being a nerd and for still describing me to your friends as "cool". Love you dude!

To my partner Ben Lee, I am deeply grateful for your patience and support. I am sure I became unreasonable and trying at times during my PhD as frustration built, but you were always there to disassemble it and give me the strength to continue on.

To my aunt Teesha Borelli, I would not have even been able to afford applying to grad school without you generously paying my application fees. Thank you aunty!

To my wonderful post-doc mentors of Thomas Dienel and Moe Rashidi, you taught me everything I know about scanning probe microscopy. Thanks for inspiring me to be a better scientist through example, for teaching me, and for helping to keep the imposter syndrome at bay. I would not be half the researcher I am without your generously given patience and knowledge.

To my fellow "suffering students" Roshan Achal, Jeremiah Croshaw, and Wyatt Vine, I would never have guessed a PhD would be so much fun. This was all thanks to you being needed confidants when required and, mostly, our ridiculous lab antics. Roshan, we started our grad programs together and we finished together. Ok...you

technically beat me by two days, but as all good physicists do we will just approximate it as about the same. Thanks for taking this crazy ride with me and especially for keeping the default lab music metal. I will totally shill your awesome atomic maple leaf pattern and atomically-encoded mario theme song forever. Jeremy, if I have to hear that techno chicken song a single more time in my life I might die. Despite your terrible taste in music, I have appreciated your friendship greatly. You have blossomed into a beautiful AFM butterfly and your dedication to science is legitimately inspiring. Also, please accept my extra special thanks for tastefully angling the ball and stick models for this thesis. Wyatt, you were only here for a few short years to complete your Master's, but you were a powerhouse while you were here. Thanks for giving me detailed feedback on results and for unveiling the mystery of the streaky DBs.

I would also like to thank Mark Salomons, Martin Cloutier, and Jason Pitters. When things broke in the lab and I needed an adult who knew what they were doing to fix it, you were always there.

To Lucian Livadaru, thank you for your beautiful theory and for helping me understand many of the peculiarities of DBs and theory!

As part of writing this thesis, I am also grateful to my fine editorial and proofing staff of Thomas, Jeremy, and Samuel Ng. You three suffered through the painful process of helping me refine this thesis, making the document infinitely better with your suggestions. Thank you for taking the time!

Speaking of time consumptive things, thanks to my wonderful PhD committee of Lindsay Leblanc, Mark Freeman, Doug Barlage, and Philip Moriarty for reading and providing feedback on my thesis.

Finally, I would like to thank my supervisor Dr. Professor Robert Wolkow. The first time I met you there was no question of working in another lab. Your passion for physics was infectious and I am still blown away by your depth of knowledge. Thank you for bringing such an awesome team together, for providing the large-scale vision, and for giving a lowly student from North Dakota a chance. I feel privileged to have worked under your tutelage, so with this I say: Thank you Sensei Bob!

Contents

Preface v

Dedication vii

List of Tables xiv

List of Figures xv

1 Introduction 1

1.1 Scaling Down: Computational Limitations 1

1.2 Computation with Atoms: Requisites and History 4

1.3 Computation with Atom-Sized Quantum Dots 10

1.4 Structure of the Thesis 13

2 System and Techniques 16

2.1 The Scanning Tunneling Microscope 16

2.1.1 Types of STM Scanning: Constant-Height and Constant-Current 18

2.2 The Atomic Force Microscope 21

2.2.1 AFM Feedback Control 26

2.2.2 Relationship Between Frequency and Force 30

2.2.3 The qPlus AFM Sensor 33

2.2.4 Tip Material, Mounting, Structure, and Etching 36

2.2.5 Apex Functionalization 43

2.3 The H:Si (100) Surface 49

2.4 Surface Dangling Bonds . . . 58
2.4.1 Tip Interactions and its Effect on DB Charge States . . . 60
2.4.2 Making and Erasing DBs . . . 68
2.4.3 Seeing Charge with AFM and $\Delta f(V)$ Probing . . . 70
2.4.4 Probing DBs with STM, AFM, and $\Delta f(V)$ for Atomic Electronics . . . 74
2.5 Summary . . . 78

3 Atomic White-Out: Error Correction for Dangling Bond Structures 80
3.1 Paper and Supplementary Information: Atomic White-Out: Enabling Atomic Circuitry through Mechanically Induced Bonding of Single Hydrogen Atoms to a Silicon Surface . . . 82
3.1.1 Abstract . . . 82
3.1.2 Introduction . . . 83
3.1.3 Results and Discussion . . . 85
3.1.4 Conclusion . . . 96
3.1.5 Methods . . . 96
3.1.6 Supplementary Information: Atomic White-Out: Enabling Atomic Circuitry through Mechanically Induced Bonding of Single Hydrogen Atoms to a Silicon Surface . . . 97
3.1.7 Acknowledgment . . . 99
3.2 Appendix: Not Published Additional Supplementary Results for Atomic White-Out . . . 100
3.2.1 Conditioning Required to Produce a Tip Capable of DB Passivation, and Capping with STM . . . 100
3.2.2 Tip State Effect on Fabrication Efficiency . . . 102

4 Atomic Logic with Dangling Bonds 103
4.1 Paper and Supplementary Information: Binary Atomic Silicon Logic . . 106
4.1.1 Abstract . . . 107
4.1.2 Introduction . . . 107

4.1.3 Results and Discussion . . . 109
4.1.4 Conclusion . . . 121
4.1.5 Methods . . . 122
4.1.6 Acknowledgments . . . 123
4.1.7 Supplementary Information: Binary Atomic Silicon Logic . . . 124
4.2 Appendix: Not Published Additional Supplementary Results for Binary Atomic Silicon Logic . . . 132
4.2.1 Seeing Polarization with Different Tips and Heights . . . 132
4.2.2 Streakiness in Polarization and Lattice Relaxation . . . 136
4.2.3 Modeling DB Logic Assemblies and The Implications for Large Scale Atomic Structure Design . . . 141
4.2.4 The DB Positive Charge Transition . . . 145
4.2.5 Estimates of the DB Levels in the Bandgap . . . 146

5 The Varying Electrostatic Environment of H:Si and its Effect on DB Logic 151

5.1 Paper and Supplementary Information: Electrostatic Landscape of a H-Silicon Surface Probed by a Moveable Quantum Dot . . . 155
5.1.1 Abstract . . . 155
5.1.2 Introduction . . . 156
5.1.3 Results and Discussion . . . 158
5.1.4 Conclusions . . . 171
5.1.5 Methods . . . 172
5.1.6 Acknowledgments . . . 175
5.1.7 Supplementary Information: Electrostatic Landscape of a H-Silicon Surface Probed by a Moveable Quantum Dot . . . 176
5.2 Appendix: Not Published Additional Supplementary Results for Electrostatic Landscape of a H-Silicon Surface Probed by a Moveable Quantum Dot. . . . 186
5.2.1 Spectroscopy over Arsenic Dopants . . . 186
5.2.2 Extracting Shifts . . . 188

5.2.3 The Fitting Code 191

6 Conclusion **210**

6.1 Computation with Atom-Sized Quantum Dots: Revisiting the Requisites 210

6.2 Publications Resulting from This Work 214

Bibliography **217**

List of Tables

4.1 Truth Table for an OR Gate. 126
4.2 Table comparing extracted band gap, DB(0/-), and DB(+/0) energies. 149

List of Figures

1.1 **The First Electronic General Purpose Computer.** Picture of the warehouse home of ENIAC at the Ballistic Research Laboratory in Philadelphia Pennsylvania, the worlds first general purpose electronic computer. Two programmers can be seen entering inputs to the machine. Public domain image from Ref [2]. 2

1.2 **The First Electronic General Purpose Computer Remade Using Modern Chip Processing Techniques**. Photo of ENIAC recreated in CMOS chip format with a dime provided for scale. This chip has the same functionality as the original ENIAC, but was created at the University of Pennsylvania using 0.5 micrometer CMOS processing. Image from Ref [4]. Image credit to Felice Macera. Reproduced with permission from project principal investigator Dr. Jan Van der Spiegel. 3

1.3 **Processors Through the Decades.** Number of transistors, processor clocking frequency, typical power dissipated, and transistors bought per dollar from 1970 to 2017. The y-axis is in log scale, with the units for the relevant plotted data denoted in the figure legend. Dashed trend lines for processor clock frequency, power dissipated, and transistors bought per dollar denote the predicted values for these data types if there was a linear following of Moores law. Instead, a plateauing of these data types occurred during the mid 2000's, which continues to this day. Produced from data from Ref [7] 5

2.1 **Different STM Imaging Modes of the Same Sample Area of H-Terminated Silicon. (a)** STM constant-current empty states image, with electrons being injected from the tip into the available empty states in the sample ($V = 1.3\ V$, $I = 50\ pA$). The tip-sample distance (z-height) is adjusted by a feedback loop to maintain a constant tunneling current of $I = 50\ pA$. **(b)** STM constant-current filled states image, with electrons pulled into the tip from the filled states of the sample. **(c)** STM constant-height image of the same area. A fixed tip-sample height is selected, and current is recorded as the surface is scanned ($V = 300\ mV$, $z_{rel} = -300\ pm$). Compare units for the color bars as an additional indicator for the STM imaging type (pm *vs.* pA). All images are $25 \times 25\ nm^2$ in area, and z_{rel} is a measure of the relative tip-sample height as referenced to a known STM set-point. The set-point used is a response current of $I = 50\ pA$ over a hydrogen atom, with an applied tip-sample bias of $V = -1.8\ V$. 19

2.2 **Illustration of an AFM Sensor Interacting with a Surface.** A single-atom tip is mounted to the end of an oscillating cantilever with resonance frequency f_0. The tip is brought close enough to the surface atoms to feel the force gradient, which shifts the resonance frequency as $f_0 + \Delta f$. This shifting of the resonance (Δf) is tracked as the signal for AFM scanning. 22

2.3 **Qualitative Model of Force Components and Decay Distances Seen by AFM**. Attractive forces are plotted in green and repulsive force in blue. Summed together, these give a corresponding response curve in red, which is what is seen by the AFM sensor. The response curve has a markedly non-monotonic shape with different imaging regimes classified as weak attractive, strong attractive, and repulsive. Going right to left on the x-axis brings the tip-sample system closer together. 23

2.4 **Experimental Frequency Shift Data Converted to Force and Potential Energy.** **(a)** An experimental $\Delta f(z)$ curve obtained by approaching the AFM tip to a hydrogen atom on the H-terminated (100) surface ($V = 0.0\ V$ and $Osc.\ Amp. = 100\ pm$). **(b)** Force as a function of tip-sample distance. The curve from (a) was converted to force by means of the Sader-Jarvis method [64] assuming $f_0 = 28528\ Hz$, $k = 1800\ N/m$, and $Osc.\ Amp. = 100\ pm$. **(c)** The curve from (b), converted to potential energy through numerical trapezoidal integration. On the x-axis, 0 references a z_{rel} height defined by a STM tunneling current of $I = 50\ pA$ with $V = -1.8\ V$ applied, as taken over a surface hydrogen atom. The tip-sample relative distance is reduced by going right to left on the x-axis. 25

2.5 **Dynamic Scanning: AFM Interactions with the Surface. (a)** A tip mounted to an oscillating cantilever is brought close enough to an atom (highlighted in green) to feel the forces coming off it. **(b)** The system to first order acts as a mass with two springs. The tip has the spring constant of the cantilever on one side and the spring constant of the interaction with the target atom on the other. While $k_{Cantilever}$ is a constant, $k_{Tip-Sample}$ changes non-monotonically with height from the green atom. **(c)** Schematic of amplitude-modulated AFM. f_0 is the resonance frequency of the mass-spring system, with the corresponding black curve the resonance curve of the same system under no surface/atom interaction. In AM-AFM the system is driven slightly off-resonance at f_D, with the amplitude monitored at this frequency. The purple curve is the shift of the resonance when in interaction with an attractive feature such as the green atom. This modifies the tip-sample system as illustrated (b) to have competing springs, shifting the unperturbed resonance f_0 to $f_0 + \Delta f$. Orange dashed circles highlight the reduction in amplitude for a changing interaction. **(d)** Schematic of frequency-modulation AFM. Changes in the resonance of the system from (b) are now tracked as a Δf signal only, with the electronics watching the peak movement. 28

2.6 **Stable Constant-Height Scanning During a Change in Reactivity. (a)** Constant-current filled states STM image of a $5 \times 5\ nm^2$ area of half hydrogen-terminated Si(100) (bottom) and half bare Si(100) (top) ($V = -1.8\ V$ and $I = 50\ pA$). **(b)** Constant-height AFM image of the same area, highlighting the ability of the technique to handle significant changes in reactivity without a loss of scan stability. The hydrogen-terminated portion of the AFM image has straight rows, whereas the bare silicon portion appears as a bucked zig-zag with a double-tip artifact apparent ($V = 0\ V$, $z_{rel} = -430\ pm$, $Osc.\ Amp = 50\ pm$). 31

2.7 **The qPlus AFM Sensor.** **(a)** Top-down, **(b)** back-side, and **(c)** front-side views of a third-generation qPlus sensor. The sensor is comprised of a gold-coated base with three legs, a white ceramic square mounted and wired to the base, and a quartz cantilever glued and wired to the side of the ceramic square. Connectivity between all the parts is accomplished through either gluing with conductive epoxy, or spot-welding of the pads/wiring. Signals are transmitted from the connected pads in **(d)**, down through the legs to the relevant processing electronics in the SPM. A welded tip is mounted on the end of the cantilever, but is too small to be seen in optical images. 35

2.8 **Welding a Micro-Tip to a qPlus Sensor.** Scanning electron microscopy images depicting the fabrication process of cutting and welding a micro-tip to a first-generation qPlus sensor. **(a)** Tungsten tip selection. **(b)** Welding the FIB micro-manipulator to the tungsten tip. **(c)** Micro-tip detachment after FIB cutting of the cone. **(d)** Placing and welding of the FIB cut micro-tip on the qPlus sensor. **(e)** Detachment of the micro-manipulator, leaving the micro-tip fixed to the qPlus sensor. **(f)** Scanning electron microscope image showing the dimensions and shape of the micro-tip. The insert in (f) is an optical micrograph of the whole qPlus after FIB fabrication. Reproduced from Ref [88] [doi:10.1016/j.ultramic.2015.06.008] as a co-author on the work, with permission under their policy for reproduction in theses and dissertations. 38

2.9 **Nitrogen Etching a Tip to a Smaller Radius in FIM. (a-f)** Series of images of a tungsten tip as a nitrogen etch is performed. In (a), a large bright ring on the outside denotes the bulk tip structure as if viewing the tip head-on, with a smaller ring in the middle enclosing the crystalline tungsten atoms that make up the apex. The diameter of the inner etch ring reduces as the etch goes on in time in (b-f), indicating that the tip is sharpening. The etch is stopped in (f), when a sufficiently sharp tip has been achieved. 40

2.10 **Removing Tip Artifacts *In Situ* Through Tip Contacts (a)** Filled states STM image of the H:Si surface right after approaching a partially sharpened tip from FIM. Half a dozen DBs with a multi-tip artifact are seen as the bright features. Tip instability is evidenced by the streaky changing contrast. **(b)** Zoomed image of single DB with multi-tip artifacts presenting around it. **(c)** FIM image of the partial tip etch before it was taken to the scanner. This can be compared to the STM image in (b), showing matching features. Dashed red lines between (b) and (c) are provided as a guide to the eye. **(d)** Filled states STM image after the creation of a bare silicon tip-forming patch in the center. **(e)** Controlled-contacts are performed on the patch while scanning the area from bottom to top. After every tip contact, the tip-sample junction conductivity is altered through apex changes, with the feedback loop correspondingly adjusting the tip-sample height to maintain the tunneling current set-point. The four different contrast regions seen in (e) are evidence of four tip-contacts made while scanning upward, with the last tip-forming event producing a sharp tip. **(f)** The same area as (d,e) scanned with the sharp tip. DBs now present as point-defects. All STM images were acquired at ($V = -1.8\ V$ and $I = 50\ pA$), with scale bars equal to 5 nm. . . . 41
2.11 **Tip Forming and the Resulting Change in AFM Interaction.** $\Delta f(z)$ spectroscopy was taken over a hydrogen atom reference using a sharp single-atom tip (blue curve). Afterward, a series of gentle tip forms on a silicon patch were performed. The tip was verified to still be single-atom sharp, as evidenced by its STM contrast, and a second $\Delta f(z)$ curve was taken over the same hydrogen atom reference again (purple curve) ($Osc.\ Amp. = 50\ pm$). $z_{rel} = 0$ is referenced to a STM set-point of $V = -1.8\ V$ and $I = 50\ pA$ over a hydrogen atom. 44

2.12 **Contrast Inversion with Tip Functionalization Change.** **(a)** Filled states ($V = -1.8\ V$, $I = 50\ pA$) and **(b)** empty states ($V = 1.3\ V$, $I = 50\ pA$) STM images of a clean area of H:Si with a presumably silicon tip apex. **(c)** AFM Δf image of the same area, showing the hydrogen atoms as dark circular depressions ($V = 0\ V$, $z_{rel} = -400\ pm$, and $Osc.\ Amp = 50\ pm$). **(d)** Filled states ($V = -1.8\ V$, $I = 50\ pA$) and **(b)** empty states ($V = 1.3\ V$, $I = 50\ pA$) STM images of the same area as (a-c), but after the tip was functionalized with a single hydrogen atom. **(c)** AFM Δf image of the area, showing an inversion of the contrast with the surface hydrogen atoms presenting as white circular protrusions ($V = 0\ V$, $z_{rel} = -300\ pm$, and $Osc.\ Amp = 50\ pm$). All images are $4.0 \times 4.0\ nm^2$ 46

2.13 **Apex Change Inverts $\Delta f(V)$ Spectroscopy.** $\Delta f(V)$ spectra taken over the same DB using different tip terminations. For the silicon-terminated tip (purple curve), the step occurs at $\sim V = -0.2\ V$. For the hydrogen-terminated tip (pink curve), the overall interaction is shifted vertically down by $\sim -20\ Hz$ (all measured Δf values are more negative in frequency shift), with the step shifted to $\sim V = 0.1\ V$. Additionally, the step direction is opposite between the two cases. ($z_{rel} = -250\ pm$ and $Osc.\ Amp. = 50\ pm$ for both spectra). 48

2.14 **Mounted Silicon Sample and Sample Processing UHV Chamber**. **(a)** Molybdenum sample holder with mounted $3.5 \times 11\ mm$ silicon wafer appearing as the dark rectangle in the middle. **(b)** Picture of the UHV sample preparation chamber. The sample from (a) is loaded into the resistive heating module slot, such that the conductive fingers rest on one side of sample holder. Current can then be applied through the contacts to resistively heat the wafer for oxide removal and hydrogen termination. Molecular hydrogen is leaked in during the termination step, and cracked in to atomic hydrogen on the labeled hot cracking filament. 50

2.15 **Large Area Image of the H:Si Surface.** Constant-current filled-states STM image of a $200 \times 200\ nm^2$ area of hydrogen-terminated silicon (100) ($V = -1.8\ V$, $I = 50\ pA$). Four different terraces on the surface are visible, with one example terrace edge highlighted with the orange circle. This image would be considered average for defect areal density, with example defects of an etch pit (pink circle), dangling bond (blue circle), and two unknowns (green circles), highlighted. Zoomed images of the defects are provided on the right. All scale bars are 20 nm. 53

2.16 **H:Si(100) 2×1 Surface.** **(a)** Front-facing, **(b)** slightly-angled, and **(c)** top-down ball and stick models of H:Si(100) 2×1. Hydrogen atoms are depicted as the small white balls. All other atoms are silicon, but the first layer, second layer, and bulk silicon have been colored light blue, dark blue, and grey, respectively, to help with clarity. A single dimer is highlighted by the dashed pink box in (b-d). **(d)** Constant-height AFM Δf image, **(e)** empty states STM image ($V = 1.3\ V$, $I = 50\ pA$), and **(f)** filled states STM image ($V = -1.8\ V$, $I = 50\ pA$) of the surface, matched to the model from (c). All experimental images are $1.8 \times 2.8\ nm^2$. 54

2.17 **Constant-Height AFM Probing of H:Si at Different Heights.(a-l)** Constant-height AFM images of a $3 \times 3\ nm^2$ area of H:Si(100) 2×1 at different heights. Heights are listed in the lower right corner of every image ($V = 0\ V$ and $Osc.\ Amp = 50\ pm$). **(m)** Empty states STM image ($V = 1.3\ V$ and $I = 50\ pA$) of the same area. **(n)** $\Delta f(z)$ spectra taken over top of a hydrogen atom. The spectra location is marked in (m). $z_{rel} = 0\ pm$ is referenced to an STM set-point of $I = 50\ pA$ with $V = -1.8\ V$ over top of a hydrogen atom. 56

2.18 **A Dangling Bond.** **(a)** Ball-and-stick model of a dangling bond on the H:Si(100) 2×1 surface. Silicon atoms are depicted in beige, hydrogen atoms in white, and the dangling bond in green. **(b)** Filled states STM image ($V = -1.7\ V$, $I = 50\ pA$), **(c)** empty states STM image ($V = 1.3\ V$, $I = 50\ pA$), and **(d)** constant-height AFM Δf image ($V = 1.3\ V$, $z_{rel} = -350\ pm$, and $Osc.\ Amp. = 100\ pm$) of the same DB. 59
2.19 **Switching a DB's Charge State with Tip Interactions.** **(a)** Qualitative diagram of the DB charge states (DB^-, DB^0, DB^+) and charge transition levels (DB(0/-) and DB(+/0)). The roman numerals refer to the regions where the DB is in the designated charge state written to the left of the regions. **(b)** Qualitative tip-sample band diagram for the DB in a negative charge state. With the tip Fermi level $E_{F,Tip}$ higher than both $E_{F,Sample}$ and the DB(0/-) level (dark blue), the tip injects current to the DB faster than it can exit to the bulk ($\Gamma_{Tip-DB} > \Gamma_{DB-B}$) rendering it negative. **(c)** The tip Fermi level is lowered to be resonant with the DB(0/-) charge transition level. This allows the tip to extract an electron from that level ($\Gamma_{DB-Tip} > \Gamma_{B-DB}$) faster than the bulk can resupply it. The DB becomes neutral. **(d)** $E_{F,Tip}$ is lowered even further to be resonant with the DB(+/0) charge transition level. The last remaining electron is removed and the DB becomes positive ($\Gamma_{DB-Tip} >> \Gamma_{B-DB}$). 62

2.20 **Contact Potential Difference Diagram.** **(a)** Energy diagram of a tip and sample of differing material not connected. Each has a unique work function (ϕ_{Tip} and ϕ_{Sample}) as referenced to the vacuum energy E_{Vac}. The Fermi levels for the two materials are marked as E_{FTip} and $E_{FSample}$. **(b)** When connected, the two different materials experience a flow of electrons from the material with the higher Fermi level to the one with the lower. This causes a separation of charge in the junction (represented by the illustrated + and - charges) and thus an electric field, with an associated contact potential difference of $eV_{Contact}$. **(c)** The contact potential difference can be nullified such that no electric field exists between the materials by applying a static voltage offset $V_{Applied}$ that is equal in magnitude and opposite in sign to $V_{Contact}$. . 65

2.21 **TIBB as a Function of Tip Radius**. Calculated tip induced band bending for a tip of varying radius. All other inputs for the calculation were held fixed with $z_{rel} = -350\ pm$, a work function difference between tip and sample of 0.4 eV, and an assumed donor concentration of $10^{18} \frac{atoms}{cm^3}$ at the surface, gradually increasing to $10^{19} \frac{atoms}{cm^3}$ in the bulk over a range of 100 nm. 67

3.1 **An Illustration of the Tip Induced Manipulation That Can Result in Tip Functionalization With a Single Hydrogen Atom.** **(a)** Ball and stick model of the H:Si(100)-2 × 1 surface. **(b)** Typical defect-free empty states STM image using a non-functionalized tip and showing the dimer structure of the surface. The red dot indicates the position of the STM tip when the electronic excitation sketched in (a) is applied. **(c)** Ball and stick model of a silicon atom with a dangling bond in green and a H-functionalized tip resulting from the tip-induced desorption. **(d)** Typical STM image of a DB acquired with a H-functionalized tip showing a characteristic STM contrast enhancement. Both STM images were acquired in constant current mode with a set point of $I = 50\ pA$ at $V = 1.3\ V$. 86

3.2 **Imaging a Single Hydrogen Atom Physisorbed on the H:Si(100) Surface.** **(a)** A 5×5 nm^2 STM image at 1.3 V of a DB where the desorbed atomic hydrogen was not picked up, instead adsorbing at the location indicated by an arrow. **(b)** 3×3 nm^2 STM image of an atomic hydrogen adsorbed on the surface and **(c)** corresponding AFM frequency shift map at 0 V and a relative tip elevation of $z = -380$ pm. **(d)** An atomic hydrogen on the surface is picked up by a slow downward STM scan at $V = 1.6$ V. All STM images are constant current at $I = 50$ pA. 87

3.3 **Procedure to Mechanically Induce a Hydrogen-Silicon Covalent Bond.** **(a)** A typical filled states STM image of a silicon dangling bond on the H:Si(100)-2×1 surface using a single hydrogen atom functionalized tip. The yellow arrow indicates a defect taken as a refer]ence. **(b)** $\Delta f(z)$ curve using H-functionalized tip on a surface hydrogen atom. **(c)** Ball and stick model and **(d)** $\Delta f(z)$ curve on a single DB during the mechanically induced Si-H covalent bond capping event. The orange arrow indicates a hysteresis (zoom in inset) characteristic of the change that occurs due to the formation of the covalent bond between the H atom at the tip apex and the silicon dangling bond. **(e)** STM image and **(f)** $\Delta f(z)$ curve on the H:Si surface subsequent to the mechanically induced reaction in (d). 89

3.4 **NC-AFM Characterization of a Single DB on the H:Si(100)-2×1 Surface Using a H-Functionalized Tip.** **(a)** $\Delta f(z)$ curves recorded on the H:Si surface (blue curve) and on the silicon DB (red curve). 3×3 nm^2 frequency shift maps of a DB on the H:Si surface at relatively large **(b)** and small **(c)** tip-sample distances respectively. All data was acquired at $V = 0$ V with an oscillation amplitude of 1 Å. 92

3.5 **Altering Coupling and Artificial Molecular Orbitals in Multi-DB Structures (a)** Two pairs of coupled DBs on the H:Si(100) surface arranged along a same dimer row. **(b)** Image of the same area after the mechanically induced capping of the far right DB in (a). **(c)** A $3 \times 2\ nm^2$ STM image of three tunnel-coupled DBs. **(d)** The same area after erasing the middle DB in (c). Constant current images (a) to (d) were acquired at $V = -1.8\ V$ and $I = 50\ pA$. **(e-f)** Filled ($V = -2.0\ V$, $I = 50\ pA$) and **(g-h)** empty ($V = 1.4\ V$, $I = 50\ pA$) states STM images of a DB wire, respectively, before and after erasing the far right DB in (e). 3D models of the four **(i)** and three **(j)** DB wire. Positions of erased DBs are indicated by dotted circles. Empty state images of Figure 5(a) and Figure 5(c) are presented in Supplementary Figure 3.9. 95

3.6 **(a)** Single hydrogen atoms physisorbed on the chemically inert H:Si(100) surface could be stably imaged in filled states at low voltage ($V = 1.3\ V$). However, when the scanning voltage is increased to $V = 1.7\ V$ in **(b)**, the hydrogen atom is dragged by the tip. This dragging is not smooth, but can result in the H atom being moved close enough to the DB to cap it, as indicated by a change in contrast midway through the image and confirmed by a subsequent STM image of the same area **(c)**. (b) and (c) are larger area $10 \times 10\ nm^2$ images of the area in (a). The location of the atomic hydrogen is marked with an arrow. 97

3.7 **(a-e)** Series of raw $3 \times 3\ nm^2$ NC-AFM frequency shift maps of H:Si(100) surface at different tip-sample elevations. Images were recorded at $V = 0\ V$ and with an oscillation amplitude of 1 Å. We see the evolution from atomic to chemical bond contrast on the H:Si surface. For smaller tip elevations, much higher interaction force is seen on the DB than elsewhere on the surface. $z = 0$ Å corresponds to the tip position defined by the STM imaging set points ($V = 1.3\ V$, $I = 30\ pA$) before switching off the feedback loop. 98

3.8 **(a)** NC-AFM frequency shift map of a single DB at small tip-sample distance ($z = -4.6$ Å) and **(b)** corresponding simultaneously obtained excitation channel map. **(c)** Superposed excitation *vs.* tip elevation curves recorded on the same DB (red curve) and on the H:Si surface (blue curve). 99

3.9 **(a,b)** show empty states images ($V = 1.3\ V$, $I = 50\ pA$) corresponding to Figure 3.5(a,c) from the main text, respectively. It can be seen clearly in (a) that for Figure 3.5(a), the coupled DBs are separated by 2 hydrogens. For Figure 3.5(b), (b) shows the central DB is separated from the top-most DB by 1 hydrogen separation, and the bottom-most DB by 2 hydrogen separation. 99

4.1 **Probing charge state transitions of a DB (a-c)** $2 \times 2\ nm^2$ constant-height $\Delta(f)$ images of an DB at different bias voltages ($z_{rel} = -350\ pm$ and $V = -600\ mV$ **(a)**, $V = -300\ mV$ **(b)**, $V = -600\ mV$ **(c)**; scale bars are $1\ nm$. **(d)** Frequency shift versus sample bias ($\Delta f(V)$) measured above the hydrogen-terminated surface (teal curve) and the DB (blue curve) showing a charge transition step ($z_{rel} = -350\ pm$; see Supplementary Figure 4.5 for STM details). Colour-coded vertical lines indicate the fixed sample bias at which the $\Delta(f)$ images shown in (a-c) were taken. Green shaded regions I and II denote the negative and neutral charge state bias regions, respectively. **(e)** Scan profiles extracted from (a-c) at the dashed lines as indicated. All scale bars are $1\ nm$. **(f)** Qualitative band diagram of the tip-sample system when the DB is negatively charged. The tip Femi level is above the negative to neutral charge transition level DB(0/-), rendering it doubly occupied. **(g)** Band diagram when the DB is neutral, showing the tip Fermi level below the DB's charge transition level. Roman numerals in the green shaded regions in (f) and (g) correlate to the bias regions indicated in the DB's $\Delta f(V)$ curve in (d). VB, valence band. CB, conduction band. 110

4.2 112

4.2 **Biasing of DB Structures.** **(a,d,g,j,m)** Filled state STM images of the isolated left **(a)**, isolated right **(d)**, coupled **(g)**, biased right **(j)** and biased left **(m)** DB assemblies ($V = -1.8\ V$, $I = 50\ pA$). **(b,e,h,k,n)** Corresponding frequency shift (Δf) images. $z_{rel} = -350\ pm$ for (b,e) and $z_{rel} = -300\ pm$ for (h,k,n) with $V = 0\ V$. Qualitative potential energy well sketches are included at the bottom of each panel and the biased states in (k,n) also have their binary representation shown below. **(c,f,i,l,o)** Corresponding colour-coded $\Delta f(V)$ spectra taken on top of the quantum dots in the frequency shift maps ($z_{rel} = -300\ pm$). The charge transition onset for the isolated DB cases at $-135\ mV$ is marked with a vertical dashed line for reference. **(p-r)** DB(0/-) charge transition levels for the isolated, paired, and perturbed DBs, respectively. Red solid lines are the charge transition level experimentally measured. Blue lines are the corrected energy level in the absence of any tip-induced band bending. For (q), two degenerate energy states exist. We illustrate the case of the electron localized on the left, but localization on the right also occurs. **(s)** Corrected electrostatic energy shifts of the DB charge transition levels as a function of DB-to-DB distance for negatively charged DBs. Fits with and without screening factored in are plotted. Error bars reflect the read-out error of the electrostatic energy shift, estimated to be $\pm 10\ mV$. 113

4.3 **Information Transmission Through a DB Binary Wire. (a,b)** Filled state STM image (a) and corresponding constant-height Δf image (b) of an eight-pair wire with a non-paired perturber DB (red circle) on the right. **(c)** Symmetric nine-pair wire created from pairing up the red perturbing DB in (b). **(d)** Constant-height Δf image of the nine-pair wire, with the symmetry-splitting plane marked by a dashed purple line. **(e)** STM image of a nine-pair wire after adding a perturbing DB (red circle in f) on the left. **(f)** Constant-height Δf image showing the wire binary state under the field of the perturber (red). All STM images were taken at $V = -1.8\ V$ and $I = 50\ pA$. All Δf images are $24 \times 3\ nm^2$ in size and were taken at zero bias with a relative tip elevation of $z_{rel} = -330\ pm$. Guides are placed below (b,d,f) to show the location and bit state of the pairs. 119

4.4 **OR Gate Constructed of Dangling Bonds. (a,d,g,j,m)** Constant-current filled state STM images ($V = -1.8\ V$ and $I = 50\ pA$) of the OR gate in various actuation states. **(b,e,h,k,n)** Corresponding constant-height Δf images ($V = 0\ V$, $z_{rel} = -350\ pm$) of the gate, showing electron locations as the dark depressions, with the output marked in blue. **(c,f,i,l,o)** Models of the gate. (c) Three pairs constituting the uninitialized OR gate. (f) Initialized gate with added red perturber below to satisfy the first row of an OR gate truth table, as indicated by the gate symbol. (i,l,o) Models for the remaining OR gate truth states. All the models of the gates correspond to the experimental data shown vertically above them. Dashed boxes and numbers indicate the pairs and their binary state, and the single red perturbers are stand-ins for connecting wires or connections to other gates and structures. Scale bars are 2 nm. 120

4.5 **STM Characterization of a Dangling Bond.** **(a)** $4 \times 4\ nm^2$ filled states STM image ($V = -1.8\ V$, $I = 50\ pA$) and **(b)** $4 \times 4\ nm^2$ empty states STM image ($V = 1.3\ V$, $I = 50\ pA$) of a DB. **(c)** Tunneling current *vs.* sample bias ($I(V)$) spectroscopy plotted in log scale of the DB (blue curve) and hydrogen-terminated surface (teal curve). Spectroscopy positions indicated in (a). 127

4.6 **Frequency Shift Spectroscopy in Dangling Bond Structures.** Colour-coded spectra from main text Figure 4.2 reproduced with vertical offsets for the $\Delta f(V)$ to show key features for the pair **(a-c)**, left tipped **(d-f)**, right tipped **(g-i)**, and symmetric **(j-l)** cases (being STM, constant-height AFM, and vertically offset $\Delta f(V)$, respectively for each case). The charge transition onset for the isolated DB cases, taken from the pair in (c), is marked with a vertical long-dashed line for reference. A short-dashed line, only in (f) and (i), indicates the shifted charge transition in the presence of one additional charge (the perturber). The finely dotted lines indicate the charge transition onset for bringing in the second charge to the pair (c) as well as for the perturbed dot (f,i) in the presence of the charge of the perturber. In (l), the shifted charge transition onset of the perturbers in the presence of its symmetric perturbing partner is marked by a short-dashed line only running over the orange and red spectra. The transition for bringing in an additional electron for the middle pair is marked by the short-dashed line. STM images in (a),(d),(g), and (j) were taken with $V = -1.8\ V$, $I = 50\ pA$. The Δf images in (b), (e), (h) and (k) were taken with $z_{rel} = -300\ pm$, and $V = 0\ V$. All $\Delta f(V)$, were also taken at $z_{rel} = -300\ pm$ (the same as reported in main text Figure 4.2). 128

4.7 **Diagrams for Charge Transitions in a Dangling Bond Pair.** **(a)** Diagram of the system when both DBs are neutrally charged. The tip is assumed to be positioned above the dark blue DB. The DB's negative to neutral charge transition levels are plotted on the left, and are colour coded to the $\Delta f(V)$ reproduced from main text Figure 4.2 below. The Fermi level for tip and sample are given by the dotted lines. The tip Fermi level is below both charge transition levels, meaning both are singly occupied. This corresponds to region III for sample bias $\leq 135\ mV$. **(b)** Diagram for the same system when the sample bias is between $-135\ mV$ to $265\ mV$. Only the blue DB is negative. The teal DB is neutral, as its charge transition level has been shifted above the Fermi level of the sample from the negative charge of the blue DB. This corresponds to region II in the $\Delta f(V)$ spectra. **(c)** Diagram for sample bias values greater than $265\ mV$ (region I) in the $\Delta f(V)$ spectrum of two closely spaced DBs where both are negatively charged. The Fermi level of the tip is now above the negative to neutral charge transition level DB(0/-) of both DBs, rendering them both negative. 129

4.8 **Diagrams for Charge Transitions in a Biased Pair of Dangling Bonds.** **(a)** Diagram of the system when all DBs are neutrally charged. The DB's negative to neutral charge transition levels DB(0/-) are colour coded to the $\Delta f(V)$ spectrum at the bottom reproduced from main text Figure 4.2. The Fermi level for tip and sample are given by the dotted lines. The tip Fermi level is below all charge transition levels, meaning all are singly occupied. This corresponds to region III for bias ≤ -50 mV. **(b)** The diagrams for the same system when the sample bias is decreased to between -50 mV to 395 mV. The perturbing orange DB and blue DB are both negative, lifting the level for the teal above the Fermi level of the sample and rendering it neutral. This corresponds to region II in the $\Delta f(V)$ spectra. **(c)** Diagrams for sample bias ≥ 385 mV (region I) in. The Fermi level of the tip is now above charge transition level of all DBs, rendering them all negative. 130

4.9 **Calculated Tip-Induced Band Bending as a Function of Height and Bias.** **(a)** Tip-induced band bending as a function of tip-sample height. No bias is applied between tip and sample. **(b)** Tip-induced band bending as a function of sample bias for a fixed tip-sample separation of 0.4 nm. For both plots, we assumed a donor concentration of 10^{18} $atoms\ cm^{-3}$ at the surface, gradually increasing to 2×10^{19} $atoms\ cm^{-3}$ in the bulk over a range of approximately 100 nm, a work function difference between tip and sample of 0.4 eV, and a tip radius of 10 nm. 131

4.10 **Sequential OR Gates.** **(a)** Two OR gates in sequence (symbols and boxes in solid purple and blue), connected by a binary wire (one bit long in this example; black dashed box). Functionality is shown by adding inputs (black dots = perturber DB representing connections to other pair-based binary structures or anticipated electrical contacts) to the purple gate's upper input branches with **(b)** (1,0), **(c)** (0,1), and **(d)** (1,1).In **(e)** the input of the lower blue OR gate is toggled to (0,1). In the latter configuration, any further input to the first gate would not change the output state from 1. 132

4.11 **DB Wire with Different Apex Interactions** **(a)** Empty states STM image ($V = 1.3\ V$, $I = 50\ pA$) of a DB wire. **(b)** Corresponding constant-height Δf image of the wire showing all DBs as dark ($z_{rel} = -350\ pm$, $V = 0\ V$, and $Osc.\ Amp. = 50\ pm$). **(c)** Empty states STM image ($V = 1.3\ V$, $I = 50\ pA$) of the same wire from (a) after a series of tip forms on a hydrogen-terminated area to change the apex structure. **(d)** Corresponding constant-height Δf image of the wire showing asymmetry in the DB contrast as expected ($z_{rel} = -350\ pm$, $V = 0\ V$, and $Osc.\ Amp. = 50\ pm$). **(e)** $\Delta f(z)$ spectra taken over a hydrogen reference atom before (purple curve) and after (blue curve) tip shaping. All frames are $6 \times 2\ nm^2$. 133

4.12 **DB Wire AFM Height-Series with Different Tip Apex Structures (a-e)** Constant-height Δf images of a 5 DB wire taken at different heights with a presumed hydrogen apex denoted Tip Apex 1 ($V = 0\ V$, and $Osc.\ Amp. = 50\ pm$). **(f-j)** Constant-height Δf images of the same wire from (a-e) taken after alteration of the tip character (Tip Apex 2) to be likely silicon. **(k)** Extracted cross sections from (a) and (f) across the DB structure. Vertical black dashed lines are given as a guide to the eye. **(l)** $\Delta f(z)$ spectra taken over a reference hydrogen atom for both apex structures. The colored circles in (l) mark the correspondingly color-coded constant-height frames for the two different apex types in (a-j). All AFM constant-height images are $7.4 \times 1.7\ nm^2$, with the height they were obtained at listed in the lower right of each. z_{rel} is referenced to a height defined by a STM tunneling current of $I = 50\ pA$ with $V = -1.8\ V$ applied, as taken over a surface hydrogen atom. 134

4.13 **Continuous DB Wires with Charge-State-Induced Lattice Relaxation. (a)** Constant-current filled states ($V = -1.8\ V$, $I = 50\ pA$) and **(b)** empty states ($V = 1.3\ V$, $I = 50\ pA$) STM images of a continuous five DB chain ($7 \times 4\ nm^2$). **(c-f)** Constant-height Δf AFM images of the same five DB chain taken at different heights, with the heights listed in the lower left of each frame ($V = 0\ V$, and $Osc.\ Amp. = 50\ pm$). **(g)** $\Delta f(V)$ spectra taken over each DB in the chain, as well as over the hydrogen surface ($z_{rel} = -280\ pm$). A Savitsky-Golay filter of order 9 was applied to allow easier differentiation of the curves. **(h-j)** Constant-height Δf AFM images of the chain, but with fixed biases of $V = -1.0\ V$, $V = -0.6\ V$, and $V = -0.3\ V$ applied, respectively ($z_{rel} = -310\ pm$ and $Osc.\ Amp. = 50\ pm$). The frames are color-coded with their positions in the $\Delta f(V)$ spectra in (g). All scale bars are 1 nm. z_{rel} is referenced to a height defined by a STM tunneling current of $I = 50\ pA$ with $V = -1.8\ V$ applied, as taken over a surface hydrogen atom. 139

4.14 **OR Gate Charge Transition Levels (a)** Lattice model from SiQAD showing the OR Gate DB layout superimposed on the H:Si surface. Blue circles indicate the DB is negative and white circles that the DB is neutral. **(b)** DB(0/-) charge transition levels of the OR gate from (a) as referenced to the sample Fermi level (a transparent plane has been put through $z = 0 = E_f$ for clarity). The z-axis denotes how far the charge transition level is away from the bulk Fermi Level and the x and y axis are arbitrary position units. 143
4.15 **The DB(+/0) Charge Transition Level (a)** $\Delta f(V)$ spectra taken over a lone DB and **(b)** simultaneously obtained $I(V)$ spectra ($z_{rel} = -330\ pm$ and $Osc.\ Amp. = 50\ pm$). The $I(V)$ spectra is plotted in absolute value and log scale. The DB(0/-) charge transition is marked with the blue dashed line, and the DB(+/0) with the orange dashed line. z_{rel} is referenced to a height defined by a STM tunneling current of $I = 50\ pA$ with $V = -1.8\ V$ applied, as taken over a surface hydrogen atom. 147

5.1 **Different DB(0/-) Charge Transition Levels. (a)** Empty states STM image of a chosen area with no charge defects in frame. ($V = 1.3\ V$, $I = 50\ pA$). **(b)** Empty states STM image of the same area as (a), but after the addition of DBs in the lower left and upper right corners. **(c)** $\Delta f(V)$ spectra taken over the two created DBs, showing nonequivalent charge state transition biases ($z_{rel} = -350\ pm$ and $Osc.\ Amp. = 50\ pm$). All scale bars are 2 nm. z_{rel} is referenced to a height defined by a STM tunneling current of $I = 50\ pA$ with $V = -1.8\ V$ applied, as taken over a surface hydrogen atom. 152

5.2 **Surface Defect Shifting a DB's Charge Transition**. **(a)** Empty states STM image of an area with a dark charged defect in the lower left ($V = 1.3\ V$, $I = 50\ pA$). **(b)** STM image of the same area as (a), but after the addition of a DB near the dark defect. Both (a) and (b) are $3.0 \times 2.0\ nm^2$ in area. **(c)** $\Delta f(V)$ spectra taken over the DB patterned on top of the charge defect, showing a shift of its DB(0/-) charge transition level to $V = 0.24\ V$ ($z_{rel} = -320\ pm$ and $Osc.\ Amp. = 50\ pm$). z_{rel} is referenced to a height defined by a STM tunneling current of $I = 50\ pA$ with $V = -1.8\ V$ applied, as taken over a surface hydrogen atom. 153
5.3 162

5.3 **H:Si Imaged with Different STM Modes and Labeled Near-Surface Charged Species**. **(a)** Filled states ($V = -1.6\ V$, $I = 50\ pA$), **(b)** empty states ($V = 1.3\ V$, $I = 50\ pA$), and **(c)** constant-height ($z_{rel} = -150\ pm$ and $V = 300\ mV$) of the same area (z_{rel} referenced to a common STM set-point $-1.8\ V$ and $I = 50\ pA$ over a bonded H atom). All images are $50 \times 50\ nm^2$. **(d,e)** Constant-height STM images of arsenic: (d) positive bias ($z_{rel} = -200\ pm$ and $V = 300\ mV$) and (e) negative bias ($z_{rel} = -200\ pm$ and $V = -0.9\ V$). **(f,g)** Constant-current STM images of T2: (f) empty states ($V = 1.3\ V$, $I = 50\ pA$) and (g) filled states ($V = -1.8\ V$, $I = 50\ pA$). Images (d-g) are all $5 \times 5\ nm^2$. **(h-k)** Energy level diagrams for the defect types in their corresponding empty and filled states. (h) Dopant with modest to large positive biases can be either neutral or positive depending on the competing Γ_{T1-B} and Γ_{T-T1} rates. If positive, the bands are locally bent downward (bending depicted in blue *vs.* black curves). (i) Neutral dopant at modest negative bias. (j,k) Upward band bending due to negative T2 decreases the current in empty states (f,j), so that Γ_{T-B} in the presence of the defect (purple arrow and curve) is less than Γ_{T-B} in a defect-free region (black arrow and curve). The opposite occurs in filled states (g,k). **(l-n)** STM imaging of area containing arsenic and T2 ($10 \times 10\ nm^2$), (l) constant-height STM ($z_{rel} = -200\ pm$ and $V = 300\ mV$), (m) constant-current STM ($V = 1.3\ V$, $I = 50\ pA$), and (n) KPFM difference map compared to unperturbed surface (25×25 spectra grid, $z_{rel} = 0.0\ pm$, $V_{range} = -1.8 - 1.0\ V$). All scale bars are $5\ nm$. 163

5.4 **Probing Charged Species with a Movable DB Point-Probe**. **(a-g)** Constant-height STM images of the DB being moved 0-6 lattice sites away from its initialization point, respectively, from a near-surface arsenic atom ($z_{rel} = -250$ pm and $V = 300$ mV). **(h)** Constant-height STM image of the area before addition of a DB, with $\Delta f(V)$ locations marked ($z_{rel} = -200$ pm and $V = 250$ mV). **(i)** $\Delta f(V)$ spectroscopy taken on top of the DB for each lattice spacing, color coded with the positions in (h), as well as with the frames in (a-g) ($z_{rel} = -350$ pm). **(j-n)** Constant-current STM images ($V = 1.3$ V, $I = 50$ pA) of the DB being moved 0, 3, 6, 9, and 12 lattice sites away from its initialization point, respectively, from a T2. **(o)** Constant-current STM image marking the $\Delta f(V)$ locations. **(p)** $\Delta f(V)$ spectroscopy taken on top of the DB at the listed lattice spacing's ($z_{rel} = -300$ pm). **(q-t)** Constant-height AFM images of a DB 2, 3, 4, and 6 lattice sites away from another DB $z_{rel} = -300$ pm and $V = 0$ V). **(u)** $\Delta f(V)$ spectroscopy taken on top of the left DB at the listed lattice spacing's ($z_{rel} = -300$ pm). All scale bars are 2 nm. 165

5.5 **Fitting DB Charge Transition Shifts**. Shifts of the charge transition step for the probe DB as a function of distance from the T1+ (pink curve), T2- (blue curve), a second DB- (orange curve), and a physisorbed negative hydrogen (purple). TIBB was subtracted from the experimental data (see "Tip-Induced Band Bending" in Methods Section 5.1.5). Error bars correspond to the read-out error of the electrostatic energy shift, taken to be ± 10 mV for T1, T2, and DB cases and ± 20 mV for hydrogen. Dashed lines are an orthogonal distance regression fit of the data to the linearized form of the screened Coulomb equation. Errors of the dielectric constant and screening length correspond to the standard error (see "Fitting" in Methods Section 5.1.5). 168

5.6 **Screening for a Uniform Electrostatic Background**. **(a)** Constant-current empty states ($V = 1.3\ V$, $I = 50\ pA$) STM image of a clean H:Si area. **(b)** KPFM grid taken of the same area. Two areas with similar contrast are marked with color coded X's for patterning of a DB (grid dimensions = 25×25 points, $z_{rel} = 0.0\ pm$, $V_{range} = -1.3 - 1.0\ V$). **(c)** Constant-current image once the two DBs were patterned at opposite corners. **(d)** $\Delta f(V)$ spectroscopy taken on top of the two DBs showing similar charge transition voltages ($z_{rel} = -350\ pm$). All scale bars are $2\ nm$. 169

5.7 **Arsenic Dopant Energy Level Diagrams**. **(a-e)** Qualitative energy level diagrams of the arsenic dopant as it is swept through the voltage ranges listed underneath each panel. The dopant changes charge state depending on the tip-induced band bending conditions which tune the tunneling rates between tip and T1 (Γ_{T-T1}) and bulk and T1 (Γ_{B-T1}). 178

5.8 **Dopant at Different Biases**. **(a-i)** Constant-height STM images of the dopant from Figure 5.3(d,e) at additional bias's ($z_{rel} = -200\ pm$ and area= $12 \times 12\ nm^2$). **(j)** $I(V)$ spectra taken above the center of the dopant at the same height as panels (a-i). The curve is plotted in log scale and absolute value, unlike (a-i). From the $I(V)$ curve, the bandgap runs from $\sim -0.7\ to\ 0.1\ V$, explaining the lack of features in panels (f,g). 179

5.9 **Fitting a KPFM Curve**. Raw KPFM data from Figure 5.3(n) (reproduced on the right with location of spectroscopy marked with an X) fit with a parabolic function $z_{rel} = 0.0\ pm$, $V_{range} = -1.8\ to\ 1.0\ V$, and $Osc.\ Amp. = 50\ pm$). The maximum of the fit ($-0.53 \pm 0.02\ V$) is marked with the pink dot. Every point in a KPFM grid has this performed. The extracted maxima or V^*'s vary slightly for every point, generating a map of the electrostatic potential (*cf.* Figure 5.3(n)). The ± 0.02 on V^* represents the propagated uncertainty in the fit error. 180

5.10 **Fitting a DB KPFM Curve**. Raw KPFM data (black curve) taken over a DB ($z_{rel} = -300\ pm$). For voltages in the red shaded area, the DB is neutral. For voltages in the blue shaded area, the DB is negative. The transition from neutral to negative, or the (0/-) charge transition step is seen at $V = -0.25 \pm 0.01\ V$. The parabolas were fit to both the neutral (red) and positive (blue) charge state of the DB. The LCPD could be extracted from the maximum value for each parabolic fit. . 181
5.11 **KPFM Map of an Isolated Arsenic Dopant.**. **(a)** Larger area constant height frame of main text Figure 5.4(h). **(b)** KPFM map of the same area as (a) showing a local dark depression at the location of the dopant atom. (Grid Dimensions = 25×25 points, $z_{rel} = -200\ pm$, $V_{range} = -1.3\ to\ 600\ mV$). The contact potential difference of the surface background has been subtracted out from the map in (b). . . 182
5.12 **I(V) and Extracted Shifts for $\Delta f(V)$ Spectroscopy**. **(a)** The $\Delta f(V)$ spectroscopy from main text Figure 5.4(i) for the DB-T1 case is reproduced in the top panel, with the simultaneously obtained I(V) spectrum at the bottom. As the DB probe is moved farther away, shifts also occur in the onset of the valence and conduction bands. **(b)** $\Delta f(V)$ spectroscopy from main text Figure 5.4(p) for the DB-T2 case, along with its $I(V)$ spectroscopy. **(c)** $\Delta f(V)$ spectroscopy from main text Figure 5.4(u) for the DB-DB case and its $I(V)$ spectroscopy. For all three cases their charge transition step onsets have been marked with a color-coded dashed line. These onsets were used as the common point of reference for extracting the electrostatic energy shifts plotted in Figure 5.5. 183
5.13 **Lattice Distortion from a Hydrogen Atom.**. **(a)** Constant-current empty states ($V = 1.3\ V$ and $I = 50\ pA$) STM image of a lone hydrogen atom on the H:Si surface. **(b)** Constant-height AFM image of the same area showing the hydrogen sits at an apparent surface hollow, distorting the upper hydrogen layer ($z_{rel} = -360\ pm$, $V = 0\ V$, and $Osc.\ Amp = 50\ pm$). Both images are $3 \times 3\ nm^2$. . . 184

5.14 **Negative Hydrogen Atom Perturbing a Pair**. **(a)** Constant-current empty states ($V = 1.3\ V$ and $I = 50\ pA$) STM image of a DB pair with a physisorbed lone hydrogen visible in the upper left. Constant-height AFM images were taken at **(b)** $z_{rel} = -300\ pm$ and **(c)** $z_{rel} = -350\ pm$, of the same perturbed pair showing the upper DB lighter in contrast than the lower ($V = 0\ V$, and $Osc.\ Amp = 50\ pm$). The location of the hydrogen atom is marked by the dashed white circles. **(d)** Constant-current empty states ($V = 1.3\ V$ and $I = 50\ pA$) STM image of the pair after removal of the hydrogen. The constant-height AFM images were repeated at the same heights of **(e)** $z_{rel} = -300\ pm$ **(f)** $z_{rel} = -350\ pm$ ($V = 0\ V$, and $Osc.\ Amp = 50\ pm$). **(g)** $\Delta f(V)$ spectroscopy taken on top of the DBs both with the hydrogen present and without. Filtered curves are overlaid on the raw data. Color-coded models are provided above the panel. ($z_{rel} = -350\ pm$ and $Osc.\ Amp = 50\ pm$). Vertical color-coded dashed lines mark a common point of reference. All scale bars in images are 1 nm. 185
5.15 **KPFM Spectroscopy Shift with Height**. Constant-current **(a)** empty states ($V = 1.3\ V$ and $I = 50\ pA$) and **(b)** filled states ($V = -1.8\ V$ and $I = 50\ pA$) STM images of a lone DB. **(c)** KPFM spectroscopy performed over the same DB at different heights ($V_{range} = 0.3\ to\ -0.4\ V$ and $Osc.\ Amp = 50\ pm$), showing a shift of the neutral to negative charge transition level (0/-) as a function of height. Tip-induced band bending shifts the energetic position of the charge transition to more negative values with decreasing tip-sample separation. A black dashed line is provided as a guide to the eye. . . 186

5.16 **Charge Transition Steps Over an Arsenic Dopant**. **(a)** $\Delta f(V)$ spectra taken over the center of an arsenic dopant (The same arsenic atom as in Figure 5.8 in Section 5.1). Two possible charge transition levels for the arsenic atom are marked with the vertical dashed orange and blue lines, potentially corresponding to the D(0/-) and D(0/+) levels ($z_{rel} = -150\ pm$ and $Osc.\ Amp. = 50\ pm$). **(b)** $I(V)$ spectra simultaneously acquired during the taking of the $\Delta f(V)$ in (a). Current is plotted in log scale and absolute value. **(c)** Constant-height STM image of the dopant at a similar bias ($V = -1.2\ V$) to the orange marked D(0/-) charge transition step. The arsenic atom displays a faint dark depression around its location, perhaps suggesting it is negatively charged ($z_{rel} = -200\ pm$, $V = -1.2\ V$, and $12.0 \times 12.0\ nm^2$). z_{rel} is referenced to a height defined by a STM tunneling current of $I = 50\ pA$ with $V = -1.8\ V$ applied, as taken over a surface hydrogen atom. 187

5.17 **Tip Radius Effect on TIBB and Final Extracted Parameters**. Fit-extracted values for the dielectric constant ϵ, defect depth, and screening length L_{TF}, after the application of different TIBB corrections generated for different tip radii. The TIBB corrections for a given radius were applied to the extracted DB(0/-) charge transition shifts from Figure 5.4(i,p,u) in the Electrostatic Probe paper (Section 5.1). The differently-TIBB-corrected shifts were then fit using the same code and methodology as given in both the paper and Section 5.2.3. The tip radii assumed are denoted above each table, with the extracted values from the fits below. 190

5.18 **Fit Effects for TIBB vs. No TIBB Correction**. Fits on the extracted DB(0/-) charge transition shifts from Figure 5.4(i,p,u) from the Electrostatic Probe paper (Section 5.1) performed with and without a TIBB correction applied. 191

Glossary of Terms

- **AC**: Alternating Current.
- **AFM**: Atomic Force Microscopy.
- **AM-AFM**: Amplitude-Modulated Atomic Force Microscopy.
- **CB**: Conduction Band.
- **CMOS**: Complimentary Metal Oxide Semiconductor.
- **CO**: Carbon Monoxide.
- **CPD**: Contact Potential Difference.
- **DB**: Dangling Bond.
- **DC**: Direct Current.
- **DFT**: Density Functional Theory.
- **EDX**: Energy Dispersive X-Ray.
- **ENIAC**: Electronic Numerical Integrator and Computer.
- **EPR**: Electron Paramagnetic Resonance.
- **EUVL**: Extreme Ultra-Violet Lithography.
- **FIB**: Focused Ion Beam.

- **FIM**: Field Ion Microscopy.
- **FM-AFM**: Frequency-Modulated Atomic Force Microscopy.
- **H:Si**: Hydrogen-Terminated Silicon.
- **KPFM**: Kelvin Probe Force Microscopy. Also called $\Delta f(V)$.
- **LCPD**: Local Contact Potential Difference.
- **LDOS**: Local Density of States.
- **LT**: Low-Temperature.
- **MgO**: Magnesium Oxide.
- **ML**: Mono-Layer.
- **NaCl**: Sodium Chloride.
- **NaOH**: Sodium Hydroxide.
- **NC-AFM**: Non-Contact Atomic Force Microscopy.
- **PI**: Proportional-Integral.
- **PRL**: Physical Review Letter.
- **QCA**: Quantum Cellular Automata.
- **SEM**: Scanning Electron Microscopy.
- **SI**: Supplementary Information.
- **SiQAD**: Silicon Quantum Atomic Designer.
- **SPM**: Scanning Probe Microscope.
- **STM**: Scanning Tunneling Microscopy.

- **STS**: Scanning Tunneling Spectroscopy.
- **TIBB**: Tip Induced Band Bending.
- **UHV**: Ultra-High Vacuum.
- **VB**: Valence Band.
- **VBM**: Valence Band Maximum.

Chapter 1

Introduction

1.1 Scaling Down: Computational Limitations

The ubiquitous nature of technology has steadily infiltrated almost every aspect of our lives in the span of a few generations. We have incrementally built from the first warehouse-sized digital computers, to chips with more transistors than people in Canada. To put it in perspective, the first electronic general-purpose computer was the Electronic Numerical Integrator and Computer (ENIAC) in 1945 [1].

Mechanical computers were demonstrated before ENIAC, but this was the first fully-functional digital computer, intended for calculating projectile trajectories for World War II. ENIAC "weighed 30 tons and occupied 1,800 square feet of space. It had more than 19,000 vacuum tubes, 70,000 resistors, 10,000 capacitors and 6,000 toggle switches. It consumed 175 kilowatts of electricity..." with "...up to 5,000 calculations per second" [1]. A photo of ENIAC at the Ballistic Research Laboratory is shown in Figure 1.1.

Five decades later for ENIAC's 50th anniversary, a group of students at the University of Pennsylvania recreated ENIAC's architecture using modern 0.5 micrometer complementary metal oxide semiconductor (CMOS) processing [3]. They were able to fit the formerly 1800 square foot machine onto a small 7.44×5.29 mm^2 chip shown in Figure 1.2.

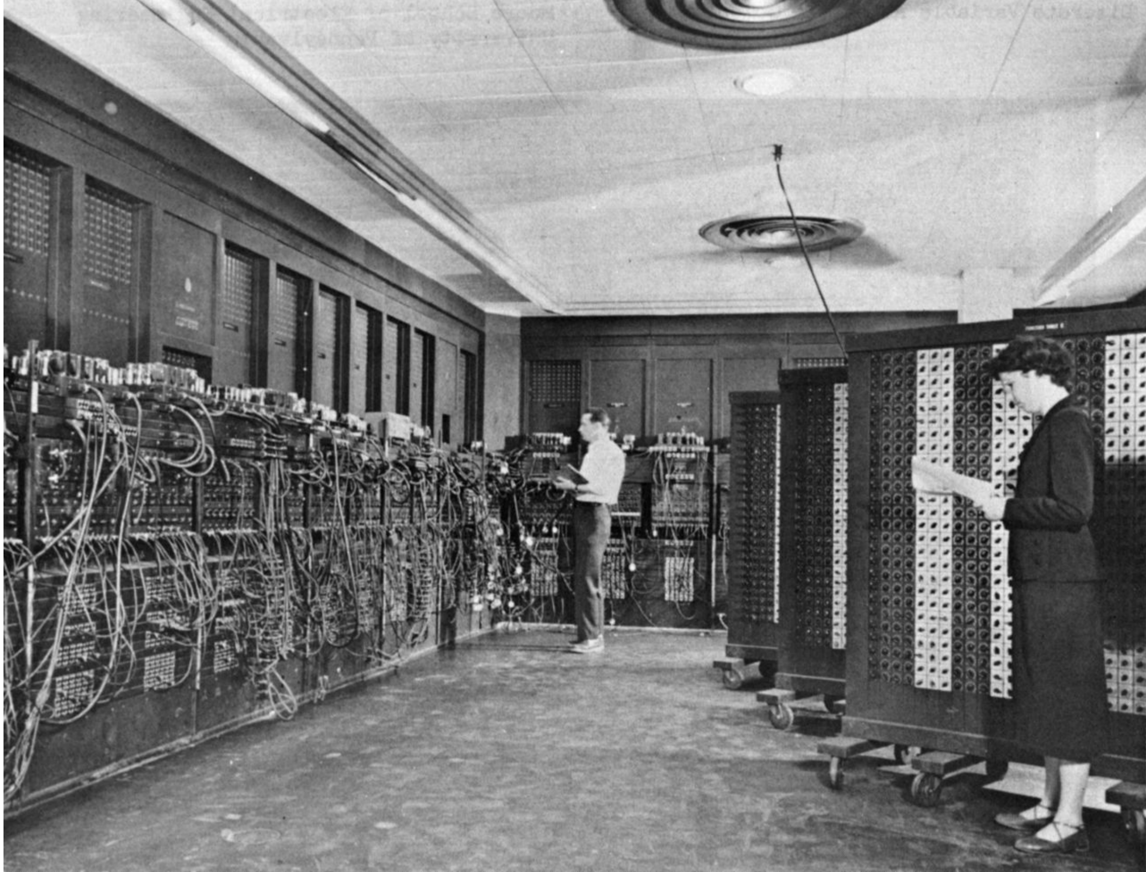

Figure 1.1: **The First Electronic General Purpose Computer.** Picture of the warehouse home of ENIAC at the Ballistic Research Laboratory in Philadelphia Pennsylvania, the worlds first general purpose electronic computer. Two programmers can be seen entering inputs to the machine. Public domain image from Ref [2].

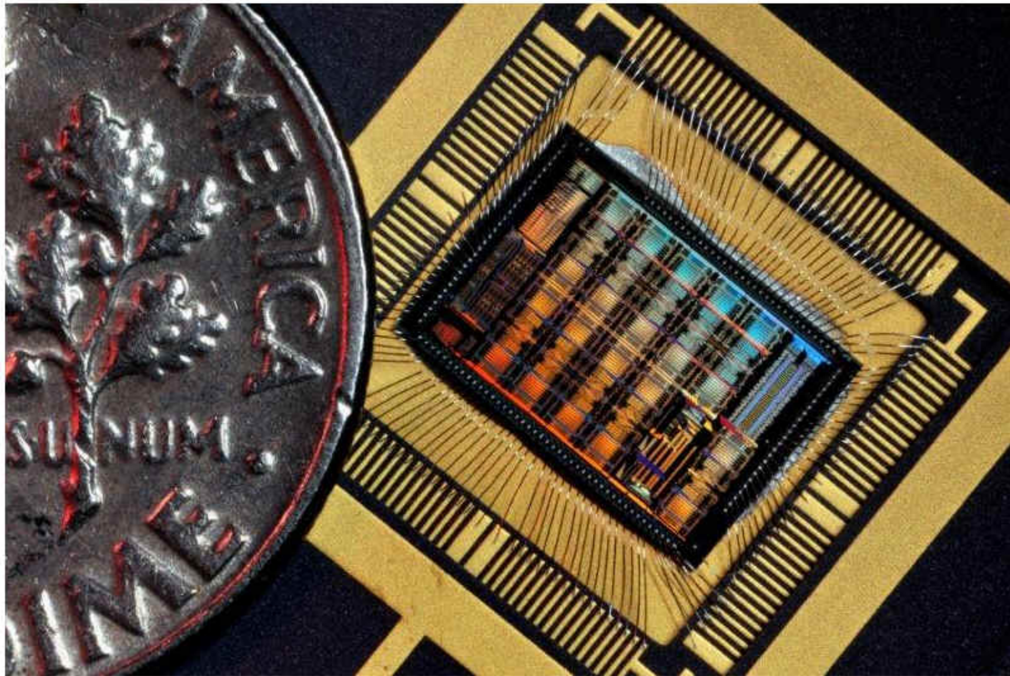

Packaged Eniac-on-a-Chip (photo by Felice Macera). Trustees University of Pennsylvania. All rights reserved, 1998

Figure 1.2: **The First Electronic General Purpose Computer Remade Using Modern Chip Processing Techniques**. Photo of ENIAC recreated in CMOS chip format with a dime provided for scale. This chip has the same functionality as the original ENIAC, but was created at the University of Pennsylvania using 0.5 micrometer CMOS processing. Image from Ref [4]. Image credit to Felice Macera. Reproduced with permission from project principal investigator Dr. Jan Van der Spiegel.

CMOS processing remains the standard to this day, but has since advanced to smaller size scales. It is expected to reach the 7 nm limit for commercially available products later this year [5] using a technique called extreme ultra-violet lithography (EUVL) [6]. Using EUVL, it is anticipated that there are potential immediate paths forward to smaller node sizes of $\sim 5 - 1\ nm$, supposing light-source developers can keep up with the power requirements of the massive EUVL machine [6]. However, despite these advances in transistor density, proportional performance increases have plateaued in the last 20 years as seen in Figure 1.3.

Transistors consume power and generate heat to run logic computations, and scaling transistors to smaller sizes has not proportionately reduced the amount of power they consume. The year 2000 was when the limit for forced-air cooling power ($150 \frac{W}{cm^2}$) was reached [8]. While superior cooling of chips could be achieved through schemes like liquid cooling, these additions to commercial technologies are prohibitive due to the increased size, complexity, and maintenance required, reducing overall mechanical reliability. Air-forced cooling is thus a natural “convenience-based” upper limit for 90% of applications. Therefore, to keep chips from thermally failing, manufactures reduced power dissipation, and thus thermal load, by limiting how many operations chips could perform per second (slower clocking frequency). This concomitantly increased the cost of manufacturing (less transistors bought per dollar) and lead to the performance plateauing shown in Figure 1.3. As we continue to demand more from our electronics as they become increasingly enmeshed in our lives, we thus must consider alternative paradigms that allow us to stay under this power dissipation threshold while still trending smaller, faster, and greener.

1.2 Computation with Atoms: Requisites and History

“There’s plenty of room at the bottom” was a famous lecture given by physicist Richard Feynman in 1959 where he said “I am not afraid to consider the final question as to whether, ultimately, in the great future, we can arrange the atoms the

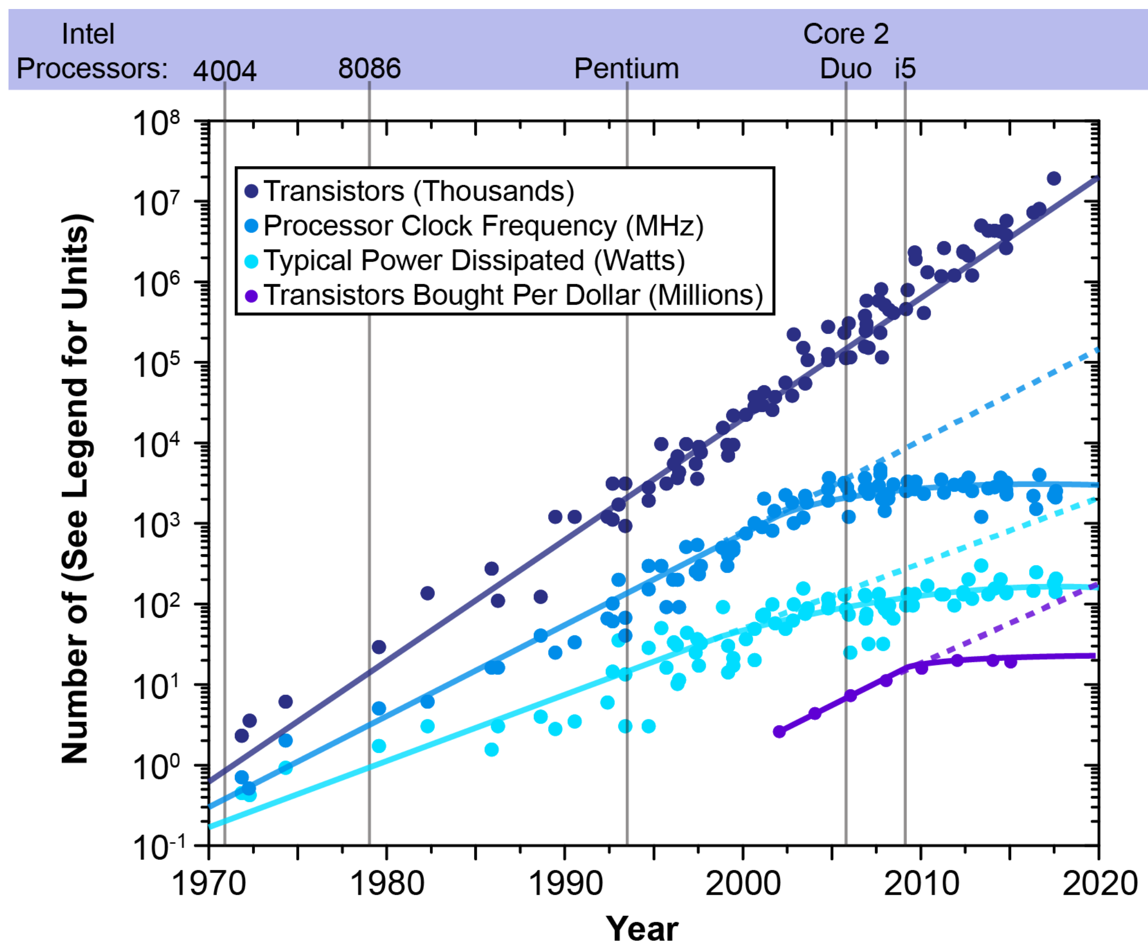

Figure 1.3: **Processors Through the Decades.** Number of transistors, processor clocking frequency, typical power dissipated, and transistors bought per dollar from 1970 to 2017. The y-axis is in log scale, with the units for the relevant plotted data denoted in the figure legend. Dashed trend lines for processor clock frequency, power dissipated, and transistors bought per dollar denote the predicted values for these data types if there was a linear following of Moores law. Instead, a plateauing of these data types occurred during the mid 2000's, which continues to this day. Produced from data from Ref [7]

way we want; the very atoms, all the way down!" [9]. This would be the ultimate in miniature circuitry; not just layering and writing in materials in the top-down approach of conventional CMOS, but writing entirely new materials from the ground up. While not at the point of 3D custom materials, technology has presently advanced to where we can reproducibly manipulate atoms on a surface using a scanning probe microscope (SPM) [10].

The first demonstration of this was done by IBM researchers Eigler *et al.* in 1990 where they controllably moved xenon atoms on a nickel surface to make the famous IBM logo [11]. Twelve years later in 2002, the same lab demonstrated the first atomic logic structures with CO molecules [12]. A CO molecule on the surface could be set up in a semi-stable physical configuration state that would quantum tunnel into a different one after a certain amount of time. Chains of these CO molecules were positioned and timed so that the toppling of the first CO would trigger sequential ones, much like a chain of dominoes [12].

This foundational work has since been steadily built on by chemists and physicists alike, with different implementations of molecular logic [13–17], and a few cases of atomic logic [18–21]. On the atomic logic side, Khajetoorians *et al.* used coupled atomic spins of adatoms adsorbed on a surface to transmit binary information [18], Yengui *et al.* demonstrated switching of the electronic states of multi-DB structures on H:Si through voltage pulses [19], Fresch *et al.* demonstrated simulation of a logic problem through measured electronic transport through a single phosphorus dopant atom in a silicon matrix [20], and Kolmer *et al.* demonstrated NOR gate logic through shifts of the electronic states in a fabricated DB structure as additional DBs were added [21]. However, the difficulty in addressing many practical considerations have kept these demonstrations firmly rooted to academic interests thus far. Some of the biggest considerations are:

(1) It should provide some existing or potential future benefit. For computing this would be an increase in packing density, processing speed, or power efficiency, with the ideal technology capable of benefiting all three. As an example, Kolmer *et al.*'s demonstration of NOR gate logic with shifts in the electronic states of a fabricated DB structure would have a difficult road to becoming fast and power

efficient; the output of the gate is measured using slow spectroscopy methods and additionally requires a non-power-efficient flow of tunneling current to deduce the logical state. While it would be unreasonable to claim the work in this thesis or from others hits these three qualifiers immediately, a successor technology should have identifiable routes toward reaching all these benefits with no "Achilles heel" that would obviously disqualify it.

(2) One obvious disqualifier for a every-day commercial technology is it must not need cryogenic temperatures. If liquid-based cooling would be impractical for every day devices, cryogenic conditions would be on a whole other level. An ideal technology would remain stable and function at room temperature where most consumers would be operating. The IBM atomic patterns mentioned earlier were delicately bound and only stable below $-230°C$ [11, 12]; the xenon atoms were physisorbed to the surface, only remaining stationary for cryogenic conditions. The atomic logic implementation by Khajetoorians *et al.* where iron atoms placed on copper were used to perform spin-based logic [18] was similarly limited.

(3) The patterned atoms or molecules need to be electrically distinct from the substrate. Without electrical insulation, the atomic logic atoms will convolute states and properties with the bulk material, enabling conduction pathways that avert the desired functionality [22, 23]. For example, Joachim *et al.* from the IBM research group looked at conductance through placed C_{60} molecules on gold. Instead of getting the expected value, they found that electronic coupling to the substrate altered the measured conductance of the molecule [23].

Attempts at electrical isolation have been tried using different types of insulating layers. Joachim *et al.* attempted to remedy the earlier coupling issue by placing their molecule of interest, a pentacene, on the inert hydrogen-terminated silicon surface (H:Si(100)), observing it fixed the issue [24]. However, the authors themselves commented "Due to the high mobility of the molecule on the surface even at 5 K, imaging orbitals of this molecule is a very difficult work" [24]. The pentacene was only weakly physisorbed, moving around easily under examination with little hope of staying in place at even modestly elevated temperatures.

Further work explored other insulator materials like MgO [25, 26] and NaCl

[27–30] grown on top of a conducting substrate. These insulator layers were made thin enough that under the application of large bias voltages between the manipulating probe and sample, a tunnel current could still measured allowing the researcher to preform the necessary atom/molecule manipulations. Lower biases were then used to look at the atoms or molecules, such that they were decoupled from the bulk substrate. However, issues arose with this method as ionic relaxations of the insulating layer were revealed to be substantial. For example, atoms were observed to get stuck in a given charge state from lattice relaxations, requiring large energetic pulses to switch between them [28]. Additionally, these insulating films are often grown with a vapor deposition method, meaning controlling layer thickness is challenging. If too thin, spontaneous loss of charge in placed atomic or molecular patterns causes errant behavior [30, 31]. If too thick, there is not enough feedback signal between the probe tip and sample to do the necessary manipulations [31].

(4) The atomic circuitry must not require mechanical or other reset processes, but be instantly reusable with toggleable inputs from an outside source. Returning to the cascading CO molecule work by IBM [12], a problem with the circuity arose in that there was no easy reset. Like their dominoes analog, every run required the CO pieces to be "set back up" manually, making the circuits one-time use. Practical technology needs to be immediately reusable.

One candidate that addressed the manual reset limitation was quantum dot based technologies. Initial implementations were not atom-sized, instead being on the order of microns, but are important to mention as they established the proof of concept we employ in our suggested successor. Lent *et al.* proposed the first scheme called quantum cellular automata (QCA) in 1993 [32]. Instead of encoding binary information in a conventional transistor, the 0's and 1's of binary could instead be encoded into the spatial position of charge in tunnel-coupled quantum dot cell structures [32]; electrons could freely tunnel (rearrange) among quantum dots in a defined logic cell, but could not tunnel between cells. Cells instead communicated electrostatically with each other; by cells being cleverly geometrically arranged to exploit electrostatic interactions, a given cell toggled into a particular binary state would subsequently cause charge rearrangements in the other cells, performing operations on the binary

information. Experimental realization was shown by Orlov *et al.* in 1997 where micron-sized aluminum islands acted as the quantum dots, which were coupled to each other through tunnel junctions [33]. Electrometers measured the charge state of the dots (if charge localized on it or not), while leads actuated the inputs electrically [33–36]. With this they solved the issue of a mechanical reset, but were still cryogenically limited. The aluminum island quantum dots were large, translating to narrow energy levels between the dot's quantized charge states; without milli-Kelvin temperatures they would not work, with the dots charge being easily thermally excited out of its ground state. They were potentially quite power efficient, but the initial trials offered no gain in other areas.

Dopant atoms implanted in silicon are another notable scheme that addresses both the need for no mechanical reset and achieves some electrical isolation. Dopant atoms in silicon can have discrete energy levels in the band gap [37, 38], meaning they should not couple with the substrate. An electrically addressable single atom transistor was demonstrated in 2012 by Fuechsle *et al.*, with a single dopant atom placed between conductive electrodes acting as the source, gate, and drain [39]. By sweeping the bias on the electrodes, they were able to observe transitions of the dopant atom between the zero, one, and two electron states, thereby causing changes in the conductivity of the transistor. However, again cryogenic temperatures were required for the correct operation of the transistor, failing the thermal stability criteria. Additionally, the electrodes were large making compactness an issue.

(5) Atomic patterns must have scalability. With average CMOS chips having tens of billions of transistors, it is conceivable that a replacement technology will eventually require a similar amount. Technologies that have a prohibitively difficult manufacturing processes with no opportunities for large scale output would be limited. This scalability includes ways to not only make the structures with acceptable yield, but also some kind of error-correction functionality.

(6) Information in atomic logic structures must be robust, with a full accounting for noise and destabilization sources. While this somewhat ties into not needing cryogenic temperatures, there are additional potential sources of information loss beyond thermal considerations; variation in the homogeneity of properties of the

surface or local defects may have a similar destabilizing effect. A deep understanding of the material substrate and the atomic patterns on it is necessary to ensure correct operation under a wide variety of parameters.

(7) An ability to build on the silicon infrastructure that already exists. This criteria is more optional than the others, but is desirable for cutting down development time by not requiring retooling of a whole industry. A path to next generation computing that preserves the current massive technological investment into silicon is conceptually desirable, as it is easier to build on existing knowledge rather than develop it anew. In addition, it enables intermediary opportunities where atom computing can be slowly phased in to perhaps optimize pieces of existing chips.

With these seven criteria in mind, we now put forth our scheme based on patternable atom-sized quantum dots that addresses, or has potential to address, all these conditions.

1.3 Computation with Atom-Sized Quantum Dots

Returning to our early quantum-dot-based predecessors, authors Orlov *et al.* commented "The scalability of QCA offers the future possibility of functional devices that, at the molecular level, can operate at room temperature." The micron-sized quantum dots they made required cryogenic temperatures because of their large size. By shrinking a quantum dot down, the gap between its energy levels are increased, making it more resistant to thermal excitation from ground state.

Here we propose the ultimately small quantum dot that capitalizes on this: dangling bonds (DBs) on the otherwise hydrogen-terminated silicon (H:Si(100) or H:Si) surface. These dangling bonds are the fundamental building block of our atomic electronics, with attractive properties that can meet many of the rigorous criteria introduced earlier. Before discussing how well they meet the criteria, we first discuss their attractive properties and how they are being deployed.

Beginning with how they are made, on H:Si every surface silicon atom is capped by a single hydrogen atom, such that all potential bonds are satisfied. If the hydrogen cap is removed, a dangling bond is left behind. Removal of a single hydrogen cap

is accomplished with atomic precision using voltage pulses from a sharp tip [40–46]. The resulting manufactured DB is fundamentally an electrically isolated atom-sized quantum dot with three quantized charge states: DB^-, DB^0, and DB^+. It is considered electrically isolated because these DB charge states all have their electronic energies within the bandgap of the bulk material, naturally keeping them from substantially mixing with bulk properties [47, 48].

A DB's quantum dot nature makes them well suited for QCA-style implementations of quantum dot computation, where some DBs form cells that can contain charge, and neighboring DB cells or inputs electrostatically act on a cell to cause charge rearrangements within. Particular spatial arrangements of charge within a cell represents the binary information [49]. Specifically, our proposed scheme deploys pairs of dangling bonds (two DBs with an intervening hydrogen atom) as the cells, with the pair containing a single moveable electron. If the electron is electrostatically coerced to localize on the left side of the pair, it represents a binary 0, and if on the right, a binary 1. Higher order logic is achieved by arranging many pairs (cells) to electrostatically interact with each other in predictable ways, as will be experimentally shown later (See Section 4.1).

Unlike the large quantum dots used previously, the small size of our dots allows close spacing. This, in turn, leads to large intra-dot energy level spacing of the aforementioned quantized charge states, and thus large interaction energies with other DBs [49–51]. At spacings of order $\sim 1\ nm$ to create a DB binary pair, the DB's have an interaction energy of $\sim 100 - 400\ meV$ depending on the spacing [49, 51, 52]. The thermal background bath at room temperature ($k_B T$) is $\sim 25\ meV$, an energy 4-16$\times$ below what would thermally destabilize (excite out of their ground state) the binary information in a pair with the above quoted interaction energies. As additional support for room temperature operation in our scheme, Pitters *et al.* performed a prior STM-based study of DB assemblies at room temperature, showing electrostatic control over the charge distribution within [51]. These results taken together imply binary information is held stably enough to withstand thermal environmental noise, while also not having an excessive cost (only a few hundred meV) required to switch the binary information in the cell.

How fast a switch of the binary information in a cell can be performed under an applied input is also anticipated to be fast. Tunneling is the mechanism thought to facilitate the rearrangement of the electron from one side of a pair to another, with prior theoretical work calculating a tunneling rate on order of 10 THz [50]. This value is a positive indicator for how fast a cell could reactively switch binary states under an applied input, supposing simultaneous development of a way to perform the required electrostatic gating on similar time scales. This estimated 10 THz value does have two *caveats* though. First, results in this thesis present new findings, such as lattice relaxation, that were not factored in to the original modeling, suggesting more sophisticated theory may be required. Second, it is only a theoretical estimate at this time, inviting future experimental testing. Both issues, that of experimental testing of the switch rate and more sophisticated modeling, are beyond the scope of this manuscript, but are well poised to be performed with the insights provided by this work.

Finally, we discuss structural stability. Structural stability, or how well the patterned DBs stay in place, is necessarily different than the previously discussed operational stability, where the binary information in retained in a given cell. Unlike all the prior atomic and molecular logic implementations discussed earlier, dangling bonds are different in that they are not weakly physisorbed on the surface. Once fabricated, prior work has shown DB motion absent up to $200°C$ [51,53,54].

We now return to the seven-point list of goals for a good successor technology. **(1)** DBs have the potential to offer miniaturization, fast switching speeds, and power efficiency increases. **(2)** They do not require cryogenic temperatures to remain structurally stable, with strong evidence supporting operational stability for binary logic at room temperature. **(3)** DBs are substantially electrically isolated from the substrate as gap states, with no complicated insulating layers required. **(4)** DB logic cells rely on electrostatic interactions, suggesting they can be controlled in the future by metallic leads without the need for mechanical reset. **(7)** They are built on a silicon platform, a material the computing industry is familiar with and greatly invested in.

Not addressed from the list, however, are advancements toward **(5)** scalability

and **(6)** an examination of non-thermal destabilization sources. In addition, while dangling bond's utility for atomic logic had been hypothesized [45, 50, 55] and even rudimentarily realized [19, 21, 51] in earlier works, results presented as part of this thesis present a significant leap forward. Here we demonstrate higher order functionality, enhanced understanding, and numerical quantification of DB logic ensembles. Thus, this thesis aims to expand on these new-found findings for DB atomic logic, and lend strength to the unaddressed areas; we enhance scalability through the introduction of error-correction, as well as undertake an examination of electrostatic destabilization sources. With this we intend to advance DB atomic logic to a new level of sophistication and utility. A final accounting of how well met these seven criteria are will be presented again in the conclusion.

1.4 Structure of the Thesis

The goal of this work is to present a comprehensive approach to atomic electronics based on patterned dangling bonds on H:Si. Three first-author papers and many co-authorships resulted from study of this material system, demonstrating the richness of physics explorable on it (See Section 6.2 for a list of publications). To present these many results in an organized package, this thesis will be centered around the three key advancements of atomic fabrication error-correction, dangling bond logic demonstration, and electrostatic environment analysis, with some of the smaller results that went into co-authored publications injected as needed. The structure is as follows:

Chapter 2 will introduce the background to the H:Si surface and the most commonly used tools and techniques employed to probe it. It introduces both the scanning tunneling microscope (STM) and the non-contact atomic force microscope (AFM), with a special focus on the extensively used AFM. This focus includes information about our particular class of AFM sensor (qPlus), tip apex structure and functionalization considerations, subtleties of tip interactions with the surface, and key spectroscopic AFM techniques like Kelvin Probe Force Microscopy (KPFM). Additionally, while dangling bonds have been briefly introduced in this section, deeper

insight will be given into how tip interactions effect DB charge states, the fabrication of DBs in the lab, and a brief introduction to error-correction of DB structures.

Chapter's 3, 4, and 5 will each focus on a separate first author paper. A brief introduction will place the corresponding result in the context of other works, the paper and paper's supplementary information will be presented, and an appendix section will follow containing additional details that did not make it into the publication or were discovered later.

Chapter 3 discusses a novel and precisely controllable error correction methodology developed for DB structures. While DBs have been easily made for several decades with voltage pulses that remove the hydrogen cap, there was no reciprocal way to correct mistakes. Our methodology relies on a single hydrogen atom from the surface being "picked up" by a tip, and subsequently brought toward a DB to mechanically-induce the formation of a silicon-hydrogen covalent bond. This perfectly erases a mispatterned DB, with no change to tip or surface except the exchange of the functionalizing hydrogen atom. It can be repeated many times over with perfect control, enabling a significant advancement in dangling bond pattern scalability.

Chapter 4 investigates one and two-dimensional DB-based logic structures. Paired dangling bonds occupied by one moveable electron form a binary electronic building block. These blocks are arranged to electrostatically communicate with each other, with the electron position in every cell representing the binary information. These pairs are deployed to make both a DB wire and a logical OR gate. Unpaired negatively charged single dangling bonds act as electrostatic inputs for these demonstrations, inducing the rearrangement of charge, and thus binary information, within the structures. Using the error correction methodology from Chapter 3, the structure's single DB inputs can also be erased as needed, toggling the gates and wires through their binary outputs as observed in AFM Δf topographic maps. AFM $\Delta f(V)$ spectroscopy is performed on a simple binary logic case, quantifying the bit energy experimentally.

Chapter 5 explores variations in the electrostatic environment of H:Si, with ramifications for DB structures. With atom-sized devices, electrostatic irregularities in

the local environment on order of the device size can affect its functionality. We look at variations in the electrostatic topography on the sub-nm scale using atomic force microscopy techniques, and develop a new surface analysis methodology based on using a DB as a moveable electrostatic point-probe. This point-probe method allows us to extract important parameters about the surface, such as its screening length and dielectric constant, through fitting of the measured spectroscopic shifts.

Chapter 6 concludes with investigating how well this preliminary work meets the technology criteria established in the introduction and provides an outlook toward future experiments.

Chapter 2

System and Techniques

In this chapter, a background on the equipment, experimental techniques, and history critical to replicating and interpreting the results presented later is given. All experiments were performed in a low-temperature (LT) commercial Scienta-Omicron scanning probe microscope (SPM), capable of both scanning tunneling microscopy (STM) and non-contact atomic force microscopy (AFM). The fundamentals of STM and AFM, the non-contact AFM qPlus sensor, tip apex structure and functionalization peculiarities, preparation of the hydrogen-terminated silicon (100) surface, sharpening procedure for our probe tips, basic properties of dangling bonds, how to create and erase dangling bonds, and the AFM spectroscopic techniques of $\Delta f(z)$ and $\Delta f(V)$, are all expanded on.

2.1 The Scanning Tunneling Microscope

Both the scanning tunneling microscope and the atomic force microscope belong to a broader category called scanning probe microscopes. Members of this family have existed for almost four decades, and have become the preferred tools to view and manipulate individual atoms. AFM and STM have a commonality in that they both rely on the principal of a sharp scanning probe tip being brought close enough to an atomic surface to receive a signal. The signal type is different between the two

techniques, but ultimately gives atomically-resolved information about the probe-surface interaction. Focusing first on STM, the microscope relies on a quantum tunneling current generated by an applied bias voltage between the probe and sample. It was invented in 1981 by researchers Binnig and Rohrer [56–58], with its astounding ability garnering them a Nobel prize a few years later in 1986.

To generate the quantum tunneling current, a conductive tip is first approached very close to a conductive sample (several Å away). A voltage V (interchangeably called bias) is applied between the two closely spaced, but critically not touching, conductors, resulting in electrons quantum mechanically tunneling across the vacuum gap barrier. If electrons tunnel tip to surface, they are being injected into the available empty states of the electronic band structure of the sample, and thus it is termed empty state STM imaging. Conversely, surface to tip electron traversal means electrons are being pulled out from the filled surface bands, with it denoted as filled state STM imaging. By convention, the surface or sample is used as the reference for where V is applied generally. This tunneling current is exponential with tip-sample distance, with a decay constant of about 1 Å. To illustrate, a distance decrease between tip and sample of 1 Å results in an order of magnitude increase in tunneling current, and *vice versa* [59]. This relationship was used by Binnig and Rohrer as a measure that their first STM system was working, saying "Such an exponential distance dependence of R(s) [distance] should only be observed for a *tunnel* current." [57]. This sensitivity with distance also highlights the need for exceptional control; as an average atom is also ∼Å in diameter, the tip and sample are consistently kept mere atomic diameters apart. Control on such small length scales is performed using the fine control afforded by piezoelectric materials.

A piezoelectric material has a reciprocal relationship between physical geometry and voltage. This means it undergoes a physical deformation when a voltage is applied to it, and, conversely, generates a voltage under physical deformation. This allows electrostatics to precisely govern movement of a tip above a surface where traditional mechanical control methods would move too coarsely. Binnig and Rohrer used piezoelectrics for their inaugural STM paper [57], although the infrastructure has been refined since. The Scienta-Omicron STM/AFM used in this work uses a

ferroelectric (a sub-class of piezoelectric) tube scanner, although some other SPMs use individual piezoelectric elements for each direction. These tube scanners can move with sub-angstrom accuracy, but only have an absolute scan range of a few microns at low temperatures. Coarse positioning of the tip before the tube scanner is required is done by a separate mechanism called a stick-slip piezoelectric motor, which moves in 200 nm coarse steps. The coarse stick-slip motor brings the tip and sample close, and the tube scanner deals with fine movements within tunneling range of the sample. To generate both STM and AFM images, the tip is raster scanned with piezoelectrics over a defined area, acquiring a signal for each pixel.

2.1.1 Types of STM Scanning: Constant-Height and Constant-Current

Within STM probing of a surface, there are two modes of scanning used in parts of this thesis: constant-current and constant-height. In the constant-current STM scanning mode a fixed bias is applied between probe and sample, and a feedback loop controls the tip-sample distance to maintain a current (I) set-point. Examples of STM constant-current scanning are shown in Figure 2.1(a,b). The feedback loop maintains $I = 50\ pA$ by increasing or decreasing the tip-sample separation distance as required, generating a height map. The scale bar below these panels denotes the height adjustment of the tip in picometers. Thus, features that conduct current easily will appear "higher" (more tip sample separation) than features that are less conductive (probe and tip are brought closer). At this point though it must clearly be stated that this topography is not purely atomic height, but is also convoluted with the local density of states (LDOS) [59]. Certain features have a differing amount of electron states at particular energies (bias values), meaning it is technically a mapping of the states available. This is also why both empty (positive sample bias) and filled (negative sample bias) state STM images are generally provided in the literature.

Figure 2.1(c) shows a constant-height STM image of the same area. In this STM mode, a fixed tip-sample distance called z_{rel} is selected and current is measured as the

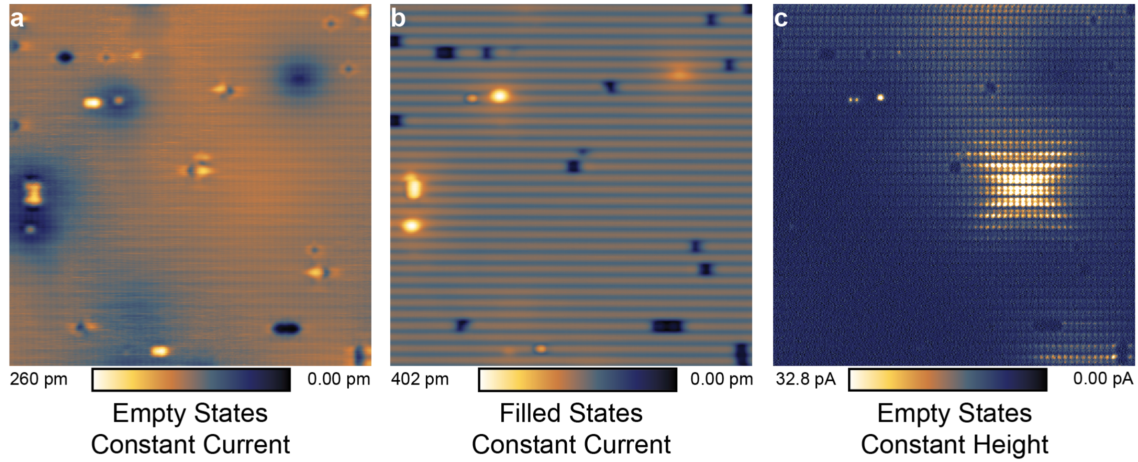

Figure 2.1: **Different STM Imaging Modes of the Same Sample Area of H-Terminated Silicon.** **(a)** STM constant-current empty states image, with electrons being injected from the tip into the available empty states in the sample ($V = 1.3\ V$, $I = 50\ pA$). The tip-sample distance (z-height) is adjusted by a feedback loop to maintain a constant tunneling current of $I = 50\ pA$. **(b)** STM constant-current filled states image, with electrons pulled into the tip from the filled states of the sample. **(c)** STM constant-height image of the same area. A fixed tip-sample height is selected, and current is recorded as the surface is scanned ($V = 300\ mV$, $z_{rel} = -300\ pm$). Compare units for the color bars as an additional indicator for the STM imaging type (pm *vs.* pA). All images are $25 \times 25\ nm^2$ in area, and z_{rel} is a measure of the relative tip-sample height as referenced to a known STM set-point. The set-point used is a response current of $I = 50\ pA$ over a hydrogen atom, with an applied tip-sample bias of $V = -1.8\ V$.

tip is raster scanned through the plane. It may be asked why both constant-current and constant-height are needed. These STM types are complimentary techniques. Figure 2.1(c) is a good example with the image showing an "X-shaped" feature that is not seen in the constant-current panels (a,b). The "X" is associated with a sub-surface arsenic atom that shows up well at modest bias ($V = 300\ mV$) but is eclipsed by band current at higher ones ($V = 1.3\ V$ or $V = -1.8\ V$). A deeper discussion is given later about these sub-surface arsenic atoms in the paper "Electrostatic Landscape of a H-Silicon Surface Probed by a Moveable Quantum Dot" in Section 5.1.

Constant-current scanning could not be attempted at $V = 300\ mV$ to find this feature either; semiconductors have a band gap where no tunneling current is generated, with $V = 300\ mV$ falling in this zero-current region. In other words, the arsenic is conductive at $V = 300\ mV$, but the areas around it are not (See the current topography in Figure 2.1(c)). If constant-current STM scanning was attempted at this modest bias value, the control electronics would attempt to meet the tunneling current set-point over these non-conductive areas by bringing the tip closer to the sample, never find any current, and eventually crash them together. Constant-height scanning has no such limitation as it just observes current in the fixed height plane.

Constant-height scanning, however, does have the limitation of requiring low-temperatures (∼4 K) to maintain full control of the tip-sample distance. The scanner components are cooled to 4 K by being in thermal equilibrium with a liquid helium cryogenic bath. This prevents any significant thermal fluctuations that could cause expansion or contraction of the STM's constituent parts, meaning the tip remains in the set height-plane without the need for active adjustment. At elevated temperatures, constant-height scanning could theoretically be performed if thermal fluctuations could be controlled for, but this is difficult. Materials often have a more sensitive coefficient of thermal expansion at elevated temperatures (fractional change in size per degree change in temperature), translating to the tip or the sample drifting about in position more for minor thermal fluctuations. This puts the tip and sample at enhanced risk of damage through unintended contact and makes constant-height scanning unachievable. Conversely, constant-current scanning has no thermal limitation, with the feedback loop constantly making adjustments for any thermally-

induced drift. Thus, while the drift is present in constant-current scanning, it is hidden by the action of the feedback loops. In conclusion, when deciding what STM scanning variation to use, the right technique must be chosen for the information desired.

The selection of z_{rel} also warrants some deeper discussion. In SPM there is no absolute way to perfectly measure tip-sample separation. It may be thought that the best measure could be to touch the probe and sample together first, then retracting to the desired target height. There are two problems with this. First, with touching it becomes likely to damage the probe or sample. Second, the idea of what constitutes *touching* is ill formed. It could be defined as when repulsive forces onset, when the electron shells touch, or when the system mechanically deforms. All of this is no less arbitrary than picking an easily accessed reference point defined by non-damaging STM values. In our case, a tunneling current of $I = 50\ pA$ over a surface hydrogen atom center with an applied bias of $V = -1.8\ V$ is arbitrarily selected. While this too is not a perfectly reproducible measure as tunneling current is dependent on the apex imaging orbital which can change (See Section 2.2.5), and there can be local variations in conductivity both from the finite size of dopant-related features (See Figure 2.1(c)) or irregular doping in general (See Section 5.1), it is the best accessible one. In addition, while different macroscopic areas or combinations of tip and sample might not be perfectly comparable with this reference, local areas should be. That is, if a tip does not change and the same local reference is used for an experiment, the height and absolute differences of the data should be consistent. Controlling for tip changes during an experiment can be challenging, but is necessary for quantitative data.

2.2 The Atomic Force Microscope

The Atomic Force Microscope is another member of the SPM family and was invented five years after the STM in 1986. Pioneered by researchers Binnig, Quate, and Gerber, their Physical Review Letter paper detailing it went on to become one of the most cited papers in the journal of all time [60]. Today, AFM is routinely used in

a wide variety of applications and fields [61], perhaps even more than STM. Despite this, the difficulty of the technique and additional precise control for AFM feedback required meant it took nearly a decade since its inception to fully mature to a tool with atomic resolution [62].

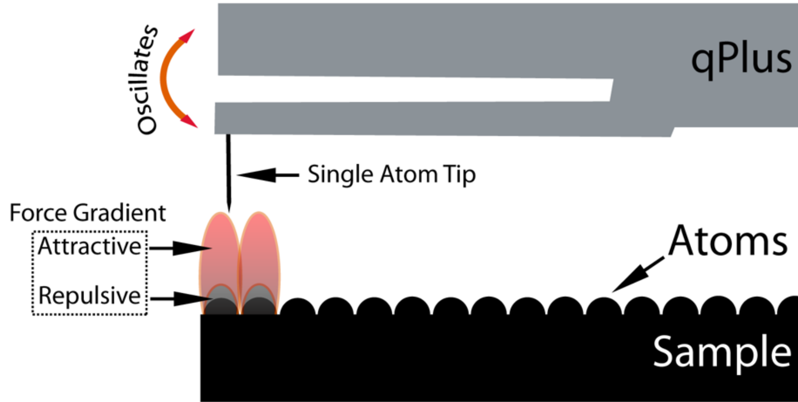

Figure 2.2: **Illustration of an AFM Sensor Interacting with a Surface.** A single-atom tip is mounted to the end of an oscillating cantilever with resonance frequency f_0. The tip is brought close enough to the surface atoms to feel the force gradient, which shifts the resonance frequency as $f_0 + \Delta f$. This shifting of the resonance (Δf) is tracked as the signal for AFM scanning.

AFM was initially developed because of a need for a technique that worked on insulators or, as in our case, in the band gap of a material where STM could not give a signal. Instead of having a conductive tip measuring tunneling current, AFM uses an oscillating tip as a force sensor. In its simplest form, it can be analogized as a "nano-finger" brought close enough to read the "atomic braille" force. An illustration highlighting the principal is shown in Figure 2.2. The probe approaches with a fixed resonance frequency f_0 defined by the geometry, Young's modulus, and mass of the oscillator. When it reaches a point that it can interact with the surface forces, this resonance is shifted to $f_0 + \Delta f$. The shift (Δf) is tracked and tells something of the probe-surface interaction.

A more detailed, but still qualitative, look at the force gradient from Figure 2.2 is plotted as a distant-dependent interaction between tip and sample in Figure

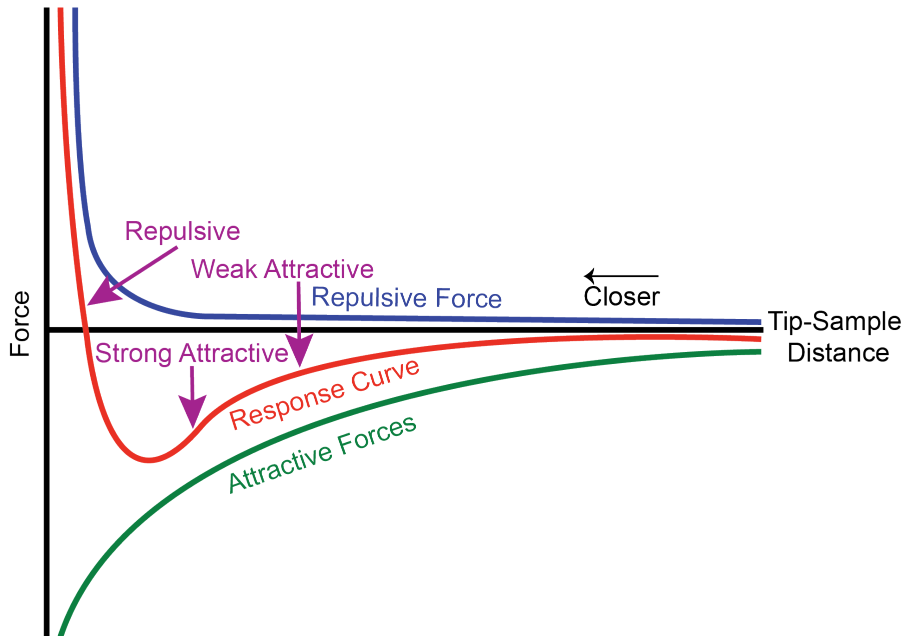

Figure 2.3: **Qualitative Model of Force Components and Decay Distances Seen by AFM**. Attractive forces are plotted in green and repulsive force in blue. Summed together, these give a corresponding response curve in red, which is what is seen by the AFM sensor. The response curve has a markedly non-monotonic shape with different imaging regimes classified as weak attractive, strong attractive, and repulsive. Going right to left on the x-axis brings the tip-sample system closer together.

2.3. While the real picture is more complicated, this figure highlights the main force components and that they have different distant-dependent decay lengths. For attractive forces (green curve), components include electrostatic interactions, van der Waals, chemical forces, and magnetic dipole forces. The distance-dependent decay for attractive forces are approximated as changing as $\frac{-1}{z^7}$ assuming a Lenard-Jones force interaction, with z being the tip-sample distance [63]. When the tip-sample distance is reduced, Pauli exclusion onsets for close approach and the tip becomes repelled (blue curve). This generally goes as $\frac{1}{z^{13}}$ in the Lenard-Jones model. The sum of these interactions leads to a non-monotonic response curve seen by the AFM sensor (red curve) as:

$$F_{LJ}(z) = -12\frac{E_{Bond}}{\sigma}\left[\left(\frac{\sigma}{z}\right)^{7} - \left(\frac{\sigma}{z}\right)^{13}\right] \tag{2.1}$$

Where $F_{LJ}(z)$ is the Lenard-Jones force between tip and sample, E_{Bond} is the bond energy, σ is the equilibrium distance, and z is the tip-sample distance [63]. E_{Bond} and σ could be fit to a real system if desired, but again it is stressed that this simple Lenard-Jones model does not capture the minutiae of a real system. It is, however, instructive; it highlights that attractive forces dominate as the larger magnitude contributor to Δf for most of the response curve, repulsive force is only significant for small tip-sample separations, and the measured force interaction is markedly non-monotonic. Additionally, three broad imaging regimes of weak attractive, strong attractive, and repulsive are labeled. Imaging in the weakly attractive part of the curve often does not provide atomic resolution, the strongly attractive regime generally allows good signal-to-noise ratio imaging of the surface, and the repulsive regime begins to display the surface as more "bond-like" (See Figure 2.17 for a height series of our surface in these regimes).

For comparison to the Lenard-Jones toy model, an experimental response curve, also called AFM $\Delta f(z)$ spectroscopy, is given in Figure 2.4(a). It can be seen that the real system presents deviations in its form when compared to the smoothly-varying toy system from Figure 2.3. The experimental data from Figure 2.4(a) was converted first from frequency shift to force in Figure 2.4(b) using the Sader-

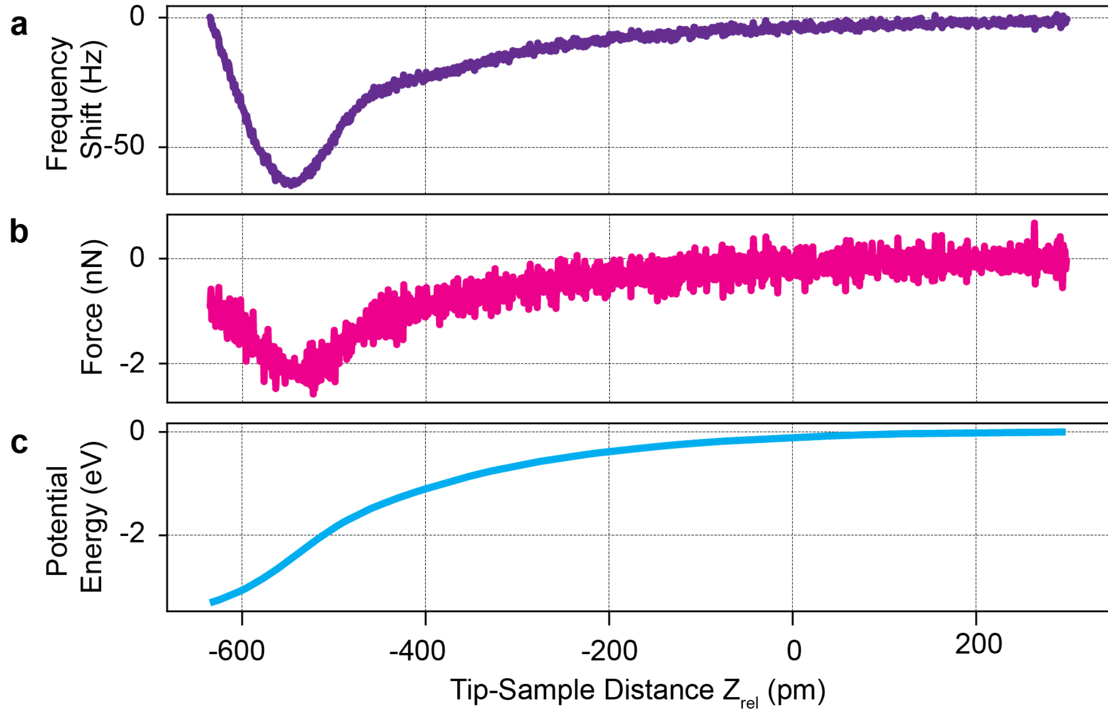

Figure 2.4: **Experimental Frequency Shift Data Converted to Force and Potential Energy.** **(a)** An experimental $\Delta f(z)$ curve obtained by approaching the AFM tip to a hydrogen atom on the H-terminated (100) surface ($V = 0.0\ V$ and $Osc.\ Amp. = 100\ pm$). **(b)** Force as a function of tip-sample distance. The curve from (a) was converted to force by means of the Sader-Jarvis method [64] assuming $f_0 = 28528\ Hz$, $k = 1800\ N/m$, and $Osc.\ Amp. = 100\ pm$. **(c)** The curve from (b), converted to potential energy through numerical trapezoidal integration. On the x-axis, 0 references a z_{rel} height defined by a STM tunneling current of $I = 50\ pA$ with $V = -1.8\ V$ applied, as taken over a surface hydrogen atom. The tip-sample relative distance is reduced by going right to left on the x-axis.

Jarvis method [64, 65], and finally to potential energy though numerical integration in Figure 2.4(c) (since $F = \frac{-dU}{dz}$). A methodology for conversion between frequency shift and force (Sader-Jarvis) exists because of the aforementioned non-monotonic shape of the response curve, which complicates the math of the conversion. As part of the conversion inputs of the cantilever spring constant (k), oscillation amplitude (*Osc. Amp.*), and resonance frequency (f_0) are required, although it is sometimes difficult to precisely know all these values. For example, Falter *et al.* found large spreads in the spring constant (k) of AFM qPlus sensors from minute manufacturing variations [66]. While qPlus sensors (See Section 2.2.3 for details on these) are often quoted to have $k = 1800\ N/m$, Falter's work concluded "differences of 50% are typically found" [66]. Due to the problematic nature of extracting accurate values for these inputs combined with the fact that no experiments presented herein require quantitative force modeling, no further experimental data in this work is converted to force. Good analysis of the involved mathematics and limitations of the Sader-Jarvis method are available in the literature though [63, 64].

2.2.1 AFM Feedback Control

Precise feedback control is required for stable AFM operation. Examining the y-axis of the force curve in Figure 2.4(b), AFM is capable of measuring forces in the nN range requiring feedback to be sensitive. In addition, the sensitive forces can change rapidly in sign and magnitude as a surface with diverse features of different reactivity is scanned, requiring feedback to also be robust to change. This was not the case for early AFM systems.

One of the reasons for the long implementation time of AFM was a phenomena called "jump to contact" [67]. In early AFM, the tip was not oscillated and the cantilever had a very weak spring constant. The weak spring constant was necessary so that if it was brought close to a feature, it would mechanically deflect enough for detection. A single feedback loop operating on tip-sample height would continually adjust the separation, maintaining a fixed deflection set-point. This combination of a weak spring constant and no oscillation meant that if the tip was scanned from a

passive to reactive feature, the feedback loop could not adjust fast enough and the probe would crash into the surface. This scanning variety was called “Static AFM”.

Today, almost all AFMs use “Dynamic Scanning” where an oscillation is applied to the cantilever, such that the oscillating probe stores enough energy to make it robust to destabilizing upon a sudden change in force [67]. Within the realm of dynamic scanning there are two particular sub-classes: amplitude-modulated AFM (AM-AFM) and frequency-modulated AFM (FM-AFM).

To elaborate briefly on both, the tip-sample system can first be approximated as a mass suspended between two springs as illustrated in Figure 2.5(a,b). The tip is mounted on the end of an oscillating cantilever, which has a spring constant $k_{Cantilever}$ consistent with its material and geometry [66]. Interactions of the tip with the atom being probed are treated as a non-monotonic varying spring $k_{Tip-Sample}$. To be clear on the relationship between force and $k_{Cantilever}$, it is known from Hooke's Law that $k = -\frac{\partial F}{\partial x}$. Thus, the derivative in position of the non-monotonic response curve from earlier in Figure 2.3 is equivalent to $k_{Tip-Sample}$, which is necessarily also non-monotonic. $k_{Tip-Sample}$ will thus vary in strength with tip-sample distance.

Figure 2.5(c) illustrates the principal of AM-AFM. The black curve is the resonance response of the cantilever as a free oscillator, with eigenfrequency f_0. The AM-AFM is set up such that the cantilever is excited at a fixed frequency near, but critically not on, resonance. This is shown as the control electronics applying the driving energy a bit off resonance at f_d and measuring the corresponding amplitude for this point in the curve (labeled 1 in Figure 2.5(c)). As the tip is scanned across an area with an attractive interaction the resonance of the system is shifted to a lower value (purple curve in Figure 2.5(c)). Looking at the dashed orange circles, this shift produces a significant reduction in amplitude at f_d (labeled 2 in Figure 2.5(c)), as the electronics are now attempting to drive the oscillator even further off resonance. Conversely, a modest repulsive interaction would shift the driving impulse to be applied more on resonance, thereby increasing the amplitude. The control electronics look to match a fixed amplitude set-point in AM-AFM, which is accomplished by adjusting the tip-sample height upon these amplitude-changing interactions. While this was a more robust form of AFM than static scanning, issues with stability still

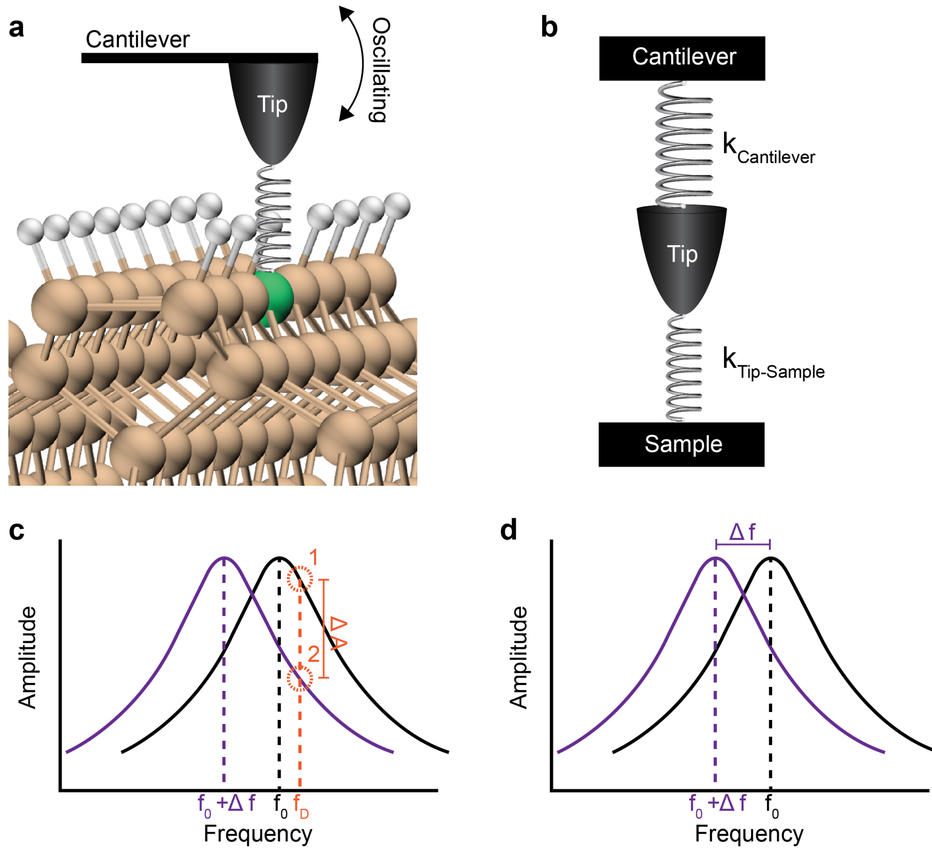

Figure 2.5: **Dynamic Scanning: AFM Interactions with the Surface.** **(a)** A tip mounted to an oscillating cantilever is brought close enough to an atom (highlighted in green) to feel the forces coming off it. **(b)** The system to first order acts as a mass with two springs. The tip has the spring constant of the cantilever on one side and the spring constant of the interaction with the target atom on the other. While $k_{Cantilever}$ is a constant, $k_{Tip-Sample}$ changes non-monotonically with height from the green atom. **(c)** Schematic of amplitude-modulated AFM. f_0 is the resonance frequency of the mass-spring system, with the corresponding black curve the resonance curve of the same system under no surface/atom interaction. In AM-AFM the system is driven slightly off-resonance at f_D, with the amplitude monitored at this frequency. The purple curve is the shift of the resonance when in interaction with an attractive feature such as the green atom. This modifies the tip-sample system as illustrated (b) to have competing springs, shifting the unperturbed resonance f_0 to $f_0 + \Delta f$. Orange dashed circles highlight the reduction in amplitude for a changing interaction. **(d)** Schematic of frequency-modulation AFM. Changes in the resonance of the system from (b) are now tracked as a Δf signal only, with the electronics watching the peak movement.

persisted.

If a repulsive interaction is taken to an extreme in AM-AFM, the amplitude would decrease as the peak of the resonance curve was passed due to the symmetric nature of the curve. This would be a false attractive force, with feedback systems tending to overdrive and crash the cantilever. This was termed the AM-AFM jump to contact. In addition, amplitude can be a slow signal to acquire. As with any mass on a spring system, there is an associated ring down time for the oscillator in the presence of damping. Waiting for the amplitude to stabilize after an interaction (damping) with a high quality factor oscillator can be prohibitively time consumptive. Due to these limitations, AM-AFM fell out of favor for the more robust FM-AFM.

FM-AFM was introduced by T.R. Albrecht *et al.* in 1991 [68], with Figure 2.5(d) demonstrating the tracked signal of FM-AFM: the shifting resonance frequency. It is perhaps slightly more complicated than AM-AFM in the sense that it requires multiple feedback loops simultaneously operating. The feedback loops in our system are all proportional-integral (PI) controllers part of our Nanonis SPM control software. Under the umbrella of general FM-AFM scanning, there are a few sub-classes of scan type which are defined by the particular feedback loops in operation. The first mode of FM-AFM involves three feedback loops operating: one maintaining a fixed oscillation amplitude by adjusting the applied driving excitation, a second tracking phase such that the excitation is applied on resonance and the Δf shift is known, and a third adjusting tip-sample height to maintain a fixed shift off resonance (a desired Δf set-point). This style was not used in this work due to stability considerations; the H:Si(100) surface is relatively inert with small frequency shifts on the order of -2 to -15 Hz, but dangling bonds however, our entity of interest, could prompt shifts on the order of -90 Hz. This dramatic change in reactivity during scanning from one entity to the other would often bring one of the three feedback loops out of stable operation range, crashing the tip. A second mode of FM-AFM operation did prove to be stable for DB analysis though.

The FM-AFM scanning mode used exclusively in this work is a constant-height version of the priorly discussed three-feedback-loop one. As with constant-height STM, first a fixed z_{rel} height from the surface is selected. The desired image is taken

in this fixed height plane with varying Δf measured as the signal. This mode reduces the number of feedback loops to two. Again, the first feedback loop maintains a fixed amplitude by regulating excitation. This regulation is done through adjustments to the sine wave voltage applied to the z-piezo stage the AFM sensor sits on, varying how hard it is driven. The second feedback loop monitors the phase, ensuring excitation is applied on resonance and also that the shift off resonance (Δf) is being tracked. No feedback is used on height, with this mode referred to as constant-height AFM scanning. To be technically correct, non-contact constant-height FM-AFM was used for all experiments in this thesis, but the catch-all term of just "AFM" will be used in the remainder of this work for simplicity. Like its STM counterpart, constant-height AFM requires low-temperatures to maintain full control of the tip-sample distance, but has the benefit of being a robust scanning mode for our desired DB analysis.

As proof of constant-height AFM's robustness, Figure 2.6 shows an example where part of the image was taken on inert hydrogen-terminated silicon (bottom half), and the other part is over reactive bare silicon (top half). Figure 2.6(a) shows the STM image of the area and (b) the AFM constant-height scan. Despite the change in reactivity, the feedback loops encountered no issues in scanning the area. As an added point of interest, the AFM image on bare silicon shows the characteristic buckled dimer structure of (100) [69–71], whereas the H:Si portion shows the stabilized non-buckled rows (See Section 2.3).

2.2.2 Relationship Between Frequency and Force

Earlier it was discussed that the non-monotonic nature of $k_{Tip-Sample}$ complicates the mathematics of converting from Δf to force. While that remains true for driven FM-AFM motion in the large amplitude limit, approximations can be made for small amplitudes. To give a flavor for how Δf and force are linked, the mathematics involved in the small amplitude approximation are described starting from the two spring principal introduced in Figure 2.5(b). We start with the formalism for the eigenfrequency (resonance) of a harmonic oscillator:

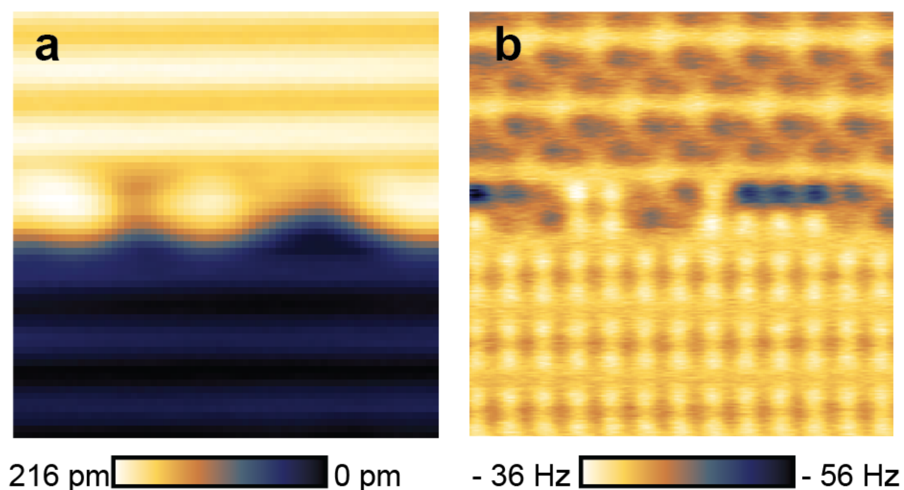

Figure 2.6: **Stable Constant-Height Scanning During a Change in Reactivity.** **(a)** Constant-current filled states STM image of a 5×5 nm^2 area of half hydrogen-terminated Si(100) (bottom) and half bare Si(100) (top) ($V = -1.8$ V and $I = 50$ pA). **(b)** Constant-height AFM image of the same area, highlighting the ability of the technique to handle significant changes in reactivity without a loss of scan stability. The hydrogen-terminated portion of the AFM image has straight rows, whereas the bare silicon portion appears as a bucked zig-zag with a double-tip artifact apparent ($V = 0$ V, $z_{rel} = -430$ pm, $Osc.$ $Amp = 50$ pm).

$$f_{0,1} = \frac{1}{2\pi}\sqrt{\frac{k_{Cantilever}}{m}} \tag{2.2}$$

Where $k_{Cantilever}$ is the cantilever spring constant, m its effective mass, and $f_{0,1}$ its eigenfrequency under no perturbation. This oscillator is then brought close to the surface such that it can feel the second spring $k_{Tip-Sample}$:

$$k_{total} = k_{Cantilever} + k_{Tip-Sample} \tag{2.3}$$

This gives a new resonance for the system as:

$$f_{0,2} = \frac{1}{2\pi}\sqrt{\frac{k_{Cantilever} + k_{Tip-Sample}}{m}} \tag{2.4}$$

With $f_{0,2}$ the new resonance frequency after the addition of $k_{Tip-Sample}$. The shift of resonance is thus:

$$\Delta f = f_{0,2} - f_{0,1} = \frac{1}{2\pi}\left(\sqrt{\frac{k_{Cantilever} + k_{Tip-Sample}}{m}} - \sqrt{\frac{k_{Cantilever}}{m}}\right) \tag{2.5}$$

Earlier it was shown that $k_{Tip-Sample}$ is non-monotonic since the tip-sample force curve is non-monotonic (See Section 2.2.1). For large amplitudes this non-monotonic nature means weighting has to be applied to $k_{Tip-Sample}$ for a correct mathematical interpretation [63, 64]. In the limit of small oscillations where $k_{Tip-Sample} << k$, Equation 2.5 can be simplified using a binomial expansion of the square-root giving:

$$\Delta f = \frac{1}{4\pi}\left(\frac{k_{Tip-Sample}}{\sqrt{mk_{Cantilever}}}\right) \tag{2.6}$$

Going back to Equation 2.2, $\sqrt{m}$ can be solved for and substituted into Equation 2.6 to get:

$$\Delta f = \frac{f_{0,1}k_{Tip-Sample}}{2k_{Cantilever}} \tag{2.7}$$

To relate this expression to force it can be observed that force and spring constant are linked through Hooke's Law:

$$k_{Tip-Sample} = \frac{-\partial F_{Tip-Sample}}{\partial z} \tag{2.8}$$

This expression is substituted into Equation 2.7 to give the small amplitude approximation for FM-AFM:

$$\Delta f = \frac{-f_{0,1}}{2k_{Cantilever}} \frac{\partial F_{Tip-Sample}}{\partial z} \tag{2.9}$$

Force could be obtained through integration of this expression, with this derivation hopefully inspiring an intuitive understanding of the link between frequency shift and force. This limit is applicable for experiments where the decay length of the force examined is on the order with the amplitude of the oscillator [67]. This relationship is also important for understanding contact potential difference measurements, which are discussed later in Section 2.4.3.

2.2.3 The qPlus AFM Sensor

The first AFM sensor was hand fabricated from gold and diamond [60]. Shortly thereafter, processing was refined with micro-machining of tips from SiO_2 and Si_3N_4 [72, 73]. In this work, the qPlus type of AFM sensor (third-generation) was exclusively used, which is capable of both STM and AFM thanks to a metallic tip with connection for the tunneling current.

The prototype of the qPlus sensor was developed by Giessibl in 1998 [74] and originally consisted of a quartz tuning fork, taken from the watch industry, with one of two prongs glued to a ceramic stage [73]. Giessibl selected these forks as the basis for his sensors because of their superior properties for AFM; namely, their self-sensing piezoelectric nature, high stiffness (or spring constant) enabling small amplitude scanning, and exceptional operational stability under varying thermal load. In more detail, quartz shows remarkable frequency stability with changing temperature, making it ideal for variable-temperature SPM set-ups [75]. In addition,

quartz is a naturally piezoelectric material. As discussed earlier in Section 2.1, small mechanical deformations on a piezoelectric material will produce a corresponding voltage signal. By oscillating this quartz cantilever through mechanical driving, a periodic voltage signal is generated that can directly be read, making it "self-sensing" [73]. This periodic voltage is processed in the SPM control electronics by a pre-amplifier, with perturbations in the voltage signal from interactions with the surface correlated to a shift in the resonance frequency.

qPlus sensors are also comparatively stiff. The micro-machined cantilevers employed before qPlus had spring constants of $k = 0.01 - 15\ N/m$, but qPlus sensors are orders of magnitude stiffer at $k = 1800\ N/m$ [76]. This high spring constant is advantageous because it allows for stable small amplitude scanning, while still allowing the sensor to store enough energy to avoid jumping to contact. Small amplitudes allow an operator to be more targeted in the forces they want to examine, enabling probing of a dominant force contributor in small ranges of the tip-sample response curve [67, 73, 77, 78]. Larger amplitudes tend to convolute the differently-decaying forces, as the oscillation averages over a larger portion of the distant-dependent curve.

Figure 2.7(a-c) show a top-down, back-side, and front-side view of a typical qPlus sensor, respectively, as used for all experiments in this work. It is comprised of a gold-plated base with three conductive legs, a ceramic mounting square with electrodes placed on the sides, a quartz cantilever glued to the ceramic mount, and a tip placed on the end of the cantilever. The tip is not visible in any of these optical views due to its small size of a few μm (See Figure 2.8 for scanning electron microscope images of it). This qPlus is a third generation design [73], where improvements have been made in the connectivity. Examining Figure 2.7(d), this sensor has a top electrode that transmits the AFM qPlus deflection signal, a middle electrode that carries the STM current signal, and a bottom electrode that is grounded and encompasses the current electrode. These are connected to gold pattering on the sides of the ceramic mounting stage by means of conductive epoxy or spot-welds, such that it can transmit the relevant signals through the legs to the scanner's processing electronics. This separation of the signals is different than the early AFM qPlus sensors, where less care was devoted to shielding them. While the self-sensing nature

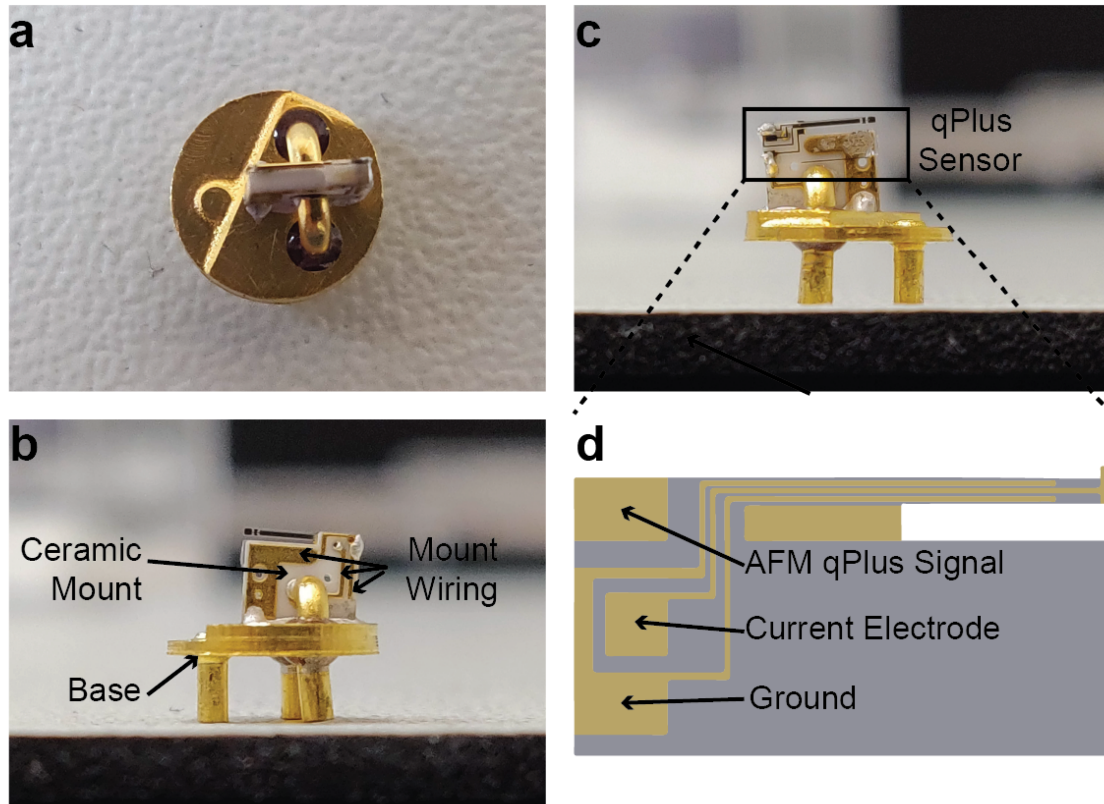

Figure 2.7: **The qPlus AFM Sensor.** **(a)** Top-down, **(b)** back-side, and **(c)** front-side views of a third-generation qPlus sensor. The sensor is comprised of a gold-coated base with three legs, a white ceramic square mounted and wired to the base, and a quartz cantilever glued and wired to the side of the ceramic square. Connectivity between all the parts is accomplished through either gluing with conductive epoxy, or spot-welding of the pads/wiring. Signals are transmitted from the connected pads in **(d)**, down through the legs to the relevant processing electronics in the SPM. A welded tip is mounted on the end of the cantilever, but is too small to be seen in optical images.

of qPlus was overall a benefit, it carried the complication that the presence of a tunneling current may introduce an undesired interference (cross-talk) between the current signal and the AFM deflection signal [78]. Older designs simply had parallel wires running beside each other for the current and AFM deflection signal, where they were close enough to experience capactive coupling between the channels. When this capacitance was discovered, groups started developing ways to reduce it with separate tunneling current wires running to the tip, or clever shielding or insulation [78–80]. With the third generation qPlus design, the shielding is built in with the current electrode surrounded by a ground wire to prevent signal contamination.

However, we stress that even with these improvements for the sensor, cross-talk may still be present. Some cross-talk is the result of capacitance in the instrumentation, meaning it can appear if the SPM is operated in a non-optimized set-up. To reduce instrument capacitance issues, we thus use the Omicron manufacturer-recommended optimized set-up for qPlus scanning, which requires that the tip is grounded and the sample biased.

2.2.4 Tip Material, Mounting, Structure, and Etching

AFM tips made with a plethora of materials are available and have been demonstrated in the literature [67, 76]. In this work, however, tungsten (W(100)) was exclusively used, which either comes pre-mounted to purchased qPlus sensors or, as will be shown shortly for our tips, is welded on using a focused ion beam (FIB) methodology. This tip material was chosen for two reasons. First, is its robustness; tungsten has the highest melting point of any pure metal and the highest tensile strength [81]. This hardiness is an important consideration for keeping a sharp patterning tip that can survive the rigors of many DB creation events (See Section 2.4.2 on making DBs). Second, it can be sharpened to a single-atom tip using an *in-situ* tip etching methodology developed in 2006 by Rezeq *et al.* [82, 83]. This sharpening is important because tip structure effects both the imaging quality of AFM, and its ability to do experiments targeted at specific atom sites. As discussed earlier in Section 2.2, some interaction forces in AFM operate over a large distance and involve tip

atoms well beyond the apex. Having a sharp tip can reduce the contribution of long range forces, while simultaneously minimizing interaction with neighboring surface atoms. This is especially important for this work, as ensembles of closely-spaced atomically-sized dangling bonds are probed.

In more detail about the sharpening process, it starts by first electrochemically etching a piece of $0.1 - 0.13$ mm diameter tungsten wire *ex-situ* in 2 Molar NaOH to a radius of ∼5 nm [84–86]. In this process, the tungsten tip wire serves as an anode for the etch reaction, and a separate piece of coiled tungsten wire in a solution of NaOH acts as the cathode. The tip is dipped in the solution and a DC voltage is applied to control the etch reaction. AC etching is also possible [87], but gives a less sharp apex with more irregular features. For a DC etch, the reaction eats away at the submerged part of the tip wire, with sharpening happening dominantly at the air-solution interface. This interface point reduces in diameter continuously until the lower part of the wire drops off, opening the circuit and stopping the reaction. A sloppy etch will achieve a radius of curvature equal to 50 nm, but radii of $\sim 5 - 10$ nm are regularly seen [82]. This small radius is essential for the next step, involving focused ion beam cutting and welding.

The sharpened tips are put into a FIB where an operator cuts the sharp cone of the apex off, and welds it to the appropriate pad of the qPlus cantilever [88]. This technique was developed to get sensors with more well-defined properties, with a process sequence of the cutting and welding provided in Figure 2.8. Before this methodology, the standard way of mounting a tip on a qPlus cantilever was to glue it by hand with conductive epoxy. This often resulted in long tips with large volumes of epoxy, overly mass loading the oscillator. This mass loading reduced both the resonance frequency and quality factor of the cantilevers, parameters that effect the detection sensitivity of a qPlus [68]. With FIB cutting and welding of a tungsten cone only a few μm in height, these problems are mitigated. More details about FIB welding can be found Ref [88].

With the sensor fully fabricated and ready with a mounted tip, it can be loaded into ultra-high vacuum (UHV) for *in-situ* additional sharpening. The tip is moved to the field ion microscopy (FIM) chamber, with FIM being a technique that allows

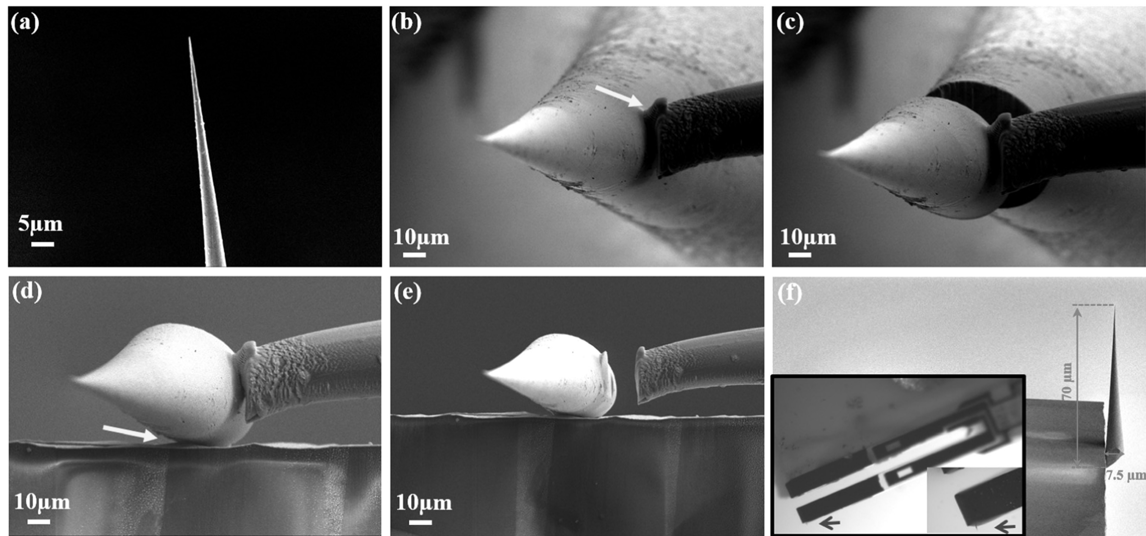

Figure 2.8: **Welding a Micro-Tip to a qPlus Sensor.** Scanning electron microscopy images depicting the fabrication process of cutting and welding a micro-tip to a first-generation qPlus sensor. **(a)** Tungsten tip selection. **(b)** Welding the FIB micro-manipulator to the tungsten tip. **(c)** Micro-tip detachment after FIB cutting of the cone. **(d)** Placing and welding of the FIB cut micro-tip on the qPlus sensor. **(e)** Detachment of the micro-manipulator, leaving the micro-tip fixed to the qPlus sensor. **(f)** Scanning electron microscope image showing the dimensions and shape of the micro-tip. The insert in (f) is an optical micrograph of the whole qPlus after FIB fabrication. Reproduced from Ref [88] [doi:10.1016/j.ultramic.2015.06.008] as a co-author on the work, with permission under their policy for reproduction in theses and dissertations.

visualization of the sharpening process as a projected image of the apex atoms on a screen. Pioneered by Muller and Bahadur in 1955 [89], FIM was the first technique to allow individual atoms to be spatially resolved [90]. It works by the sharp tungsten tip having a positive voltage of ∼10s of kV applied to it in an atmosphere of an imaging gas. Helium at pressures of $\sim 10^{-5}$ $Torr$ is used which, as it comes in range to the tip apex, is ionized by the strong field to form a positively charged Helium ion [82]. Since the tip has a positive voltage applied, the positive ion is accelerated perpendicularly away from its position on the tip. These ions hit a multi-channel plate followed by a phosphor screen, converting them into photons that replicate the tip atomic structure [90]. To sharpen as part of this process, an etching gas is concurrently added to the chamber.

Molecular nitrogen is added to pressures of 10^{-6} $Torr$ while the first image of the tip with atom resolution is visible in FIM [82, 83]. Nitrogen sharpens the tip by attacking the sides to reduce the apex radius, while not being able to access the apex itself. The apex of the tip has the highest electric field due to its sharp radius, and N_2 has a lower ionization energy than helium. Thus, it cannot get to the apex without first being ionized and ejected away. At the periphery of the tip apex where the field is lower, N_2 reacts with the sides of the tungsten tip to chemically adsorb and dissociate to form strong W-N bonds. These W-N entities protrude from the bulk of the tip, becoming themselves high-field points and evaporating away. This is repeated until the diameter reduces to, ideally, a perfect single-atom tip. An example of the etching process as shown in FIM is given in Figure 2.9, with more details about the methodology in Refs [65, 82].

One point to note from Figure 2.9 is that the tip was not etched to a perfect single atom, instead ending with a small cluster in (f). Irregular starting shapes as in this case can make it challenging to sharpen to a single atom. The tip structure would ideally be perfectly circular in FIM imaging, ensuring an equal nitrogen attack from all sides. The case of an irregular etch and the associated consequences for STM imaging is now discussed as part of Figure 2.10.

Focusing first on Figure 2.10(c), a close-up of the final FIM image of the tip after a partial-etch is displayed. This tip was taken to the SPM scanner and approached

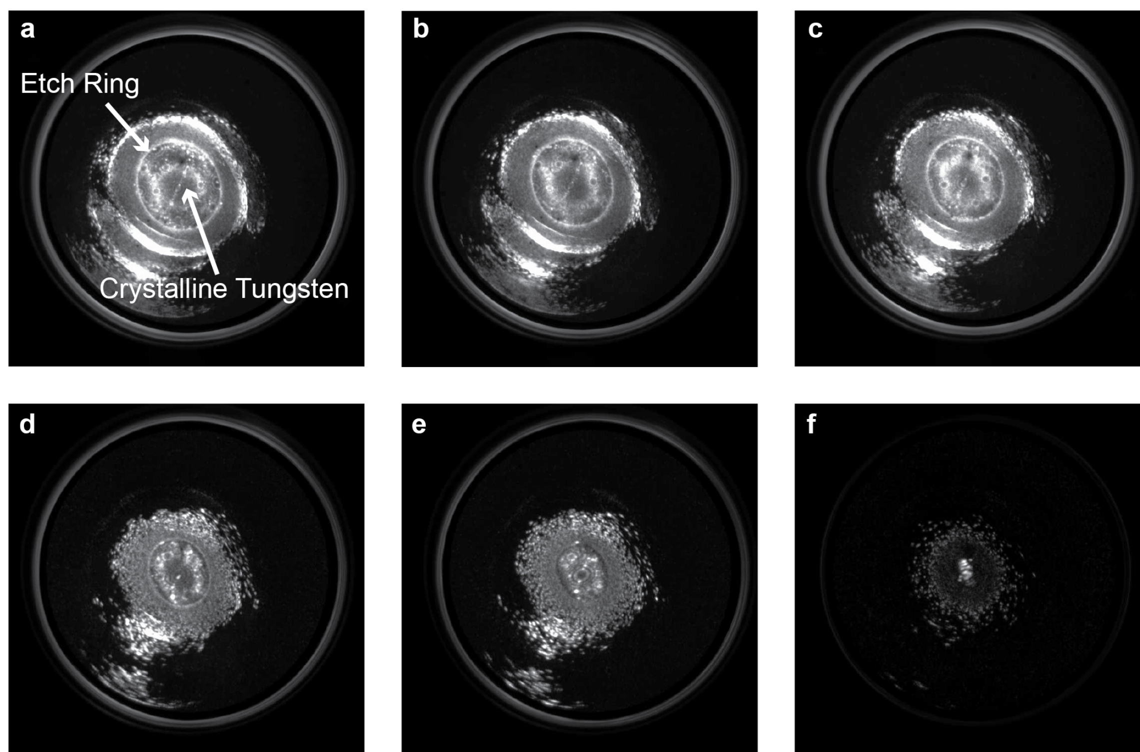

Figure 2.9: **Nitrogen Etching a Tip to a Smaller Radius in FIM. (a-f)** Series of images of a tungsten tip as a nitrogen etch is performed. In (a), a large bright ring on the outside denotes the bulk tip structure as if viewing the tip head-on, with a smaller ring in the middle enclosing the crystalline tungsten atoms that make up the apex. The diameter of the inner etch ring reduces as the etch goes on in time in (b-f), indicating that the tip is sharpening. The etch is stopped in (f), when a sufficiently sharp tip has been achieved.

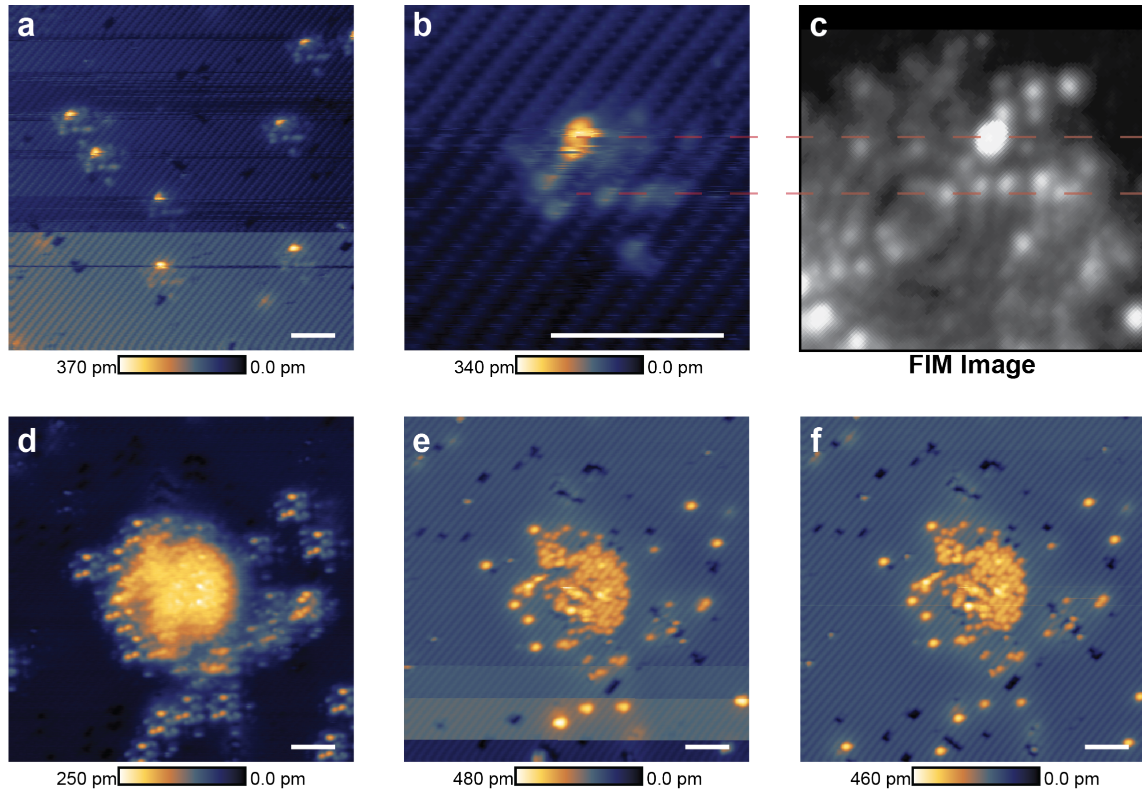

Figure 2.10: **Removing Tip Artifacts *In Situ* Through Tip Contacts (a)** Filled states STM image of the H:Si surface right after approaching a partially sharpened tip from FIM. Half a dozen DBs with a multi-tip artifact are seen as the bright features. Tip instability is evidenced by the streaky changing contrast. **(b)** Zoomed image of single DB with multi-tip artifacts presenting around it. **(c)** FIM image of the partial tip etch before it was taken to the scanner. This can be compared to the STM image in (b), showing matching features. Dashed red lines between (b) and (c) are provided as a guide to the eye. **(d)** Filled states STM image after the creation of a bare silicon tip-forming patch in the center. **(e)** Controlled-contacts are performed on the patch while scanning the area from bottom to top. After every tip contact, the tip-sample junction conductivity is altered through apex changes, with the feedback loop correspondingly adjusting the tip-sample height to maintain the tunneling current set-point. The four different contrast regions seen in (e) are evidence of four tip-contacts made while scanning upward, with the last tip-forming event producing a sharp tip. **(f)** The same area as (d,e) scanned with the sharp tip. DBs now present as point-defects. All STM images were acquired at ($V = -1.8\ V$ and $I = 50\ pA$), with scale bars equal to 5 nm.

to examine the surface, with the first STM image shown in Figure 2.10(a). The tip is both unstable, as evidenced by the streakiness, and shows what is called a multi-tip artifact; the roughly half a dozen bright features are actually single DBs that are not appearing as point-features as they should. A single-atom tip would measure a given DB only once, but if a multi-tip raster scans over the DB it has many atoms at the apex that are each within a distance to measure duplicate images. Similar artifact features also arise in AFM images with multi-tips. Examining a zoom of a single DB in Figure 2.10(b), it can be seen that the image artifacts match similar protruding atoms from the FIM image in (c) (dashed red lines have been provided as a guide to the eye). If a tip is incompletely etched, flattened in a tip-sample crash, or loses its apex from an event, multi-tip artifacts will appear.

Multi-tips are fixed through a procedure which involves creating a patch of bare silicon through hydrogen desorption, positioning the tip over the patch, and performing controlled-contacts of the tip to the surface [91–93], as shown in Figure 2.10(d-f). While it seems counter-intuitive that contacts with the surface would sharpen a tip, it is a staple technique of the SPM world, often returning a tip to single-atom character given enough time. Figure 2.10(d) shows the tip-forming patch immediately after its creation. The bright bare silicon area in the middle was created by slowly scanning over a $10 \times 10\ nm^2$ square at STM set-points of $I = 150\ pA$ and $V = 4.0\ V$. Tip-forming contacts are done by "dipping" the tip in $\sim 600 - 1000\ pm$ from an initial height set-point defined by the STM scan parameters of $I = 50\ pA$ and $V = -1.8\ V$. Changes in tip character from these contacts are evidenced by the changing brightness at the bottom of Figure 2.10(e). The four regions of differing brightness as the scan was conducted suggest four tip contacts were made; after every tip contact the tip-sample junction conductivity is altered through apex changes, with the feedback loop correspondingly adjusting the relative tip-sample height to maintain the tunneling current set-point. These tip contacts are performed until good DB contrast with sharp edges is achieved, as in the top two-thirds of (e). A final scan of the patch area with the sharp tip given in Figure 2.10(f). Additionally, as a point of interest, it can be seen that the tip contacts on the bare patch ended up passivating pieces of the hydrogen-desorbed square, suggesting the desorption process coated the tip

in hydrogen. When the tip is single-atom sharp, it is ready to be used for AFM or STM experiments.

2.2.5 Apex Functionalization

One important factor not yet discussed is the terminating (functionalizing) apex atom for a tip. The apex atom is known to drastically effect the imaging in AFM. For example, a silicon tip would have its contrast dominated by the formation of covalent bonds with the surface [94, 95]; CO functionalized tips, pioneered by researchers at IBM Zurich [96], use Pauli repulsion to give exceptional resolution [97]; and metal tips are generally non-reactive but can have large induced dipoles due to the Smoluchowski effect [98, 99], where electron redistribution occurs to minimize energy [100]. Some tips, like the CO ones, are hyper flexible leading to imaging artifacts. Others, like nitrous oxide [101] and copper oxide [102], are rigid due to a higher coordination number. Thus, each functionalization has its own chemical structure, flexibility, and charge distribution [103], which in turn has consequences for AFM contrast, how perturbative the measurements are, if imaging artifacts are generated from flexibility, the absolute spatial resolution achievable [101], and how AFM spectroscopy like $\Delta f(z)$ and $\Delta f(V)$ presents [103]. The last point is especially important, as both these spectroscopy types are commonly used in this work. To highlight this sensitivity in our system, several case examples are provided.

Figure 2.11 illustrates the case of tip-forming's effect on measured interactions in $\Delta f(z)$. This is not necessarily a case of changing only the apex atom, as tip-forming is not an exactingly controlled experiment, with it being equally possible that the coordination of the apex atom was changed, or the relative proportion of silicon/-tungsten/hydrogen comprising the apex altered. Despite this, it is an instructive example of the magnitude of change that can be expected for comparatively minor tip alterations. In Figure 2.11, a $\Delta f(z)$ curve was taken over a reference hydrogen atom to probe the interaction potential with a sharp artifact-free single-atom tip (blue curve). The tip was then taken to a silicon patch, tip-formed several times gently (no more than $\sim 700-800$ pm in from the STM set-point) while ensuring the

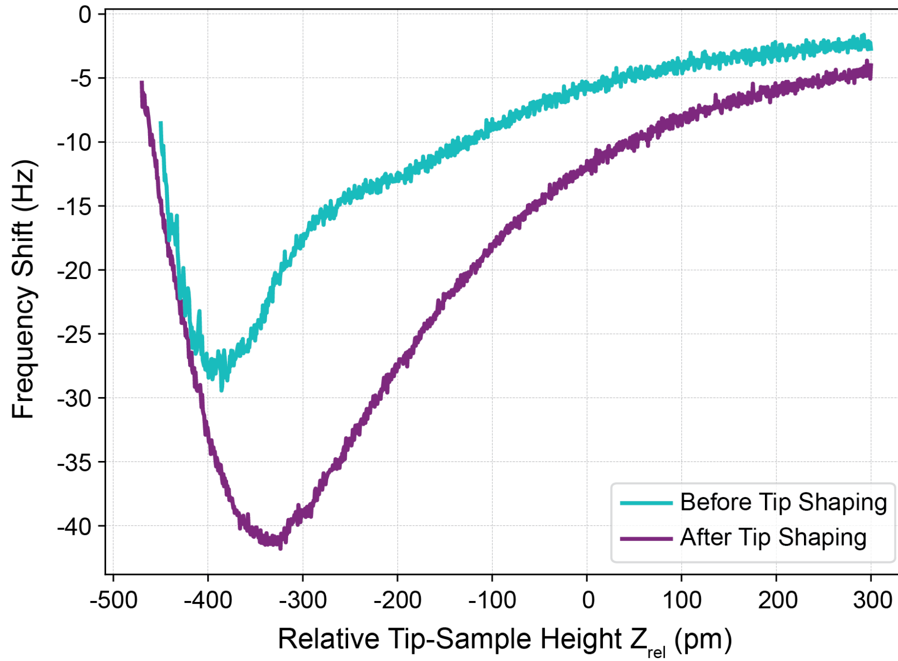

Figure 2.11: **Tip Forming and the Resulting Change in AFM Interaction.** $\Delta f(z)$ spectroscopy was taken over a hydrogen atom reference using a sharp single-atom tip (blue curve). Afterward, a series of gentle tip forms on a silicon patch were performed. The tip was verified to still be single-atom sharp, as evidenced by its STM contrast, and a second $\Delta f(z)$ curve was taken over the same hydrogen atom reference again (purple curve) ($Osc.\ Amp. = 50\ pm$). $z_{rel} = 0$ is referenced to a STM set-point of $V = -1.8\ V$ and $I = 50\ pA$ over a hydrogen atom.

tip remained sharp and artifact-free, and the spectroscopy repeated with the newly-altered apex (purple curve). Despite being sharp and single atom in both cases, the curves are quite different. This can now be taken a step further with an experiment where only the apex atom is changed.

This experiment was done as part of the published paper (Atomic White-Out) in Section 3.1, Figure 3.3. Examining Figure 3.3(a), the tip starts out intentionally functionalized with a hydrogen atom, after which a $\Delta f(z)$ curve is performed over a reference hydrogen atom in Figure 3.3(b). The hydrogen is then carefully removed in a gentle erasure event in Figure 3.3(c,d) that changes only the apex atom (See Section 2.4.2 for functionalization and erasure details), and the $\Delta f(z)$ spectroscopy is re-performed over the common reference in Figure 3.3(f). Comparing (b) and (f), the curves are different solely due to the change of a single functionalizing apex atom. It is thought that the tip used to take Figure 3.3(f) is likely silicon, which would have a more attractive interaction. This would agree with results from Sharp *et al.* where they performed a study of silicon *vs.* hydrogen tips on the H:Si surface, finding silicon-terminated tips to be more attracted to hydrogen atoms due to their chemical reactivity [104]. The tip functionalization is not known precisely because unless the tip is intentionally functionalized with something like CO or copper oxide, it is a guess based on the materials at hand. As explained earlier (See Section 2.2.4), a common method to sharpen our tips is to do controlled contacts with a silicon patch *in situ*. It is presumable this process coats the tungsten tip in silicon, which has been verified by Sweetman *et al.* in the literature using a combined scanning electron microscopy (SEM) and energy dispersive X-ray (EDX) spectroscopy study on a STM tip that underwent similar preparation [105]. Despite knowing silicon is on the tip though, how it is coordinated and if it also has hydrogen or tungsten mixed in remains uncertain.

A third example of the importance of tip functionalization is shown in Figure 2.12, where a change in AFM Δf contrast is induced by the addition of a single hydrogen atom to the apex. Figure 2.12(a,b) show STM images of the H:Si surface using a presumed silicon tip apex, with (c) the AFM Δf image of the same area. Examining Figure 2.12(c) closer, curiously the surface hydrogen atoms running in

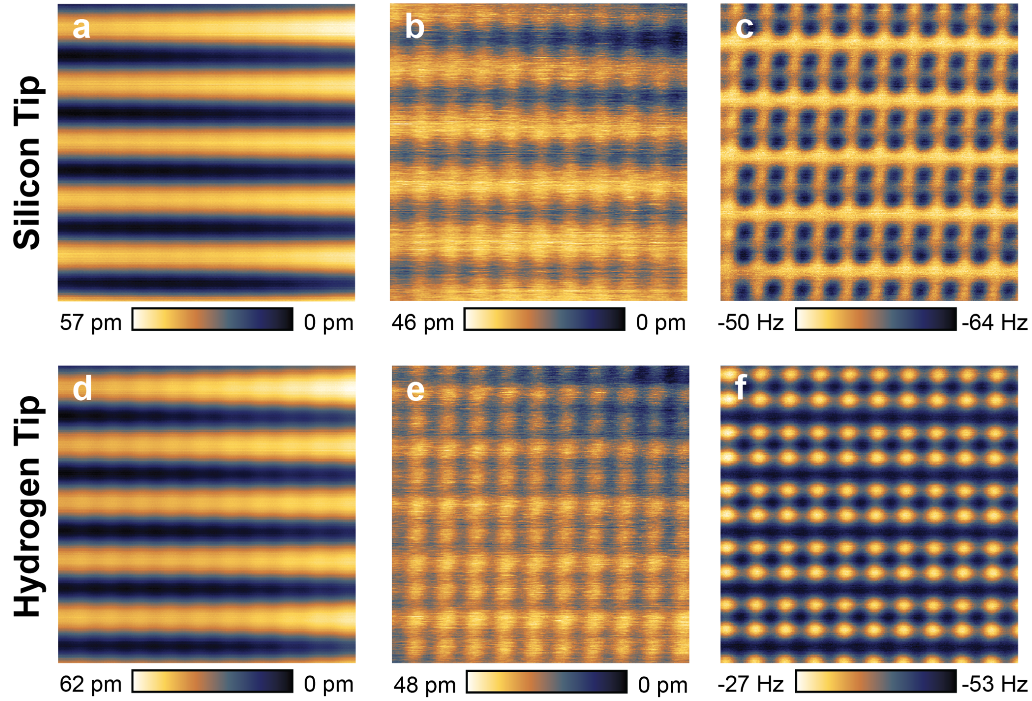

Figure 2.12: **Contrast Inversion with Tip Functionalization Change.** **(a)** Filled states ($V = -1.8\ V$, $I = 50\ pA$) and **(b)** empty states ($V = 1.3\ V$, $I = 50\ pA$) STM images of a clean area of H:Si with a presumably silicon tip apex. **(c)** AFM Δf image of the same area, showing the hydrogen atoms as dark circular depressions ($V = 0\ V$, $z_{rel} = -400\ pm$, and $Osc.\ Amp = 50\ pm$). **(d)** Filled states ($V = -1.8\ V$, $I = 50\ pA$) and **(b)** empty states ($V = 1.3\ V$, $I = 50\ pA$) STM images of the same area as (a-c), but after the tip was functionalized with a single hydrogen atom. **(c)** AFM Δf image of the area, showing an inversion of the contrast with the surface hydrogen atoms presenting as white circular protrusions ($V = 0\ V$, $z_{rel} = -300\ pm$, and $Osc.\ Amp = 50\ pm$). All images are $4.0 \times 4.0\ nm^2$

rows horizontally across the frame show up as dark circular depressions, with the in between row areas bright. The tip was then taken a small distance away, functionalized with a single hydrogen atom (See Section 2.4.2 for how functionalization is performed), and the imaging repeated in Figure 2.12(d-f). The STM images in (d,e) show an enhancement in resolution not seen with the silicon tip. Additionally, in the AFM image in Figure 2.12(f) the hydrogen contrast has been inverted; the hydrogen atoms now display as circular white protrusions, and the in between row areas as dark.

Contrast inversion like this has been reported in the literature for similar material systems. Sweetman *et al.* published a study examining inversion of contrast for the bare (not hydrogen terminated) Si(100) surface [105]. They explored a range of different tip apexes with corresponding alteration of the imaging mechanism, even reporting they could sometimes get double-apex tips where one apex was attractive and the other more repulsive [105]. Another study was done on H:Si by Sharp *et al.* examining the properties of hydrogen passivated tips [104]. They reported observation of contrast inversion on the surface when using a silicon-terminated tip *vs.* hydrogen functionalized ones; silicon tips showed a higher attractive interaction, and hydrogen ones a lower. This is in agreement with our contrast observations in Figure 2.12.

A final example of changes induced by an altered tip functionalizing atom is given in Figure 2.13, but now with implications for $\Delta f(V)$ spectroscopy. $\Delta f(V)$'s utility for probing charge in AFM is discussed in depth in Section 2.4.3. As a quick prelude for the purposes of understanding this example, $\Delta f(V)$ can be correlated to a measurement of the local contact potential difference underneath the apex. The "step" seen in Figure 2.13 as bias is swept is an indicator of a single-electron charge state change of the entity underneath, which in this case is a single dangling bond. The purple curve in Figure 2.13 was taken over the DB with what is presumed to be a silicon apex. Subsequently, a hydrogen atom was picked up (Details of how are in Section 3.1) to change the tip functionalization. The spectroscopy was then repeated over the same DB from the same relative tip-sample height, and is displayed as the pink curve in Figure 2.13. Comparing the curves, firstly they show quite different

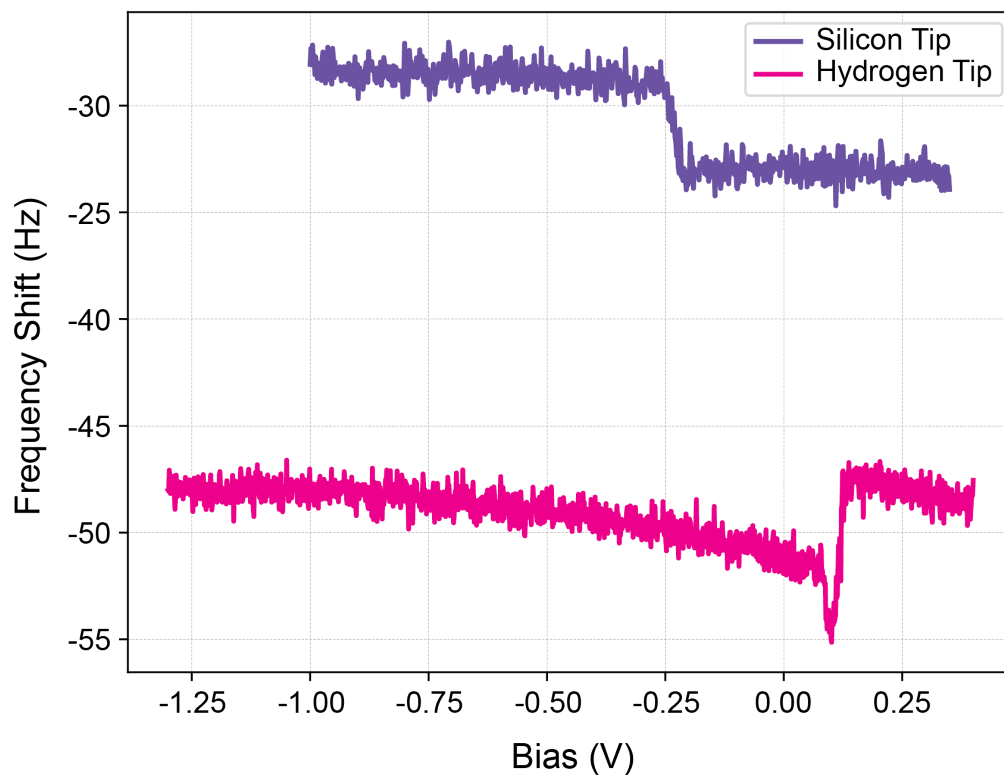

Figure 2.13: **Apex Change Inverts $\Delta f(V)$ Spectroscopy.** $\Delta f(V)$ spectra taken over the same DB using different tip terminations. For the silicon-terminated tip (purple curve), the step occurs at $\sim V = -0.2\ V$. For the hydrogen-terminated tip (pink curve), the overall interaction is shifted vertically down by $\sim -20\ Hz$ (all measured Δf values are more negative in frequency shift), with the step shifted to $\sim V = 0.1\ V$. Additionally, the step direction is opposite between the two cases. ($z_{rel} = -250\ pm$ and $Osc.\ Amp. = 50\ pm$ for both spectra).

absolute frequency shift values. Second, the tips show the charge transition step going in different directions, with one stepping "up" and the other stepping "down". Third, the location of the step is at different bias values for both, with an absolute shift totaling $\sim 0.3\ V$. It is evident that a single-atom change of the apex can have considerable implications for $\Delta f(V)$ measurements.

In summary, when preforming and interpreting any experiments in AFM, tip structure and termination is crucial to control for. A single apex or structural change can mean a data set has to be discarded. For all experiments in the presented papers in Sections 3.1, 4.1, and 5.1, tip changes were systematically controlled for within any given experiment, with a common reference being regularly checked to indicate if there was any change.

2.3 The H:Si (100) Surface

Silicon has been a standard in the semiconductor industry for five decades now. It is a favored material because of its general abundance on earth, and ability to be doped with substitutional atoms that can change its conductivity to specification. To retain the benefit of decades of development already put into silicon-based semiconductors, silicon is used in this work but with the small modification of hydrogen-terminating the surface of it.

Thus, all work was performed on the hydrogen-terminated silicon (100) surface with the 2×1 reconstruction. The silicon wafers used were highly-doped with arsenic (n-doped) to a manufacturers volume concentration of $10^{19} \frac{atoms}{cm^3}$ (or a resistivity of 0.003-0.004 $\Omega \cdot cm$). Samples for our experiments are cleaved from commercially purchased wafers to a size of $3.5 \times 11\ mm$, with cleaving preformed using a sapphire scribe, glass microscope slides to guide the scribe, and ceramic tweezers to handle the sample. Care was taken to use nickel-free tools, as nickel is highly mobile in silicon and known to cause surface roughening [106, 107]. Cleaved samples are mounted in Omicron-SPM-compatible molybdenum sample carriers, as pictured in Figure 2.14(a).

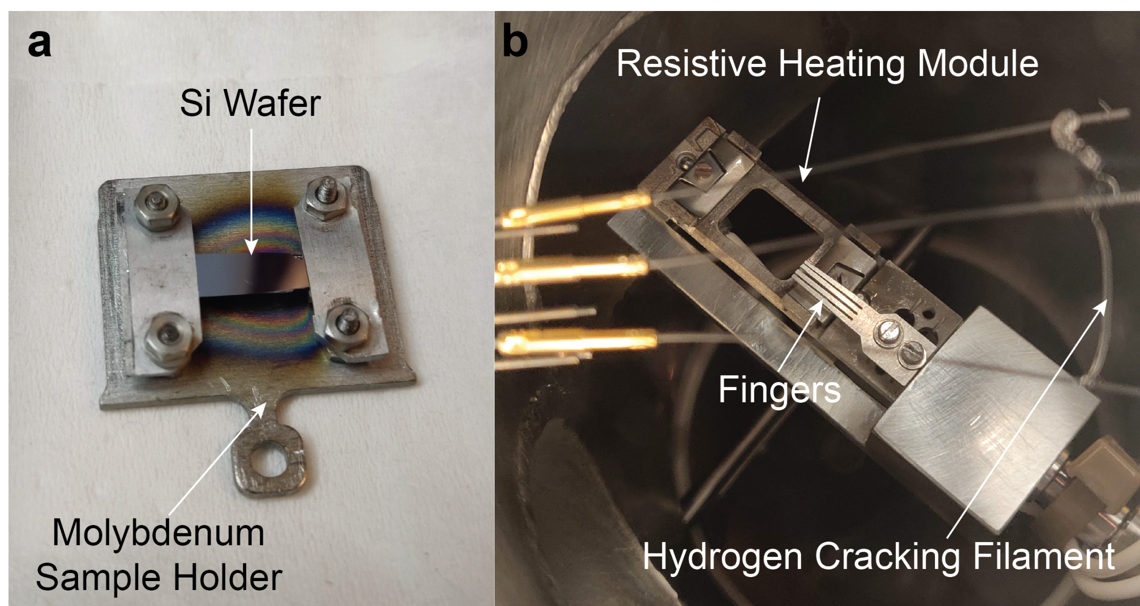

Figure 2.14: **Mounted Silicon Sample and Sample Processing UHV Chamber**. **(a)** Molybdenum sample holder with mounted 3.5×11 mm silicon wafer appearing as the dark rectangle in the middle. **(b)** Picture of the UHV sample preparation chamber. The sample from (a) is loaded into the resistive heating module slot, such that the conductive fingers rest on one side of sample holder. Current can then be applied through the contacts to resistively heat the wafer for oxide removal and hydrogen termination. Molecular hydrogen is leaked in during the termination step, and cracked in to atomic hydrogen on the labeled hot cracking filament.

To prepare a sample for scanning, the sample is first loaded into UHV and then moved into a separate sample preparation chamber for *in situ* processing. It is slotted into the resistive heating module shown in Figure 2.14(b) such that the conductive "fingers" touch one side of the flat molybdenum plate clamping the sample down, while the other side is grounded. Current can thus be run through the wafer with a power supply to induce resistive heating of the crystal. An optical pyrometer, calibrated for the thermal emissivity of silicon, measures the sample temperature. The heating sequence to prepare a wafer starts with an overnight degas at a temperature of $570°C$. This temperature is enough to remove contaminants like water, while not so high as to start removing silicon or oxide [108]. When sufficiently degassed such

that the pressure is not reducing anymore, a series of high temperature "flashes" are applied to remove the oxide layer. Flashing implies a quick rise to the target temperature of $1250°C$, following by a reduction to room temperature. "Quick" is determined by how fast the sample-preparer can turn the power supply knob, although some efforts beyond the scope of this work are being made to automate and standardize sample preparation more rigorously. Oxide removal occurs at roughly $900°C$ [108], with the additional bump in temperature to $1250°C$ intended to remove other more strongly-bound types of contamination like carbide [109], as well as alter the surface charge-carrier concentration through dopant depletion as detailed by Pitters *et al.* [110]. Pitters work found that for $1250°C$ flashes on $10^{19}\frac{atoms}{cm^3}$ n-doped crystals, secondary ion mass spectrometry analysis showed a reduction in the near-surface region of dopant atoms. This dopant-depleted region extended $\sim 70\ nm$ below the sample surface, with a reduced donor concentration of $\sim 10^{18}\frac{atoms}{cm^3}$ [110, 111]. If one wanted to not alter the donor concentration but still remove the oxide coating, $1050°C$ flashes could be done instead [110]. $1250°C$ flashes were used for all experiments in this work, as it often produces cleaner surfaces with larger defect-free areas. After three to four $1250°C$ flashes, the oxide would be removed and a bare dopant-depleted silicon surface left behind.

The final step involves hydrogen-terminating the bare surface at a precise temperature to ensure the intended surface reconstruction. During the last oxide removal flash, instead of returning to room temperature, the DC value necessary to hold the crystal at $330°C$ is found and recorded. This is the optimal temperature to achieve a dominantly 2×1 reconstruction of H:Si(100) [112, 113]. Lower temperatures tend to produce the 3×1 ($\sim 127°C$) and 1×1 ($\sim 30°C$) reconstructions [114–116]. Higher temperatures will increase DBs as thermal desorption begins to compete with H adsorption [117]. With the current for $330°C$ known, the crystal is again cooled to room temperature, diatomic H_2 gas is added to the chamber to a pressure of 10^{-6} Torr, and a hydrogen "cracking" tungsten filament at $1600°C$ is turned on. The hot cracking filament splits the diatomic H_2 into lone H atoms, such that they can bond with the surface [118]. While the cracking is ongoing, the sample is flashed a final time to $1250°C$, and immediately brought to the target reconstruction temperature

for 2×1 of $330°C$. The termination is allowed to progress for 2 minutes to allow sufficient hydrogen coverage, which generally ends up being in the 99% range. After 2 minutes, everything is shut off and the sample is rapidly transferred to the scanner.

It may be asked why the H:Si(100) 2×1 reconstruction was chosen when higher surface-symmetry reconstructions like H:Si(111) 1×1 may be more desirable for atomic electronics. The reasoning is the ease of making the surface. The procedure for making *in situ* H:Si(100) 2×1 is well established and results in comparatively large and clean areas. Brief attempts to make H:Si(111) 1×1 *in situ* using the methodology from Ref [117] produced unstable, for SPM scanning, surfaces with only small patches of 1×1.

To give an idea of what constitutes large and clean areas for H:Si(100) 2×1, a typical large-scale filled-states STM image of our surface created using the above procedure is shown in Figure 2.15. This image illustrates the typical defect density and that it tends to reconstruct itself as large flat terraced areas. A terrace edge is highlighted with an orange circle. For defects, one can observe dark squares which are etch pits one layer down (pink circle), bright point-defects that are DBs (blue circle), and a smattering of "other defects" (green circles). A concerted effort is presently being made to categorize the nature and cause of these defects to enable better surfaces, but is currently beyond the scope of this work (See "Atomic defects of the hydrogen-terminated silicon(100)-2x1 surface imaged with STM and nc-AFM" in the co-authorship list in Section 6.2 or [119]). Regardless, there are often large clean areas of 10's of nm^2 produced using this methodology, which were sufficient for the experiments in this work.

Going into more detail for the 2×1 reconstruction, every silicon atom is able to make a total of four bonds (four-coordinated). Bulk silicon exhibits the diamond tetrahedral structure, with each atom bonding with its four nearest neighbors. Surface silicon is bonded to two other sub-surface silicon atoms, but due to not having an "upper layer", has a strain imposed from two unsatisfied sp^3 bonds. One sp^3 bond is satisfied by coaxing it to reconstruct into the 2×1 structure through selection of the thermal energy during sample preparation. This facilitates it forming a bond with an equivalently frustrated silicon-atom neighbor, reducing the number of

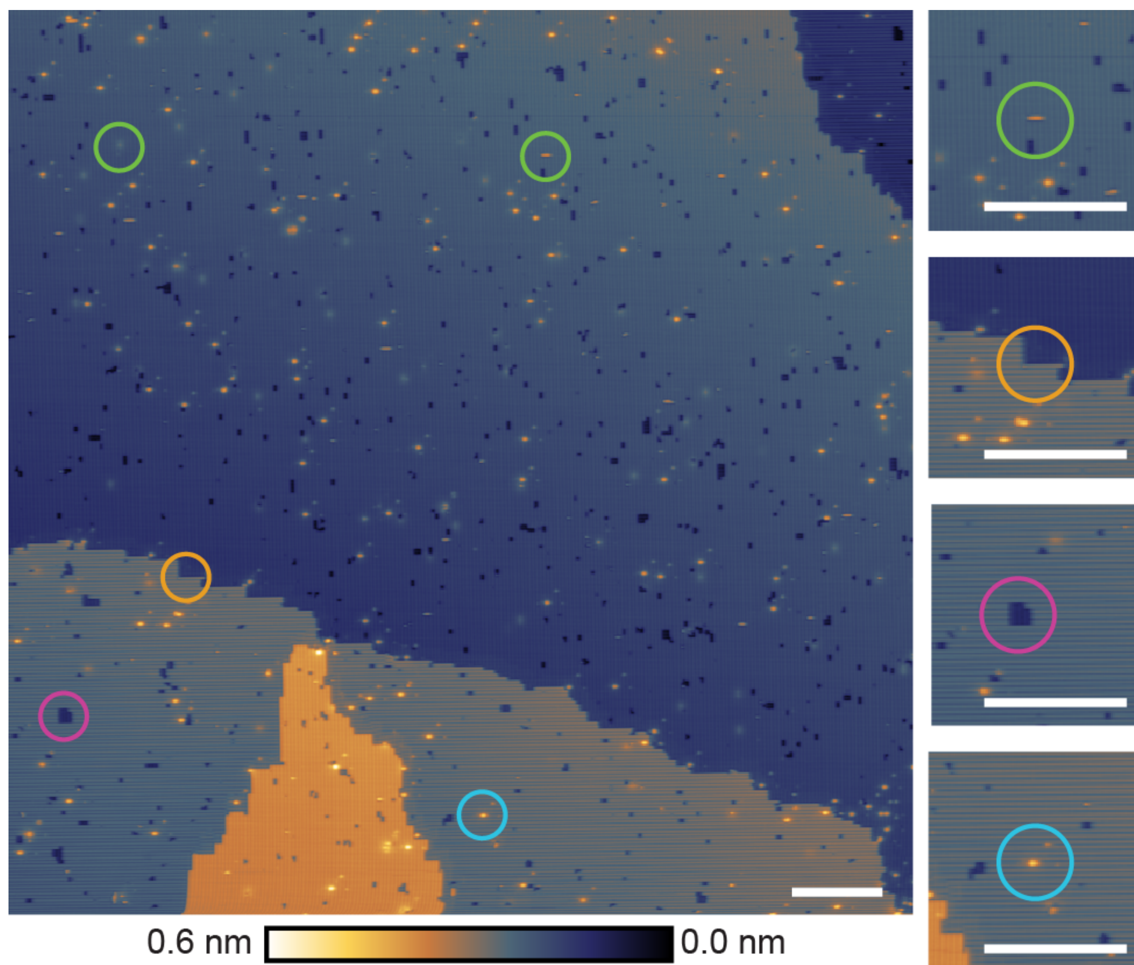

Figure 2.15: **Large Area Image of the H:Si Surface.** Constant-current filled-states STM image of a 200×200 nm^2 area of hydrogen-terminated silicon (100) ($V = -1.8$ V, $I = 50$ pA). Four different terraces on the surface are visible, with one example terrace edge highlighted with the orange circle. This image would be considered average for defect areal density, with example defects of an etch pit (pink circle), dangling bond (blue circle), and two unknowns (green circles), highlighted. Zoomed images of the defects are provided on the right. All scale bars are 20 nm.

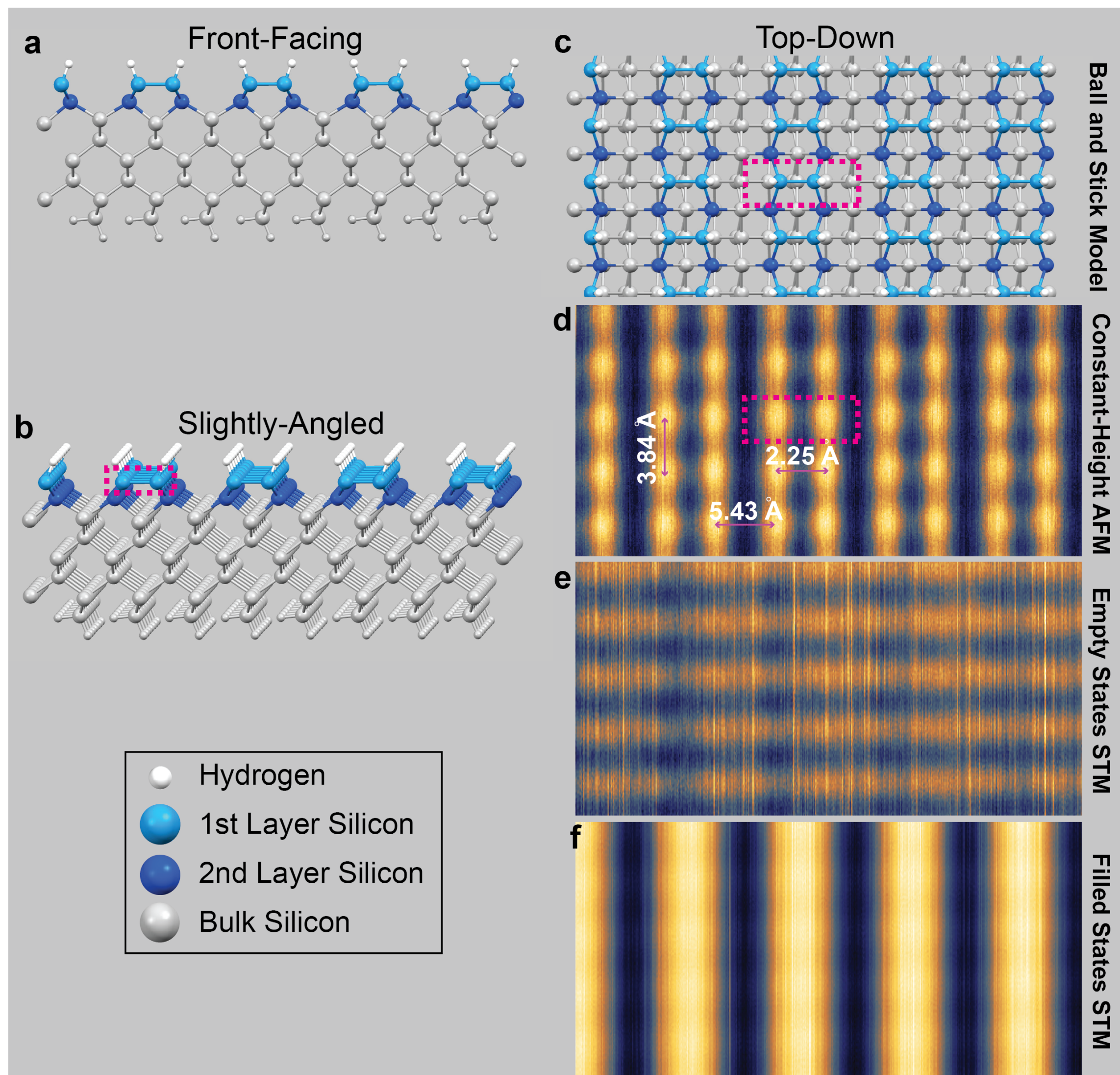

Figure 2.16: **H:Si(100) 2×1 Surface.** **(a)** Front-facing, **(b)** slightly-angled, and **(c)** top-down ball and stick models of H:Si(100) 2×1. Hydrogen atoms are depicted as the small white balls. All other atoms are silicon, but the first layer, second layer, and bulk silicon have been colored light blue, dark blue, and grey, respectively, to help with clarity. A single dimer is highlighted by the dashed pink box in (b-d). **(d)** Constant-height AFM Δf image, **(e)** empty states STM image ($V = 1.3\ V$, $I = 50\ pA$), and **(f)** filled states STM image ($V = -1.8\ V$, $I = 50\ pA$) of the surface, matched to the model from (c). All experimental images are $1.8 \times 2.8\ nm^2$.

dangling bonds by one per surface silicon atom, and accounting for the observed row structure of 2×1. Without hydrogen termination, these row-arranged surface silicon atoms would assume the buckled Si(100) configuration, reducing the energy cost of symmetric adjacent dangling bonds [69–71]. With hydrogen termination though, the remaining sp^3 dangling bond is passivated, allowing the rows to exist in an unbuckled state (See juxtaposed buckled bare Si rows *vs.* hydrogen-terminated unbuckled rows in Figure 2.6 from earlier).

Ball and stick models of the hydrogen-terminated silicon(100) 2×1 surface from different perspectives are shown in Figure 2.16(a-c). Two surface hydrogen-capped silicon atoms bonded together are called a dimer, and are highlighted in Figure 2.16(b-d) with the dashed pink boxes. These arrange themselves into the aforementioned rows (dimer rows), which run vertically from top to bottom in Figure 2.16(c-f). The top-down ball and stick model in (c) has been matched to the experimental data in Figure 2.16(d-f). Figure 2.16(d) is a constant-height AFM Δf image, with surface dimensions shown on the figure. In regard to these dimensions, it can be seen that there is anisotropy in the spacing; an important consideration for the atomic electronics presented later that have a distant-dependent decay in their interactions. Additionally, while these bond lengths are consistent for a perfectly ordered surface, in the vicinity of defects there can be lattice strain which alters them (See Section 4.2.2 for a discussion and examples). Figure 2.16(e,f) are constant-current STM images, with (e) probing the empty states and (f) the filled states. As touched on earlier, different biases and imaging types reveal different aspects of the surface, with each having their utility. In our machine, AFM is almost always a higher resolution imaging form but with the disadvantage of having scan times $\sim 10\times$ slower. Filled states STM allows fast scanning and to see if a tip has multi-tip artifacts by using DBs for reference, but does not show individual hydrogen atoms in a row well. Empty states STM is good for fast scanning and patterning of DBs since it resolves individual hydrogen atoms, but will not show tip artifacts as readily as filled states. Thus, the proper imaging type must be used for the intended task.

As a final methodology for characterizing the surface, a series of constant-height AFM images of H:Si(100) 2×1 is shown in Figure 2.17. This example is used to

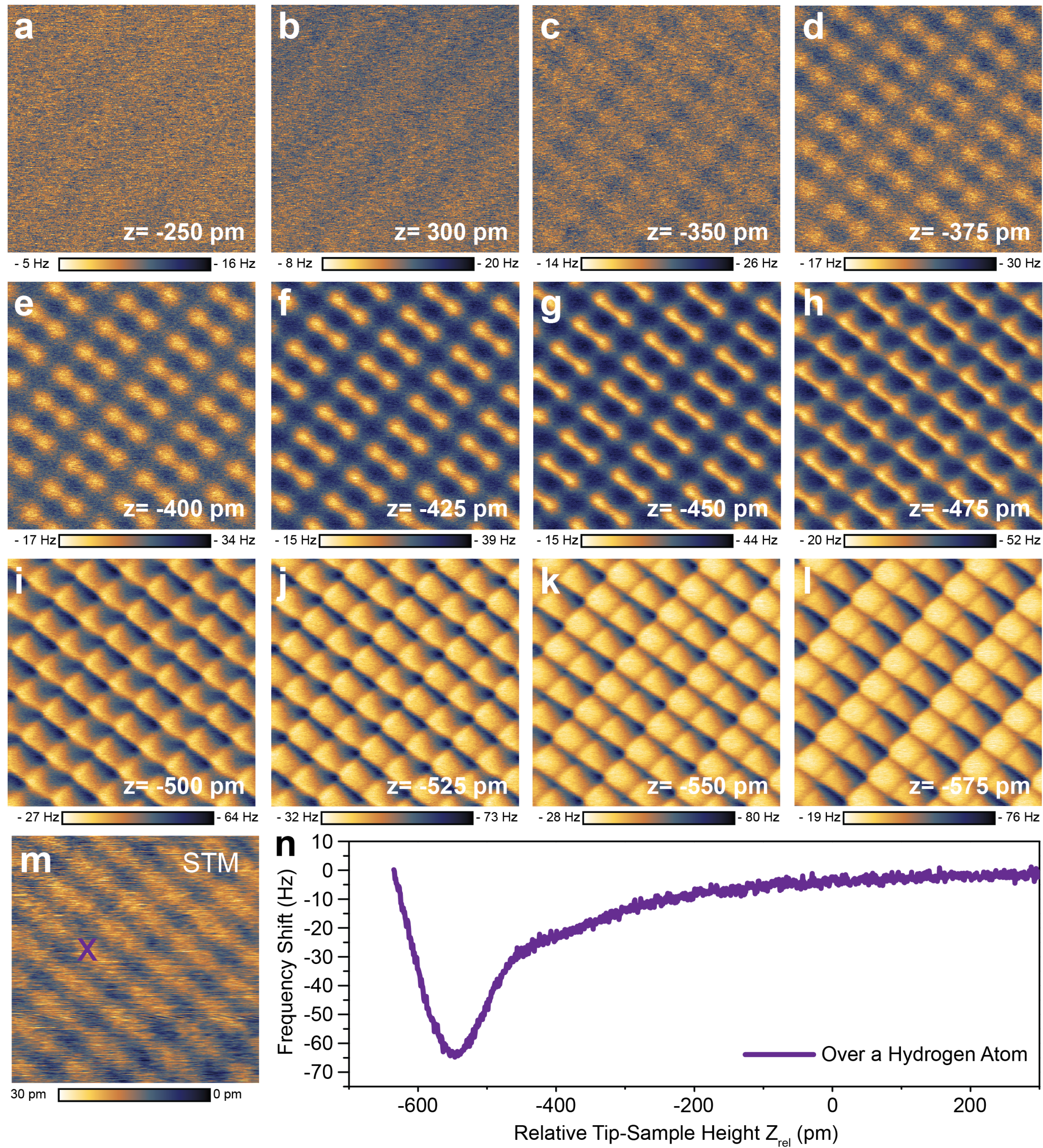

Figure 2.17: **Constant-Height AFM Probing of H:Si at Different Heights.(a-l)** Constant-height AFM images of a $3 \times 3\ nm^2$ area of H:Si(100) 2×1 at different heights. Heights are listed in the lower right corner of every image ($V = 0\ V$ and $Osc.\ Amp = 50\ pm$). **(m)** Empty states STM image ($V = 1.3\ V$ and $I = 50\ pA$) of the same area. **(n)** $\Delta f(z)$ spectra taken over top of a hydrogen atom. The spectra location is marked in (m). $z_{rel} = 0\ pm$ is referenced to an STM set-point of $I = 50\ pA$ with $V = -1.8\ V$ over top of a hydrogen atom.

highlight AFM's capability of probing certain dominant force contributors through small amplitude scanning in different parts of the interaction curve. Returning briefly to the discussion of differences between AFM and STM capability (See Section 2.2), AFM has the additional consideration that its scanning is not entirely dominated by the apex atom. In STM, tunneling current decays exponentially (See Section 2.1), meaning it can be assumed that almost all of the current measured is going through a single apex atom. For AFM, referring back to Figure 2.3 and Equation 2.1, some of the forces have much longer range character and tip atoms well-removed from the apex contribute to the measured frequency shift. To illustrate, consider the example of two fictional forces summed together. The first is a short range force with a magnitude of 1 nN acting for tip-sample distances of 0 to 100 pm from the sample. This is combined with a second force, long range in nature, which is also magnitude 1 nN, but acts over distances of 0 to 1000 pm from the surface. If using an oscillation amplitude of 80 pm on the AFM sensor, the position of the tip in relation to the sample will determine what force dominates. If the tip is $< 100\ pm$ from the surface, the contribution from the short range force will be an order of magnitude greater than that of the long range one. Conversely, if the tip is far from the surface, the short range force has decayed and the long range dominates. This also only applies if the oscillation amplitude is small enough to not convolute the two ranges (*i.e.* it is of the order of the decay length of the force). All this highlights that selection of a dominant force contributor can be achieved through varying the relative tip-sample height, which is what is exploited in Figure 2.17.

Far away from the surface in Figure 2.17(a-c), low resolution is achieved. Examining the $\Delta f(z)$ curve in (n), these are in the weakly attractive part of the response curve, as illustrated earlier in Figure 2.3, with most of the shift from long-range attractive forces. As the tip-sample distance is reduced, the surface starts to look atom-like with the hydrogen atoms showing up as spherical white protrusions in Figure 2.17(d-h). These images are in the strongly attractive part of the curve. As the tip-sample system is pushed even closer together in Figure 2.17(i-l), the surface starts looking less atom-like and takes on a bond-like character as the repulsive contribution to the total force increases; the surface becomes boxy and irregular looking,

with the irregularity due to a flexible tip-terminating hydrogen atom being repelled (Pauli exclusion) as the surface is scanned (Reference the flexibility discussion in Section 2.2.5). This is a replication of a similar experiment published in an earlier paper in Ref [93], and highlights AFM's powerful ability to view the surface under different force contributions.

2.4 Surface Dangling Bonds

A dangling bond is a surface silicon atom where the hydrogen cap has been removed, leaving behind an orbital of sp^3 character. A ball and stick model of a DB is depicted in Figure 2.18(a), with typical filled states STM, empty states STM, and constant-height AFM images of the same DB in (b-d), respectively. Patterning of these DBs are used to make the atomic electronics introduced in the introduction. Earlier work established DBs can be viewed as zero-dimensional artificial quantum dots, due to their widely-separated quantized charge states isolated from the bulk [48, 49, 120], ability to localize charge [49, 51], way they interact with each other to hybridize [45, 121, 122], and the ability to control DB ensemble's charge occupation with local electrostatic perturbers [49, 51].

In regard to their quantized charge states, DBs can be occupied by zero, one, or two electrons, depending on the doping of the bulk crystal, local electric fields, and their proximity to other DBs [120,123]. A DB with zero electrons will be in a positive charge state, a DB with a single electron is neutral, and a DB with two electrons is negative [45, 49, 120]. They stably hold these quantized amounts of charge because the electronic states for the different occupations all lie in the bandgap of H:Si. The bandgap substantially isolates them, limiting mixing with bulk properties.

As an example of what constitutes mixing, more details are given for some of the highlighted mixing examples from the introduction (See Section 1.2). Joachim *et al.* [23] experimentally studied conductance through a C_{60} molecule placed on gold, but found that electronic coupling to the substrate altered the value predicted by theory. The molecular orbitals of the C_{60} molecule were broadened and shifted through coupling to the surface, a problem all potential molecules or atoms on metal

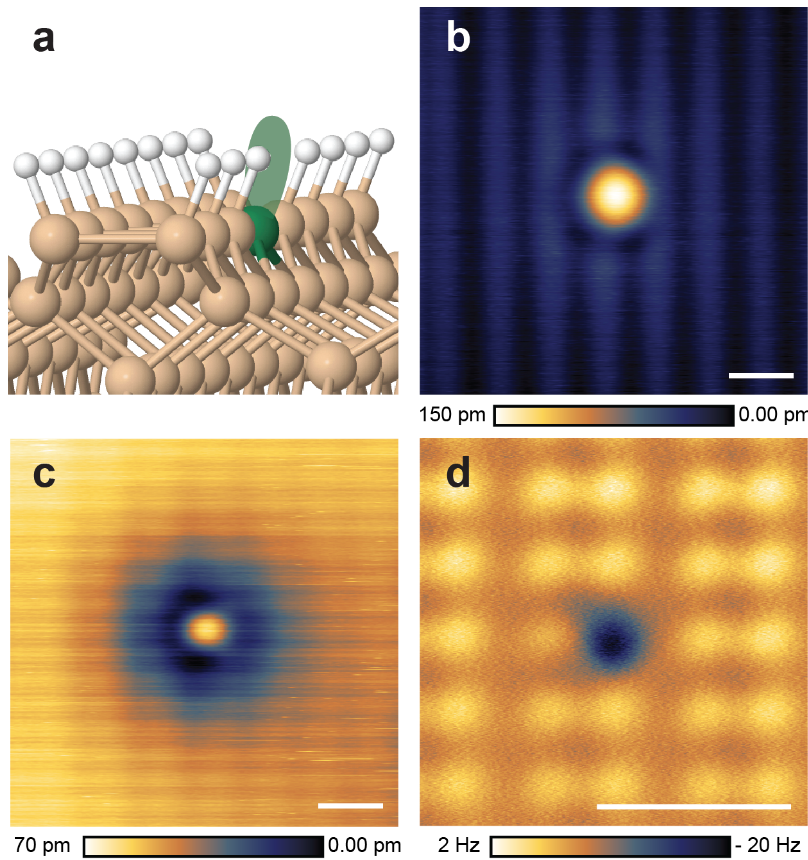

Figure 2.18: **A Dangling Bond.** **(a)** Ball-and-stick model of a dangling bond on the H:Si(100) 2×1 surface. Silicon atoms are depicted in beige, hydrogen atoms in white, and the dangling bond in green. **(b)** Filled states STM image ($V = -1.7\ V$, $I = 50\ pA$), **(c)** empty states STM image ($V = 1.3\ V$, $I = 50\ pA$), and **(d)** constant-height AFM Δf image ($V = 1.3\ V$, $z_{rel} = -350\ pm$, and $Osc.\ Amp. = 100\ pm$) of the same DB.

surfaces would face [22]. Other groups have explored electrical isolation by depositing molecules on an insulating layer. A followup study by Joachim *et al.* [24] solved the coupling problem by putting pentacene molecules on inert H:Si(100), seeing no hybridization of the orbitals with the surface. The problem with studies of this type is that physisorption on a non-reactive medium is weak. Other groups tried growing their own thin insulating layers made of MgO [25, 26] and NaCl [27–30, 124] over a conducting medium to isolate structures. These salt insulating layers tend to hold the molecules more firmly due to their ionic nature, though remain limited to cryogenic temperatures, and can be as thin as a few mono-layers. This thin nature of the layers allows for SPM manipulation under more extreme tip-sample bias parameters, and decoupling of the molecules/atoms under more modest ones. For example, Steurer *et al.* did experiments on single electron transfer between pentacenes placed on a salt layer [30]. While the pentacenes were isolated thanks to the salt, it was found that the thickness of the insulating films effected which charge states could be stabilized, making more elaborate experiments difficult to interpret. Controlling for uniformity of layer thickness was also found to be tough work, with spontaneous loss of charge to the substrate problematic for both the aforementioned Steurer experiments [30], as well as the experiments by Olsson *et al.* examining silver atoms on salt [31]. While these issues could potentially be remedied for these systems, it is easier to capitalize on the simplicity of the DBs built-in electrical isolation from possessing gap states [47, 48]; the states should not substantially mix with the bulk, but can still interact with other DBs, electrostatic inputs, or a probing tip that “gates” the charge state of the DBs.

2.4.1 Tip Interactions and its Effect on DB Charge States

A qualitative band diagram of a single DB is shown in Figure 2.19(a). The DB has three charge states (DB^+, DB^0, DB^-), but in the literature often the charge transition levels DB(+/0) and DB(0/-) are referenced; these being the energies at which the DB switches between its quantized charge states shown in Figure 2.19(a). This avoids a confusion about energy levels; while the negative and neutral state

of the DB have defined energies, the question of what the energy is of the positive DB state, since it has no electron, is ill formed. An excellent thought experiment elaborating more on this can be found in Ref [125]. For simplicity, the most common literature convention of referencing the transition levels, DB(+/0) and DB(0/-), is used in the rest of this work.

In Figure 2.19(b-c) the gating effect of a SPM tip is illustrated, with qualitative band diagrams of a DB while it is swept through its three charge states. As with many systems and experiments, the act of observing the system is perturbative. The SPM tip when brought in to examine a DB bends the silicon bands locally by hundreds of meV, even under zero applied tip-sample bias. This is an effect known as tip induced band bending (TIBB), which has been studied for many semiconductors [49,123,126–128] and is qualitatively shown as the bent conduction and valence bands in Figure 2.19(b-d). In addition to bending the bands, TIBB has the additional effect of shifting the electronic charge transition levels of the DB, with the effect most pronounced directly under the tip apex. The amount of bending depicted in Figure 2.19(b-c) varies, due to the effect of "tuning" the amount of bending through variation of the applied tip-sample bias. This can alter the DB's charge state in two ways.

First, since the strength of TIBB is varied by altering bias, the position of the DB(0/-) level could be moved such that it was pushed above or below the Fermi level of the bulk. Because of the degenerate doping of our surface (See sample details in Section 2.3), all DBs in their unperturbed state are negative (two electron occupied), holding this charge because the DB(0/-) electronic state is below the surface's Fermi level $E_{F,Sample}$. If the DB(0/-) level is pushed above $E_{F,Sample}$ through TIBB, it loses an electron to become neutral.

The second way TIBB can change a DB's charge state is through alteration of the competing electron emptying and filling rates, which is illustrated in Figure 2.19(b). Once again, this is done through sweeping the relative tip-sample bias to control the band bending and thus the tunneling rates, as this concomitantly alters the shape of the tunneling barriers. The rate of electron tunneling from tip to DB is denoted as Γ_{Tip-DB} in Figure 2.19(b), and the rate of from DB to bulk as Γ_{DB-B}. In this case,

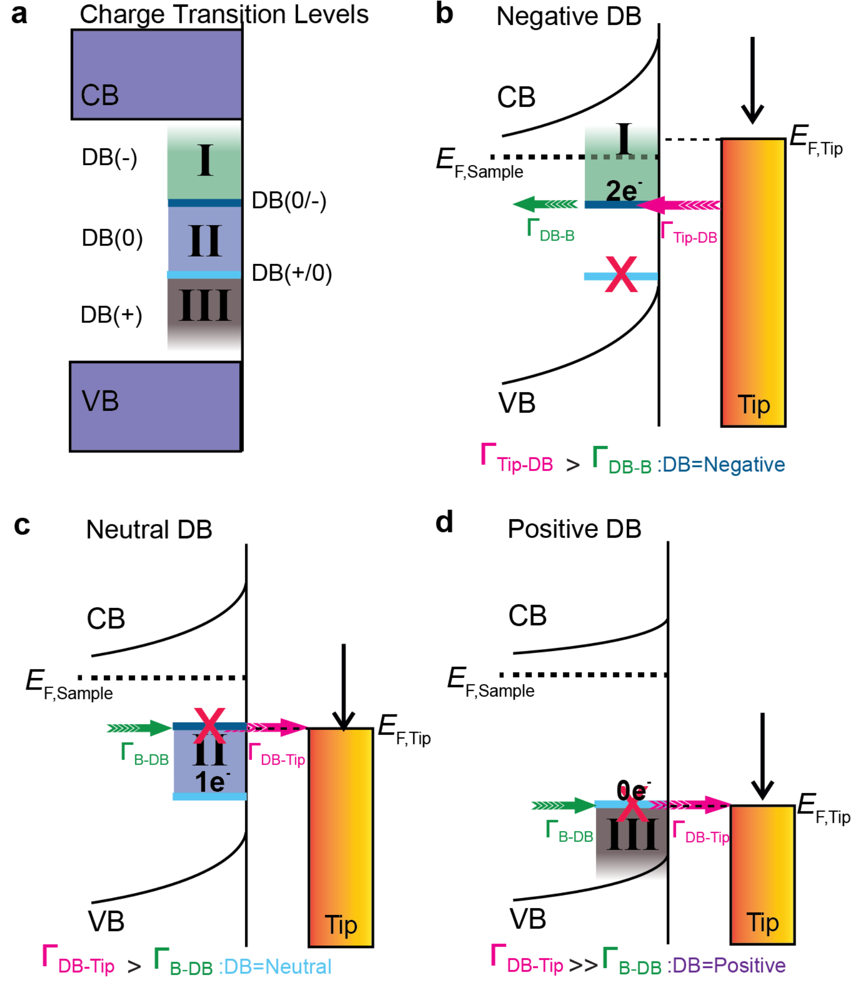

Figure 2.19: **Switching a DB's Charge State with Tip Interactions. (a)** Qualitative diagram of the DB charge states (DB^-, DB^0, DB^+) and charge transition levels (DB(0/-) and DB(+/0)). The roman numerals refer to the regions where the DB is in the designated charge state written to the left of the regions. **(b)** Qualitative tip-sample band diagram for the DB in a negative charge state. With the tip Fermi level $E_{F,Tip}$ higher than both $E_{F,Sample}$ and the DB(0/-) level (dark blue), the tip injects current to the DB faster than it can exit to the bulk ($\Gamma_{Tip-DB} > \Gamma_{DB-B}$) rendering it negative. **(c)** The tip Fermi level is lowered to be resonant with the DB(0/-) charge transition level. This allows the tip to extract an electron from that level ($\Gamma_{DB-Tip} > \Gamma_{B-DB}$) faster than the bulk can resupply it. The DB becomes neutral. **(d)** $E_{F,Tip}$ is lowered even further to be resonant with the DB(+/0) charge transition level. The last remaining electron is removed and the DB becomes positive ($\Gamma_{DB-Tip} >> \Gamma_{B-DB}$).

the bias is such that the tip Fermi level $E_{F,Tip}$ is above both the sample Fermi level $E_{F,Sample}$ and the DB(0/-) level. Thus, the DB(0/-) level is negative both because it is below the sample Fermi level, and because even if it did lose an electron it would be immediately filled by tunneling from the tip which has a higher Fermi level.

As the tip Fermi level is reduced through sweeping bias, it eventually comes into resonance with the DB(0/-) level in Figure 2.19(c), extracting one of the two electrons from the DB. While the DB(0/-) level is below $E_{F,Sample}$ suggesting it should be negative, the presence of the tip is altering the balance of the tunneling rates such that $\Gamma_{B-DB} < \Gamma_{DB-Tip}$. In different phrasing, the rate at which the bulk resupplies the DB with electrons is slower than the tip's ability to extract them, leaving the DB with only a single bound electron on average (neutral).

The tip Fermi level can continue to be swept down until it comes into resonance with the DB(+/0) level in Figure 2.19(d). At this point, the remaining bound electron is extracted leaving the DB positive, as $\Gamma_{B-DB} << \Gamma_{DB-Tip}$. Thus with a tip, it is easy to modulate the charge state of the DB.

A concerned reader might note here that if a tip would always be required to change the charge state of a DB, DB-based electronics would remain a curiosity. While the tip is used to probe quantitative parameters for DB electronics such as how well held an electron is, it is not a required participant in the final atomic designs. As mentioned earlier in this section, one way to change a DB's charge state is to push the DB(0/-) level above or below the sample Fermi level. A tip is only one way to do this, with the electrostatic effect of other DBs or electrostatic inputs also capable. In the paper "Binary Atomic Silicon Logic" presented later in Section 4.1, one of the crucial results was showing the atom electronics would work in the absence of the tip by subtracting the TIBB contribution from the experimentally measured values. This allowed demonstration that DBs can interact with each other to transmit binary information in the expected ways, by means of altering each others DB(0/-) positions in the absence of the tip. One thing that must be kept in mind though is that TIBB is difficult to precisely estimate.

Estimating Tip Induced Band Bending

The total TIBB contribution, or how much the bands and levels are shifted, is a product of several factors. Some factors are variable and others are fixed, with the contributors being: the contact potential difference between the tip and sample (semi-fixed), the sample doping (fixed), the tip apex radius (fixed), applied bias in the tip-sample junction (variable), and the relative tip-sample distance (variable). These values are input to a 3D finite-element Poisson equation solver built on the foundation established in Refs [129–131], which generates a TIBB correction estimate. This is an estimate only because precisely knowing all the contributing values is difficult. To facilitate understanding of TIBB corrections and its limitations, these estimates are discussed.

Starting with contact potential difference (CPD), this is a potential that can be measured between two materials of different work function when electrically connected. When not connected, the materials are as shown in Figure 2.20(a). Every material uniquely binds their electrons less or more strongly, evidenced by the distance between the two material's Fermi levels (E_{FTip} and $E_{FSample}$) and the vacuum energy level (E_{Vac}). When connected, the two materials want to reach electrochemical equilibrium *via* the exchange of electrons to minimize energy; the material with the lower Fermi level has unoccupied states that the electrons from the material with the higher Fermi level can fill. This exchange creates a separation of charge and thus a potential ($eV_{Contact}$), as shown in Figure 2.20(b). This potential can, of course, be offset by the reintroduction of an opposite potential between the two materials of $-eV_{Contact}$, which is shown in Figure 2.20(c). This is called nullifying (or minimizing) the CPD. The AFM spectroscopic technique called Kelvin Probe Force Microscopy (KPFM), synonymous with $\Delta f(V)$ spectroscopy, is able to measure the value where this occurs and is discussed in detail later in Section 2.4.3.

Tungsten tips were exclusively used in this work, with tungsten having a work function of $4.5 - 5$ eV, depending on the crystallographic direction. For a highly n-doped silicon sample, the work function is estimated at 4.1 eV. This number would decrease for higher sample doping and increase for lower, explaining why

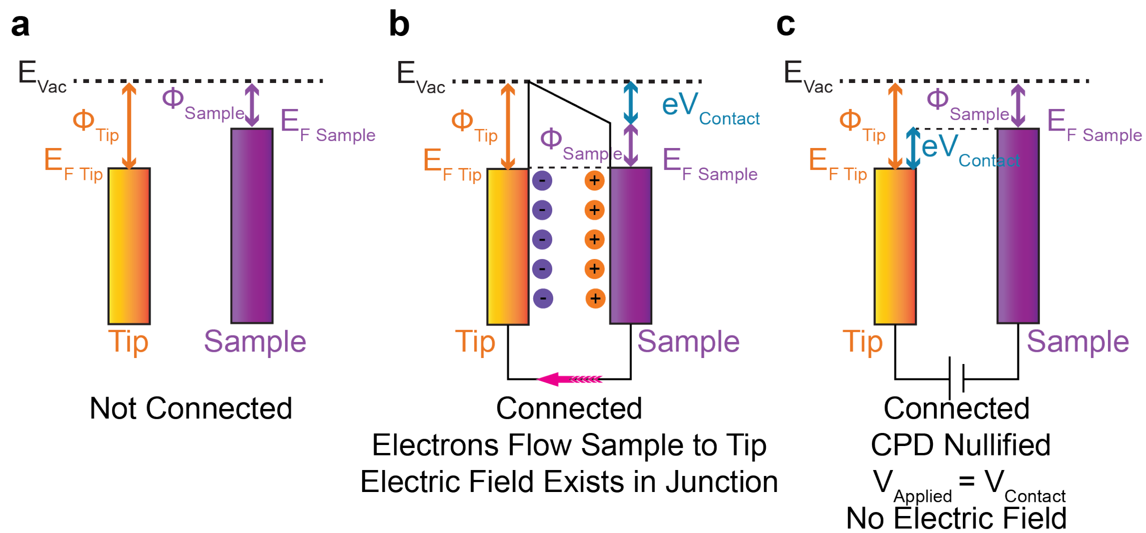

Figure 2.20: **Contact Potential Difference Diagram.** **(a)** Energy diagram of a tip and sample of differing material not connected. Each has a unique work function (ϕ_{Tip} and ϕ_{Sample}) as referenced to the vacuum energy E_{Vac}. The Fermi levels for the two materials are marked as E_{FTip} and $E_{FSample}$. **(b)** When connected, the two different materials experience a flow of electrons from the material with the higher Fermi level to the one with the lower. This causes a separation of charge in the junction (represented by the illustrated + and - charges) and thus an electric field, with an associated contact potential difference of $eV_{Contact}$. **(c)** The contact potential difference can be nullified such that no electric field exists between the materials by applying a static voltage offset $V_{Applied}$ that is equal in magnitude and opposite in sign to $V_{Contact}$.

doping is also a factor in TIBB. Taking the tip work function to be 4.5 eV based on the most common crystallographic face observed, the tip-sample system when connected exchanges charge carriers causing upward band bending at the surface of $\sim 4.5 - 4.1 = 0.4\ eV$. This explains why even at zero applied bias, upward band bending of hundreds of meV is present.

Next, some subtleties about estimating sample doping are examined. As discussed earlier in Section 2.3, all work in this thesis was conducted on a surface doped with arsenic to a volume concentration of $10^{19}\frac{atoms}{cm^3}$. The *in situ* sample preparation method discussed involved a series of 1250°C flashes, which are known to deplete the dopant volume concentration near the surface to $10^{18}\frac{atom}{cm^3}$. Thus, a fixed dopant concentration cannot be used as an input for the TIBB correction in the utilized 3D finite-element Poisson equation solver. Instead, it is required that the concentration is specified as $10^{18}\frac{atoms}{cm^3}$ at the surface, with this value gradually increasing to $2 \times 10^{19}\frac{atoms}{cm^3}$ in the bulk over a range of 100 nm.

Discussing tip radius next, an alteration of this changes the number of atoms within a distance able to participate in a force interaction with the surface, a bit like changing the area of two capacitors. The tip radius is generally taken to be 10 nm, but it has been observed to vary between 5 to 20 nm on average. Figure 2.21 highlights how small variations in tip radius can effect the calculated TIBB, while all other parameters as part of the calculation are held constant. In small bias windows the TIBB is fairly linear, with a changing slope for different assumed radii. A minor change in tip radius for the calculation can thus over or under estimate the true TIBB correction.

Finally, the two varying parameters of tip-sample bias and height are discussed, with Supplementary Figure 4.9 from the paper (Binary Atomic Silicon Logic) in Section 4.1 referenced. In Supplementary Figure 4.9(a) (left panel), TIBB varies as a function of only height with bias held fixed at $V = 0\ V$. In Supplementary Figure 4.9(b) (right panel), the tip is now set at a fixed height above the surface and the tip-sample junction bias is swept. The dependence on both height and bias gives a large parameter space for TIBB variation, requiring that both are known for accurate TIBB calculation within a given experiment.

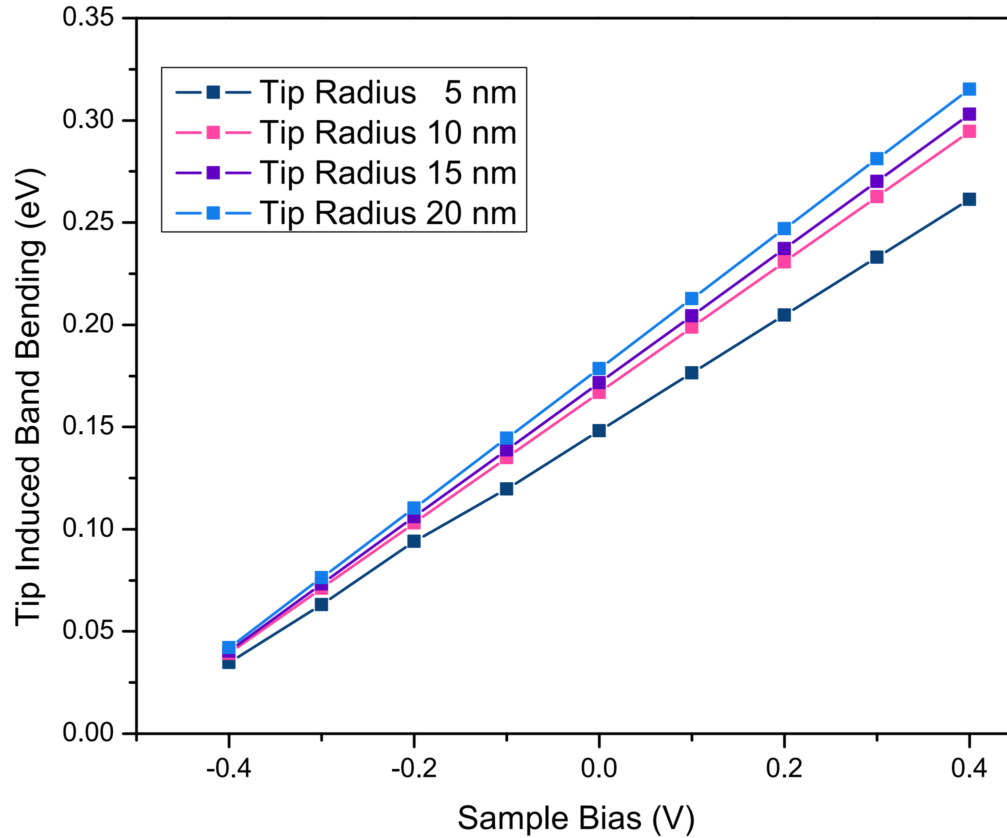

Figure 2.21: **TIBB as a Function of Tip Radius**. Calculated tip induced band bending for a tip of varying radius. All other inputs for the calculation were held fixed with $z_{rel} = -350\ pm$, a work function difference between tip and sample of 0.4 eV, and an assumed donor concentration of $10^{18}\frac{atoms}{cm^3}$ at the surface, gradually increasing to $10^{19}\frac{atoms}{cm^3}$ in the bulk over a range of 100 nm.

In summary, all of the inputs for TIBB are best estimates. It is likely for any given TIBB correction that only most of the tip perturbation has been removed, but not conclusively all. For example, in regards to the tip it is assumed it is a hemisphere with radius 10 nm, but after doing many surface alterations the shape may change or become irregular. In addition, the work function difference between H:Si and tungsten is assumed at 0.4 eV. As discussed earlier in Section 2.2.5, a tip apex is realistically a combination of silicon, hydrogen, and tungsten, with the exact proportions not precisely known. Different coatings may alter this estimate. Variations also likely exist for sample doping. For TIBB modeling it is assumed the dopant volume concentration changes with depth, but is more or less uniformly volume distributed otherwise. On the length scales of atomic devices though, this may not be the case. Imperfect sample prep and the dopant depletion phenomena for high temperature flashes may mean it clusters or becomes non-uniform on small scales. This is something explored and discussed later in the paper "Electrostatic Landscape of a Hydrogen-Terminated Silicon Surface Probed by a Moveable Quantum Dot" in Section 5.1. Despite all being best estimates, TIBB correction using this methodology is the best available option to remove tip perturbation from an experiment. Of interest for future explorations would be a more thorough examination of TIBB corrections, and the amount of "incorrectness" that can be introduced with bad estimates.

2.4.2 Making and Erasing DBs

Creating DBs on H:Si has been performed since 1995. It involves bringing a single-atom sharp tip over a target hydrogen atom and applying a voltage pulse to break the Si-H bond to leave behind a DB [40, 42]. To find the target hydrogen atom, imaging is typically conducted in empty states STM ($V = 1.3\ V$, $I = 50\ pA$), as it quickly and easily resolves the individual surface hydrogen atoms. From a starting height over the target hydrogen defined by its STM scanning parameters ($V = 1.3\ V$, $I = 50\ pA$), individual voltage pulses are applied of magnitude $\sim 1.8 - 2.5\ V$ over a time period of 10 ms per pulse, until the hydrogen cap is seen to be desorbed. Electrons are injected during these pulse events, with low-energy inelastic electron

scattering the dominant process by which the bond is broken [40,42]. Some variation in the voltage value of the pulse exists due to variations in tip geometry, the local environment, and the apex atom. For example, patterning with a silicon-terminated tip was been found to be both more successful in correct placement of a DB, as well as use lower pulse voltages when compared to a hydrogen functionalized one. This agrees with recent results in the literature detailing which tip states are best for desorption, as published by Moller *et al.* [132].

The DB creation process is relatively high energy in the 2-5 eV range [42] when compared to the hundreds of meV required to move physisorbed atoms on a surface [133]. In general, atom fabrication of structures robust enough to withstand relatively high operating temperatures are more difficult to make, with larger energy inputs from the scanned probe required to dislodge strongly bound atoms. This large creation energy, however, means DBs on the surface are structurally robust with a diffusion barrier in excess of 1.4 eV [53, 54]. To illustrate, if a DB was held at room temperature, it would be expected to experience only one hop in position over a period of 500 years [134]. A negative consequence of the large energy required to create DBs though is that covalent bonds within the SPM probe break occasionally [135]. Conservatively, about 20 DBs in a row can be manufactured using this pulse technique [134] before a change in tip is observed that would require *in situ* tip sharpening (See Section 2.2.4 for the tip sharpening procedure).

Notification of the aforementioned tip-change during patterning usually comes in the form of an incorrectly placed DB, which for multi-DB ensembles used to require the entire structure be discarded and started anew. In 2018 however, we developed a novel error-correction methodology to erase mispatterned DBs in the paper titled "Atomic White-Out: Enabling Atomic Circuitry through Mechanically Induced Bonding of Single Hydrogen Atoms to a Silicon Surface" presented in Section 3.1. The full details are left to the manuscript, but to summarize it involves intentionally functionalizing the tip with a single hydrogen atom, which can then mechanically be brought in to a DB to bond and erase it [134, 136, 137]. Functionalization is done by simply making a DB using the pulse parameters discussed above, where some percentage of the time it hops to the apex. This process is controllable and repeat-

able, with a yield comparable to that of making DBs. Error-correction functionality has greatly expanded the realm of experiments that can be performed on the H:Si surface and was an integral advancement enabling all the work presented in this thesis. With this utility, DB patterning has reached a new age of maturity where not only can patterning be performed at increasingly large scales [45,134,138], but it can be merged with error-correction [134,136,137] and automation of the tip-forming process using machine learning [139]. Hopefully this will eventually enable users to input a desired DB pattern, with the SPM automatically taking care of all the finer details.

2.4.3 Seeing Charge with AFM and $\Delta f(V)$ Probing

AFM as a technique for detecting single charging events was first shown in 1990, where it was used to examine single-charge-carrier recombination events on Si_3N_4 films [140]. It was taken to new spatial resolution limits in 2009, with demonstration of the first instance of resolving differently charged adatoms by Gross *et al.* [141]; they showed one-electron charge state changes in gold atoms correspondingly changed the force on the AFM tip by a few pN. Kelvin Probe Force Microscopy (KPFM or, interchangeably, $\Delta f(V)$ spectroscopy) was also employed to confirm the charge state changes by measuring the altered contact potential difference (CPD). In other words, the stabilized (by salt lattice relaxation) Au^+, Au^0, and Au^- charge states showed markedly different V_{CPD}'s, allowing discrimination. The same $\Delta f(V)$ technique is used extensively in results presented later to examine charge state changes of DBs. To motivate an intuitive understanding of the technique, a brief mathematical background is given.

Measuring The Contact Potential Difference with $\Delta f(V)$ Spectroscopy: Mathematical Background

Earlier in Section 2.4.1, the origin of contact potential difference was discussed with Figure 2.20 illustrating it; a metallic tip and semi-conducting sample each have their own unique work function, which when connected together reach electrochemical

equilibrium *via* exchange of carriers. This results in an electric field in the junction between them, with the tip-sample system forming, essentially, a capacitor [142]. The electric field in a capacitor to first order can be described as:

$$F_{electric} = -\frac{1}{2}\frac{\partial C}{\partial z}(\Delta V)^2. \tag{2.10}$$

Where $F_{electric}$ is the force between the two materials, C the capacitance, z the distance between tip and sample, and ΔV the potential between the materials. Within ΔV two factors are present:

$$\Delta V = V_{Tip-Sample} - V_{CPD} \tag{2.11}$$

Here, $V_{Tip-Sample}$ is the applied DC tip-sample bias and $V_{CPD}=\frac{\phi_{Tip}-\phi_{Sample}}{e}$ is the naturally existing contact potential difference due to the different work functions from Figure 2.20(b). Substituting Equation 2.11 into Equation 2.10 gives:

$$F_{electric} = -\frac{1}{2}\frac{\partial C}{\partial z}(V_{Tip-Sample} - V_{CPD})^2. \tag{2.12}$$

With this expression, finding the CPD equates to minimizing the electric field in the junction ($F_{electric}$) as was illustrated in Figure 2.20(c). V_{CPD} is fixed as it is a function of the materials, but $V_{Tip-Sample}$ can be changed. Thus, $V_{Tip-Sample}$ is swept in the instrumentation until it cancels out V_{CPD} ($V_{Tip-Sample} - V_{CPD} = 0$), corresponding to a minimization of $F_{electric}$ and the nullifying of the contact potential difference.

One issue with the form of this equation as it stands now is it relates $F_{electric}$ to $V_{Tip-Sample}$, but AFM experimentally measures frequency shift as a function of bias ($\Delta f(V)$). As derived earlier in Section 2.2.2 however, Δf and F can be linked with Equation 2.9. To generalize this capacitor formalism to an AFM $\Delta f(V)$ measurement, Equation 2.12 is changed into an acceptable form for substitution by taking the derivative of it with respect to z. Afterwards, it can be substituted directly into Equation 2.9, with the final result:

$$\Delta f = \frac{f_0}{4k}\frac{\partial^2 C}{\partial z^2}(V_{Tip-Sample} - V_{CPD})^2 \tag{2.13}$$

Now when $V_{Tip-Sample}$=V_{CPD}, it minimizes Δf. In other words, where Δf is at a minimum corresponds directly to where $F_{electric}$ is at a minimum, which is where the contact potential has been nullified ($V_{Tip-Sample}$=V_{CPD}).

Measuring The Contact Potential Difference with $\Delta f(V)$ Spectroscopy: Examples of Experimental Extraction

An experimentally obtained $\Delta f(V)$ curve over H:Si is shown in Supplementary Figure 5.9 from the "Electrostatic Landscape of a Hydrogen-Terminated Silicon Surface Probed by a Moveable Quantum Dot" paper in Section 5.1. The raw data of the measurement is shown as the purple curve, with the black curve a fit with a parabolic function. The apex of the fit is marked in pink (V^*), which is the point where Δf has been minimized (the smallest shift off resonance) correlating to a nullification of the CPD. This curve was taken as part of a $\Delta f(V)$ map displayed on the right of the figure, also sometimes referred to as a local contact potential difference (LCPD) map or KPFM map. These are taken by defining a grid and performing a $\Delta f(V)$ curve for every point. Fits are performed for each curve using a parabolic function (Ax^2+Bx+C), with the CPD maxima extracted from the fit. All experimental curves display this parabolic shape due to the squared term in Equation 2.13. The final map displays the extracted CPD values, telling something of the surface electrostatic variation. These maps have been done on surfaces like silicon [143], Pb [144], and NiO(001) [145], as well as on molecules like naphthalocyanine [124]. In this paper it was used to probe electrostatic variation on the H:Si surface, which will be discussed in more detail later as part of the paper (Section 5.1).

Some considerations are now discussed for any given $\Delta f(V)$ spectra. Equation 2.9 is for linking Δf with $F_{Tip-Sample}$. Within $F_{Tip-Sample}$ certainly exists $F_{electric}$, but it also contains all the other force contributors talked about in Section 2.2. At close tip-sample separations other force terms could exist that may not give a true parallel plate capacitor model agreement. The solution to this is to take the $\Delta f(V)$

curves far from the surface where $F_{electric}$ is the dominant contributor (See Section 2.3 from earlier for a thought experiment highlighting dominant force contributors with distance). This has the added benefit that it moves the tip far enough away that there is little to no tunneling current for our material system, which is another important consideration for $\Delta f(V)$ spectra.

Current is known to induce artifacts in AFM as ohmic effects outside the junction can distort the measurements, an effect colloquially termed "Phantom Force" [146, 147]. $\Delta f(V)$ is also susceptible to this, with Weymouth *et al.* finding that at close tip-sample separations they were able to induce distortions and even inversions of their $\Delta f(V)$ curves [148]. They also had to discard the parallel plate capacitor form of the equation at these close distances and model the tip more accurately as a hemisphere (instead of a flat plane) to get good agreement.

Also, in a true parallel plate capacitor the electric field can be completely nullified. Realistically, however, the tip is an irregular shape adding an inherent inhomogeneity in the tip–sample junction. This means that the electrostatic field can only be minimized, but not fully nullified in most cases. Thus, to minimize the complexities of these considerations, that of both current and tip-shape irregularities, all $\Delta f(V)$ maps in this work were taken far from the surface in bias regions preferably in the band gap of H:Si.

An additional simplification in the discussed mathematics linking $\Delta f(V)$ to a capacitor is that Equation 2.13 only has a single capacitance term. For real systems, more detailed modeling exists that factors in the capacitance of the tip-adatom, adatom-substrate, and cantilever-substrate as in the work done by Stomp *et al.* [149]. At this time, it was merely intended to show the link between CPD and Δf, so more rigorous quantitative modeling was never attempted. Future work attempting a fit on such a detailed model could be of interest though.

2.4.4 Probing DBs with STM, AFM, and $\Delta f(V)$ for Atomic Electronics

So far $\Delta f(V)$ probing of CPD has only been discussed in terms of measuring static charge. When performed over entities capable of changing charge state in a discretized way, the switch from one quantized energy to another presents as a "step" in the spectra between charge parabolas. Some notable examples can be discussed to elaborate. Steurer *et al.* demonstrated charge transfer between weakly coupled pentacene molecules on NaCl. The NaCl is necessary to electrically isolate the molecules for modest bias ranges, but is grown over a conductive substrate so that manipulations can still be performed at higher bias values. $\Delta f(V)$ curves taken over isolated pentacenes showed dynamic switching of the charge state through parabola jumps. By doing the same spectra over closely spaced pentacenes, they saw similar $\Delta f(V)$ parabola jump signatures of charge transfer between the coupled molecules [30]. The second class of example was done by Stomp *et al.* [150] and Miyahara *et al.* [151], who both looked at grown InAs quantum dots. $\Delta f(V)$ spectra taken over the quantum dots showed 10's of these charge jumping steps to different parabolas, which was a result of their quantum dots being large and able to host many electrons and thus charge states. This can be directly compared to this thesis's dangling bond quantum dots, albeit with less steps due to their smaller size only making a few quantized states possible.

All of this analysis was done as part of the paper "Binary Atomic Silicon Logic" (BASiL) from Section 4.1, where a combined AFM, STM, and $\Delta f(V)$ approach was employed to look at DBs. As DB electronics are the central result of this thesis, an attempt to give a guided preview of those results will be given here, while leaving the full details to be discussed as part of the manuscript.

Supplementary Information (SI) Figure 4.5 of the BASiL paper in Section 4.1 is first examined to highlight the process for STM measurement of the bandgap. In SI Figure 4.5(a,b), filled and empty states images are shown of an isolated DB, with two spectroscopy locations marked in (a). At these locations, that of over the DB and over the H:Si surface, a STM $I(V)$ spectroscopic curve was taken and plotted in SI

Figure 4.5(c). Two interesting features become apparent. First, the bandgap of the material substrate is evident in the H:Si teal curve and runs from $\sim -1.0 - 0.5\ V$. The second interesting point is that the DB has a smaller range of non-conductivity compared to H:Si; as the DB possess gap states, it can act as a "stepping-stone" for current under specific band-bending conditions, allowing conductivity earlier for particular bias ranges [47, 120]. Keeping the bandgap range in mind from the H:Si curve, AFM data taken over an isolated DB is now examined as presented in Figure 4.1 of the main text of BASiL in Section 4.1.

Figure 4.1(a-c) show constant-height AFM Δf images of the DB taken at different fixed tip-sample biases, with the DB charge state labeled at the top of each frame. The reason for this will become more apparent after briefly discussing Figure 4.1(d).

$\Delta f(V)$ curves taken over entities that can change charge state in a quantized way show steps between charge-state parabolas. The step in Figure 4.1(d) at $\sim -0.38\ V$ for the $\Delta f(V)$ curve taken over the DB (dark blue), is indicative of it changing from a negative charge state (Region I, DB^-), to a neutral charge state (Region II, DB^0). Corresponding band diagrams showing the tip-sample system as the DB is switched charge state are shown in Figure 4.1(f,g) (Reference to Figure 2.19 from earlier). No corresponding step is seen in the H:Si $\Delta f(V)$ spectra (teal curve), with it presenting as a section of a regular parabola due to not having quantized charge states. The charge-state change at $\sim -0.38\ V$ is also firmly in the zero-current bandgap region measured from the $I(V)$ curves in SI Figure 4.5. This charge transition had been inferred from STM studies [48, 51], but was always masked by the bandgap. This AFM probing was the first time direct observation was shown [49].

The constant-height panels in Figure 4.1(a-c) can now be reexamined and linked to Figure 4.1(d). The frame edges of Figure 4.1(a-c) are color-coded to their respective constant-voltage "slices" marked in the $\Delta f(V)$ spectra in (d). The DB when neutral in Figure 4.1(a) is lighter in contrast than when it is scanned with a bias that enforces it to be negative as in Figure 4.1(b,c). Cross-sections of Figure 4.1(a-c) were provided in Figure 4.1(e) to highlight this. Thus, neutral DBs will always present as lighter in contrast than negative DBs, showing that the DB contrast in constant-height AFM Δf images can be used to infer the DB's charge states. In addition, a

full constant-height Δf image does not necessarily need to be taken to see the DB's charge state at a given bias, but can also be inferred by the relative contrast implied in a slice in the $\Delta f(V)$ spectra. These observations can now be extended to more than one DB.

Figure 4.2 of BASiL highlights key DB-DB interactions and introduces important considerations when making DB ensembles. As above, Figure 4.2(a-c) shows another example of a single DB case with the same analysis performed in both in STM and AFM. This DB was then erased using the error-correction capability discussed in Section 2.4.2, and another lone DB, two lattice sites over, was patterned in Figure 4.2(d-f). It was characterized with similar methods, showing identical behavior to the first one. Next, the original DB from Figure 4.2(a-c) was re-pattered in Figure 4.2(g-i) to create a pair. Lone DBs are negative due to the crystal degenerate doping, but putting two negative DBs close together is not stable. When two are spaced $< 1\ nm$ apart, Coulombic repulsion causes one of the pair's extra electrons to delocalize in the conduction band, as inferred in prior STM results [51, 152]. This is done by the electrostatic effect of one DB pushing the other DB's charge transition level (DB(0/-)) above the bulk Fermi level. This change in charge occupation explains the existence of the extra step feature seen in the $\Delta f(V)$ spectra taken of the pair in Figure 4.2(i). From $-1.0\ V$ to the first step at $-0.135\ V$, both DBs are neutral; from $-0.135\ V$ to the second smaller step at $0.265\ V$, one is neutral and the other negative; and from $0.265\ V$ on, both DBs are negative. Thus, for bias values between the first and second step, including $0.0\ V$, the ensemble will have one DB negative and the other neutral. $0.0\ V$ is specifically mentioned because this is the fixed bias the constant-height Δf image in Figure 4.2(h) was taken at, which shows a strange "streakiness" between the DBs.

When this streakiness was first observed, it was thought to be evidence of the facile electron tunneling that had been hypothesized for DB pairs in the literature [50]. The low ($\sim 0.5\ eV$) and narrow barrier between the quantum dots was thought to make tunneling on the order of THz possible [152]. Further investigation found the streakiness observed was on a time scale of milliseconds, a far cry from the expected THz, and that it was also dominantly occurring in the raster scan direction of the

tip. More experiments showed that an attractive tip-surface interaction existed such that as it scanned over a pair, "...mechanically manipulates the equilibrium position of a surface silicon atom, causing rehybridization that stabilizes a negative charge at the dangling bond" [153]. Or, in simpler terms, the tip mechanically toggled the DB pair as it scanned them such that the electron would switch sides between the two degenerate (in energy) configurations. Thus, while no tunneling was observable with AFM, the electron could be manipulated to one side or the other. This led to trying to enforce a stronger localization of the electron on a particular pair side with a local electrostatic perturber.

In Figure 4.2(j-l), an asymmetric perturber DB is added as marked by the orange triangle in the AFM constant-height frame of Figure 4.2(k). Critically for a design like this, the perturber must be far enough away to not lose its electron due to Coulomb repulsion, but still close enough to tilt the potential energy landscape of the pair. The addition of the perturber enforces the teal triangle-marked DB to be neutral and the blue triangle-marked DB to be negative, as evidenced by their relative contrast in Figure 4.2(k). If the pair polarizes in this fashion, it is denoted as a binary 0 (See below Figure 4.2(k)). Examining the ensemble's $\Delta f(V)$ in Figure 4.2(l), the two negative DBs (blue and orange) have perfectly overlaying curves, but the neutral DB (teal) has its DB(0/-) step shifted to 0.395 V. In different wording, if sweeping bias over the teal DB to change its charge state, a larger energy is required due to the electrostatic stabilization effect of the others. Another point of interest is the two negative DBs (orange and blue) shift away from the dashed vertical black line marking all the $\Delta f(V)$ panels. This dashed black line was put at the voltage of the DB(0/-) charge transition of the isolated cases. In this new perturbed case in Figure 4.2(l), there is a deviation from the isolated shifts because the negative DBs (orange and blue) are electrostatically interacting with each other. Explained differently, the perturber DB was made close enough to the pair to enforce a given tilt, but the two negative DBs in the ensemble are still close enough to mutually shift their charge transition points slightly.

In Figure 4.2(m-o), it is demonstrated that the electron localization of the pair can be switched. The orange perturber DB from Figure 4.2(j-l) is erased, and a different

perturber DB is patterned on the opposite side as marked by the red triangle. Now, the AFM and $\Delta f(V)$ results in Figure 4.2(n,o) are the mirror image of Figure 4.2(k,l), with the constant-height Δf image in Figure 4.2(n) showing the blue DB neutral and the teal DB dark. This opposite polarization represents a binary 1 (See below Figure 4.2(n)).

This forms the central result for the construction of multiple-DB atomic logic structures: a perturbing electrostatic input can localize a single electron to one side or the other of a double well potential formed of two DBs, with the binary information contained in the spatial localization. Many of the two-DB pair building blocks can be cleverly geometrically arranged to electrostatically interact, providing higher-order function. The BASiL paper provides two such examples later, with a binary wire and logical OR gate demonstrated (See Section 4.1). These DB pair building blocks are robust with large interaction energies of hundreds of meV; if the voltage of the DB(0/-) step of the teal curve from 4.2(l) is subtracted from the voltage of the blue/orange DB's DB(0/-) step, a stabilization voltage of $\sim 445\ mV$ is found. Since $E = QV$ and it is a single electron charge change, that value can be directly translated to an energy of 445 meV. DB-based circuitry would approximately have a bit energy of this order, which is many times greater than $k_B T$ at room-temperature (25.7 meV), suggesting operation beyond cryogenic conditions. "Approximately" is used as a qualifier for the bit energy at this time because clustering of many negative DBs in a small area can reduce this stabilization energy. A detailed discussion looking at this effect in regard to the fabricated OR gate is given later in Section 4.2.3. While much testing remains to be done, minimal energy consumption per operation is expected (at worst on order with the bit energy), as well as little device heating (no conventional current flowing and causing resistive heating). With this quick background, the rest of the details are left to the publication in Section 4.1.

2.5 Summary

In review, the basics of STM and AFM scanning, the qPlus AFM sensor, characteristics of the doped H:Si surface, tip-influence on measurements, and common AFM

techniques to probe the surface have been covered. For the AFM types of analysis, special considerations must be made to factor in the mesoscopic tip shape, the terminating apex atom, and the height at which the analysis is performed, as all can alter the measured interactions. Despite these extra complexities, AFM is a powerful complimentary tool to STM. Its ability to measure atomically resolved features and single electron charge changes without the need for flowing current makes it a critical tool for examining DBs under parameters STM can not access. With AFM, DB contrast in constant-height Δf scans can be used to look at electron re-arrangement in DB structures in a minimally perturbative way. Additionally, AFM $\Delta f(V)$ analysis provides a measure of the electrostatics, and can deduce how strongly stabilized a particular DB is. In the presentation of the three papers that make up this thesis to follow, these techniques and principals are applied often, with this chapter hopefully having motivated a deeper understanding of the remaining parts of this work.

Chapter 3

Atomic White-Out: Error Correction for Dangling Bond Structures

The ability to lithographically write on H:Si with a SPM tip led to significant interest from the scientific community when it was first demonstrated, with groups initially showing that nm-scale features could be created through desorption of patches of hydrogen [135, 154, 155]. A few years later, the spatial preciseness of the technique was refined, with the first examples of atomically precise desorption demonstrated [42, 156]. Today, groups routinely desorb exactly the hydrogen atoms they want, demonstrating perfect structures comprised of 10's of DBs [45, 51, 132, 157]. The one functionality missing over the last two decades of development, however, was a reverse methodology wherein hydrogen atoms could also be precisely put back.

Historically, passivation ("capping") of dangling bonds had been demonstrated, but with practical limitations. Dogel *et al.* added DEHA(Et_2NOH) to their scan chamber and observed the passivation of some DBs [158]. Unfortunately, complete passivation never occurred, with some DBs nonreactive to DEHA even after large doses were introduced [158]. Labidi *et al.* was able to passivate entire bare dimers in a controlled fashion by leaking in gaseous H_2, and then applying positive STM

bias pulses to induce passivation [159]. This technique only worked on bare dimers (not individual DBs) however, and also contaminated the UHV scan chamber with excess H_2. Our group reported a prior mechanical passivation method where we showed tip contacts over a bare silicon tip-shaping patch could induce the passivation of individual or groups of dimers [93] (also See Figure 2.10). This earlier study had limited utility though, as the procedure could only be performed over bare Si with crude targeting. The dimer passivation methods, that of pulsing and mechanically bonding, are additionally unattractive as they are likely to alter the tip. Even minor tip changes can drastically alter the tip-sample junction interactions, leaving comparison within an experiment circumspect (See the discussion in Section 2.2.4). Thus, to overcome these limitations we developed and reported a "gentle" method of picking up a single hydrogen atom, which is subsequently mechanically bonded to a single DB [136].

After a localized tip-induced excitation on the Si-H surface to create a DB, we found that the desorbed single hydrogen atom hopped to the tip apex 50% of the time. If transferred to the tip apex, the hydrogen-functionalized tip could be identified through a unique signature in $\Delta f(z)$ curves, as well as from observed enhancement of the spatial resolution in STM (See Figure 2.12). By bringing the H-functionalized tip apex close to a DB in the absence of bias and current, a covalent bond between the hydrogen and DB is formed, erasing it. This process is accompanied by a return of the STM contrast and $\Delta f(z)$ spectra to the same character as before functionalization. This suggests the process has no damaging effects on tip or sample structure, other than the intended loss of the functionalizing H atom to the DB.

With error-correction for DB fabrication in hand, this opened up new possibilities for DB-based experiments. It facilitated demonstration of the largest perfect DB structures to date [134], in addition to enabling the two subsequent papers that are part of this thesis. In "Binary Atomic Silicon Logic" (Section 4.1) it is used to test electron reconfiguration in our binary logic bits by erasing perturbing input DBs as required. In "Electrostatic Landscape of a H-Silicon Surface Probed by a Moveable Quantum Dot" (Section 5.1) , we deploy it to successively pattern and erase a "probe" dangling bond in the vicinity of charge defects, measuring spectroscopic shifts as a

function of distance. With the ease and controllability of this erasure methodology, we envision "Atomic White-Out" will continue to be an invaluable technique for H:Si researchers, enabling testing of a multitude of complex dangling bond structures and phenomena.

3.1 Paper and Supplementary Information: Atomic White-Out: Enabling Atomic Circuitry through Mechanically Induced Bonding of Single Hydrogen Atoms to a Silicon Surface

Reproduced under the American Chemical Society's blanket permission policy for students to include in their theses and dissertations their own articles. Copyright 2017 American Chemical Society [https://pubs.acs.org/doi/full/10.1021/acsnano.7b04238] [136].

Authors: Taleana R. Huff[1,2], Hatem Labidi[1,3], Mohammad Rashidi[1,3], Mohammad Koleini[3], Roshan Achal[1,2], Mark H. Salomons[2,3], and Robert A. Wolkow[1,2,3].

[1] Department of Physics, University of Alberta, Edmonton, Alberta, T6G 2E1, Canada

[2] Quantum Silicon, Inc., Edmonton, Alberta, T6G 2M9, Canada

[3] National Institute for Nanotechnology, National Research Council of Canada, Edmonton, Alberta, T6G 2M9, Canada

3.1.1 Abstract

We report the mechanically induced formation of a silicon-hydrogen covalent bond and its application in engineering nanoelectronic devices. We show that using the

tip of a non-contact atomic force microscope (NC-AFM), a single hydrogen atom could be vertically manipulated. When applying a localized electronic excitation, a single hydrogen atom is desorbed from the hydrogen passivated surface and can be transferred to the tip apex as evidenced from a unique signature in frequency shift curves. In the absence of tunnel electrons and electric field in the scanning probe microscope junction at 0 V, the hydrogen atom at the tip apex is brought very close to a silicon dangling bond, inducing the mechanical formation of a silicon-hydrogen covalent bond and the passivation of the dangling bond. The functionalized tip was used to characterize silicon dangling bonds on the hydrogen-silicon surface, which was shown to enhance the scanning tunneling microscope (STM) contrast, and allowed NC-AFM imaging with atomic and chemical bond contrasts. Through examples, we show the importance of this atomic scale mechanical manipulation technique in the engineering of the emerging technology of on-surface dangling bond based nanoelectronic devices.

3.1.2 Introduction

Due to the continuous improvement of scanning probe microscopy techniques, the long thought inaccessible goal of inducing and visualizing chemical reactions at the atomic scale is now routinely achievable by many groups around the world. In the framework of so-called mechanochemistry [160], mechanical force induced reactions have been studied using NC-AFM [161]. Recent works reported force induced atomic-scale switching [162], quantitative force measurements to induce the diffusion of single atoms [133] and molecules [163], as well as studying molecular conformers [164] and tautomerization [165]. A few earlier studies also showed examples of mechanically induced vertical manipulation of single atoms [166,167]. However, direct observation of mechanically induced covalent bonding of two different atoms using NC-AFM remain scarce [168].

Recently, the silicon dangling bond (DB) on the technologically relevant H:Si(100) surface was established as a very promising building block for beyond CMOS technology [51, 55]. A DB corresponds to a desorbed single hydrogen atom from the

otherwise passivated silicon surface. It is approximately an sp^3 hybrid orbital that can be occupied by 2, 1, or 0 electrons resulting, respectively, in a negative, neutral, or positively charged DB. Thus, a DB behaves essentially as a single atom quantum dot, with charge state transitions reported in STM experiments [48, 88]. DBs can be found natively on the surface as a result of imperfections during the hydrogen termination procedure or artificially created using the STM tip. Different works have shown that controlled atom-by-atom lithography, *i.e.* hydrogen desorption, on the H:Si surface allows creation of DB based circuits for next generation ultimately-miniaturized low power nanoelectronic devices [21, 45, 50, 51, 55].

Although STM tip induced desorption of hydrogen from the H:Si(100) surface was extensively studied [40–46], the reverse manipulation of selective adsorption of a single hydrogen atom to passivate a silicon DB has not been as rigorously examined [137]. In this context, AFM can bring more insights by allowing identification of different tip dynamics [96, 104] and probing chemical reactivity at the atomic scale [169, 170].

Here, we report the controlled vertical manipulation of a single H atom using the tip of an AFM sensor and its application in characterizing and engineering silicon DB-based structures of relevance to nanoelectronic devices. We show that following a localized tip induced excitation on the H:Si surface, a single hydrogen atom is desorbed and could be either deposited on the surface with stable imaging in STM and AFM, or transferred to the tip apex. The single H atom functionalized tip was identified through a unique signature in frequency shift *vs.* displacement curves (*i.e.* $\Delta f(z)$) and a characteristic enhancement of STM images in filled and empty states. By bringing the H-functionalized tip apex very close to a DB in the absence of bias and current, a covalent bond between the single hydrogen and silicon atoms is formed. Subsequent changes in the STM images and $\Delta f(z)$ curves confirmed that this mechanically induced reaction results in the passivation of the DB with the hydrogen from the tip apex.

It has become clear that CO functionalized tips are effective for characterization of adsorbed molecules on metal surfaces [96, 171]. It is clear also that accessible and effective tips are required for other systems of study. Preparing and identifying such

a tip is described in this work. Moreover, the H functionalized tip is shown to allow characterization and also induce changes in DB-based structures on the H:Si(100) surface through selective mechanically induced hydrogen passivation, or "capping".

3.1.3 Results and Discussion

Tip Functionalization with a Single Hydrogen Atom

In the Si(100)-2 $\times$ 1 reconstruction, silicon atoms at the surface are organized in dimers. When the surface is passivated with hydrogen in the monohydride reconstruction, each silicon atom at the surface is covalently bonded with a single hydrogen atom as represented in Figure 3.1(a). Figure 3.1(b) shows a typical defect-free empty states STM image acquired using a non functionalized tip (see methods and Ref [93] for details on *in-situ* tip preparation).

Figure 3.1(c) shows a 3D ball and stick model of a silicon dangling bond (represented in green) on the H:Si(100) surface. To create a single DB, the STM tip is positioned on top of a hydrogen atom (red dot in Figure 3.1(b)), then the feedback loop is switched off, and a voltage pulse of about 2.3 V is applied for a few milliseconds. As illustrated in Figure 3.1(c), this results in the selective desorption of the hydrogen atom under the tip apex which is often transferred to the tip. Figure 3.1(d) shows a typical STM image of the created single DB. In accordance with earlier studies in the literature, the DB in empty states appears as a bright protrusion surrounded by a characteristic dark halo [51, 88].

While the tip-induced desorption of hydrogen from the H:Si(100) surface has been studied by researchers for over two decades (see Ref [88] for details), the location and mode of attachment of the H atom after desorption has remained rarely studied [172]. Following procedures described here and tracking desorption events for several different tips, we found that DB creation through a voltage pulse resulted in the desorbed H atom being transferred to the tip apex roughly 50% of the times, *i.e.* forming a H-functionalized tip. In 30% of cases, the desorbed H atom is found on the H:Si surface close to the just created DB as shown in Figure 3.2(a), agreeing with similarly reported values of H returning to the surface in a study done by Ballard *et*

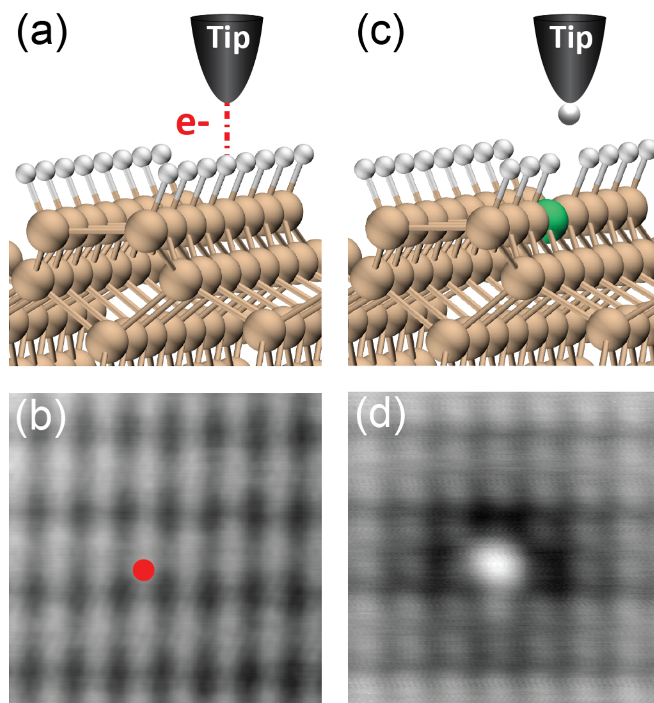

Figure 3.1: **An Illustration of the Tip Induced Manipulation That Can Result in Tip Functionalization With a Single Hydrogen Atom. (a)** Ball and stick model of the H:Si(100)-2×1 surface. **(b)** Typical defect-free empty states STM image using a non-functionalized tip and showing the dimer structure of the surface. The red dot indicates the position of the STM tip when the electronic excitation sketched in (a) is applied. **(c)** Ball and stick model of a silicon atom with a dangling bond in green and a H-functionalized tip resulting from the tip-induced desorption. **(d)** Typical STM image of a DB acquired with a H-functionalized tip showing a characteristic STM contrast enhancement. Both STM images were acquired in constant current mode with a set point of $I = 50\ pA$ at $V = 1.3\ V$.

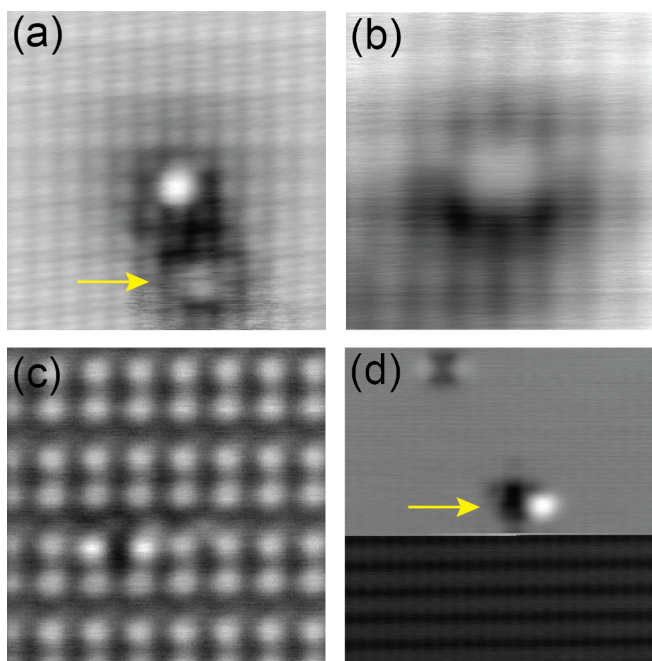

Figure 3.2: **Imaging a Single Hydrogen Atom Physisorbed on the H:Si(100) Surface.** **(a)** A 5×5 nm^2 STM image at 1.3 V of a DB where the desorbed atomic hydrogen was not picked up, instead adsorbing at the location indicated by an arrow. **(b)** 3×3 nm^2 STM image of an atomic hydrogen adsorbed on the surface and **(c)** corresponding AFM frequency shift map at 0 V and a relative tip elevation of $z = -380$ pm. **(d)** An atomic hydrogen on the surface is picked up by a slow downward STM scan at $V = 1.6$ V. All STM images are constant current at $I = 50$ pA.

al [172]. In the remaining 20% of cases, the tip apex does not change and a hydrogen atom could not be seen in the vicinity of the newly created DB, suggesting it was possibly adsorbed on the tip away from the apex atom, deposited on the surface farther from the DB, or ejected to the vacuum.

Figure 3.2(a) shows an example of a single hydrogen atom found to be deposited on the H:Si surface immediately after tip induced creation of a DB. Such an object was confirmed to be a single hydrogen atom by dragging it with an elevated positive bias to passivate the created nearby DB (Supplementary Figure 3.6). Interestingly, the hydrogen atom appears in empty states STM images as a slightly bright protru-

sion surrounded by a dark halo as shown in Figure 3.2(b). This suggests a possible charging effect that induces a localized band bending similar to a single DB [45,88]. In the corresponding frequency shift map (Figure 3.2(c)), the physisorbed hydrogen atom appears to induce a lattice distortion of two adjacent dimer pairs. We note here that the mismatch in the position of the physisorbed H atom between STM and AFM images is due to the diffusion of the H atom triggered by the ramping down of the bias when switching the scanning mode. When imaged at relatively high positive voltage (1.6 V) in the example of Figure 3.2(d), the hydrogen atom was picked up by the tip apex as evidenced from the change in STM contrast midway through the scan.

In the examples of Figure 3.1 and 3.2, the enhanced STM contrast after creating a DB is a first strong indication of tip functionalization with the desorbed single H atom. The contrast changes from resolving dimers (Figure 3.1(b)) to resolving single atoms (Figure 3.1(d)), respectively, before and after the hydrogen desorption from the surface. This is similar to what is well known for the CO molecule, where once it is picked up by the tip apex following a voltage pulse it enhances the STM and AFM contrast [96,173,174]. In the following section, we provide further evidence of a single hydrogen atom functionalized tip using NC-AFM, which allows identification of different tip dynamics through studying force curves [93,104,175].

Mechanically Induced Covalent Bonding of Single Hydrogen and Silicon Atoms

Figure 3.3(a) shows a filled states STM image of the H:Si surface with a silicon DB created using the procedure described in the previous section. Similar to the case of empty states, we notice an enhanced STM contrast. In fact, typical filled states STM images of the H:Si surface usually show only dimer rows [88], but in Figure 3.3(a) the dimers of dimer rows are clearly resolved.

Following the creation of the single DB in Figure 3.3(a), the scanner was switched to AFM scanning mode. Figure 3.3(b) shows a frequency shift *vs.* displacement curve recorded using a hydrogen functionalized tip on top of a hydrogen atom on the

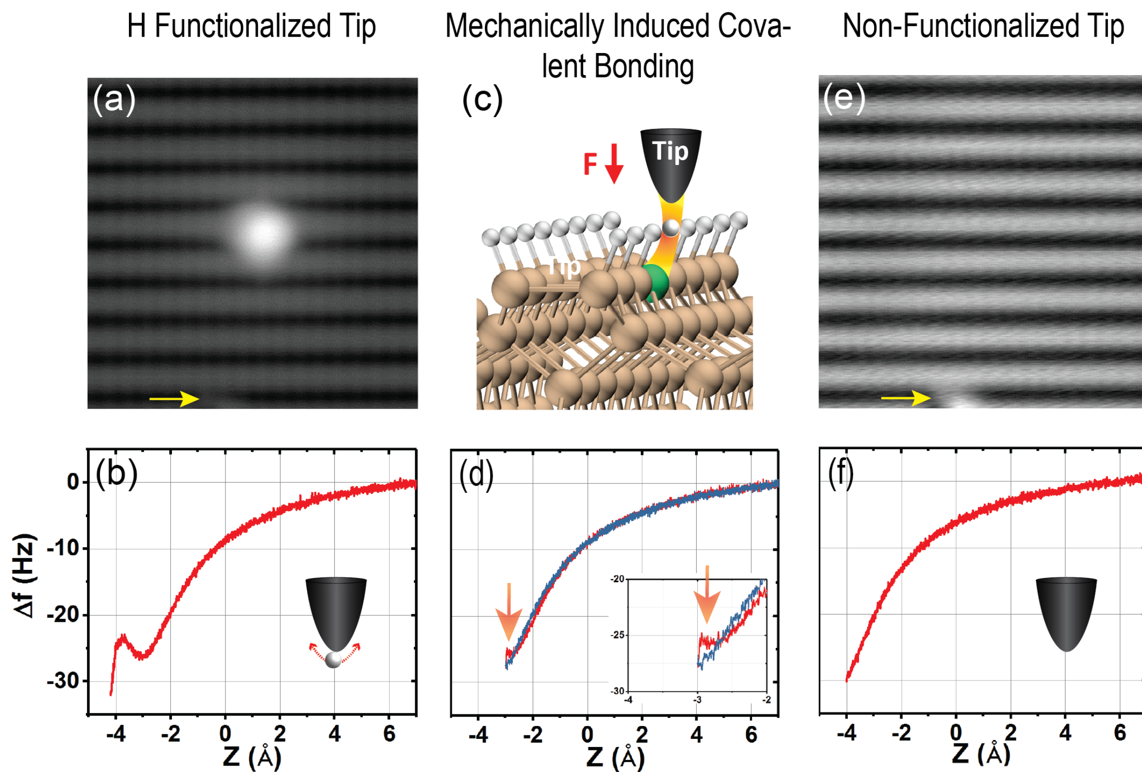

Figure 3.3: **Procedure to Mechanically Induce a Hydrogen-Silicon Covalent Bond.** **(a)** A typical filled states STM image of a silicon dangling bond on the H:Si(100)-2×1 surface using a single hydrogen atom functionalized tip. The yellow arrow indicates a defect taken as a refer]ence. **(b)** $\Delta f(z)$ curve using H-functionalized tip on a surface hydrogen atom. **(c)** Ball and stick model and **(d)** $\Delta f(z)$ curve on a single DB during the mechanically induced Si-H covalent bond capping event. The orange arrow indicates a hysteresis (zoom in inset) characteristic of the change that occurs due to the formation of the covalent bond between the H atom at the tip apex and the silicon dangling bond. **(e)** STM image and **(f)** $\Delta f(z)$ curve on the H:Si surface subsequent to the mechanically induced reaction in (d).

surface. The minima at ~ -3 Å is always seen when a functionalized tip is prepared following the procedure previously described. Such features were reported by other works in the case of functionalized tips, and are ascribed to the relaxation of the functionalizing atom at the tip apex [165, 171, 176].

When recorded on a DB using the same functionalized tip, $\Delta f(z)$ curves exhibit a hysteresis between the forward and backward sweep when the tip is brought very close to the DB as shown in Figure 3.3(c,d), which indicates a change in the AFM junction [168, 176, 177]. When acquiring a subsequent STM image, we notice that the DB was capped with a hydrogen atom. The defect indicated by the yellow arrow is used as a marker showing that Figure 3.2(e) is exactly the same area as 3.2(a). Additionally, $\Delta f(z)$ curves recorded on top of a hydrogen atom of the surface as shown in Figure 3.3(f) no longer exhibit the minima characteristic of the hydrogen functionalized tip. This unambiguously proves that the tip that yields the minima in force curves was indeed functionalized with a single hydrogen atom.

Throughout all our experimental data, we saw that a tip that produces enhanced STM also systematically produces the characteristic force curves with the shallow minima. Therefore, change in the STM contrast, such as presented in Figures 3.1(d), 3.2(a), and 3.3(a) indicates successful functionalization of the tip apex with a single hydrogen atom. This is important for technological applications related to altering DB engineered structures through capping, as changes in STM contrast to detect H-functionalized tips is a much faster indicator than the time consuming acquisition of $\Delta f(z)$ curves. In fact, regular systematic, non-tip-damaging, and reliable capping was produced using STM contrast as an indicator alone.

All $\Delta f(z)$ curves were recorded at 0 V in the complete absence of tunnel current, and the hydrogen capping of the DB only occurs when the tip is brought to a close enough interaction distance. Therefore, the silicon-hydrogen covalent bonding is mechanically induced. We note here that mechanically induced desorption was also observed, but often resulted in tip structure changes or multiple hydrogens desorbed, unlike the gentle and precise tip induced desorption. We note here, the initial tip apex structure before picking up a hydrogen atom on the tip apex is never exactly the same. So, the H-tip bond is not necessarily the same in all H-functionalized

tips, similarly to the case of CO tips. This is likely the reason we observe variation on the tip elevation to induce capping. Other factors such as the sensor oscillation amplitude or the $\Delta f(z)$ acquisition parameters might also play a role.

So far, reliable functionalization of tips mainly with CO molecules allowed different groups to achieve submolecular and bond contrast imaging of different molecular systems [96, 171]. In the following, we show that in addition to high resolution AFM imaging, H-functionalized tips can be implemented in atom-by-atom lithography to create and modify silicon DB based nanoelectronic elements.

Characterizing Silicon Dangling Bonds on the Si-H Surface with a H-Functionalized Tip

Although DBs on the H:Si surface have been extensively studied using STM, NC-AFM works remain almost nonexistent. AFM can provide an important complementary view to STM works as it allows characterizing the chemical reactivity of DBs. Moreover, unlike STM, AFM allows probing the electronic properties of DBs and DB structures in the band-gap with minimized perturbation from the tip, *e.g.* minimal tip induced band bending and electron/hole injection [50, 88].

Figure 3.4(a) shows force curves acquired using a H-functionalized tip above a surface hydrogen atom (blue curve) and a single silicon DB (red curve). These force curves were recorded subsequently with $z = 0$ Å corresponding to the tip position defined by the STM imaging set points ($I = 30\ pA$ and $V = 1.3\ V$) before switching off the feedback loop. Hence, superposing the 2 curves allows direct comparison of the interaction force between tip-surface and tip-DB. We notice that for relatively large tip-sample distances, the two curves are almost identical. Only for small tip elevations (around $z = -3.5$ Å in this example) is a difference seen, with the DB showing a much larger increase in attractive interaction with the tip. This indicates that short range forces are the main contributor to the interaction force [178]. This is also consistent with the DB being a reactive chemical center on the chemically inert H:Si surface where deposited molecules can selectively adsorb [179, 180]. Similar to what was reported previously for the case of gold atoms adsorbed on NaCl over

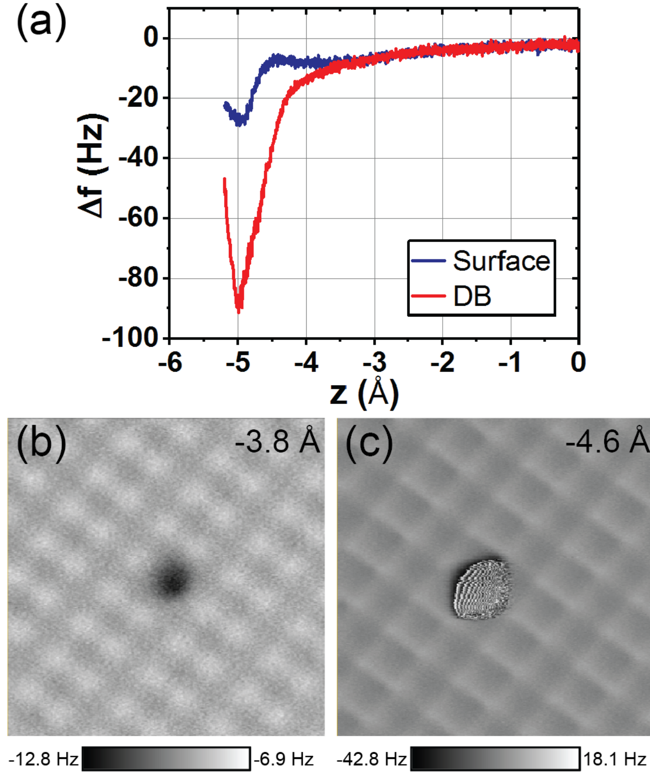

Figure 3.4: **NC-AFM Characterization of a Single DB on the H:Si(100)-2×1 Surface Using a H-Functionalized Tip. (a)** $\Delta f(z)$ curves recorded on the H:Si surface (blue curve) and on the silicon DB (red curve). 3×3 nm^2 frequency shift maps of a DB on the H:Si surface at relatively large **(b)** and small **(c)** tip-sample distances respectively. All data was acquired at $V = 0$ V with an oscillation amplitude of 1 Å.

Cu(111) [141, 181], the short range electrostatic force due to the localized negative charge on the DB [48, 51, 88] is most likely the main contributor to the large tip-sample interaction on the DB.

Figures 3.4(b,c) show frequency shift maps acquired at different tip elevations using a H-functionalized tip. At relatively large tip-sample distances (Figure 3.4(b)), each hydrogen atom decorating a silicon atom clearly appears and follows the dimer structure of the 2×1 reconstruction. The DB arising from the desorbed hydrogen atom on the surface appears as a dark atom-sized protrusion, introducing a much

higher tip-sample interaction force localized on the DB. As we get closer to the surface (Supplementary materials, Figure 3.7), an evolution from atomic to bond contrast is seen on the H:Si surface as discussed in detail in reference [93]. In Figure 3.4(c), as a result of the larger attractive forces, the DB appears as a enlarged feature. The perturbations seen inside are an artifact in the excitation channel (Supplementary materials, Figure 3.8) reflecting the inability of the feedback loop to maintain a constant oscillation amplitude due to quick changes in the interaction profile during lateral movement of the tip from the passivated region to the reactive DB feature. We comment that the instability is not visible in $\Delta f(z)$ curves as shown in Figure 3.4(a) due to the absence of such quick changes.

We note here that high resolution bond contrast imaging is rendered possible thanks to the passivation of the tip apex with a hydrogen atom [93, 96]. The later can be attracted to form a covalent bond with the silicon DB, but only at very small tip-sample elevations. This shows that the H-functionalized tip is robust and can be used to image reactive adsorbates or surface defects.

Altering Engineered On-Surface DB-Based Quantum Structures

Recent works have shown that a DB can behave as a single atom quantum dot. Additionally, using atom-by-atom lithography with the STM tip, the coupling between DBs can be exploited to create functional DB structures such as QCA circuits, binary wires and logic gates [21,51,55,182]. For large many-atom circuits this necessitates a precise control of desorption, which is difficult to achieve and has not been reported for more than a few DBs so far. Hence, a technique to correct or change multi-DB structures is highly desirable. Additionally, capping DBs would allow modulating the engineered quantum states from coupled DBs [45].

Figure 3.5(a) shows a filled state STM image of two separate pairs of coupled DBs along the same dimer row. Each pair has 2 hydrogen atoms separating the DBs within the pair (see Supplementary Figure 3.9). We note here the enhanced STM contrast characteristic of a H-functionalized tip. In Figure 3.5(b), the right side DB was selectively capped using the mechanically induced H:Si covalent bonding

described in the previous section. We notice in Figure 3.5(b) the change in the STM contrast as previously shown in Figures 3.1 and 3.3. Additionally, the new single DB on the right side of the image appears as a bright protrusion surrounded with a small dark halo, while the appearance of the two other coupled DBs shows no change [51].

A similar experiment is shown in Figure 3.5(c) where three tunnel coupled DBs are imaged using a H-functionalized tip. The central DB was then erased, the tip re-functionalized by picking up another hydrogen atom, and the remaining two DBs re-imaged in Figure 3.5(d). Using an equivalent hydrogen tip for the before and after images highlights that changes in brightness are the result of coupling alterations, not simply a change of the terminating atom.

Figure 3.5(e) shows a filled state image of four DBs along the same dimer row with each DB separated by a single H atom as illustrated in the 3D model of Figure 3.5(f).

In the corresponding empty states image (Figure 3.5(g)), a more complex structure is seen with four additional bright protrusions between the visible end atoms. Theoretical analysis from Schofield *et al.* [45] have reported similar results, explaining the extra protrusions as an excited state molecular orbital from wave function overlap of multi-DB systems. We show here an active modification of these artificial molecular orbitals through the controlled mechanical covalent bonding of a Si atom (DB) with a hydrogen atom on the tip apex causing nodes to disappear.

Figure 3.5(f,h) show the altered filled and empty state molecular orbitals from erasing the far right DB in Figure 3.5(e). The filled state image shows up as three bright protrusions corresponding to three DBs, whereas the empty state image has been altered to now only have 2 bright protrusions instead of the prior 4.

We note that in the example of Figure 3.5(e-h), DB structures were imaged using a non-functionalized tip both before and after alteration. This further highlights that changes in the coupling between DBs visible from the different additional nodes that appear/disappear is not due to changes in the tip, but rather the result of erasing a DB with a hydrogen on the tip apex.

Through the examples of Figure 3.5, we can see how the controlled mechanically induced H and Si covalent bonding allows the non-destructive editing of a DB struc-

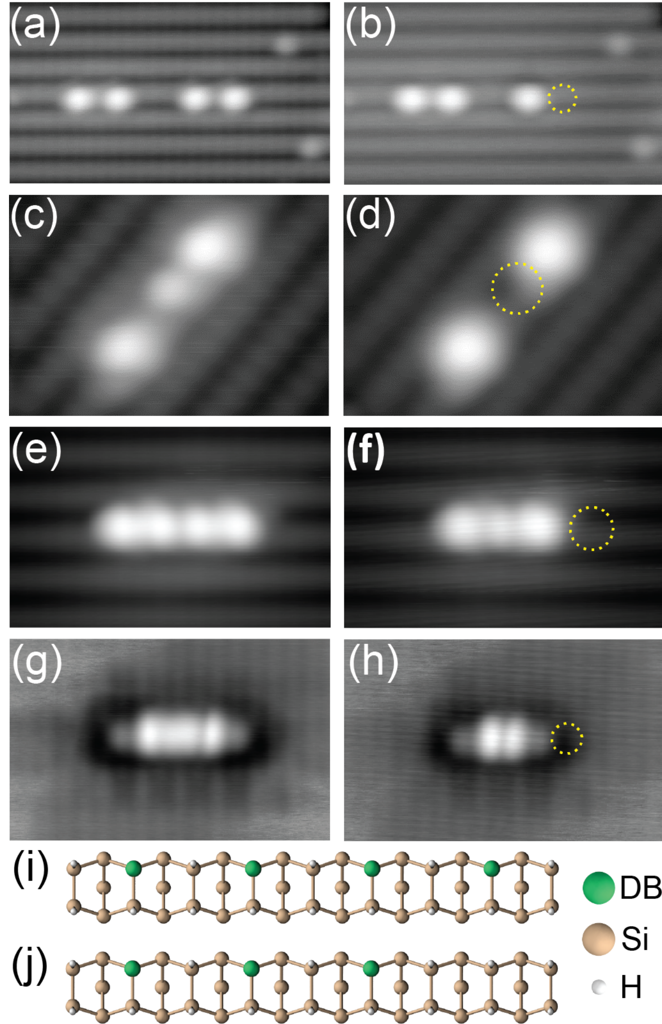

Figure 3.5: **Altering Coupling and Artificial Molecular Orbitals in Multi-DB Structures (a)** Two pairs of coupled DBs on the H:Si(100) surface arranged along a same dimer row. **(b)** Image of the same area after the mechanically induced capping of the far right DB in (a). **(c)** A $3 \times 2\ nm^2$ STM image of three tunnel-coupled DBs. **(d)** The same area after erasing the middle DB in (c). Constant current images (a) to (d) were acquired at $V = -1.8\ V$ and $I = 50\ pA$. **(e-f)** Filled ($V = -2.0\ V$, $I = 50\ pA$) and **(g-h)** empty ($V = 1.4\ V$, $I = 50\ pA$) states STM images of a DB wire, respectively, before and after erasing the far right DB in (e). 3D models of the four **(i)** and three **(j)** DB wire. Positions of erased DBs are indicated by dotted circles. Empty state images of Figure 5(a) and Figure 5(c) are presented in Supplementary Figure 3.9.

ture. This technique could be further applied to actuation of more complicated DB based patterns and elements as well, with erasure of a DB acting as a type of switch.

3.1.4 Conclusion

To summarize, we showed that following a tip induced desorption, a hydrogen atom can be deposited on the surface or transferred to the tip apex resulting in a H-functionalized tip. The physisorbed single hydrogen atom on the chemically inert H:Si surface could be stably imaged in STM and AFM modes.

The H-functionalized tip was used to **(1)** characterize silicon dangling bonds and **(2)** to mechanically induce the covalent bonding of single hydrogen and silicon atoms. We showed the potential of this mechanically induced reaction to precisely modify multiple DB structures such as coupled DBs and artificial molecular states.

3.1.5 Methods

Experiments were carried out using a commercial (Omicron) LT-STM/AFM system operated at 4.5 K.

We used qPlus sensors exhibiting a quality factor $Q \simeq 30,000$ and a resonance frequency $f_0 \simeq 25\ kHz$. Tips were direct current etched in a NaOH solution from a 50 μm thick polycrystalline tungsten wire. In ultra high vacuum (UHV), tips were first cleaned from their oxide layer by a series of electron beam heating treatments, followed by field evaporation in a field ion microscope (FIM). Then, they were further sharpened using a FIM nitrogen etching process to ensure small tip radius of curvature [88]. The sensor was equipped with a separate wire for tunneling current to minimize cross-talk problems [78]. Additionally, all AFM data was recorded at $V = 0\ V$ to avoid both coupling between frequency shift and tunnel current, as well as imaging artifacts such as phantom force [146, 183].

In-situ, tips were further processed to obtain artifact free images by first creating a bare silicon patch through tip induced hydrogen desorption, then by controlled nano-indentation on the created patch. This procedure usually results in a clean

and stable tip. From prior work, this treatment was shown to result in a silicon tip [93, 184].

We used highly arsenic-doped ($\sim 1.5 \times 10^{19}\, atom\, cm^{-3}$) silicon (100) samples. Following 12 hours degassing at $\sim 600\,°C$ in UHV, samples underwent a series of resistive flash anneals at $1250\,°C$. [88] Samples were then exposed to atomic hydrogen while being kept at $\sim 320\,°C$ to ensure a 2×1 reconstruction.

To minimize drift during AFM image acquisition, the tip was left to settle for about 12 hours after approach to allow piezo scanner stabilization. Additionally, an atom tracking program implemented in the Nanonis control electronics was used.

3.1.6 Supplementary Information: Atomic White-Out: Enabling Atomic Circuitry through Mechanically Induced Bonding of Single Hydrogen Atoms to a Silicon Surface

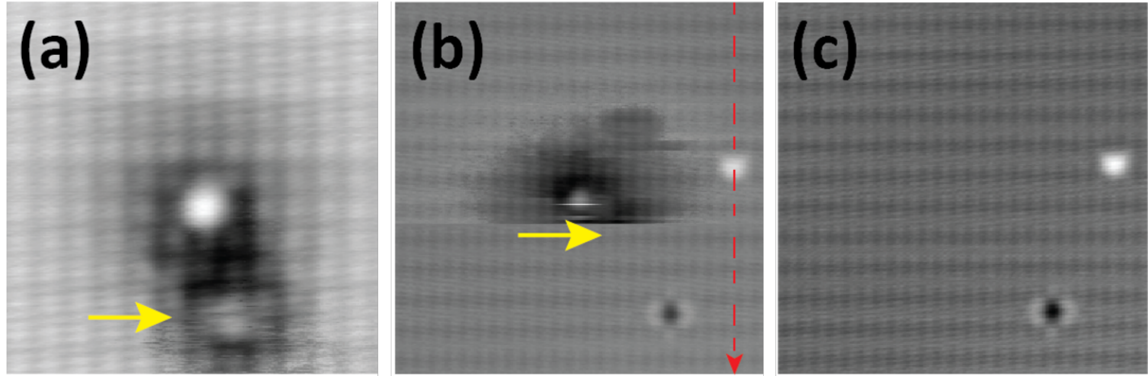

Figure 3.6: **(a)** Single hydrogen atoms physisorbed on the chemically inert H:Si(100) surface could be stably imaged in filled states at low voltage ($V = 1.3\ V$). However, when the scanning voltage is increased to $V = 1.7\ V$ in **(b)**, the hydrogen atom is dragged by the tip. This dragging is not smooth, but can result in the H atom being moved close enough to the DB to cap it, as indicated by a change in contrast midway through the image and confirmed by a subsequent STM image of the same area **(c)**. (b) and (c) are larger area $10 \times 10\ nm^2$ images of the area in (a). The location of the atomic hydrogen is marked with an arrow.

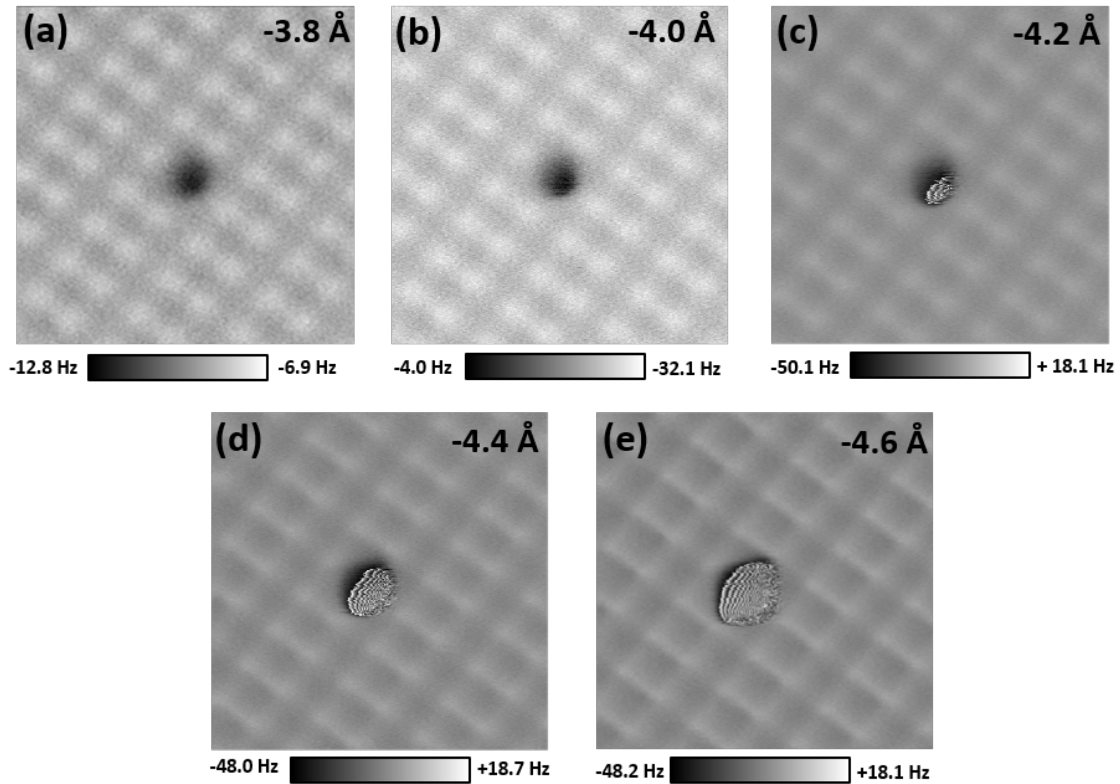

Figure 3.7: **(a-e)** Series of raw $3 \times 3\ nm^2$ NC-AFM frequency shift maps of H:Si(100) surface at different tip-sample elevations. Images were recorded at $V = 0\ V$ and with an oscillation amplitude of 1 Å. We see the evolution from atomic to chemical bond contrast on the H:Si surface. For smaller tip elevations, much higher interaction force is seen on the DB than elsewhere on the surface. $z = 0$ Å corresponds to the tip position defined by the STM imaging set points ($V = 1.3\ V$, $I = 30\ pA$) before switching off the feedback loop.

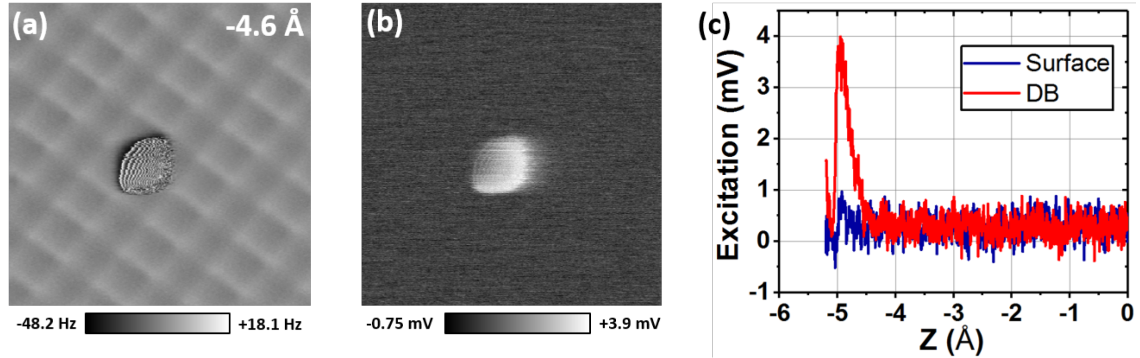

Figure 3.8: **(a)** NC-AFM frequency shift map of a single DB at small tip-sample distance ($z = -4.6$ Å) and **(b)** corresponding simultaneously obtained excitation channel map. **(c)** Superposed excitation *vs.* tip elevation curves recorded on the same DB (red curve) and on the H:Si surface (blue curve).

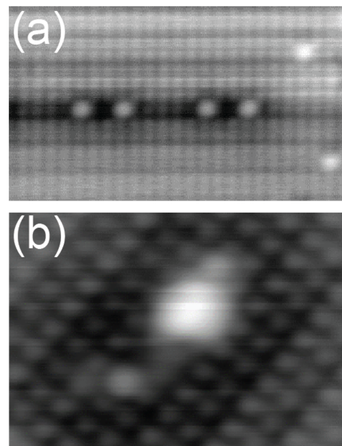

Figure 3.9: **(a,b)** show empty states images ($V = 1.3\ V$, $I = 50\ pA$) corresponding to Figure 3.5(a,c) from the main text, respectively. It can be seen clearly in (a) that for Figure 3.5(a), the coupled DBs are separated by 2 hydrogens. For Figure 3.5(b), (b) shows the central DB is separated from the top-most DB by 1 hydrogen separation, and the bottom-most DB by 2 hydrogen separation.

3.1.7 Acknowledgment

We thank M. Cloutier for his technical expertise and J. Pitters for valuable discussions. We also thank NRC, NSERC, QSi, and AITF for financial support.

3.2 Appendix: Not Published Additional Supplementary Results for Atomic White-Out

3.2.1 Conditioning Required to Produce a Tip Capable of DB Passivation, and Capping with STM

Controlled passivation for single DBs was discovered accidentally. When performing constant-height AFM scans of DBs at different heights, it was observed that on close approach they sometimes, but not always, disappeared. Because of the inconsistency in this passivation event occurring, figuring out a deterministic process to produce a tip that could cap took months of trial and error. All tips are capable of capping under suitable conditioning, but the number of conditioning steps to get the tip to that state can vary (minutes to days).

Tips directly from FIM imaging and etching (See Section 2.2.4), expected to be dominantly tungsten, have never been observed to be capable of capping. The tips with the highest chance of being ideal for erasure events were tips that had been in use for a while; ones that had created many tip forming patches and had been tip formed on both silicon and hydrogen. This suggests a coating on the apex or particular structure is key to giving the correct energetics for passivation events. The current procedure to produce a capping tip is to perform tip forms dozens of times, alternating between them being performed on a bare silicon patch and the hydrogen-terminated surface. Tip forms are $\sim 600 - 1000\ pm$ in from a STM starting height defined by $V = -1.8\ V$ and $I = 50\ pA$, with the bias held fixed ($V = -1.8\ V$) during the tip contacts. STM contrast consistent with a silicon tip, as described in the publication, is looked for.

When silicon-tip contrast is obtained, a DB creation event is attempted over a hydrogen atom until characteristics of apex H-functionalization are observed. Functionalizing with hydrogen is attempted in empty states STM ($V = 1.3\ V$, $I = 50\ pA$), as it more easily resolves individual hydrogen atoms for easy targeting. DB creation voltage pulses range from $\sim 1.8 - 2.5\ V$ over a pulse duration of $10\ ms$, from a starting height defined by $V = 1.3\ V$ and $I = 50\ pA$. A successful H-functionalization can

be inferred from the shallow and early minimum in $\Delta f(z)$ spectra or enhancement of the STM contrast, as described in the paper. In addition, one other quick metric not yet discussed that generally informs successful H-functionalization of the tip is the STM relative tip-sample height telemetry. DB creation is done in constant-current STM mode, with the control electronics adjusting height to maintain the current set-point. If the DB is created and the hydrogen does not go to the tip, an instantaneous increase in current occurs as DBs are more conductive than the surface at this bias. The control electronics detect this increase in current and move the tip further away from the DB, as observed in the control software relative tip-sample height telemetry. Conversely, if the hydrogen is picked up, often a decrease in current is seen with the tip-sample system being moved closer together in the tip-sample height telemetry. We hypothesize this difference in conductivity is due to a change in orbital overlap for STM tunneling. Silicon tips should have sp^3 character like the DBs themselves, such that upon creation of a DB there is instantaneously more overlap between these orbitals, and a corresponding increase in current. In the alternate case where the hydrogen jumps to the tip apex, it should theoretically have a more s-like orbital. This would have less overlap with the DB's sp^3 one, leading to an instantaneous reduction in tunneling current and the subsequent approach of the tip to the DB by the control electronics. If no DB is created, the baseline relative height remains the same and the SPM operator should try more pulses or increase the pulse voltage intensity. Density functional theory (DFT) modeling would lend much needed support to these claims, but for now we have found a change in height in relation to the observed conductance, as described above, generally informs correctly and quickly about the hydrogen tip character. For the cases where it breaks down, we hypothesize an off-apex mechanism.

Follow up work done on capping involved implementing it in STM without the AFM feedback, so as to generalize this technique to the full SPM family [134]. In this STM methodology hydrogen atoms were picked up in the same manner, but capping involved the mechanical approach of tip and DB with a modest bias applied to provide feedback. Changes in conductance were used to infer a capping event, but this work also reported some anomalous cases where the hydrogen atom used

in the capping event did not end up coming from the apex, but rather an off-apex site [134]. It was found that the tip could be loaded with many hydrogen atoms that could be used in sequential capping events, without the need to re-functionalize the apex in between. This meant the tip has to be approached closer to access hydrogen atoms from off-apex sites, with an associated enhanced risk of damaging the probe. However, this observation enabled faster error-correction of structures, with handfuls of sequential capping events possible with a suitably hydrogen-loaded tip.

3.2.2 Tip State Effect on Fabrication Efficiency

Discovered after the publication of Atomic White-Out was that the tip apex state had strong implications not only for erasing DBs, but also for creating them. Moller *et al.* published a paper the same year where they reported that dimer-row resolving STM contrast tips desorbed H atoms more efficiently when compared to atom-resolving ones, likely due to a differing density of states for different apex types [132]. The dominant mechanism for creating a DB is inelastic scattering of tunneling electrons to break the Si-H bond (See Section 2.4.2). Tunneling probability is dependent on the local density of states, and Moller hypothesized row-resolving STM tips might have a greater density of states in the energy window defined by the tip-sample bias than other classes of tip apex [132].

Comparing this to the work in Atomic White-Out, we reported that the STM contrast changes from resolving rows for a silicon tip, to resolving single hydrogen atoms for a hydrogen-functionalized one. As we were able to recognize silicon *vs.* hydrogen tips in the course of our analysis, we too found that the row-resolving silicon tips had more accurate single-atom desorption. Conversely, the hydrogen-functionalized tips either required more pulses or a higher pulse energy for the successful creation of a DB, and tended to make them at incorrect lattice sites more often. While no rigorous statistics have been collected, it does anecdotally agree with the results of Moller *et al.*, inviting future rigorous exploration.

Chapter 4

Atomic Logic with Dangling Bonds

Nanoelectronics has long striven for the ultimate limit of fabrication; reliable use of single atoms as building blocks for computational components. This has required years of development in tools not only to preform manipulation of single atoms with sub-angstrom precision, but also in tools that can read the sensitive single-electron outputs. “Binary Atomic Silicon Logic” reports the first example of reversible information transmission through a fabricated binary wire and logical OR gate made of dangling bonds. A pair of fabricated DBs with a single hydrogen atom intervening between them forms a binary electronic building block. These blocks contain a single moveable electron each, with the spatial arrangement of the electron in a pair representing the binary information; if the electron is electrostatically coerced to localize on the left side of the pair, it represents a binary 0, and if localized on the right side of the pair, it represents a binary 1 (A quick introduction was provided in Section 2.4.4). Higher order logic is achieved by arranging many of these building block pairs to electrostatically interact with each other in predictable ways, resulting in the correct binary output under particular electrostatic inputs. Electrostatic inputs are provided by adding or removing single “perturber” dangling bonds as needed, with the single-electron sensitivity of AFM deployed to look at electron (binary state) rearrangement in the interacting DB pairs.

To put this work in context, other groups have explored different variations on atomic and molecular electronics. Notable studies mentioned in the introduction

include tipping molecules [12], spin-based logic with iron atoms [18], molecular devices [16, 17, 185], a single-atom transistor made with an implanted phosphorous atom [39], and DB-based devices where shifts in the electronic density of states, as measured by STM, represented the binary information [19, 21]. While all are compelling from an academic standpoint, each of these proposed schemes had limitations.

The biggest limiter for most in regard to becoming a commercial technology is thermal fragility. Atoms or molecules placed on top of surfaces were only physisorbed, necessitating temperatures below 10 K to keep them from moving around or detaching. DB-based devices do not have this limitation, with prior studies demonstrating that they will not move lattice sites up to 200 $°C$ [51, 53, 54], and additionally that the charge distribution in coupled-DB structures can be electrostatically controlled for at room-temperature [51]. Since this temperature requirement eliminates most non-DB-based schemes from a practicality standpoint, we focus on comparing ours to the other proposed DB logic paradigms [19, 21].

The DB logic implementations by Kolmer *et al.* [21] and Yengui *et al.* [19] are thermally stable, but may be unsuitable due to energy efficiency limitations. Both studies required an STM tip to measure dI/dU scanning tunneling spectroscopy (STS) over particular DB configurations. STS dI/dU is a measurement done to provide information about the local density of electronic states for a probed entity, with the spectroscopy taken in one of two ways. The first way is to sweep through a bias range while measuring current and then take the derivative of the measured $I(V)$ spectra to get dI/dU. The second method involves a modulation voltage added to a fixed bias, with dI/dU measured by a lock-in amplifier. The final result for both is a curve with peaks that correspond to the measured density of states, with shifts in the energetic location of these peaks determining the logical state of both Kolmer and Yengui's paradigms. This meant that probing the logical state using dI/dU was neither fast or power efficient, as acquiring the spectra requires a tunneling current measured for a range of tip-sample bias values. In addition, alteration of the logical states in between STS probing required either pulses [19], or the addition of local DBs to shift the dI/dU peaks [21]. While it could be argued our demonstrated logic also uses local DBs as perturbers that are slowly mechanically altered, we use it to

a different effect. Instead of shifting peaks requiring a tunneling current signal to measure as in dI/dU, local DB perturbers are used to shift the position of a single electron in a DB pair. Our perturber DBs are temporary stand-ins for demonstration purposes, with envisioned paths toward replacement of them with actuating atomic wires [186]. Additionally, our logic will work in the absence of a tip, as explored in the publication, but these other DB-based examples are rooted to their dependence on a tip for the dI/dU measurement of their logical states.

What held up development of DB-based logic until now was a few key factors only recently addressed. First, was the difficulty of making complicated structures. In general, atom fabrication of structures robust enough to withstand relatively high operating temperature are more difficult to make. This is because larger energy inputs from the scanned probe are required to dislodge and move strongly bound atoms, and under such conditions covalent bonds within the probe itself break with some probability comparable to that of the target bond [135]. With the new insights about DB creation being more reliable with silicon tip states (See Section 3.2.2), refinements in our *in situ* tip forming and sharpening procedures (Section 2.2.5), and development of a reliable and non-damaging error correction methodology (Section 3), we can now routinely make structures consisting of dozens of DBs. The second limitation preventing further development of DB structures was a way to look at their delicate single-electron states in a minimally perturbative way. All prior studies had been conducted in STM at relatively high tunneling currents. As discussed earlier (Section 2.4.4), DBs are artificial quantum dots with a few electrons contained at most, meaning looking at them with STM, which requires a flow of tunneling electrons, is not an optimal way to examine DBs. Fortunately, AFM provided the perfect tool.

As discussed earlier in Section 2.4.4, prior work examining charged species with AFM on other substrates showed great success in resolving single electron charge state changes of molecules [27, 187, 188], electron transfer between molecules [30], and charge state changes in quantum dots [149]. Thus, we employed this charge sensitivity of AFM to our DB systems. The transition of a DB from negative at zero bias, to neutral at a modest negative bias had been inferred, but never directly

seen, because no current is available in the bandgap for STM to generate an image. AFM has no such limitation, allowing us to show direct evidence of this priorly "hidden" transition. Additionally, we easily probe electron re-arrangement in more complicated DB structures, like our wire and OR gate, with a minimized perturbative influence; no current is required but there still remains tip induced band bending. Efforts are made to calculate the effect of tip induced band bending though (See Section 2.4.1 for details on TIBB estimates), which is removed from the experimental measurements through subtraction. We anticipate that these DB structures should have many attractive qualities for atomic-logic applications, which we will provide a final accounting for in the conclusion.

4.1 Paper and Supplementary Information: Binary Atomic Silicon Logic

Reproduced under Springer Nature's policy to reproduce the contribution in whole or in part in any printed volume (book or thesis) of which I am the author. Copyright Springer Nature [https://www.nature.com/articles/s41928-018-0180-3] 2018 [49].

Authors: Taleana R. Huff[1,2], Hatem Labidi[1,3], Mohammad Rashidi[1], Lucian Livadaru[2], Thomas Dienel[1], Roshan Achal[1,2], Wyatt Vine[1], Jason Pitters[2,3], and Robert A. Wolkow[1,2,3].

[1] Department of Physics, University of Alberta, Edmonton, Alberta, T6G 2E1, Canada

[2] Quantum Silicon, Inc., Edmonton, Alberta, T6G 2M9, Canada

[3] National Institute for Nanotechnology, National Research Council of Canada, Edmonton, Alberta, T6G 2M9, Canada

4.1.1 Abstract

It has been proposed that miniature circuitry will ultimately be crafted from single atoms. Despite many advances in the study of atoms and molecules on surfaces using scanning probe microscopes, challenges with patterning and limited thermal structural stability have remained. Here we demonstrate rudimentary circuit elements through the patterning of dangling bonds on a hydrogen-terminated silicon surface. Dangling bonds sequester electrons both spatially and energetically in the bulk bandgap, circumventing short-circuiting by the substrate. We deploy paired dangling bonds occupied by one moveable electron to form a binary electronic building block. Inspired by earlier quantum dot-based approaches, binary information is encoded in the electron position, allowing demonstration of a binary wire and an OR gate.

4.1.2 Introduction

The prospect of atom-scale computing was initially indicated by molecular cascades in which sequentially toppling molecules were arranged in precise configurations to achieve binary logic functions [12]. Many notable approaches towards molecular electronics [13–16, 189], atomic electronics [18, 20, 190] and quantum-dot-based electronics [33, 34, 51, 55, 191, 192] have also been explored. The quantum dot-based approaches [32, 193–196] are particularly attractive, as they could provide a low power yet fast basis [197] to go beyond today's CMOS technology [198]. These approaches, however, require cryogenic temperatures to minimize the population of thermally excited states and achieve the desired functionality. Variability among quantum dots and sensitivity to uncontrolled fields are known to pose additional challenges [199]. The prospect of partially circumventing these issues was reported in studies of silicon dangling bonds (DBs)–that is, unsatisfied bonds–on the otherwise hydrogen-terminated silicon surface (H:Si) [51, 53, 200].

Silicon DBs behave like quantum dots because they are zero-dimensional and exhibit three distinct charge states (positive, neutral, and negative) depending on their electron occupation (zero, one, or two electrons, respectively) [48, 201]. Consequently,

DBs have two charge transition levels: the neutral to negative (0/-) transition and positive to neutral (+/0) transition. Crucially, because these DB energy levels lie within the bulk bandgap they are electronically isolated from the bulk [201, 202]. Silicon DBs approach the ultimate small size (single atom) for a quantum dot and therefore exhibit a larger energy level spacing, relaxing temperature requirements compared to larger conventional quantum dots [55]. Because all dots are identically composed of only one atom, inhomogeneities are limited to local environment variability, which in principle can be effectively eliminated.

H:Si was first identified as an attractive candidate for nanoscale patterning in 1996 [200]. DBs can be patterned at precise lattice locations, allowing their positions and spacing to be exactingly defined [40, 134, 200]. Only recently have capabilities reached the levels necessary to enable prototyping of structures on this surface. DBs can now be deterministically placed or erased (controlled H atom placement) using a scanned probe [134,136,137]. Very recently, prospects for atom-scale fabrication have improved through the application of machine learning methods to automate some of the most challenging aspects of scanned probe atom-scale imaging and fabrication [139]. It has also been established that structures made from DBs on the silicon surface are robust, being stable against diffusion even at 200°C, corresponding to a diffusion barrier of 1.4 eV (Ref. [51, 53, 54]). In this Article, we use these new tools and methods to characterize the charge distribution in DB ensembles, and extend earlier scanning tunneling microscope (STM) [19, 45, 51, 123, 152, 182, 202–204] and non-contact atomic force microscope (nc-AFM) studies [136,153,201]. Pairs of closely spaced DBs have only a single negative net charge at low bias [153]. Addition of a nearby negative charge can sufficiently bias or "tilt" the potential landscape of the DB pair so as to place the shared charge to one side of the pair or the other, corresponding to a well-defined binary zero or one. Thus, the pairs become the natural medium to encode binary information by localization of charge, as well as to perform logic operations. The ability to create [134, 135, 200] and perfectly erase [136, 137] DBs is then used to fabricate and actuate rudimentary circuit elements. We employ the single-electron charge sensitivity of nc-AFM to probe the charge configuration and functionality of a fabricated binary wire and a logical OR gate (Supplementary Video

1. Link to Video: [205]).

4.1.3 Results and Discussion

Charge Transitions in DBs

The nc-AFM images and spectra in Figure 4.1(a-e) characterize the neutral and negative charge states of an isolated DB (corresponding STM details in Supplementary Figure 4.5) [201]. In frequency shift (Δf) images, recorded at constant height and selected fixed biases (Figure 4.1(a-c)), the background H:Si appear as bright protrusions arranged in the 2×1 surface reconstruction of Si(100) [93] and the DB appears as a variably-dark depression, agreeing with previous AFM observation [136]. The charge transition of the DB is observed as a step-like feature at -350 mV in the blue Δf versus bias voltage spectrum ($\Delta f(V)$, Figure 4.1(d)). Steps in $\Delta f(V)$ spectra taken above molecules and atoms are known to correspond to single-electron charge transitions [27, 149, 187, 201, 206], as changing the charge state of an entity underneath the tip changes the electrostatic force experienced by the tip, registering as a shift in resonance frequency.

The $\Delta f(V)$ spectrum of the DB can be explained qualitatively by considering its (0/-) charge transition level relative to the position of the tip's Fermi level as the bias voltage is swept, as detailed in other works [48, 123, 201]. Isolated DBs on a highly n-type doped crystal, as studied here, are negatively charged at zero bias [45, 123, 203]. When the tip's Fermi level is energetically above the (0/-) charge transition level of the DB (Figure 4.1(f)), the DB is doubly occupied and therefore negative (region I in Figure 4.1(d)). At the step in the $\Delta f(V)$ curve, the tip's Fermi level becomes resonant with the (0/-) charge transition level and the tip extracts an electron from the DB. Because the (0/-) charge transition level of the DB at this bias voltage lies in the bandgap, the coupling to the tip is stronger than to the bulk and there is no efficient re-supply of electrons from the bulk to refill the DB. As a result, the DB is rendered neutral (Figure 4.1(g)). Consequently, the step in $\Delta f(V)$ in Figure 4.1(d) corresponds to the transition of the DB between its negative (right of the step, I) and neutral (left of the step, II) charge states [201]. The associated difference in Δf

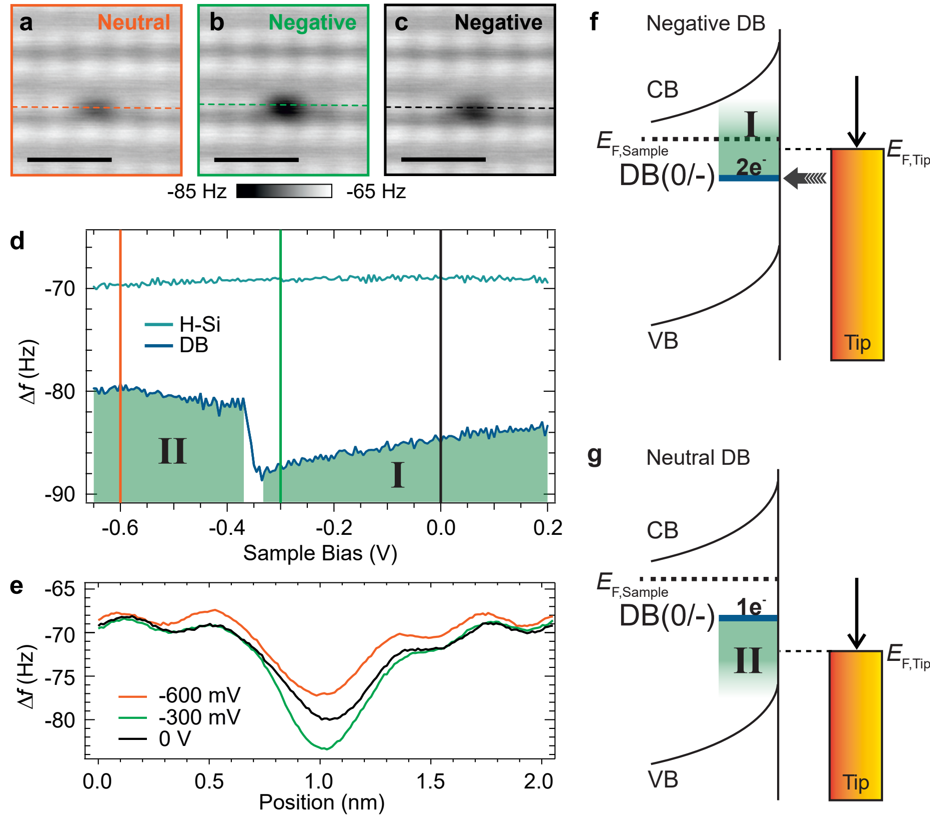

Figure 4.1: **Probing charge state transitions of a DB (a-c)** $2 \times 2\ nm^2$ constant-height $\Delta(f)$ images of an DB at different bias voltages ($z_{rel} = -350\ pm$ and $V = -600\ mV$ **(a)**, $V = -300\ mV$ **(b)**, $V = -600\ mV$ **(c)**; scale bars are $1\ nm$. **(d)** Frequency shift versus sample bias ($\Delta f(V)$) measured above the hydrogen-terminated surface (teal curve) and the DB (blue curve) showing a charge transition step ($z_{rel} = -350\ pm$; see Supplementary Figure 4.5 for STM details). Colour-coded vertical lines indicate the fixed sample bias at which the $\Delta(f)$ images shown in (a-c) were taken. Green shaded regions I and II denote the negative and neutral charge state bias regions, respectively. **(e)** Scan profiles extracted from (a-c) at the dashed lines as indicated. All scale bars are $1\ nm$. **(f)** Qualitative band diagram of the tip-sample system when the DB is negatively charged. The tip Femi level is above the negative to neutral charge transition level DB(0/-), rendering it doubly occupied. **(g)** Band diagram when the DB is neutral, showing the tip Fermi level below the DB's charge transition level. Roman numerals in the green shaded regions in (f) and (g) correlate to the bias regions indicated in the DB's $\Delta f(V)$ curve in (d). VB, valence band. CB, conduction band.

between the hydrogen atoms (teal curve in Figure 4.1(d)) and the DB at the marked fixed biases explains the contrast differences in the constant height nc-AFM scans of Figure 4.1(a-c). Profiles taken across the DBs in these images are shown in Figure 4.1(e) and highlight the difference in Δf at the DB's location. The magnitude of the attractive Δf shift indicates the charge state of the DB: a negatively charged DB (green and black line, Figure 4.1(e)) appears darker and more attractive than a neutral one (orange line, Figure 4.1(e)). Therefore, the contrast difference between DBs can be used as a direct indicator of their charge state.

Binary Electronic Building Blocks

In Figure 4.2, we build upon the established fundamental characteristics of an isolated DB to demonstrate the step-by-step fabrication and characterization of a DB pair and the biasing of that pair by a negative charge positioned nearby. We began with an isolated DB (Figure 4.2(a–c)). The isolated DB was created by applying a voltage pulse with the tip [40, 134] (see "Creating and erasing of DBs" in Methods Section 4.1.5 for details). The characterization of the isolated DB qualitatively resembles the observations presented in Figure 4.1. To show that the second DB is identical to the first, the first DB was erased by controllably capping it with an H atom [136, 137] so that the second DB could be studied in isolation. In this way it was ensured that the properties attributed to a DB pair are not due to a second DB of aberrant character. After erasure of the first DB, the new DB was created two lattice sites away (teal marker), and the characterization was repeated (Figure 4.2(d–f)). The $\Delta f(V)$ spectra of both DBs in isolation (Figure 4.2(c,f)) exhibit a charge transition step at $-135\ mV$, confirming that they are identical.

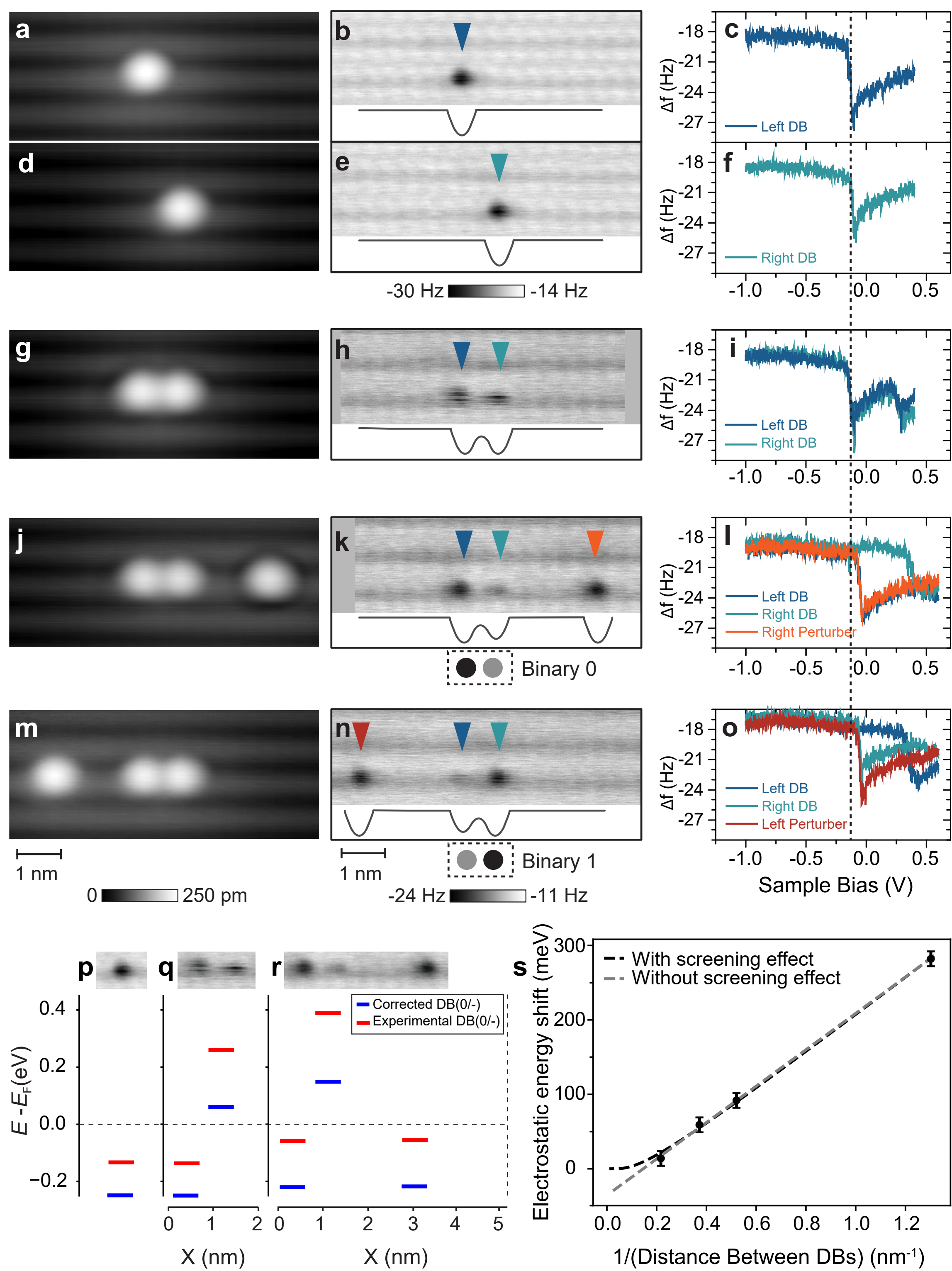

Figure 4.2

Figure 4.2: **Biasing of DB Structures.** **(a,d,g,j,m)** Filled state STM images of the isolated left **(a)**, isolated right **(d)**, coupled **(g)**, biased right **(j)** and biased left **(m)** DB assemblies ($V = -1.8\ V$, $I = 50\ pA$). **(b,e,h,k,n)** Corresponding frequency shift (Δf) images. $z_{rel} = -350\ pm$ for (b,e) and $z_{rel} = -300\ pm$ for (h,k,n) with $V = 0\ V$. Qualitative potential energy well sketches are included at the bottom of each panel and the biased states in (k,n) also have their binary representation shown below. **(c,f,i,l,o)** Corresponding colour-coded $\Delta f(V)$ spectra taken on top of the quantum dots in the frequency shift maps ($z_{rel} = -300\ pm$). The charge transition onset for the isolated DB cases at $-135\ mV$ is marked with a vertical dashed line for reference. **(p-r)** DB(0/-) charge transition levels for the isolated, paired, and perturbed DBs, respectively. Red solid lines are the charge transition level experimentally measured. Blue lines are the corrected energy level in the absence of any tip-induced band bending. For (q), two degenerate energy states exist. We illustrate the case of the electron localized on the left, but localization on the right also occurs. **(s)** Corrected electrostatic energy shifts of the DB charge transition levels as a function of DB-to-DB distance for negatively charged DBs. Fits with and without screening factored in are plotted. Error bars reflect the read-out error of the electrostatic energy shift, estimated to be $\pm 10\ mV$.

By recreating the left DB (blue marker, Figure 4.2(h)) a pair is formed [51,153]. The $\Delta f(V)$ spectra (Figure 4.2(i)) taken at each of the paired dots are identical. When compared with $\Delta f(V)$ spectra obtained above the isolated DBs (Figure 4.2(c,f)), they exhibit a new step at 265 mV. The first step appears at the same energy as that of the isolated DBs ($-135\ mV$). These observations can be understood by noting that below (more negative sample bias) $-135\ mV$ both DBs are neutral, between $-135\ mV$ and 265 mV only one DB is negatively charged, and above 265 mV both are negatively charged (see section "Pair of two DBs" in Supplementary Information Section 4.1.7 for more details). Therefore, under the imaging conditions of Figure 4.2(h) (0 V), only one DB is negatively charged at a time, confirming the pair has one net negative charge, as reported in previous studies [51,153]. Furthermore, the energetic position of the charge transition level of a paired DB is the same as that of an isolated DB, because the neutral character of its partner does not give rise to an electric field. In other words, a paired DB acts like an isolated DB for much of its $\Delta f(V)$ due to the electron localization on only one DB site. This

observation of charge localization for a DB pair with a single intervening hydrogen atom is unexpected; previous explorations [19, 45, 50, 207] have reported that the individual quantum states of the two DBs should hybridize, resulting in molecular-like orbitals that would delocalize charge across the structure. This hybridization is inconsistent with the observations reported here, and we suggest two possible explanations. First, previous studies are based on STM experiments measured at higher energies and the hybridized states are believed to be related to excited states of the DB ensembles [19, 45]. At the low energies probed in our experiments, structures derived from DBs are possibly weakly coupled ground states [19, 45]. Second, DBs are known to exhibit structural relaxation depending on their charge state [19, 45, 208]. Density functional theory calculations have found an approximately 200 meV stabilization of negatively charged DBs, with the nuclear position of the host atom raised by 30 pm relative to that of the neutral state [45, 209, 210]. Work has been reported [19] that has specifically examined DB pairs and structures made of DB pairs, with anisotropy in structural relaxation accounting for the reported device functionality. However, despite factoring in this structural relaxation, it was still found that charge was delocalized across the pairs, in contrast to our work. The full implications of lattice relaxation on the electronic structure of DB ensembles when combined with low-energy examination warrants future detailed investigation to explain these contradictory results.

Adding to the argument for localization, the streaky appearance of the DBs observed in Figure 4.2(h) indicates that the localization fluctuates between a left and right state. The charge fluctuations we observe here are suspected to be the result of the tip, which, as it is scanning over the pair, occasionally gets too close due to noise in the oscillation amplitude set point, mechanically lifting the silicon atom beneath it and making the switch energetically favourable [153, 162]. This behaviour is due to short-range interactions between the tip and sample, and occurs with small tip–sample separations (< 400 pm absolute tip height). The dividing line between the two regimes, one where charge states are imaged stably, and the other where the tip mechanically displaces the surface atoms, can be of the order of 20 pm (Ref. [153]), which is in line with amplitude set point noise estimates (see "Measurement system

set-up" in Methods Section 4.1.5). Here, the tip height was chosen to provide optimal contrast, while on average ensuring the tip was not interacting strongly. However, we acknowledge other explanations are possible to explain streakiness. The charge could access the conduction band and be repopulated from the bulk, the tip may aid as a tunnel "hopping" island from left to right, electrons could tunnel from tip to DB, or electron-hole recombination could periodically destabilize the charge.

Next, a third DB is added five lattice sites away from the teal DB (orange marker, Figure 4.2(k)). The Δf image now reveals a clear contrast between DBs in the pair (blue and teal marker, Figure 4.2(k)). The $\Delta f(V)$ spectra taken above the three DBs (Figure 4.2(l)) confirm that the blue and orange DBs are both negatively charged at 0 V where the Δf image was obtained, whereas the teal DB remains neutral. As the negatively charged DB appears darker than a neutral one in the Δf image; this demonstrates that the charge is biased to reside on the blue DB in the pair. We denote this pair's charge configuration a binary zero and refer to the orange DB as an electrostatic perturber. By subsequently erasing the orange DB and adding a perturber (red marker) on the left side (five lattice sites away from the blue DB), we demonstrate that the opposite biased case can be achieved giving a binary one (Figure 4.2(m–o)). Taken together, these observations show the binary character of the DB pair.

Some perturbation of DB spectra [201] and pairs of DBs [152] using local charges has been examined using STM methods before, as have charge state change dynamics in isolated DBs using an applied bias between tip and sample [48, 123]. These STM observations, however, were done under high-bias conditions. As observed in Figure 4.2(j,m) the two perturbing DBs exhibit different characters in the STM image. This is a consequence of the perturbative tip field under high-bias conditions, which can ionize deep dopants [47], affecting the local potential landscape and in turn changing the STM contrast of the DB. However, at the low-bias conditions used in AFM imaging and spectroscopy, these effects are not present, permitting a uniform potential landscape, where all the DBs exhibit the same character. Additionally, free of these strong tip fields, AFM provides new information about these charge transitions that were previously hidden in the bandgap of the material, and allows us to extract

information about the DB interactions from shifts in the AFM spectroscopy.

We note here that for both tipped cases, the charge transition of the negative DBs are shifted to $-50\ mV$ from $-135\ mV$ for an isolated DB (marked by the dashed vertical line). This is due to the two negative DBs being in close enough proximity to interact and mutually shift their charge transition levels to a less negative value,that is, they are close enough to slightly perturb each other without one or the other being ionized as in the paired case from Figure 4.2(h). The neutral DB exerts no effect on the negative DBs. In contrast, the presence of two negatively charged DBs next to the neutral DB strongly shifts its charge transition to 395 mV (Supplementary Figure 4.6(f,i)).

The experiments in Figure 4.2 can be explained with simple electrostatics and by assuming that negative DBs act as point charges. The red lines in Figure 4.2(p-r) depict the measured energies of the DBs' (0/-) charge transition levels for the isolated, paired, and biased cases, respectively, extracted from the $\Delta f(V)$ spectra of Figure 4.2. The tip-induced band bending (see the section "Details on Tip-Induced Band Bending" in Supplementary Information Section 4.1.7) was calculated and factored in to obtain the corrected DB(0/-) charge transition levels in the absence of the tip (solid blue lines, Figure 4.2(p-r)). The (0/-) charge transition level of the corrected isolated DB (Figure 4.2(p)) is 0.23 eV below the Fermi level. This is in agreement with (0/-) charge transition energies for $Si(100)/SiO_2$ interface dangling bonds (P_{b0} centres) [211] where a value of $0.27 \pm 0.1\ eV$ was reported. We note that *ab initio* calculations report notably lower values for the negative DB state than our obtained value [45, 50, 202, 212, 213].

Figure 4.2(q) highlights that closely spaced DB pairs have a single negative charge on one side or the other. As a result of Coulomb repulsion only the (0/-) charge transition level of one of the DBs is below the Fermi level and that of the other DB is lifted above the Fermi level, rendering it neutral. However, the pair system is degenerate. We have illustrated the case where the right DB is neutral and the left DB is negative, but note that the opposite can occur, as evidenced by the streakiness discussed earlier. However, whichever side it chooses in the pair, it appears to stay localized until an outside force changes it.

Adding the perturber DB (Figure 4.2(r)) is such an example, and fixes the charge on one side. From the corrected DB(0/-) charge transition levels we can extract the energy shift as a function of its separation from another negatively charged DB ((Figure 4.2(s)). We fit the data with the screened Coulomb energy equation [214],

$$U_r = \frac{e}{4\pi\epsilon_0\epsilon} e^{\frac{-r}{L_{TF}}} \tag{4.1}$$

where e is the elementary charge, ϵ_0 is the permittivity of free space, ϵ is effective dielectric constant at the surface, r is the distance between DBs and L_{TF} is the Thomas-Fermi screening length. From the fit (black dashed line, Figure 4.2(s)), ϵ and L_{TF} were extracted to be 5.6 and 5 nm, respectively. We note that without factoring in the screening effect, the fit results in a physically invalid negative offset energy (grey dashed line, Figure 4.2(s)).

Figure 4.2 summarizes the underlying principles of our approach, where we define the two biased configurations of the pair as two binary states. By creating larger ensembles, more complex functionality can be achieved. We now provide two additional examples: a binary wire and a logical OR gate.

Binary Wire

Figure 4.3 demonstrates that the electrostatically determined binary state of a DB pair can be extended over a line formed of many paired DBs. Figure 4.3(a) shows an STM image of a wire constructed from eight pairs, with a lone perturber on its right. The constant-height Δf image below (Figure 4.3(b)) shows that the perturber (red marker) tips the eight pairs to the left. In Figure 4.3(c), an additional DB is patterned next to the red DB so that it forms a ninth pair. The Δf image (Figure 4.3(d)) demonstrates that such an ensemble, lacking a perturbing electrostatic input, becomes self-polarized, with the pairs on either side of its midpoint adopting opposite polarizations (division indicated by the purple dashed line). In Figure 4.3(e,f) a new perturber (red marker) is patterned on the left side of the ensemble, reversing the state. The sequence of images in Figure 4.3 demonstrates the basis for a binary wire. Because we are limited at this point to negative charges as inputs, we are restricted

to demonstrating the two states of the wire by pushing with charges from an input placed at one end of the line or the other.

Logical OR Gate

Figure 4.4 shows a logical OR gate can also be achieved through a two-dimensional arrangement of DBs. In its uninitialized form the gate consists of three pairs arranged in a Y shape (Figure 4.4(a-c)). We define the two upper branches as the gate's inputs, and the lower branch as the gate's output (the dashed boxes depict the three pairs defining the gate). In the absence of perturbers, the mutual electrostatic repulsion among the electrons within the pairs causes the electrons to localize to the outermost DBs (Δf image in Figure 4.4(b)). The addition of a perturber below the output branch (Figure 4.4(d-f)) forces the output electron towards the centre of the gate structure and initializes the gate (Figure 4.4(e,f)). The perturber (red dot in Figure 4.4(f)) allows the first row of the truth table for an OR gate to be realized (see Supplementary Table 4.1). The inputs can now be toggled with perturbers placed at either of the input branches (Figure 4.4(g-i) and (j-l) or both (Figure 4.4(m-o)), with the effect being that the electrostatic push from the perturber below the output branch is overcome, enforcing an output of 1 at the designated output. Together these configurations satisfy the remaining rows of the truth table. The charge fluctuations observed in Figure 4.4(n) are suspected to be the result of the tip scanning over the structure (compare discussion of Figure 4.2(h)).

It is anticipated that more complex functionality can be achieved by linking multiple gates together with the binary wires presented in Figure 4.3. Such a theoretical design is shown in Supplementary Figure 4.10, with two interconnected OR gates linked by a single-bit binary wire. There, the bottom OR gate has an initializing electrostatic perturber and sets the correct state for the whole ensemble, allowing more complex operation. This design was simulated using SimAnneal, a ground-state electron configuration testing package [215] (details in section "SimAnneal" in Supplementary Information Section 4.1.7). Through patterning of bits in different arrangements and with varied coupling strengths, other gate designs are foreseen (as

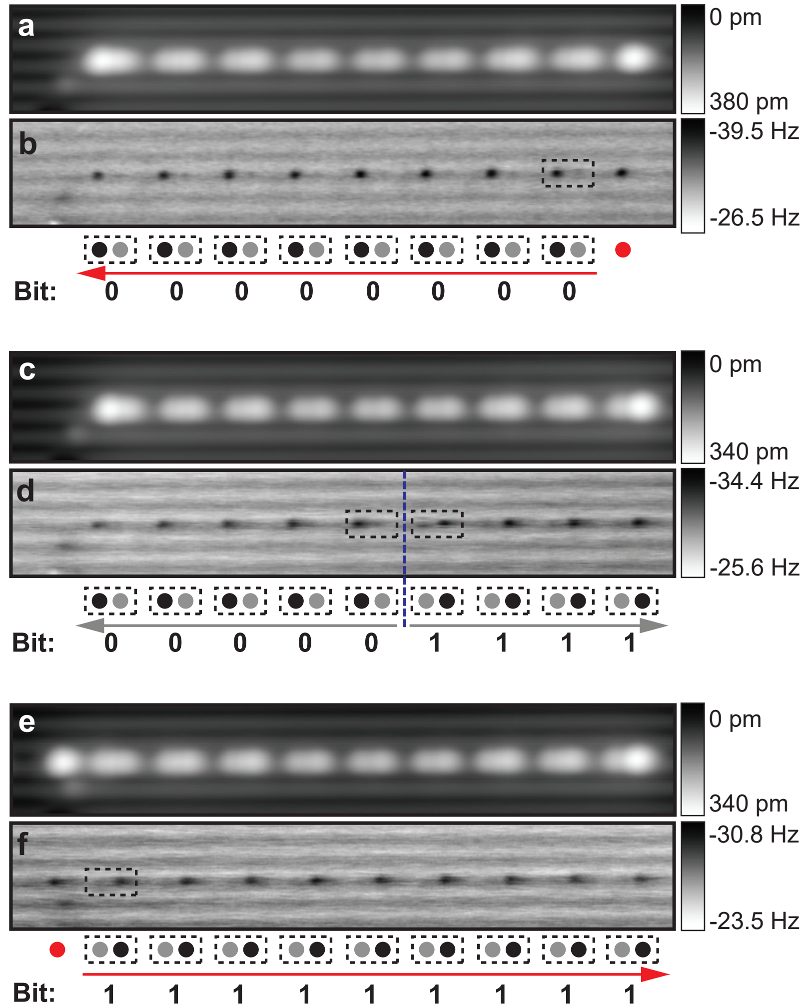

Figure 4.3: **Information Transmission Through a DB Binary Wire. (a,b)** Filled state STM image (a) and corresponding constant-height Δf image (b) of an eight-pair wire with a non-paired perturber DB (red circle) on the right. **(c)** Symmetric nine-pair wire created from pairing up the red perturbing DB in (b). **(d)** Constant-height Δf image of the nine-pair wire, with the symmetry-splitting plane marked by a dashed purple line. **(e)** STM image of a nine-pair wire after adding a perturbing DB (red circle in f) on the left. **(f)** Constant-height Δf image showing the wire binary state under the field of the perturber (red). All STM images were taken at $V = -1.8\ V$ and $I = 50\ pA$. All Δf images are $24 \times 3\ nm^2$ in size and were taken at zero bias with a relative tip elevation of $z_{rel} = -330\ pm$. Guides are placed below (b,d,f) to show the location and bit state of the pairs.

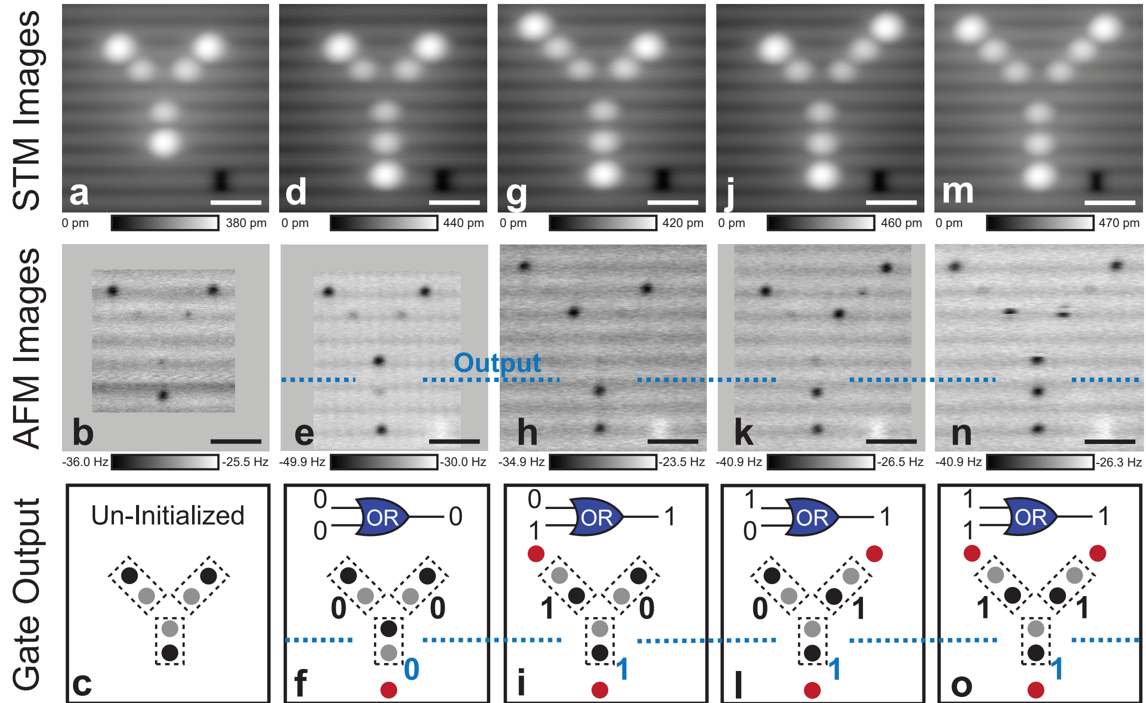

Figure 4.4: **OR Gate Constructed of Dangling Bonds. (a,d,g,j,m)** Constant-current filled state STM images ($V = -1.8\ V$ and $I = 50\ pA$) of the OR gate in various actuation states. **(b,e,h,k,n)** Corresponding constant-height Δf images ($V = 0\ V$, $z_{rel} = -350\ pm$) of the gate, showing electron locations as the dark depressions, with the output marked in blue. **(c,f,i,l,o)** Models of the gate. (c) Three pairs constituting the uninitialized OR gate. (f) Initialized gate with added red perturber below to satisfy the first row of an OR gate truth table, as indicated by the gate symbol. (i,l,o) Models for the remaining OR gate truth states. All the models of the gates correspond to the experimental data shown vertically above them. Dashed boxes and numbers indicate the pairs and their binary state, and the single red perturbers are stand-ins for connecting wires or connections to other gates and structures. Scale bars are 2 nm.

shown in Ref. [215]). The perturber inputs used in all tested and theorized logic designs are intended to be replaced in future implementations with binary wires or metallic leads [186].

4.1.4 Conclusion

We have demonstrated a set of rudimentary binary circuit elements formed of silicon DB gap states. Precise atomic fabrication allowed the reproducible patterning of bits formed of DB pairs holding only one negative charge. Electrostatic perturbers were used to tip the potential energy landscape of the pairs and thus set the binary state of the bits, mapped as the electrons' spatial arrangements. Assemblies of bits formed a binary wire and a logical OR gate.

We anticipate that, with our approach, connections to external circuitry can be made through atomic wire leads [186] with readout transduced by single-electron transistors (Refs. [39, 216, 217]) or quantum point contacts [194, 218]. A wafer bonding approach [190, 219] could also be used to permanently encapsulate and environmentally protect the circuitry, allowing it to be removed from the fabrication environment and transported. Although there are indications that field-controlled computing approaches like ours might operate in a very low power and yet ultra-fast regime [32, 33, 192], detailed studies of power consumption and speed of operation remain to be done. There have also been previous indications that the polarization of a bit persists at room temperature [51, 55, 152], but, because effects such as excitation of electrons to the conduction band [50, 123] could disrupt logic functions, further testing is required to understand whether room-temperature operation is feasible. Many challenges remain, but recent advances towards exact and automated DB patterning suggest that increased complexity could be possible [134, 136, 139].

4.1.5 Methods

Measurement System Set-Up

Experiments were carried out using a commercial (Scienta Omicron) qPlus AFM system operating at 4.5 K. Nanonis control electronics and software were used for both STM and AFM data acquisition. For all constant-height frequency shift images and the bias-dependent spectroscopy, $z_{rel} = 0\ pm$ corresponds to the relative tip elevation defined by the STM imaging set points on the site of hydrogen-terminated silicon $I = 50\ pA$ and $V = -1.8\ V$. The tuning fork had a resonance frequency of 32.8834450 kHz, with a quality factor of 40,000. The tuning fork was driven with an oscillation amplitude of 50 pm and recorded to be at 50 +/- 20. To minimize drift during AFM image acquisition, the tip was left to settle for 12 hours after approach to allow piezo scanner stabilization. All STM and AFM images are raw data. The tip height has to be carefully chosen for every tip-sample combination to obtain optimal contrast, while ensuring the tip does not mechanically displace the surface atoms due to covalent or van der Waals interactions [153,162]. The transition region where the regimes blend is approximately $20-30\ pm$ wide and is centred at approximately $z_{rel} = -300\ pm$ from the specified STM set point. This approximate z_{rel} will change slightly for different tip-sample combinations.

Sample Preparation

Highly arsenic-doped ($\sim 1.5 \times 10^{19}\ atom\ cm^{-3}$) Si(100) was used. Sample preparation involved degassing at $\sim$ 600°C for 12 hours in ultra-high-vacuum (UHV), followed by a series of resistive flash anneals reaching $\sim$ 1250°C to remove oxide, and finally holding the Si substrate at $\sim$ 330°C for two minutes while molecular hydrogen (pressure of $10^{-6}\ Torr$) was cracked on a $\sim$ 1600°C tungsten filament. The series of resistive flash anneals has been shown to reduce surface dopant density, creating a depletion region $\sim 70\ nm$ below the sample surface with a donor concentration $\sim 10^{18}\ atom\ cm^{-3}$ (Refs. [203,220]).

Tip Preparation

A focused ion beam (FIB) was used to cut a micro-tip from electrochemically etched 50 µm polycrystalline tungsten wire, then weld it to the end of a qPlus-style AFM sensor [88]. UHV preparation involved having the oxide layer removed by electron bombardment heating treatments, followed by field evaporation to clean the apex in a field ion microscope (FIM) [82]. Further sharpening was conducted using a FIM nitrogen etching process to obtain the smallest possible tip radius of curvature [82]. Final *in situ* tip processing was done through creation of a bare silicon patch through tip-induced hydrogen desorption, followed by gentle controlled contacts with the tip on the reactive patch [93].

Creating and Erasing DBs

To create a DB, a sharp artefact-free tip is positioned on top of a surface hydrogen atom at 1.3 V and 50 pA, and pulses of $2.0 - 2.5$ V for 10 ms are applied until the hydrogen is removed [40, 134, 200]. Some percentage of the time, the removed single hydrogen atom ends up functionalizing the tip apex. This functionalized tip can be positioned over a DB and mechanically brought towards it to induce a covalent bond and passivate it [136, 137].

4.1.6 Acknowledgments

We thank M. Cloutier, D. Vick and M. Salomons for their technical expertise. We thank NRC, NSERC, QSi, Alberta Innovates, and Compute Canada for financial support. We thank F. Giessibl for providing us with the tuning forks for building the qPlus sensors. We thank K. Gordon for valuable suggestions and discussions. We thank B. Hesson for making and rendering the 3D animated Supplementary Video.

4.1.7 Supplementary Information: Binary Atomic Silicon Logic

Further Details on $\Delta f(z)$ Spectroscopy

Supplementary Figure 4.6 reproduces the bias-dependent frequency shift spectra shown in Figure 4.2 of the main text, but with a vertical offset. The vertical offset allows clear discernment of all features and shifts in the graph for the DB pair (Supplementary Figure 4.6(a-c)), the pair biased to the left (Supplementary Figure 4.6(d-f)), the pair biased to the right (Supplementary Figure 4.6(g-i)), and the symmetrically biased pair (Supplementary Figure 4.6(j,k,l)). The error to read out the corresponding shifts of the change transition energies are estimated to be $\pm 10\ mV$.

Pair of Two DBs

For both DBs, the charge transition step is observed at $-135\ mV$, identical to the case of the individual DBs (Figure 4.2(c,f) in the main text). The reason is that only one DB of the pair can harbour an electron in this voltage range ($-135\ mV$ to $265\ mV$) and the remaining neutral DB does not exert an electric field on its neighbouring DB. Furthermore, once the negative charge is localized on one DB, its neighbouring DB has its negative to neutral charge transition level instantaneously shifted upward by the Coulomb field of its charged neighbour above the Fermi level of the sample. This is qualitatively depicted in Supplementary Figure 4.7(b). Assuming the blue DB is negative in this example case, as the sample bias is increased further past the second step ($\geq 265\ mV$), the Fermi level of the tip is raised above the charge transition level DB(0/-) of the teal DB, which captures an electron and becomes negative too (Supplementary Figure 4.7(c)). This corresponds to both DBs being negative, and to the second step in the $\Delta f(V)$ spectrum at 265 mV in Supplementary Figure 4.6(c). Both DBs can also be made neutral by reducing the sample bias to bring the tip Fermi level below the charge transition levels for both DBs, as shown in Supplementary Figure 4.7(a).

One DB Perturbing a Pair

We next consider the “2+1” experiment with a single negative DB perturbing a pair as shown in Figure 4.2 (j-o) of the main text. The $\Delta f(V)$ spectra with added offset are reproduced in Supplementary Figure 4.6(f,i). First, we examine the curves for the perturber and the paired DB furthest from the perturber (orange and dark blue in Supplementary Figure 4.6(e,f), red and teal in Supplementary Figure 4.6(h,i)). In all cases the sharp charge transition step is observed at approximately $-50\ mV$. Contrasting this with the charge transition value for a lone DB ($-135\ mV$), it is apparent that an absolute shift of 85 mV occurred. This shift can be explained by the presence of the negative charge at the perturbing DB (for bias values between $-50\ mV$ to 395 mV), electrostatically shifting all nearby DB levels. In other words, referencing specifically Supplementary Figure 4.6(f), when a $\Delta f(V)$ spectrum is taken with the tip over the blue DB, the step is at $-50\ mV$ because the far orange perturbing DB is negative and shifts the level 85 mV closer to zero. The related qualitative band-bending diagram is depicted in Supplementary Figure 4.8(b) (corresponding to region II in the reproduced $\Delta f(V)$ spectra at the bottom). When both orange and blue are negative ($-50\ mV$ to 395 mV), they cause a potential energy increase for the middle teal DB pushing its DB(0/-) level above the sample Fermi level, leaving it neutral. Hence, when taking a $\Delta f(V)$ spectrum over the teal DB, the tip level must be swept to 395 mV before it can cross the teal's DB(0/-) transition level and capture an additional electron to become negative (Supplementary Figure 4.8(c)). As done for the pair, the tip level can also be swept below the charge transition levels for all three ($\leq -50\ mV$) rendering them all neutral (Supplementary Figure 4.8(a)).

Symmetrically Perturbed Pair of DBs

We finally consider the “1+2+1” experiment where the two close DBs were symmetrically perturbed by two DBs. The “outside” DBs (red and orange labels, Supplementary Figure 4.6(j-l)) show a relatively small shift of 22 mV of the (0/-) charge transition levels, due to the distance of 12 lattice sites between the perturbers. Furthermore, the presence of two negative charges raises the charge transition levels of

the inner dots (blue and teal) to 80 mV.

Truth Table of an OR Gate

Table 4.1: Truth Table for an OR Gate.

OR Gate Input 1	OR Gate Input 2	Output	Figure
0	0	0	4.4(e,f)
0	1	1	4.4(h,i)
1	0	1	4.4(k,l)
1	1	1	4.4(n,o)

Sim-Anneal

The sequential OR gates of Supplementary Figure 4.10 were simulated and output using the Sim-Anneal engine in the Silicon Quantum Atomic Designer software [215]. Each iteration of the gate inputs was run for $10,000$ anneal cycles at 4 K assuming a DB (0/-) level $V_0 = 0.270$ eV below the Femi-level of the sample and a Debye Length (L_{TF}) of 4.3 nm.

Details on Tip-Induced Band Bending

During AFM imaging, even at zero applied bias, the tip affects the electrostatic potential and, under certain conditions, the occupation of the DB system. The effect can be linked to the contact potential difference, whose source is the difference between the work functions of the tip and the sample. For a tungsten tip, the work function varies with the crystal orientation and is typically taken to be between 4.5 and 5 eV. For a silicon sample, the work function varies significantly with doping type and level. For n-type Si at low temperature, the work function is close to the electron affinity, typically 4.05 eV, being less than this value for a degenerate sample, and greater for a non-degenerate sample. In our case, for our tungsten tip the work function was assumed to be 4.5 eV, while for the silicon sample, considering the low-

temperature and a surface dopant concentration of 10^{18} $atom\ cm^{-3}$, it was estimated at 4.1 eV.

This difference in work functions leads to band-bending locally under the tip apex that can shift the electronic levels of dangling bonds, thereby potentially emptying or filling them. We refer to the shift as tip induced band bending (TIBB). TIBB is strongest immediately under the tip apex. For the above quoted work functions, the TIBB is in the upward direction at zero applied bias voltage, *i.e.*, levels get shifted upward with respect to the sample Fermi level $E_{F,sample}$. While the contact potential difference is a constant, the TIBB changes with both tip-sample separation, as well as applied tip-sample bias (See Supplementary Figure 4.9). If an electronic level for a DB is shifted above $E_{F,sample}$, then it cannot stay filled (occupied) in electrochemical equilibrium.

The exact value of TIBB depends not only on the contact potential V_c, but also on the following parameters: sample doping level (N_d), tip-sample bias (V_{ts}), tip shape, apex radius (R_t), and the distance (height) between the tip and the surface (d). The TIBB in Supplementary Figure 4.9 was calculated using our best estimates for the above parameters. A 3D finite-element Poisson equation solver was employed to calculate the TIBB using methodology described in reference [131].

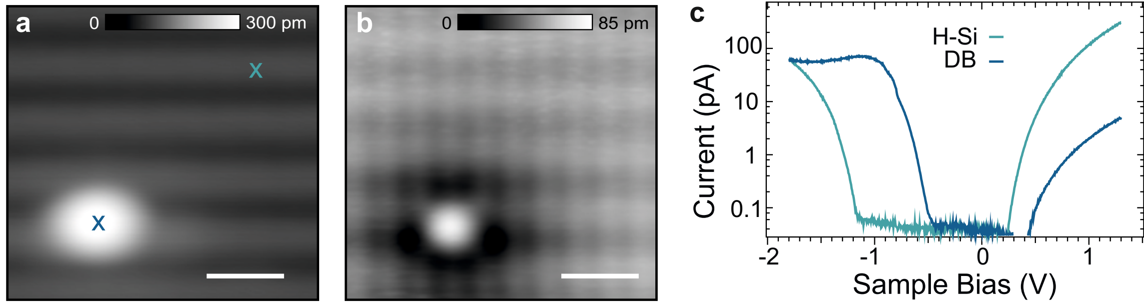

Figure 4.5: **STM Characterization of a Dangling Bond. (a)** $4 \times 4\ nm^2$ filled states STM image ($V = -1.8\ V$, $I = 50\ pA$) and **(b)** $4 \times 4\ nm^2$ empty states STM image ($V = 1.3\ V$, $I = 50\ pA$) of a DB. **(c)** Tunneling current *vs.* sample bias ($I(V)$) spectroscopy plotted in log scale of the DB (blue curve) and hydrogen-terminated surface (teal curve). Spectroscopy positions indicated in (a).

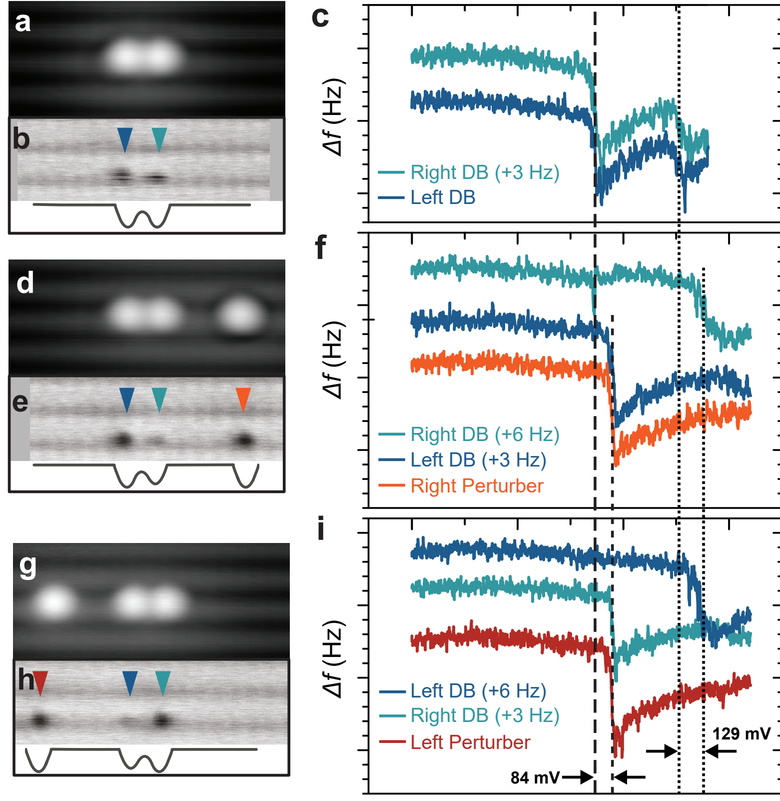

Figure 4.6: **Frequency Shift Spectroscopy in Dangling Bond Structures.** Colour-coded spectra from main text Figure 4.2 reproduced with vertical offsets for the $\Delta f(V)$ to show key features for the pair **(a-c)**, left tipped **(d-f)**, right tipped **(g-i)**, and symmetric **(j-l)** cases (being STM, constant-height AFM, and vertically offset $\Delta f(V)$, respectively for each case). The charge transition onset for the isolated DB cases, taken from the pair in (c), is marked with a vertical long-dashed line for reference. A short-dashed line, only in (f) and (i), indicates the shifted charge transition in the presence of one additional charge (the perturber). The finely dotted lines indicate the charge transition onset for bringing in the second charge to the pair (c) as well as for the perturbed dot (f,i) in the presence of the charge of the perturber. In (l), the shifted charge transition onset of the perturbers in the presence of its symmetric perturbing partner is marked by a short-dashed line only running over the orange and red spectra. The transition for bringing in an additional electron for the middle pair is marked by the short-dashed line. STM images in (a),(d),(g), and (j) were taken with $V = -1.8\ V$, $I = 50\ pA$. The Δf images in (b), (e), (h) and (k) were taken with $z_{rel} = -300\ pm$, and $V = 0\ V$. All $\Delta f(V)$, were also taken at $z_{rel} = -300\ pm$ (the same as reported in main text Figure 4.2).

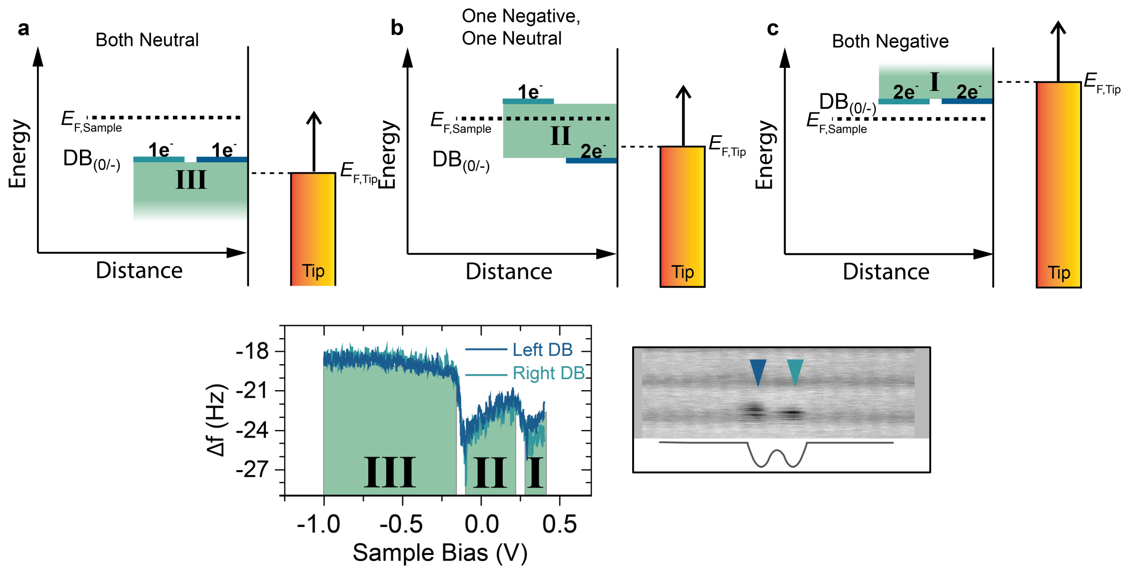

Figure 4.7: **Diagrams for Charge Transitions in a Dangling Bond Pair. (a)** Diagram of the system when both DBs are neutrally charged. The tip is assumed to be positioned above the dark blue DB. The DB's negative to neutral charge transition levels are plotted on the left, and are colour coded to the $\Delta f(V)$ reproduced from main text Figure 4.2 below. The Fermi level for tip and sample are given by the dotted lines. The tip Fermi level is below both charge transition levels, meaning both are singly occupied. This corresponds to region III for sample bias $\leq 135\ mV$. **(b)** Diagram for the same system when the sample bias is between $-135\ mV$ to $265\ mV$. Only the blue DB is negative. The teal DB is neutral, as its charge transition level has been shifted above the Fermi level of the sample from the negative charge of the blue DB. This corresponds to region II in the $\Delta f(V)$ spectra. **(c)** Diagram for sample bias values greater than $265\ mV$ (region I) in the $\Delta f(V)$ spectrum of two closely spaced DBs where both are negatively charged. The Fermi level of the tip is now above the negative to neutral charge transition level DB(0/-) of both DBs, rendering them both negative.

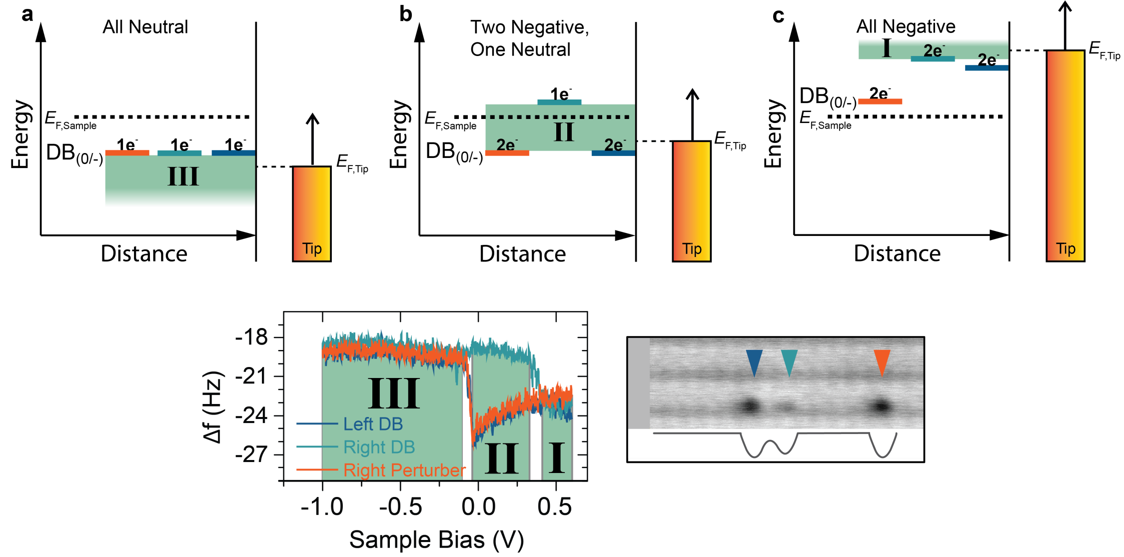

Figure 4.8: **Diagrams for Charge Transitions in a Biased Pair of Dangling Bonds.** **(a)** Diagram of the system when all DBs are neutrally charged. The DB's negative to neutral charge transition levels DB(0/-) are colour coded to the $\Delta f(V)$ spectrum at the bottom reproduced from main text Figure 4.2. The Fermi level for tip and sample are given by the dotted lines. The tip Fermi level is below all charge transition levels, meaning all are singly occupied. This corresponds to region III for bias $\leq -50\ mV$. **(b)** The diagrams for the same system when the sample bias is decreased to between $-50\ mV$ to 395 mV. The perturbing orange DB and blue DB are both negative, lifting the level for the teal above the Fermi level of the sample and rendering it neutral. This corresponds to region II in the $\Delta f(V)$ spectra. **(c)** Diagrams for sample bias $\geq 385\ mV$ (region I) in. The Fermi level of the tip is now above charge transition level of all DBs, rendering them all negative.

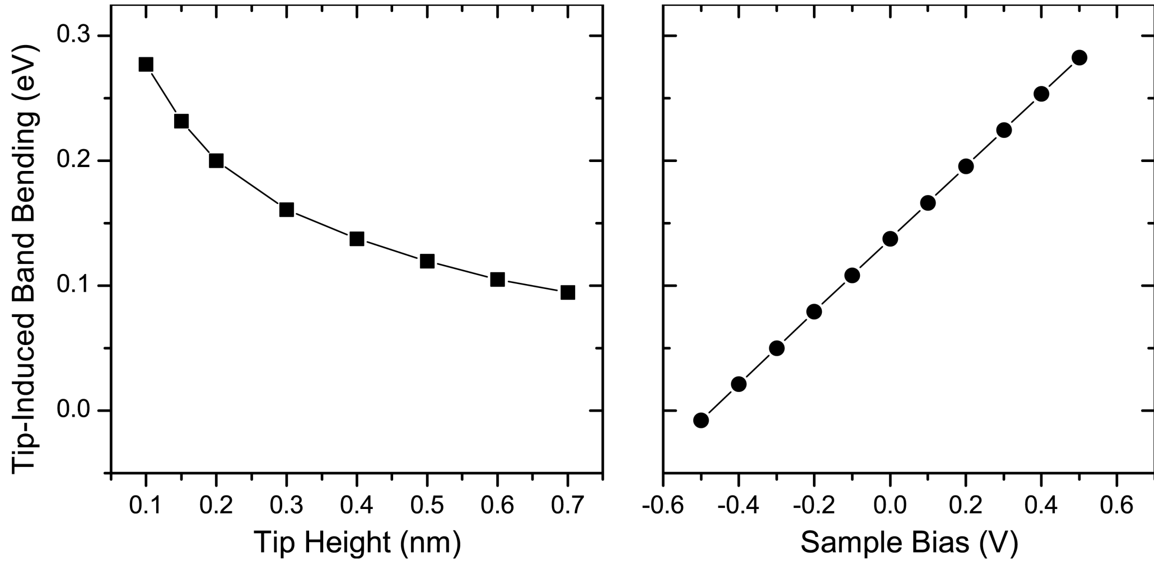

Figure 4.9: **Calculated Tip-Induced Band Bending as a Function of Height and Bias. (a)** Tip-induced band bending as a function of tip-sample height. No bias is applied between tip and sample. **(b)** Tip-induced band bending as a function of sample bias for a fixed tip-sample separation of 0.4 nm. For both plots, we assumed a donor concentration of 10^{18} $atoms\ cm^{-3}$ at the surface, gradually increasing to 2×10^{19} $atoms\ cm^{-3}$ in the bulk over a range of approximately 100 nm, a work function difference between tip and sample of 0.4 eV, and a tip radius of 10 nm.

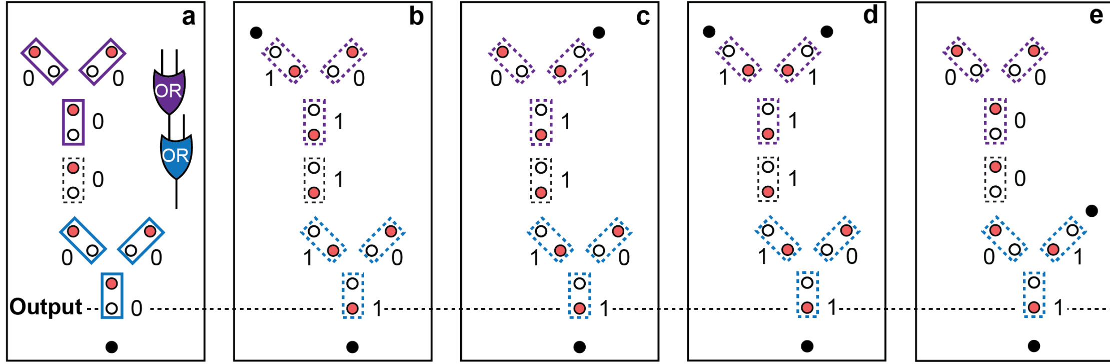

Figure 4.10: **Sequential OR Gates.** **(a)** Two OR gates in sequence (symbols and boxes in solid purple and blue), connected by a binary wire (one bit long in this example; black dashed box). Functionality is shown by adding inputs (black dots = perturber DB representing connections to other pair-based binary structures or anticipated electrical contacts) to the purple gate's upper input branches with **(b)** (1,0), **(c)** (0,1), and **(d)** (1,1).In **(e)** the input of the lower blue OR gate is toggled to (0,1). In the latter configuration, any further input to the first gate would not change the output state from 1.

4.2 Appendix: Not Published Additional Supplementary Results for Binary Atomic Silicon Logic

4.2.1 Seeing Polarization with Different Tips and Heights

In Chapter 2 we discussed the apex's effect on the primary imaging mechanism in AFM (Section 2.2.5). Now we discuss its effect on measuring charge localization in our binary building block pairs.

Figure 4.11(a) shows a DB wire consisting of an asymmetric perturber on the far left and two binary pairs in line with each other to the right of it. As per results from BASiL, it is expected that the left members of the DB pairs will appear as lighter in contrast than the right members. Examining the constant-height AFM image in (b), it is instead seen that they all display as dark. The tip was then contacted several times gently on a hydrogen-terminated area and brought back to re-examine the wire in Figure 4.11(c,d). The constant-height AFM frame in (d)

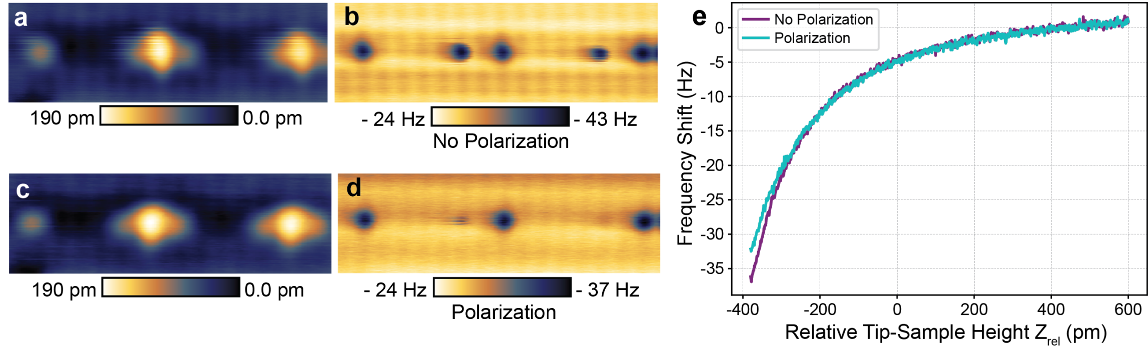

Figure 4.11: **DB Wire with Different Apex Interactions (a)** Empty states STM image ($V = 1.3\ V$, $I = 50\ pA$) of a DB wire. **(b)** Corresponding constant-height Δf image of the wire showing all DBs as dark ($z_{rel} = -350\ pm$, $V = 0\ V$, and $Osc.\ Amp. = 50\ pm$). **(c)** Empty states STM image ($V = 1.3\ V$, $I = 50\ pA$) of the same wire from (a) after a series of tip forms on a hydrogen-terminated area to change the apex structure. **(d)** Corresponding constant-height Δf image of the wire showing asymmetry in the DB contrast as expected ($z_{rel} = -350\ pm$, $V = 0\ V$, and $Osc.\ Amp. = 50\ pm$). **(e)** $\Delta f(z)$ spectra taken over a hydrogen reference atom before (purple curve) and after (blue curve) tip shaping. All frames are $6 \times 2\ nm^2$.

now shows the expected contrast for the DBs at the same relative tip-sample height, with the $\Delta f(z)$ spectra in (e) showing the tip has only changed minimally (small deviation of the curves below $z_{rel} = -300\ pm$). When this was initially observed, it was thought that maybe only certain apex terminations could see polarization, as each has a different imaging mechanism [94, 105], dipole moment [221], and electron density [222]. Additional experiments revealed, however, that while different apex terminations can effect how strong the polarization looks and the relative tip-sample height at which differentiable contrast is visible, all tips seem to be able to measure polarization. To motivate this, we show examination of an identical wire with two differently-interacting tip structures at multiple heights.

Figure 4.12 shows AFM examination of another "1+2+2" binary DB wire. The AFM Δf height series in Figure 4.12(a-e) was taken shortly after creation of the DB wire with a hydrogen-coated tip (Tip Apex 1). This is the suspected apex due to the high-resolution of the AFM frames shown; the hydrogen atoms display as well-defined, bright, and highly resolved individual atoms (See Figure 2.12 for reference).

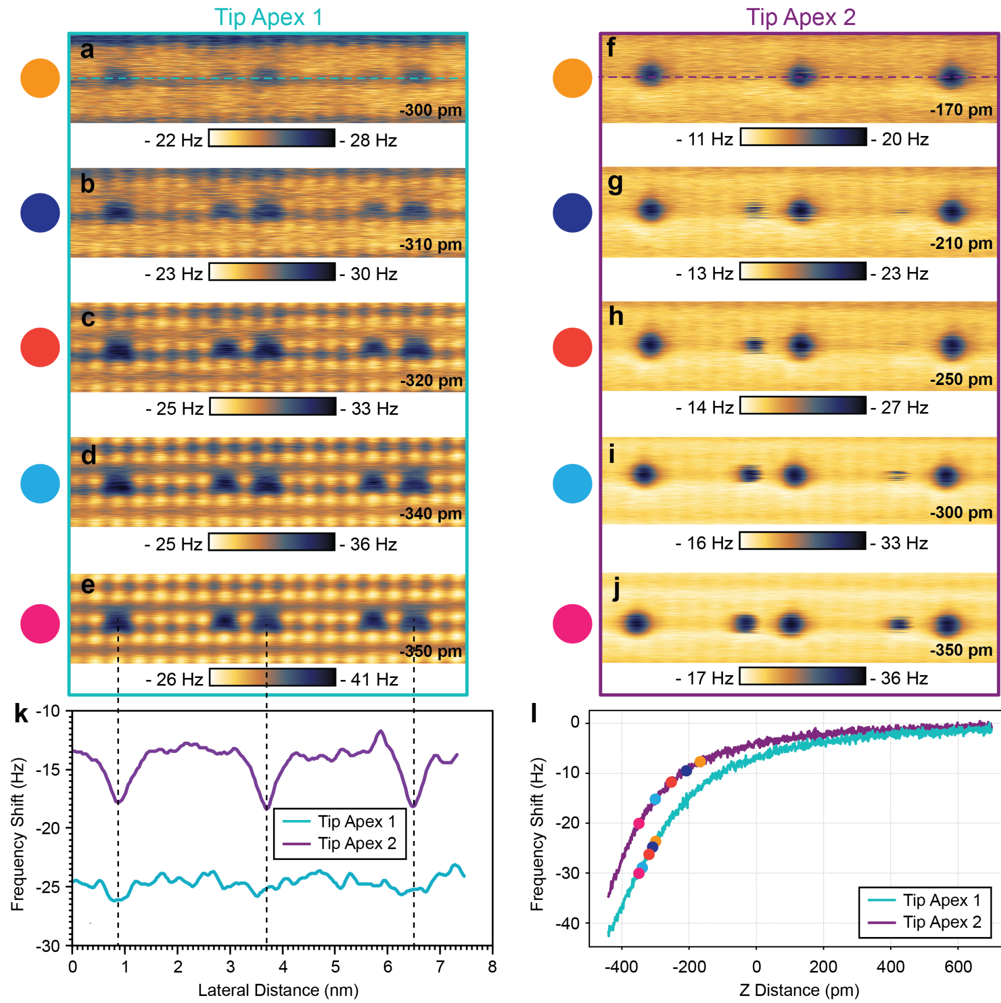

Figure 4.12: **DB Wire AFM Height-Series with Different Tip Apex Structures (a-e)** Constant-height Δf images of a 5 DB wire taken at different heights with a presumed hydrogen apex denoted Tip Apex 1 ($V = 0\ V$, and $Osc.\ Amp. = 50\ pm$). **(f-j)** Constant-height Δf images of the same wire from (a-e) taken after alteration of the tip character (Tip Apex 2) to be likely silicon. **(k)** Extracted cross sections from (a) and (f) across the DB structure. Vertical black dashed lines are given as a guide to the eye. **(l)** $\Delta f(z)$ spectra taken over a reference hydrogen atom for both apex structures. The colored circles in (l) mark the correspondingly color-coded constant-height frames for the two different apex types in (a-j). All AFM constant-height images are $7.4 \times 1.7\ nm^2$, with the height they were obtained at listed in the lower right of each. z_{rel} is referenced to a height defined by a STM tunneling current of $I = 50\ pA$ with $V = -1.8\ V$ applied, as taken over a surface hydrogen atom.

Examining (a-e), polarization of the electrons in the pairs is most apparent for the larger tip-sample separations in (a,b), with all the DBs displaying dark when the tip-sample relative height is reduced in (c-e). The tip was then used for six days to do other experiments and eventually brought back to examine the same wire in Figure 4.12(f-j). Now, the contrast over the hydrogen atoms is inverted with them showing up as dark (Tip Apex 2), which is the signature of a silicon apex (Again see Figure 2.12). As with Apex 1, asymmetry in the DB contrast is readily apparent at larger tip-sample separations in Figure 4.12(f,g), with closer tip-sample separations in (h-j) showing all the DBs as dark. In spite of this, we highlight that even for close-tip sample separations where all the DBs display as dark, both apex types show asymmetry in the DB's appearance. For example, in both Figure 4.12(d) for Apex 1 and Figure 4.12(j) for Apex 2, the left-most members of the pairs (expected to be neutral) are slightly smaller in size or distorted. We conclude that all tips can likely measure polarization of DBs at all heights, but some heights and tips will present it differently. This could mean a large difference in Δf for a neutral *vs.* negative DB, or it could be just a visual asymmetry in the DB's appearance. To highlight the larger Δf measured between Apex 1 and 2 for neutral *vs.* negative DBs, cross sections for frames (a) and (f) are plotted in Figure 4.12(k). These frames were selected because they showed the highest signal to noise ratio for resolving differently charged DBs within the height ranges probed. Examining Figure 4.12(k), the absolute Δf difference for differently charged DBs for Apex 2 is greater than that displayed for Apex 1 by approximately a factor of three. In other words, Apex 2 resolves neutral and negative DBs with a more dramatic spread in Δf than Apex 1.

We now examine the $\Delta f(z)$ spectra for the two apex types in Figure 4.12(l). Apex 2 shows a less reactive (less negative Δf) curve on average, with both curves deviating for tip-sample separations below $z_{rel} = 200\ pm$. This suggests the mesoscopic structure of the tip has changed, with some alteration of both tip structure and the types of atoms comprising the apex. This has correspondingly changed the overall measured tip-sample interaction potential, which effects both the AFM's ability to resolve differently charged DBs and the tip-sample heights where polarization

is apparent. Color-coded dots are overlaid on the $\Delta f(z)$ curves in (l), corresponding to the heights the AFM Δf images in (a-e) and (f-j) were taken at. Looking more closely, the points are clustered into a smaller range of the curve for Tip Apex 1 than for Tip Apex 2. Additionally, for Tip Apex 1, despite being further into the strongly attractive part of the curve, resolution is starting to become poor at the maximum tested tip-sample height in (a). For Tip Apex 2, the DBs present clearly for all probed heights which span a larger percentage of its $\Delta f(z)$ curve. Again, this suggests that some tips may resolve DBs for a wider parameter space than others.

In summary, this experiment highlights a few key results. First is that polarization is likely resolvable for all apex types, but may have a varying signal to noise ratio; some tips may have a wider spread between the measured Δf signal over neutral and negative DBs, making them objectively better for examining electron re-arrangement in DB structures. This observation may also translate to DB charge state differences being resolvable for a wider range of heights among different tips and tip terminations. Second, height effects the DB contrast and how polarization presents itself. For both apex types, polarization at close tip-sample separations is evidenced by subtle asymmetry in the DBs as viewed in Δf scans. At greater tip-sample separations, the DBs return to the condition of showing polarization with light *vs* dark contrast between a neutral and negative DB, respectively. It is known that tip induced band bending increases for reduced tip-sample separations, which may account for why the DBs look dark during close probing at a fixed bias. $\Delta f(V)$ performed over each atom could show if this is the case, as it would show the DB(0/-) charge transition level shifted to larger negative bias values (For an example of such a shift on a single DB, see Figure 5.15 in the Supplementary Information for "Electrostatic Landscape of a H-Silicon Surface Probed by a Moveable Quantum Dot" in Section 5.1).

4.2.2 Streakiness in Polarization and Lattice Relaxation

During the peer-review process for BASiL, we received comments on the "streakiness" apparent in the Δf maps in Figure 4.2(h) and Figure 4.4(n). This streakiness

followed the raster scan direction of the tip and when one DB in a pair had a dark streak the other had a light one, suggesting we were toggling the localized electron back and forth. This phenomena ended up being interesting enough that it resulted in its own Physical Review Letter (PRL) paper, “Initiating and Monitoring the Evolution of Single Electrons Within Atom-Defined Structures” [153].

The streakiness was found to be a height-mediated tip effect. Dangling bonds of different charge state have an associated lattice relaxation. Density functional theory modeling found that negative DBs undergo a relaxation where the nuclear position of the host silicon atom is raised by 30 pm, relative to the neutral charge state of the DB [45,209,210]. This lattice relaxation was reported to have a $\sim 200\ meV$ stabilization energy effect on a DB. When an AFM tip with an attractive apex is brought into close proximity to a DB, it can mechanically manipulate the equilibrium position of the surface silicon atom hosting the DB, switching its charge state. Rashidi *et al.* showed in this PRL paper several examples of this mechanical manipulation. First, the charge state of individual DBs could be switched with $\Delta f(z)$ spectra taken over DBs, where a change in DB charge state was detected as a “step” in the spectroscopy from one tip-sample interaction curve to another. Second, they showed streakiness with pairs being raster scanned by a tip, demonstrating that upon close tip-sample approach single electrons could be manipulated within DB structures by using the probe to mechanically manipulate the DBs. Finally, they identified two distinct scanning regimes for AFM constant height scans: a “write” regime where the tip and sample are close enough for the tip’s attractive Van der Waals force to mechanically manipulate the equilibrium position of the DB-hosting Si atoms to change the charge state, and a “read” regime where the tip merely looks at the electrostatic arrangement in the assembly. Thus, when probing these DB assemblies to look at the electron positions, it is best to be as far away as possible to minimize the tip influence on the charge arrangement. Figures 4.2(h) and 4.4(n) from BASiL should have been taken at a larger tip-sample separation to not display streakiness, or with a different apex type. In regard to apex type, examining again Figure 4.12 Tip Apex 1 never shows streakiness in the probed heights, whereas Tip Apex 2 shows it for intermediary ones. This suggests the apex must be of the right character to

have an attractive force capable of overcoming the $\sim 200\ meV$ stabilization energy to manipulate the host silicon atoms.

As an ancillary example to the strong correlation between lattice relaxation and streakiness, we show the case of enforcing precise control over the appearance of this phenomena in the case of a continuous (no intervening H) five DB chain in Figure 4.13. Focusing first on the STM images in (a,b), we see that in filled states the five DB chain only shows four nodes and in empty states it appears as a continuous feature. Two other STM studies have examined chains of DBs such as this, which we briefly discuss to explain our results. First, Wood *et al.* was able to reproduce similar STM features to ours for DB chains of the same length, attributing the observed number of STM nodes to strong hybridization of constituent DBs that created new electronic structures as "artificial molecules" [223]. The other STM study of chains of DBs was performed by Hitosugi *et al*, where using first-principal calculations they predicted that the reason why the number of nodes seen in STM imaging did not always correlate to the number of atoms comprising it was because of lattice relaxations [182]. They found that second-layer Si atoms are displaced alternately to form pairs with charge redistribution; a type of Jahn-Teller distortion in an artificial pseudomolecule. In Figure 4.13, we show the first AFM analysis of a chain, visually confirming the predicted lattice relaxation from Hitosugi *et al.* .

Figure 4.13(c-f) show constant height AFM images of the five DB chain taken at different heights. Far from the surface in (c), it can be seen that the chain naturally hosts three electrons. Upon closer scanning in (d-f), the characteristic streakiness from an attractive tip becomes apparent, with the aforementioned trend of alternating light and dark for adjacent sites observed. This alternating of dark/light for DBs agrees with results published in the PRL from Rashidi *et al.*, where they reported that even if the attractive tip is able to interact with charges in DB structures to move the electrons [153], lower-energy configurations (either [DB^-, DB^0, DB^-, DB^0, DB^-] or [DB^0, DB^-, DB^0, DB^-, DB^0]) are preferred over higher-energy ones (two DB^-'s adjacent).

$\Delta f(V)$ spectroscopy was then performed over each DB in the chain, as shown in Figure 4.13(g). Compared to the $\Delta f(V)$ data presented in BASiL, these curves

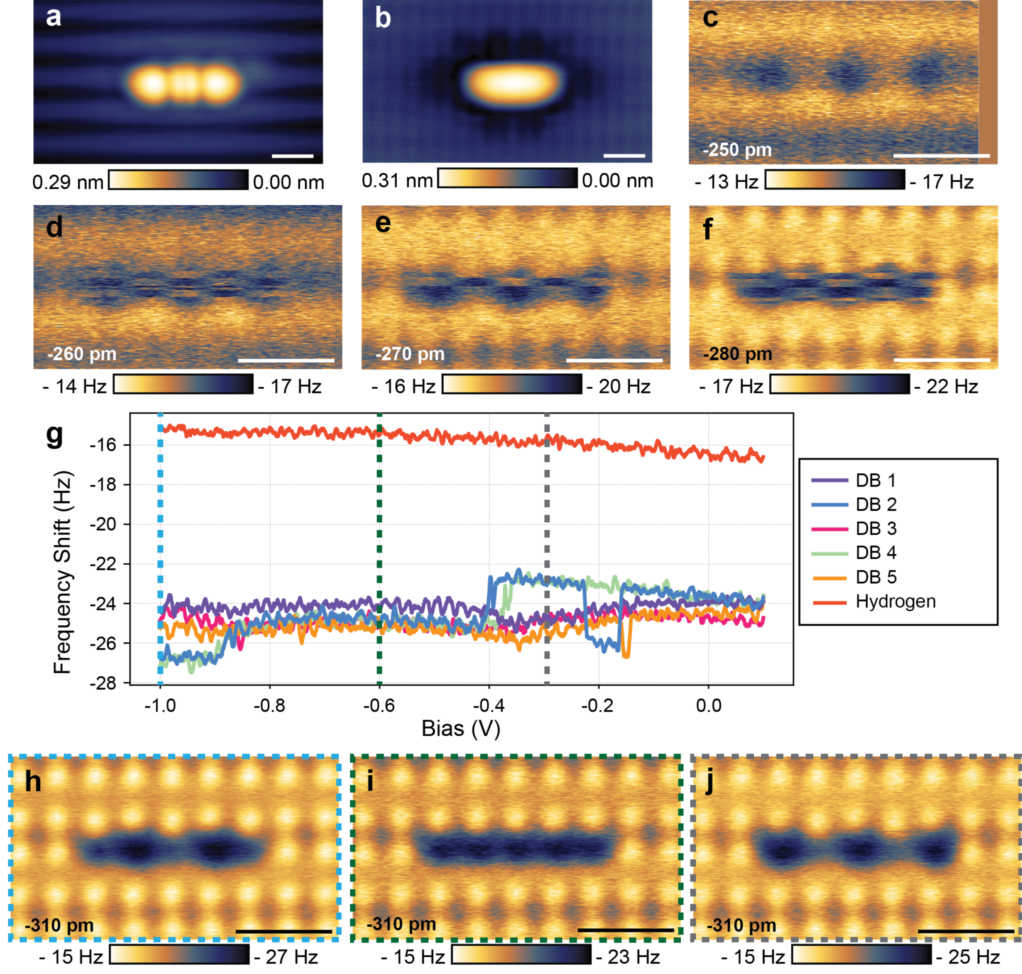

Figure 4.13: **Continuous DB Wires with Charge-State-Induced Lattice Relaxation.** **(a)** Constant-current filled states ($V = -1.8\ V$, $I = 50\ pA$) and **(b)** empty states ($V = 1.3\ V$, $I = 50\ pA$) STM images of a continuous five DB chain ($7 \times 4\ nm^2$). **(c-f)** Constant-height Δf AFM images of the same five DB chain taken at different heights, with the heights listed in the lower left of each frame ($V = 0\ V$, and $Osc.\ Amp. = 50\ pm$). **(g)** $\Delta f(V)$ spectra taken over each DB in the chain, as well as over the hydrogen surface ($z_{rel} = -280\ pm$). A Savitsky-Golay filter of order 9 was applied to allow easier differentiation of the curves. **(h-j)** Constant-height Δf AFM images of the chain, but with fixed biases of $V = -1.0\ V$, $V = -0.6\ V$, and $V = -0.3\ V$ applied, respectively ($z_{rel} = -310\ pm$ and $Osc.\ Amp. = 50\ pm$). The frames are color-coded with their positions in the $\Delta f(V)$ spectra in (g). All scale bars are 1 nm. z_{rel} is referenced to a height defined by a STM tunneling current of $I = 50\ pA$ with $V = -1.8\ V$ applied, as taken over a surface hydrogen atom.

are noisy and irregular. As discussed in BASiL Figure 4.2(i) for the case of the DB pair, the electrostatic field from the tip is long range enough to effect other nearby DBs. For the chain, this effect manifests as accidental jumps during $\Delta f(V)$, such as observed in the blue curve of DB 2 at $\sim -0.2\ V$. It also leads to some DBs not even displaying a charge transition step, such as DB 3 (pink curve) and 5 (orange curve). It was initially hoped $\Delta f(V)$ curves could be a quicker way to probe charge in DB structures without the need for timely Δf maps, but these inadvertent noisy features in the spectra become problematic for dull or irregular tips probing closely-spaced ensembles. Regardless, slices in the $\Delta f(V)$ spectra are known to inform on the observed contrast for a particular fixed bias and can also change the charge occupation depending on which side of a given charge transition step the selected bias value falls. Thus, we tested if certain charge occupations of the chain could be enforced with fixed bias values applied during constant-height scans.

From Figure 4.13(g) we chose three fixed bias values of $V = -1.0\ V$, $V = -0.6\ V$, and $V = -0.3\ V$, where there seemed to be maximal deviation of the DB contrasts as evidenced by the $\Delta f(V)$ spectra. These correspond to the fixed bias values that color-coded frames in Figure 4.13(h-j) were taken at. Starting with (h), based on the DB's contrast in Δf and the splitting seen in the $\Delta f(V)$ spectra for the selected bias this image was obtained at ($V = -1.0\ V$), the charge in the structure seems to correspond to the case of [DB^0, DB^-, DB^0, DB^-, DB^0]. Of particular interest is the first direct imaging of the Jahn-Teller distortion of the lattice. Hydrogen atoms above neutral DBs are pulled toward the chain and hydrogen atoms above negative DBs are pushed out. This agrees with Hitosugi's predictions of alternately displaced second layer Si atoms [182]. Additionally, now that we have fixed a particular charge occupation for the chain through bias selection, there is no observed streakiness as the attractive tip can no longer sufficiently lift the host Si atom enough to change its charge state. Next, we altered the observed lattice distortion by applying a different tip bias in Figure 4.13(i). The $\Delta f(V)$ spectra from (g) for this frame suggests all DBs should be the same charge state, which is confirmed by their appearance as all dark in (i). Since they are all in the same charge state, no lattice distortion is seen for the hydrogen atoms on the other side of the dimer row the chain is in. Finally, we explore

the last re-arrangement of the lattice in Figure 4.13(j). Based again on the relative DB contrast in Δf and the bias value selected in $\Delta f(V)$ ($V = -0.3\,V$), the structure contains now three electrons with the chain presenting as [DB^-, DB^0, DB^-, DB^0, DB^-]. Once again, hydrogen atoms above neutral DB sites are pulled in toward the chain and hydrogen atoms above negative DBs are pushed out. This result not only confirms the first-principals calculations of Hitosugi *et al.* in Ref. [182], but shows that exact control can be exerted over chain electron population and lattice relaxations.

4.2.3 Modeling DB Logic Assemblies and The Implications for Large Scale Atomic Structure Design

Creating DB structures and probing them in AFM is time intensive. Fabricating structures can take anywhere from minutes to hours, depending on tip stability and the size of the desired structure. For AFM analysis, a single constant-height Δf image of area 10×10 nm^2 takes $\sim 10 - 15$ minutes to acquire. To enhance our ability to test new designs, collaborators at the University of British Columbia, led by Ng *et al.*, created a computer-aided design tool to enable the rapid design and simulation of DB logic patterns called the "Silicon Quantum Atomic Designer" or SiQAD [215].

Their framework contains several simulation tools including a ground-state electron configuration finder, a non-equilibrium electron dynamics simulator, and an electric potential landscape solver with clocking electrode support [215]. Thus, a user can prototype different DB designs quickly and efficiently before undertaking time intensive *in situ* fabrication and testing. In this work, Ng *et al.* were able to retroactively simulate the logical OR gate presented in BASiL, as well as put forth designs for additional gate types like AND, XOR, NAND, and NOR, providing a complete catalog satisfying functional completeness.

To examine the utility of the software for DB logic designs and highlight important design considerations for DB atomic structures, we simulate and discuss one of the possible logical input configurations of the OR gate from BASiL. We use only

one of the available simulation tools from SiQAD for this called “Sim Anneal”, which is the ground-state electron configuration package [215]. With it we output the position of the DB(0/-) charge transition levels relative to the Fermi level of the surface. Before showing these results, we first briefly discuss how the annealing algorithm works.

In general, simulated annealing algorithms attempt to find a solution that minimizes an energetic objective function by heuristically exploring a defined problem space. At each time step, the algorithm selects a solution close to the current one, assesses the quality of the new solution, and decides either to accept the solution or discard it in favor of the current one. Solutions which lead to a reduction in the energetic objective function are desirable, but those that raise the energy can also be accepted based on some probability conditions in order to break out of local minima. The probability of accepting a solution with higher energy depends on an artificial temperature which often starts at a high value and decreases at each simulation time step. This allows a wider problem space to be explored in earlier time steps, finally converging on a single solution by the end of the simulation. The probability of converging on the global minimum can be improved by the choice of artificial temperature schedule, sufficient run time allocation, as well as sufficient repeated number of attempts.

Relating this to simulating DB structures, the toy-model case of a pair polarized by a single DB can be examined as shown in Figure 4.2(k) from BASiL. The lowest energy configuration is to have the negative DBs as far away from each other as possible. If the electron contained in the pair from Figure 4.2(k) were on the teal triangle-marked DB instead of the blue triangle-marked DB, this might be a possible configuration, but it would be higher in energy and thus has a high probability of relaxing to lower energy states. Sim Anneal works by looking at many configurations of charge arrangement within a given DB structure and attempts to return the global optimum (global energy minimum) to give the charge arrangements expected to correspond with experimental observations. In each simulation time step, SimAnneal allows inter-DB hopping as well as DB-reservoir hopping; the former allows SimAnneal to find low energy charge configurations without changing the surface

charge population, and the latter allows the surface charge population to change by letting charges hop between DB sites and an infinite charge reservoir. The heuristic probability function governing DB-reservoir hopping is inspired by a Fermi-Dirac distribution. At each iteration of this simulated hopping, the thermal energy of the reservoir is reduced and the distance between the DBs and the reservoir is increased. This gradually inhibits hopping as time goes on, tending to fix the number of electrons in the structure. At the end of this annealing schedule, “The lowest energy metastable state is presented to the user in SiQAD.” [215].

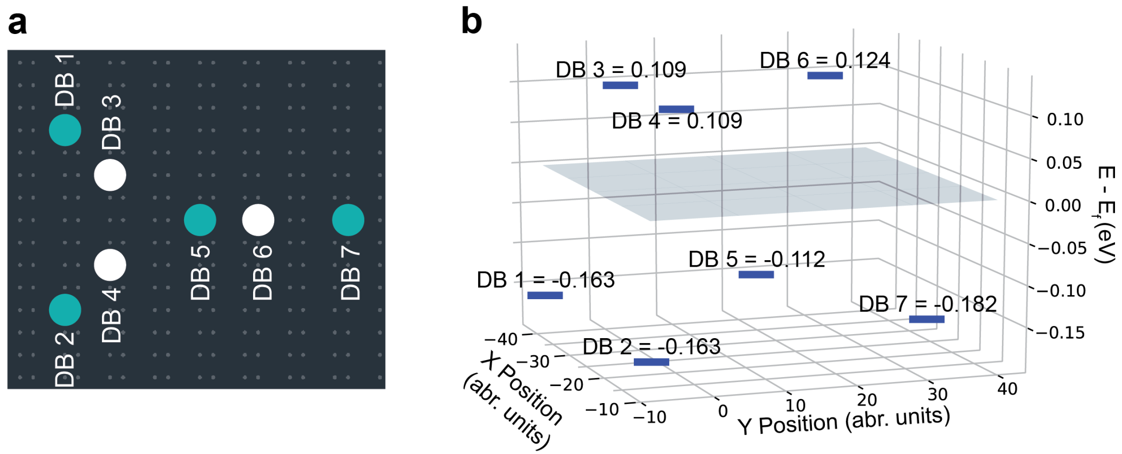

Figure 4.14: **OR Gate Charge Transition Levels (a)** Lattice model from SiQAD showing the OR Gate DB layout superimposed on the H:Si surface. Blue circles indicate the DB is negative and white circles that the DB is neutral. **(b)** DB(0/-) charge transition levels of the OR gate from (a) as referenced to the sample Fermi level (a transparent plane has been put through $z = 0 = E_f$ for clarity). The z-axis denotes how far the charge transition level is away from the bulk Fermi Level and the x and y axis are arbitrary position units.

Returning to the discussion regarding the application of simulation tools on the BASiL OR gate, we attempt to simulate the OR gate *via* Sim Anneal using physical parameters fitted in BASiL: screening length λ_{TF} = 5 nm and dielectric constant ϵ_r = 5.6. A selection must also be made for how far an isolated DB's DB(0/-) level is below the Fermi level, which is encompassed by a parameter μ set as $\mu = DB(0/-) - E_f = -0.28\ eV$. The program was then set to run for 10,000

annealing cycles, with the calculated lowest energy state for Figure 4.4(e) of BASiL in Figure 4.14. Figure 4.14(a) depicts the layout of the DBs in respect to the background 2×1 H:Si lattice (See Section 2.3 for the surface lattice spacing), as well as the charge occupation for DBs in the structure. This is a panel taken directly from the SiQAD simulation software, with the blue DBs being in a negative charge state and the white DBs in a neutral one. Figure 4.14(b) shows the calculated DB(0/-) charge transition levels from Sim Anneal, as referenced to the Fermi level of the bulk. This highlights an interesting consideration for 2D structures: crowding can effect how strongly an electron is bound.

Two-dimensional DB structures are electrostatically anisotropic. All DBs with a negative charge electrostatically interact and, depending on the DB positions, the pair-wise electrostatic interactions will sum differently. For example, the negative DBs 1, 2, 5, and 7 in Figure 4.14(b) are all below the Fermi level, but DB 7 is the furthest below at -0.182 eV and DB 5 is the least at -0.112 eV. All of these negative DBs also have much shallower confining potentials compared to what was set for μ originally.

As a point of interest, we were unable to replicate our OR gate functionality in the SiQAD software using the experimentally extracted $\mu = -0.23\ eV$ from BASiL Figure 4.2(p). Such a shallow confining potential did not reproduce the experimentally observed charge arrangement of Figure 4.4 in BASiL, necessitating that we make it deeper with $\mu = -0.28$. We explain this with two justifications. First, there may be a stabilization effect from the TIBB that the software does not account for, or the TIBB correction from Figure 4.2(p) was slightly off (See TIBB estimate considerations in Section 2.4.1). Second, Figure 4.4 was taken with a different tip on a different crystal than the data from Figures 4.1, 4.2, and 4.3 in BASiL. As will be discussed in detail in "Electrostatic Landscape of a H-Silicon Surface Probed by a Moveable Quantum Dot" (Section 5.1), our crystal preparation method can introduce some variation into λ_{TF}, ϵ_r, and μ. While these three parameters would be expected to be order of magnitude consistent, small deviations are expected for different crystals and tips.

In summary, there are several important implications from these results. Elec-

trostatic fields are radially symmetric, so 2D structures must have the cumulative effect of other local negative DBs within a critical screened length factored in to their design. Too many local negative perturbers and entire branches of logical structures can be depopulated by having their DB(0/-) levels pushed above the bulk Fermi level, returning incorrect binary states. Next, it also means there is a critical distance that structures must be from one another, limiting the areal density for atomic logic structures. What is considered an acceptable shift of a DB level will depend on the local concentration of point charges and the local carrier concentration as a function of doping and sample preparation. Finally, how shallow these levels are relative to the Femi-level also may have implications for their operational stability at room temperature. Ignoring that parameters like the screening length will also change with a rise in temperature, the closer a DB(0/-) level comes to the Fermi level, the more likely a phonon mediated event [50, 224] can destabilize it. While earlier work did demonstrate room temperature charge polarization of coupled DB structures in STM [51], this reduction of confining potential for electrons in DBs invites further experimental testing at elevated temperatures.

4.2.4 The DB Positive Charge Transition

The DB(0/-) charge transition has primarily been focused on, but the positive charge transition DB(+/0) is also of interest. The DB(+/0) charge transition state was rarely measured as its location (bias value) was in a region that would induce current in the 10s to 100s of pA. Due to concern about cross-talk (See Section 2.2) we thus focused mainly on the DB(0/-) charge transition, which was almost always in regions with zero tunneling current (See Supplementary Figure 5.12 in Section 5 for an exception where a local charge defect shifted the DB(0/-) level to a current-inducing bias region). Many more interesting studies remain to be done on this charge state beyond the scope of this work, but we give a brief intro to some preliminary findings.

For the few cases where the DB(+/0) charge transition was probed, it showed up less as a discrete charge transition step and more like a dip or distortion as shown in Figure 4.15(a). We suggest this distorted character of the DB(+/0) is

in line with a rate-mediated charge state change. As in, the tip is able to extract electrons faster than the bulk can fill the level, but the bulk is actively trying to fill it such that it is only positive on average (not a perfectly maintained single electron charge state change). This interpretation has literature precedence, with some prior works reporting that continuous changes in the charge state led to dip-like features in their $\Delta f(V)$ measurements [149, 206, 225, 226]. This rate mediated charge state change is also in line with other STM evidence in the literature. Using time-resolved STM, it was reported that the carrier capture rates for DBs could be tuned based on modification of the competing filling and emptying of the levels [201]. In another publication, negative differential resistance (NDR) observed over a DB was attributed to "a many body phenomenon related to occupation dependent electron capture by a single atomic level" [120]. The DB presented in Figure 4.15 is one such NDR-displaying DB, where instead of having current always increase in proportion to voltage, it temporarily decreases around $\sim -1.1\ V$. This current decrease is explained with competing rates to the DB level too, with full detailed analysis of the effect available in Ref. [120] (See also Figure 2.19(d) for a qualitative band diagram of the competing rates for the DB(+/0) level).

In the absence of a tip, as we intend to eventually implement for DB logic structures, local electrostatic inputs of sufficient magnitude should be able to enforce this state without competing rates. The DB(+/0) level then becomes of interest as it can be used in the design of logic devices. To illustrate, in the SiQAD modeling from Ref [215], some of their proposed logical gate designs in the publication rely on fully depopulating certain binary pairs to give correct logical state at the output. Positively charged DBs could perhaps be similarly utilized in logic designs, allowing new functionality.

4.2.5 Estimates of the DB Levels in the Bandgap

In Figure 2.19 we qualitatively illustrated the case of the tip Fermi level being swept into resonance with the DB(0/-) and DB(+/0) levels to change the DB's charge state. The quantitative energetic position of these levels between the conduction and

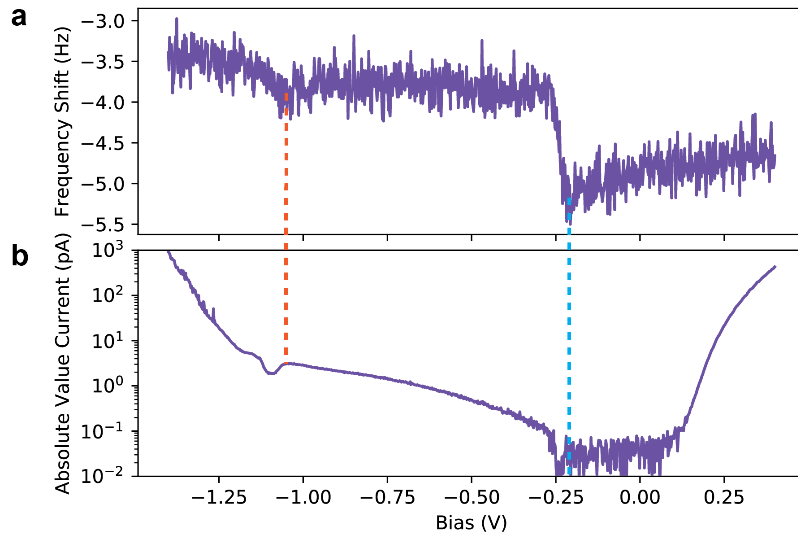

Figure 4.15: **The DB(+/0) Charge Transition Level (a)** $\Delta f(V)$ spectra taken over a lone DB and **(b)** simultaneously obtained $I(V)$ spectra ($z_{rel} = -330$ pm and $Osc.\ Amp. = 50$ pm). The $I(V)$ spectra is plotted in absolute value and log scale. The DB(0/-) charge transition is marked with the blue dashed line, and the DB(+/0) with the orange dashed line. z_{rel} is referenced to a height defined by a STM tunneling current of $I = 50$ pA with $V = -1.8$ V applied, as taken over a surface hydrogen atom.

valence band has been debated [202]. While both levels are consistently observed experimentally, theoretical modeling has reported varying positions in the bandgap, depending on the chosen theoretical constraints.

To illustrate, we start by highlighting an experimental study that used electron paramagnetic resonance (EPR) to find the bandgap and DB charge transition level energies as $E_{Gap} = 1.17$ eV, DB(+/0) = 0.26 eV, and DB(0/-) = 0.84 eV [227], with the levels referenced to the valence band maximum (VBM). Years later, Broqvist *et al.* undertook a theoretical study to match these experimentally extracted values using a class of hybrid density functions [228]. They found that the defect levels relative to the VBM were dependent on the chosen model size (number of atoms in the modeled tip and surface), and that they also had to tailor a dielectric-dependent hybrid exchange value functional (α) to reproduce the experimentally extracted values [228]. They first focused on model size in their study, finding that smaller model slabs (less layers of modeled surface atoms) tended to put both the DB(+/0) and DB(0/-) levels in the band gap, but larger slabs had the DB(+/0) level only a minuscule amount above the valence band edge at DB(+/0) = 0.02 eV. This modeling did not have the α value factored in yet and was thus severely underestimating the bandgap at $\sim E_{Gap} = 0.63$ eV (it is generally $\sim 1.1\ eV$). Common electronic-structure methods based on semilocal density-functional calculations quite often underestimate electronic band gaps [228]. Broqvist *et al.* then went on to tailor the α parameter to better match experiment and were able to eventually get good agreement with the experimental values (provided in Table 4.2) finding both charge transition levels fell within the band gap.

The study by Broqvist can be compared to another more recent theoretical undertaking using newer density functional theory methods [202]. In this study, Scherpelz *et al.* found, again, that if the model slabs were small the DB levels all fell within the bandgap. For thicker modeling slabs the positive DB level fell below the VB edge, with the researchers concluding "we demonstrate that a stable positively charged DB state is accessible only in thin (1.2 nm) Si samples." [202]. As the relative position of these levels have important implications for how decoupled they are from mixing with bulk properties, and thus the robustness of our atomic logic, we attempt to

estimate the position of the charge transition levels in the bandgap from our AFM experimental data.

The charge transition levels of the DB were extracted from Figure 4.15 with $DB(0/-)$ = -0.212 V (blue dashed line) and $DB(+/0)$ = -1.06 V (orange dashed line). To estimate the gap width, generally $I(V)$ curves taken over H:Si are used; current should sharply onset when the tip Fermi level comes into resonance with both the valence band and conduction band edges, allowing extraction of the gap width from subtracting the bias values where these current onsets occur at. The extracted values, however, would have to be TIBB corrected to get an accurate measurement. Unfortunately, no such $I(V)$ curve was taken over H:Si to go with the data-set in Figure 4.15. Looking through the literature though, a prior publication reported the needed $I(V)$ measurement of the H:Si bandgap taken at a similar height in Ref. [201] (Figure 4.15 was taken with $z_{rel} = -330\ pm$ and their measurement was taken with $z_{rel} = -335\ pm$). In their publication, they showed tunneling current onsets at -1.27 V for the valence band (VB) and 0.3 V for the conduction band (CB).

Using these values for our calculation, along with the extracted charge transition voltages, we TIBB correct all to get E_{VB} = -1.03 eV, E_{CB} = 0.04 eV, $DB(0/-)$ = -0.31 eV, and $DB(+/0)$ = -0.89 eV. Referencing the levels to the valence band maximum for easier comparison with the other results, $E_{Gap} = 1.07\ eV$, $DB(0/-)_{VBM} = 0.72\ eV$ and $DB(+/0)_{VBM} = 0.14\ eV$. A table comparing our extracted values to those from the EPR study [227] and Broqvist's modeling [228] is provided in Table 4.2.

Table 4.2: Table comparing extracted band gap, DB(0/-), and DB(+/0) energies.

Energies	E_{Gap} (eV)	DB(0/-) (eV)	DB(+/0) (eV)
EPR Study	1.17	0.84	0.26
Theory By Broqvist	1.10	0.80	0.26
AFM Values	1.07	0.72	0.14

Our values are in rough agreement with the EPR experimental study and Broqvist's theoretical modeling, with both AFM-calculated charge transitions found to fall in the bandgap. This finding, however, disagrees with the results of Scherpelz

et al. that implied the DB(+/0) state was below the VB. This suggests some critical factor is not being accounted for in the theoretical modeling. We stress to take these attempted calculations from the AFM data with a critical eye though; a more detailed analysis examining the error in our measurements combined with statistics on many DBs is needed. In addition, an ideal data set would have the bandgap measurement taken with the same tip at the same time as the DB data, since different tips are known to have different TIBB corrections. Furthermore, bad estimates in the TIBB correction such as height, tip radius, apex-termination, work function, and crystal doping can also empirically alter the extracted values. However, the rough agreement of our values with those extracted from others is encouraging, and illustrates how AFM can be used to probe this information.

Chapter 5

The Varying Electrostatic Environment of H:Si and its Effect on DB Logic

After publishing BASiL, a concerted effort was made to start testing new gates, wires, and designs. These structures did not always display the intended binary states though, even when known priorly-working geometries were replicated. Initially this was hypothesized to be due to a tip-effect, but further investigation revealed cases like Figure 5.1.

In Figure 5.1(a) an area for DB fabrication is selected, with DBs patterned in the lower left and upper right corner as shown in (b). These DBs then had $\Delta f(V)$ spectra taken over them, with the results displayed in Figure 5.1(c). Both DBs would be expected to have equivalent charge transition bias values and yet both are quite different. The difference in the DB's charge transition onsets cannot be attributed to a tip effect either as both were taken sequentially.

This was accompanied by additional observations where when DBs were patterned near certain surface defects, the defects could shift the DB charge transition levels. An example is shown in Figure 5.2. A charge defect is shown in (a) as the dark depression in the lower left of the frame. A DB was then patterned near this defect

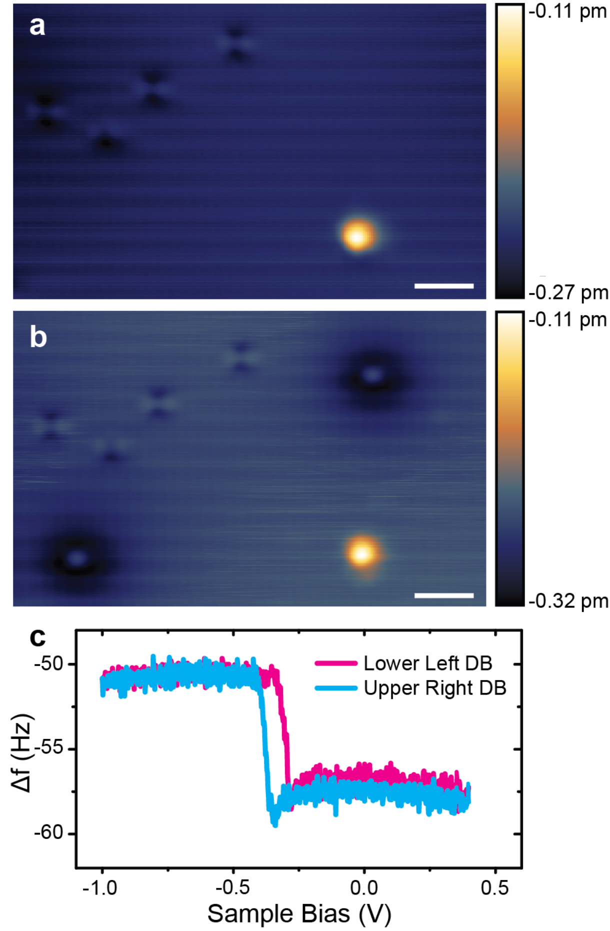

Figure 5.1: **Different DB(0/-) Charge Transition Levels. (a)** Empty states STM image of a chosen area with no charge defects in frame. ($V = 1.3\,V$, $I = 50\,pA$). **(b)** Empty states STM image of the same area as (a), but after the addition of DBs in the lower left and upper right corners. **(c)** $\Delta f(V)$ spectra taken over the two created DBs, showing nonequivalent charge state transition biases ($z_{rel} = -350\,pm$ and $Osc.\ Amp. = 50\,pm$). All scale bars are 2 nm. z_{rel} is referenced to a height defined by a STM tunneling current of $I = 50\,pA$ with $V = -1.8\,V$ applied, as taken over a surface hydrogen atom.

in Figure 5.2(b), with its corresponding $\Delta f(V)$ curve in (c). Instead of the DB having its charge transition at the expected value of $\sim -0.20\ V$ as shown for other cases, its charge transition is at $\sim 0.24\ V$ as if shifted by a negative perturber.

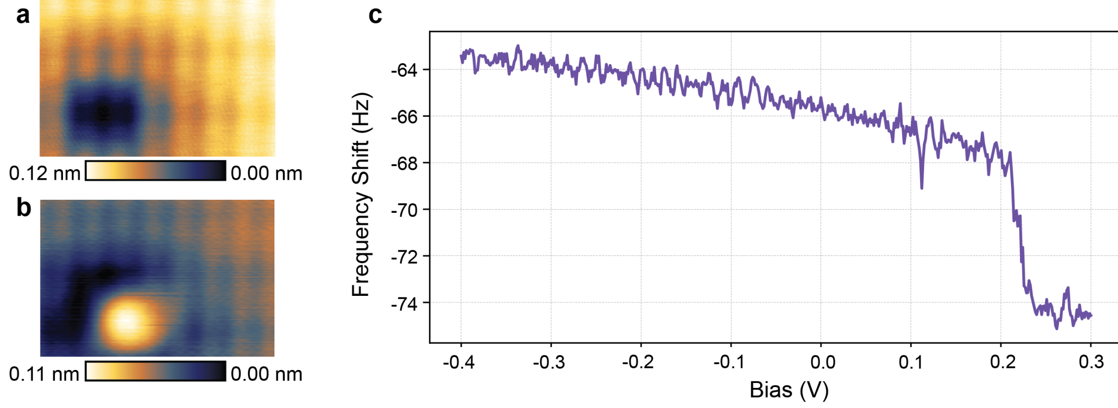

Figure 5.2: **Surface Defect Shifting a DB's Charge Transition**. **(a)** Empty states STM image of an area with a dark charged defect in the lower left ($V = 1.3\ V$, $I = 50\ pA$). **(b)** STM image of the same area as (a), but after the addition of a DB near the dark defect. Both (a) and (b) are $3.0 \times 2.0\ nm^2$ in area. **(c)** $\Delta f(V)$ spectra taken over the DB patterned on top of the charge defect, showing a shift of its DB(0/-) charge transition level to $V = 0.24\ V$ ($z_{rel} = -320\ pm$ and $Osc.\ Amp. = 50\ pm$). z_{rel} is referenced to a height defined by a STM tunneling current of $I = 50\ pA$ with $V = -1.8\ V$ applied, as taken over a surface hydrogen atom.

These results lead to the conclusion that not all areas were electrostatically equal. Local charge defects could shift DB behavior necessitating care in avoiding them and even if patterning in charge-defect-free areas as in Figure 5.1, DBs still showed variation in the onset voltage of their DB(0/-) level. This suggested a lack of electrostatic homogeneity that was not visible in the STM contrast. Thus, a study was undertaken to begin exploring if there was a way to quantify how varied the electrostatic topography was.

Earlier, $\Delta f(V)$ curves were discussed as being a way to probe the surface electrostatics (See Section 2.4.3). The tip-sample system acts as a capacitor and the apex of the parabolic $\Delta f(V)$ curve indicates the point where the electrostatic field has been minimized in the tip-sample junction. If the tip-sample junction has more or

less charge inside of it, the apex of the parabola would be shifted right or left, respectively. By taking a grid of these $\Delta f(V)$ curves over an area, fitting the parabolas, and looking at the variation in the contact potential difference, information can be extracted about the surface electrostatic homogeneity.

In addition, it was also found that the magnitude of the shift in DB(0/-) charge transition levels when near defects was intrinsically related to the distance it was away from said defect. This lead to the notion of using the DB as an electrostatic point-probe, which could be used to extract information about the surface and defects. In BASiL, the electrostatic shifts from Figure 4.2 were fit using a screened Coulomb equation of the form:

$$U(r) = \frac{e^2}{4\pi\epsilon_0\epsilon r} e^{\frac{-r}{L_{TF}}} \tag{5.1}$$

Where e is the elementary charge, ϵ the dielectric constant, ϵ_0 the vacuum permittivity, r the distance between the DBs, and L_{TF} the Thomas-Fermi screening length. As all fabricated DBs are in the same height plane in BASiL and the distance they were from each other could be deduced from the lattice constants, this was a fit on the two free parameters of dielectric constant ϵ and screening length L_{TF}. Here, with the examination of sub-surface charge defects, r now contains an unknown depth component in addition to the known lateral distance the probe DB is moved:

$$r = \sqrt{(lateral\ distance)^2 + (depth)^2} \tag{5.2}$$

Thus, Equation 5.1 now had three free parameters. Fitting on three free parameters was difficult for the fit algorithm, necessitating two final adaptions. First, Equation 5.1 was linearized by taking the logarithm of both sides and simplifying to:

$$ln(U(r)r) = ln(\frac{e^2}{4\pi\epsilon_0\epsilon}) - \frac{r}{L_{TF}} \tag{5.3}$$

Now linear in form, this was easier for the fitting algorithm to handle. The second adaption made was to manually iterate depth within reasonable bounds.

In other words, depth is iterated and the fit is still performed on only two free parameters. These two adaptions resulted in a reduced error for the fits, with more details provided in Section 5.2.3 with the given fitting code.

5.1 Paper and Supplementary Information: Electrostatic Landscape of a H-Silicon Surface Probed by a Moveable Quantum Dot

Reproduced under the American Chemical Society's blanket permission policy for students to include in their theses and dissertations their own articles. Copyright 2019 American Chemical Society [https://doi.org/10.1021/acsnano.9b04653] [52].

Authors: Taleana R. Huff[1,2], Thomas Dienel[1], Mohammad Rashidi[1], Roshan Achal[1,2], Lucian Livadaru[2], Jeremiah Croshaw[1], and Robert A. Wolkow[1,2,3].

[1] Department of Physics, University of Alberta, Edmonton, Alberta, T6G 2E1, Canada

[2] Quantum Silicon, Inc., Edmonton, Alberta, T6G 2M9, Canada

[3] National Institute for Nanotechnology, National Research Council of Canada, Edmonton, Alberta, T6G 2M9, Canada

5.1.1 Abstract

With nanoelectronics reaching the limit of atom-sized devices, it has become critical to examine how irregularities in the local environment can affect device functionality. Here, we characterize the influence of charged atomic species on the electrostatic potential of a semiconductor surface at the sub-nanometer scale. Using non-contact atomic force microscopy, two-dimensional maps of the contact potential difference are used to show the spatially varying electrostatic potential on the (100) surface

of hydrogen-terminated highly doped silicon. Three types of charged species, one on the surface and two within the bulk, are examined. An electric field sensitive spectroscopic signature of a single probe atom reports on nearby charged species. The identity of one of the near-surface species has been uncertain in the literature, and we suggest that its character is more consistent with either a negatively charged interstitial hydrogen or a hydrogen vacancy complex.

5.1.2 Introduction

The ultimate miniaturization of technology will be constructed of individually placed atoms or molecules. Many notable studies have been presented including atomic-spin-based logic [18], molecular devices [12, 16, 185], patterned dangling bond (DB) devices and structures [19, 45, 49, 121, 153], single atom transistors [39], probabilistic finite-state machines [20], and qubits [229–231]. Vital for all of these applications is a precise knowledge of the local electrostatic environment [232]; maintaining a regular electrostatic background on a scale comparable to the device or device component size is necessary to prevent aberrant behavior. Using the charge sensitivity of non-contact atomic force microscopy (nc-AFM), we study local variations in the electrostatic environment at the surface of highly arsenic doped hydrogen-terminated silicon (H:Si).

We apply two established AFM techniques. First, we use grid-based Kelvin probe force microscopy (KPFM) [124, 146, 233] maps to resolve electrostatic variations on a nm length scale. This technique has been previously used to examine charge distribution within single molecules [124, 234] and in the proximity of surface species [235, 236] by extracting the local contact potential difference for each point in an area, generating a two-dimensional surface map of the potential energy landscape (see "KPFM Maps" in Methods Section 5.1.5). Here we apply this technique to the surface of a heavily doped semiconductor. We investigate two charged near-surface species of different character that display opposite electrostatic contrast.

Second, we apply a variant of scanning quantum dot microscopy [206, 237, 238] to individually probe the surrounding of the charged species. Scanning quantum

dot microscopy typically relies on functionalizing the apex of the AFM tip with a quantum dot. Subtle changes of the quantum dot's charging behavior are employed to sense the electrostatic field emanating from the scanned surface [206,237]. Due to the functionalization of the tip with large clusters or organic molecules and the required large bias range applied during probing (up to several volts), this methodology has been classified as a "far-field" method with moderate spatial resolution [237].Instead of functionalizing the tip's apex, here we "move" a single-atom quantum dot across the surface, enhancing the spatial resolution for our sample system.

We use DBs on the otherwise hydrogen-terminated silicon surface as our moveable quantum dots [49, 51, 201]. DBs possess gap states that are electronically isolated from the silicon bulk. DBs can hold zero, one, or two electrons resulting in a positive, neutral, or negative charge state, respectively [19,45,48,208]. In correspondence with these three charge states, there exist two distinct charge transition levels, (+/0) and (0/-), the specific energies of which are sensitive to their local electrostatic environment [48, 49, 201]. Other articles have detailed the precise patterning [134, 135, 239] and erasing [136, 137] of DBs on H:Si (see "Creating and Erasing Dangling Bonds" in Methods in Section 5.1.5), which we employ here to progressively march a probing DB through the vicinity of charged species (*e.g.*, a second DB or a near-surface dopant atom). Moving the probe DB with respect to a charge of fixed position results in a bias shift at which the probe DB's (0/-) charge transition is measured by KPFM ($\Delta f(V)$) spectroscopy (see KPFM Maps in Section 5.1.5) [27,30,49,240]. Examination of the observed shifts allows us to determine the sign and location of the fixed charge within the substrate as well as the effective local dielectric constant and local screening length in the vicinity of the charge.

The identities of two species are firmly established in the literature as an ionized arsenic atom (a positive species) and a negatively charged DB. Previous work has suggested that a third may be either a boron contaminant atom or negatively charged arsenic atom [37,241]. We reconsider these assignments and find that the third species is more likely a negatively charged interstitial hydrogen atom or a hydrogen-vacancy complex.

5.1.3 Results and Discussion

Concentration of Charged Features

Scanning tunneling microscopy (STM) images of the same surface area of H:Si(100) 2×1 under three different tunneling conditions are displayed in Figure 5.3(a-c). Figure 5.3(a) shows a typical filled state STM image with the characteristic rows of paired silicon atoms (dimers) running horizontally across the frame [242, 243], wherein each surface silicon atom is capped by a single hydrogen atom. The scattered, irregularly shaped dark areas are etched pits (missing silicon atoms of the top layer), and the small bright protrusions are natively occurring DBs. The features highlighted by dashed circles (labeled T1-Type 1 and T2-Type 2) are the two near-surface charged species being examined in this work. While Type 1 features are known to be arsenic dopants [37, 38, 244, 245], the identity of Type 2 features remains less certain [37, 244, 246]. The appearance of the arsenic dopants strongly depends on their depth, the imaging orbital of the STM tip, and the lattice site the dopant occupies [245]. Similarly, variations in STM topography are reported for T2s, suggesting that they can reside in different near-surface layers [37], but with less variety observed compared to arsenic dopants. The correlation between STM appearances and the charge states of the dopant atom will be discussed in detail later.

In order to determine the volume concentration of the two near-surface species, their appearance in five large area frames (70×70 nm^2) was analyzed. Arsenic dopants were found to have an area concentration of $(1.8 \pm 0.3) \times 10^{11}$ $atom\ cm^{-2}$ and T2s $(6 \pm 1) \times 10^{10}$ $atom\ cm^{-2}$. The maximum depth wherein dopants create assignable features in STM topography have been reported to range from 5 monolayers (ML) [37, 244, 247] to 36 ML [245]. The volume concentration based on these lower and upper bounds are $(2.6 \pm 0.4) \times 10^{18}$ $atom\ cm^{-3}$ (5 ML) and $(3.6 \pm 0.5) \times 10^{17}$ $atom\ cm^{-3}$ (36 ML) for arsenic dopants and $(1.0 \pm 0.2) \times 10^{18}$ $atom\ cm^{-3}$ (5 ML) and $(1.3 \pm 0.3) \times 10^{17}$ $atom\ cm^{-3}$ (36 ML) for T2s. Previous studies have reported that the As concentration near the surface is reduced during the sample preparation conditions applied here, from the bulk value of 1.5×10^{19} $atom\ cm^{-3}$ (see "Sample Preparation"

in Methods Section 5.1.5) [203, 220]. The resulting dopant depleted layer extends $\sim 70\ nm$ into the bulk and has an As concentration of $1.0 \times 10^{18}\ atom\ cm^{-3}$ at the surface [203, 220], in agreement with the values observed here.

Electrostatic Variation from Near-Surface Charges

When probed, the charge state of the arsenic dopants can be neutral, positive, or negative depending on tip-surface distance and the applied bias which controls the competing filling and emptying rates from the tip and to the bulk, as reported in prior works [37, 248]. Here, we explore conditions consistent with the positive and neutral charge states of the dopant.

Beginning with Figure 5.3(d), taken at positive sample bias ($V = +300\ mV$ corresponding to empty sample states), the charge state of the dopant is, on average, neutral. Examining the corresponding energy level diagram in Figure 5.3(h), when imaged in energy regimes above the onset of the bulk conduction band edge, the tip-induced band bending (TIBB) at positive sample biases raises the dopant level above the bulk Fermi level (E_{FS}), but leaves it lower than the tip Fermi-level (E_{FT}). The charge state of the dopant depends on the competition among the filling rate from the tip (Γ_{T-T1}) and the emptying rate to the bulk (Γ_{T1-B}). If the tunneling rates to the dopant are tuned through adjustment of tip-sample separation or applied bias such that $\Gamma_{T1-B} < \Gamma_{T-T1}$, the dopant is rendered neutral with a single bound electron on average. However, for $\Gamma_{T1-B} < \Gamma_{T-T1}$, which would occur for modest biases between $0\ V$ and the flat band condition, the dopant would be positive, in agreement with the presented electrostatic topography maps and spectroscopic shifts of our probe presented later. At $0\ V$, where there cannot be a net tunneling current, the dopant would be positively charged because of the upward band bending from the contact potential difference between the tip and sample [49] lifting the dopant level higher than both tip and sample Fermi levels (Supporting Information, Figure 5.7(c)). The positive charge reduces the local band bending (blue lines) in the vicinity of the dopant [48]. Below the flat band condition, but above $\sim -1.2\ V$, the dopant is again neutral. A constant-height STM image is presented in Figure 5.3(e), with its

corresponding energy level diagram in Figure 5.3(i). The dopant becomes resonant with the bulk conduction band, and due to the narrower tunneling barrier between the dopant and the bulk conduction band, electrons tunnel to the dopant faster than the tip can extract them ($\Gamma_{B-T1} > \Gamma_{T1-T}$). The dopant opens up an additional channel for electrons to conduct from the tip to the conduction band, resulting in an increased conductivity over dopants compared to H:Si [47]. Below $\sim -1.2\ V$, the dopant can become negative [38, 245] or positive [47] depending on the dopant concentration at the surface and the relative magnitude of filling and emptying rates. A full energy level diagram progression over an arsenic atom from positive tip-sample biases to $\sim -1.2\ V$ is given in Supporting Information, Figure 5.7 for clarity. A series of experimentally obtained constant-height STM images of the same dopant as Figure 5.3(d,e) but at different biases is given in Supporting Information, Figure 5.8.

A T2 charge defect is shown in Figure 5.3(f) where it appears as a region of reduced brightness in empty states and in Figure 5.3(g) as a region of enhanced brightness in filled states. This appearance is consistent with the defect being negatively charged, as reported elsewhere [37]. In the qualitative empty states energy level diagram (Figure 5.3(j)), the upward band bending from the presence of the negatively charged T2 defect reduces the tunneling current from the tip to the conduction band (purple bands and purple Γ_{T-B}), resulting in the T2 showing up as a dark depression [37]. Without the T2 present, the bands are not altered (black bands and Γ_{T-B}). In filled states, the defect's bright contrast (Figure 5.3(g)) indicates that it remains negatively charged, with the resulting local upward band bending (purple lines and purple Γ_{B-T} in Figure 5.3(k)), opening up a larger energy window for tunneling from the valence band to the tip [37]. These observations strongly suggest that the defect remains in the same negative charge state over the range of bias voltages examined here.

Both an arsenic and a T2 are shown together in the STM constant-height image Figure 5.3(l) and the corresponding constant-current image Figure 5.3(m). To map out the local electrostatic potential of the area, a 25×25 point grid was overlaid and constant-height $\Delta f(V)$ curves were taken above each grid site. The $\Delta f(V)$ spectra appear as parabolas with a maximum voltage V^* representing the bias where the lo-

cal contact potential difference has been nullified [124, 234–236] (see “KPFM Maps” in Methods Section 5.1.5 and Supporting Information, Figures 5.9 and 5.10). While some other surface defects are present in Figure 5.3(l,m), they are charge neutral and do not alter the measured contact potential difference. An average V^*, representing the electrostatic background, was calculated to be -0.49 V from averaging 15 measurements over H:Si far from any charge defects. Figure 5.3(n) presents the KPFM map of the extracted maxima (V^*) mapping out the variation in the local electrostatic potential, with the background V^* of H:Si subtracted. The upper left of the frame shows a dark area due to the presence of the arsenic dopant, indicating that at energies below the bulk Fermi level and above the flat band condition, it is positively charged reducing the contact potential difference in the area (bands are bent down as shown in Supporting Information Figure 5.7(c)). Conversely, the T2 gives rise to an enhancement in the contact potential difference in the lower right, in agreement with STM observations [37].

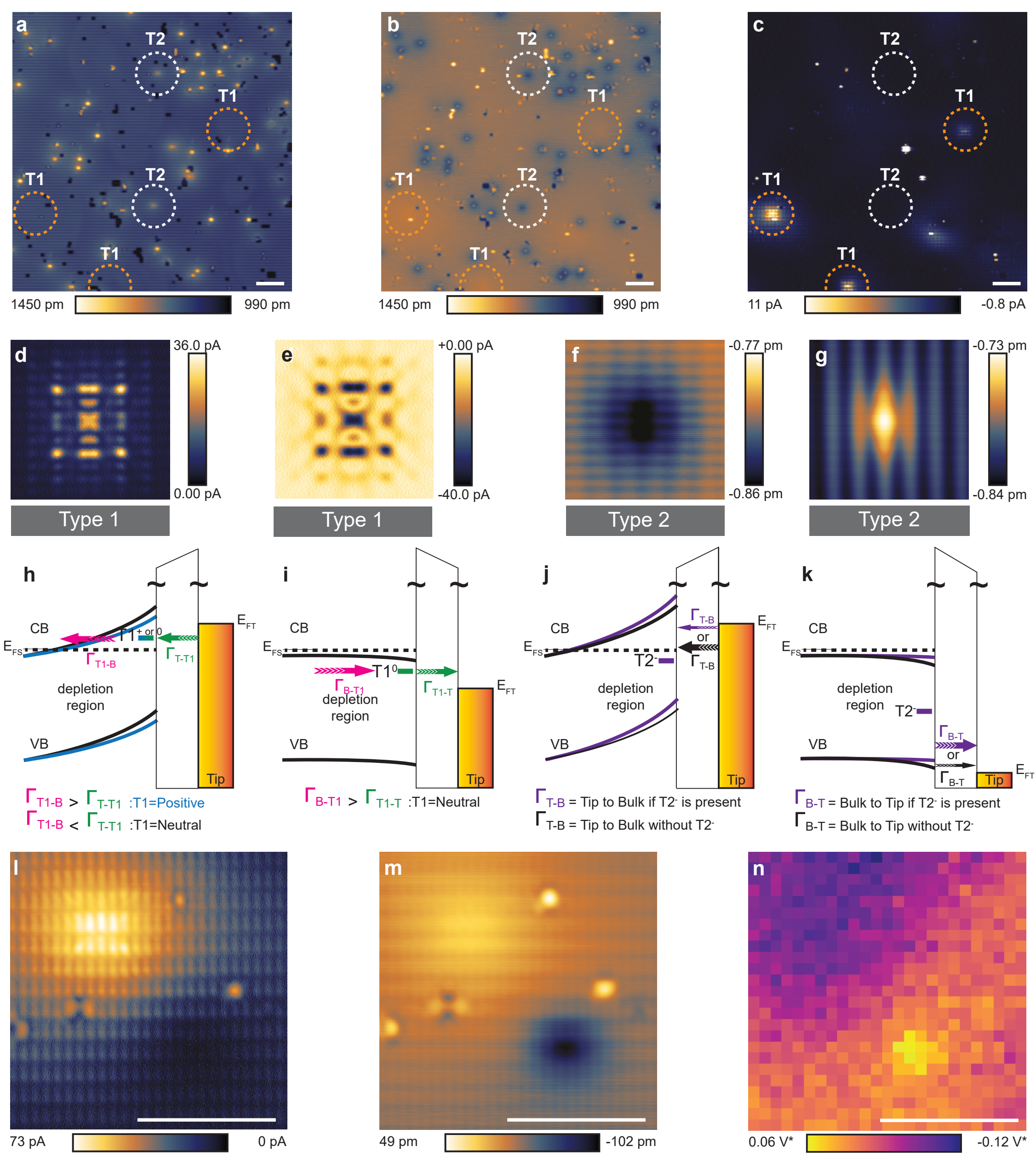

Figure 5.3

Figure 5.3: **H:Si Imaged with Different STM Modes and Labeled Near-Surface Charged Species**. **(a)** Filled states ($V = -1.6\ V$, $I = 50\ pA$), **(b)** empty states ($V = 1.3\ V$, $I = 50\ pA$), and **(c)** constant-height ($z_{rel} = -150\ pm$ and $V = 300\ mV$) of the same area (z_{rel} referenced to a common STM set-point $-1.8\ V$ and $I = 50\ pA$ over a bonded H atom). All images are $50 \times 50\ nm^2$. **(d,e)** Constant-height STM images of arsenic: (d) positive bias ($z_{rel} = -200\ pm$ and $V = 300\ mV$) and (e) negative bias ($z_{rel} = -200\ pm$ and $V = -0.9\ V$). **(f,g)** Constant-current STM images of T2: (f) empty states ($V = 1.3\ V$, $I = 50\ pA$) and (g) filled states ($V = -1.8\ V$, $I = 50\ pA$). Images (d-g) are all $5 \times 5\ nm^2$. **(h-k)** Energy level diagrams for the defect types in their corresponding empty and filled states. (h) Dopant with modest to large positive biases can be either neutral or positive depending on the competing Γ_{T1-B} and Γ_{T-T1} rates. If positive, the bands are locally bent downward (bending depicted in blue *vs.* black curves). (i) Neutral dopant at modest negative bias. (j,k) Upward band bending due to negative T2 decreases the current in empty states (f,j), so that Γ_{T-B} in the presence of the defect (purple arrow and curve) is less than Γ_{T-B} in a defect-free region (black arrow and curve). The opposite occurs in filled states (g,k). **(l-n)** STM imaging of area containing arsenic and T2 ($10 \times 10\ nm^2$), (l) constant-height STM ($z_{rel} = -200\ pm$ and $V = 300\ mV$), (m) constant-current STM ($V = 1.3\ V$, $I = 50\ pA$), and (n) KPFM difference map compared to unperturbed surface (25×25 spectra grid, $z_{rel} = 0.0\ pm$, $V_{range} = -1.8 - 1.0\ V$). All scale bars are $5\ nm$.

Dangling Bond Point-Probe

A single DB was employed as a charge sensor. Figure 5.4(a-g) shows the progressive patterning [134,135,239] and erasure [136,137] of a single probe DB in the vicinity of an arsenic dopant. The lateral distance from the DB to the apparent center ranges from zero (directly on top of the arsenic dopant) to six surface lattice sites away, as indicated in Figure 5.4(h) (color-coded throughout frames (a-g) and the spectra in Figure 5.4(i)).

The $\Delta f(V)$ spectra for the different lattice positions are displayed in Figure 5.4(i), with the black curve being closest to the arsenic dopant and the dark orange farthest away. As mentioned earlier, the DB is capable of having three different charge states with two charge transition levels. A change of the DB's charge state is manifested as a single-electron-charge transition step [27,30,49,141] in the AFM

$\Delta f(V)$ spectroscopy, with the DB switching from negative (doubly occupied) for bias voltages to the right of the step in the spectra, to neutral for bias voltages on the left of the step (see Supporting Information, Figure 5.10). Over the distance of 2.3 *nm* that the DB was moved, the (0/-) charge transition step is seen to shift from (-0.44 ± 0.01) V to (-0.27 ± 0.01) V, with the bias at which the step occurs being more negative closer to the arsenic. This picture is once again consistent with a positive charge at the dopant atom bending the bands locally, requiring the application of a larger negative tip-sample bias to withdraw an electron from the DB. A KPFM map taken over the arsenic dopant displayed in Figure 5.4(h) is shown in Supporting Information, Figure 5.11.

This same kind of DB point-probe analysis was also performed for a T2, shown in the constant-current STM images of Figure 5.4(j-n), with the spacing ranging from 0 to 12 lattice sites over a 4.6 *nm* distance. Figure 5.4(o) marks the locations before the DB was added. Examining the $\Delta f(V)$ curves in Figure 5.4(p), a reversed trend for the shift is observed when compared to the positively charged arsenic. Now the charge transition of the DB is shifted to (0.21 ± 0.01) V for the nearest spectra (black curve) and (-0.20 ± 0.01) V for farthest (pink curve). This is indicative of a negatively charged species.

A final analysis was done by moving a probe DB away from a second DB, as shown in the AFM constant-height images of Figure 5.4(q-t), where it was moved 2, 3, 4, and 6 lattice sites away (1.9 *nm* distance total), respectively. In Ref. [49], we showed a related analysis using the charge transition states of DBs assembled in fixed arrangements. For large separations between the DBs, the distance-dependent shift of the probe DB's charge transition level clearly indicates the negative charge located at the static DB. Unlike the prior two charge species, the $\Delta f(V)$ curves in Figure 5.4(u) completely change behavior for small separations. The black curve in Figure 5.4(u) for the closest-spaced pair (two lattice sites) exhibits two charge transition steps. The reason for this behavior is the shared occupation for the created DB-DB pair [49]. The left step at (-0.24 ± 0.01) V corresponds to the case that only one electron is present in the pair (located at one of the DBs). Sweeping to less negative bias voltages, the second DB becomes charged, creating the second charge transition

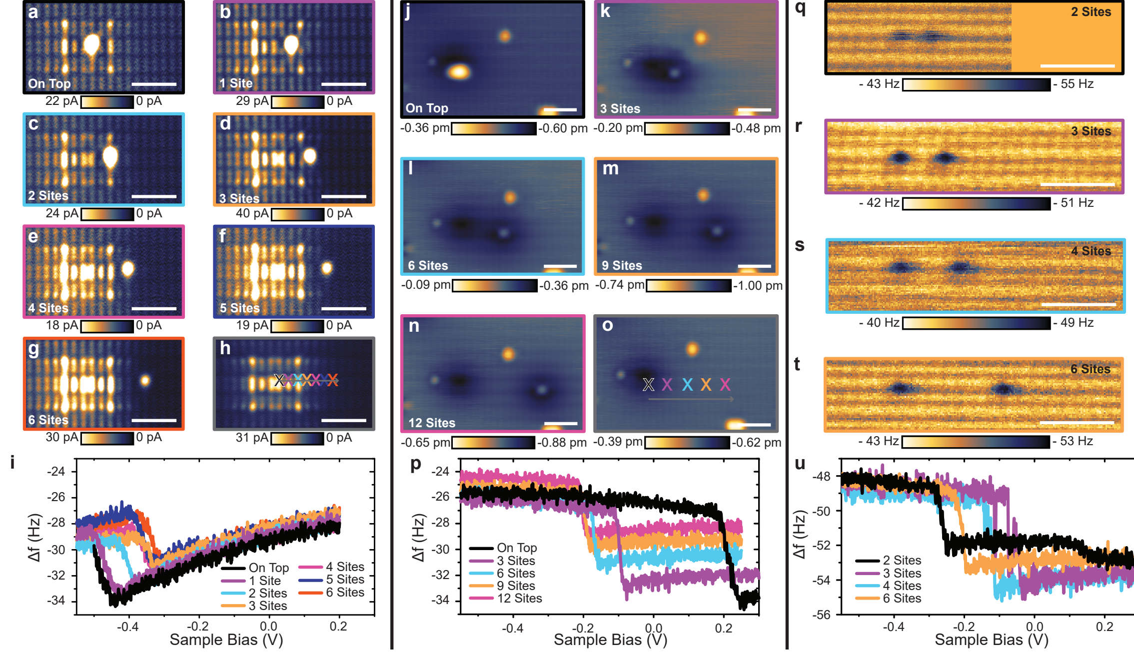

Figure 5.4: **Probing Charged Species with a Movable DB Point-Probe**. **(a-g)** Constant-height STM images of the DB being moved 0-6 lattice sites away from its initialization point, respectively, from a near-surface arsenic atom ($z_{rel} = -250\ pm$ and $V = 300\ mV$). **(h)** Constant-height STM image of the area before addition of a DB, with $\Delta f(V)$ locations marked ($z_{rel} = -200\ pm$ and $V = 250\ mV$). **(i)** $\Delta f(V)$ spectroscopy taken on top of the DB for each lattice spacing, color coded with the positions in (h), as well as with the frames in (a-g) ($z_{rel} = -350\ pm$). **(j-n)** Constant-current STM images ($V = 1.3\ V$, $I = 50\ pA$) of the DB being moved 0, 3, 6, 9, and 12 lattice sites away from its initialization point, respectively, from a T2. **(o)** Constant-current STM image marking the $\Delta f(V)$ locations. **(p)** $\Delta f(V)$ spectroscopy taken on top of the DB at the listed lattice spacing's ($z_{rel} = -300\ pm$). **(q-t)** Constant-height AFM images of a DB 2, 3, 4, and 6 lattice sites away from another DB $z_{rel} = -300\ pm$ and $V = 0\ V$). **(u)** $\Delta f(V)$ spectroscopy taken on top of the left DB at the listed lattice spacing's ($z_{rel} = -300\ pm$). All scale bars are 2 nm.

step at $(-0.03 \pm 0.01)\ V$. With increasing distance within the pair, the two DBs act independently and individual single charge transitions are observed that are mutually at less negative values (purple curve in Figure 5.4(u)). As the DBs are positioned progressively farther apart with four (blue curve) and six (orange curve) lattice sites between them, respectively, their mutual shifting effect on each other lessens and the charge transition approaches that of an isolated DB again.

Fitting Shifts of the Dangling Bond Probe

The values of the electrostatic shifts of the (0/-) charge transition voltage of the probe DB were extracted for the arsenic, the T2, and the DB interactions (see Supporting Information, Figure 5.12 for corresponding I(V) curves for Figure 5.4(i,p,u) with vertical color-coded lines marking the extracted charge transition shifts). Each shift was corrected for TIBB [127, 130, 131] (see “Tip-Induced Band Bending” in Methods Section 5.1.5), plotted as a function of distance in Figure 5.5 and fit with a linearized form of the screened Coulomb energy equation (5.3):

$$ln(U(r)r) = ln(\frac{e^2}{4\pi\epsilon_0\epsilon}) - \frac{r}{L_{TF}} \tag{5.4}$$

where e is the elementary charge, ϵ the effective dielectric constant, r is the distance between the DB and the localized charge, and L_{TF} is the Thomas-Fermi screening length (see “Fitting” in Methods Section 5.1.5 for details). The DB-DB shifts (orange) are in the same height plane, but the near-surface charges also have a depth component that can be extracted as well $r = \sqrt{(lateral\ distance)^2 + (depth)^2}$.

Other work has been able to estimate these parameters from fitting the spatially resolved spectral shift of the conduction band edge to a dielectric screened Coulomb potential [38, 127] as well as through comparison to simulated STM images created using a tight-binding framework [245]. When compared to the tight-binding framework [245], the method employed here has the advantage of being more general in that *a priori* knowledge of the identity of the defect is not needed to extract the information, nor is atomistic modeling. Our method has parallels to STM fitting of the shift in the conduction band edge [38, 127] but can access bias regimes inaccessible

to STM.

The extracted values using our method are summarized in the table in Figure 5.5. In our fitting procedure, depth has no associated error as it was incremented in the fit code with ϵ and L_{TF} being fit as free parameters (see "Fitting" in Methods Section 5.1.5). Two points extracted from a fourth experiment involving a negative physisorbed hydrogen atom (discussed in the Supporting Information Section 5.1.7) are displayed in purple, but were not fitted due to an insufficient number of data points.

Both near-surface defect types reveal dielectric constants close to the established value for bulk silicon (11.7), whereas the dielectric constant determined from the DB-DB case is closer to the expected average for the silicon/vacuum interface of 6.35 [38]. The screening length varies by several nanometers among the experiments presented here. These variations do not seem to be specific to the types of species, with the screening length extracted in a similar DB experiment in Ref. [49] being 5 nm, compared to (1.8 ± 0.1) nm here. These variations further emphasize that the carrier density is not uniform across the sample surface, highlighting the need for local characterization of the electrostatic environment.

Screening for Homogeneous Areas

For atomic devices fabricated on the surface, having a homogeneous electrostatic environment with predictable DB charge transition energies is vital to ensure consistent device operation. It has been established in this work that KPFM maps are capable of resolving small changes in the local electrostatic environment of H:Si. In Figure 5.6, this technique is used to prescreen an area for electrostatic homogeneity.

Figure 5.6(a) shows a STM image of an 8×8 nm^2 area of H:Si. A KPFM map taken of this area is displayed in Figure 5.6(b), and two areas with a similar contact potential difference value were selected (marked by the colored crosses). Figure 5.6(c) shows the area after the creation of the two DBs at the marked locations. The $\Delta f(V)$ curves taken over the DBs are shown in Figure 5.6(d), showing similar charge transition energies for both DBs.

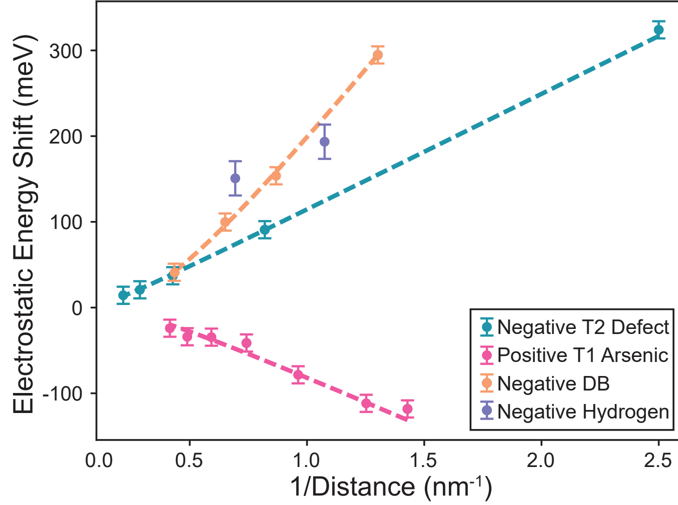

Charge Defect	Dielectric	Depth (nm)	L_{TF} (nm)
T1 Arsenic	9.7 ± 2.5	0.8	2.1 ± 0.7
T2	10.6 ± 0.5	0.4	5.9 ± 0.6
DB	4.1 ± 0.2	0.0	1.8 ± 0.1

Figure 5.5: **Fitting DB Charge Transition Shifts**. Shifts of the charge transition step for the probe DB as a function of distance from the T1+ (pink curve), T2- (blue curve), a second DB- (orange curve), and a physisorbed negative hydrogen (purple). TIBB was subtracted from the experimental data (see "Tip-Induced Band Bending" in Methods Section 5.1.5). Error bars correspond to the read-out error of the electrostatic energy shift, taken to be $\pm 10\ mV$ for T1, T2, and DB cases and $\pm 20\ mV$ for hydrogen. Dashed lines are an orthogonal distance regression fit of the data to the linearized form of the screened Coulomb equation. Errors of the dielectric constant and screening length correspond to the standard error (see "Fitting" in Methods Section 5.1.5).

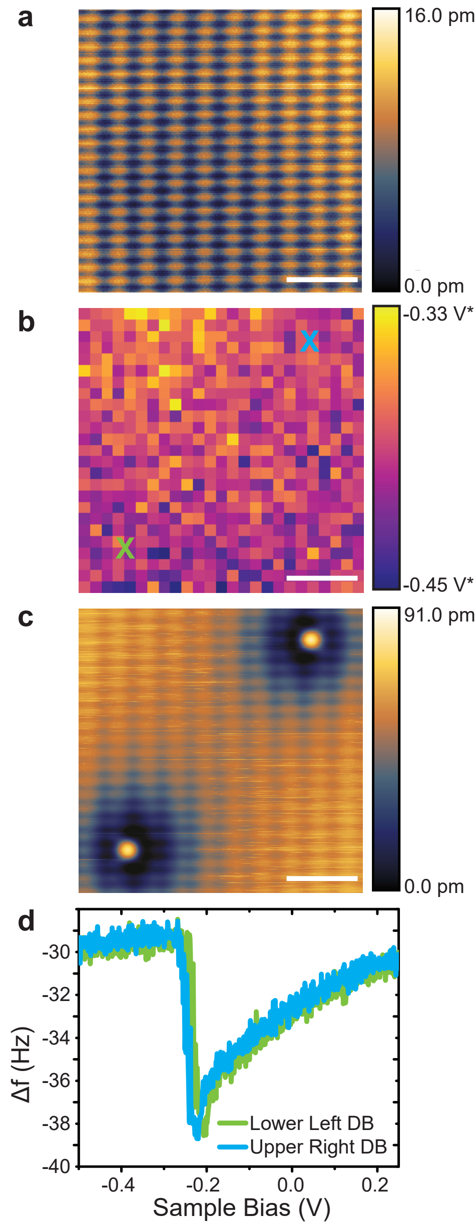

Figure 5.6: **Screening for a Uniform Electrostatic Background**. **(a)** Constant-current empty states ($V = 1.3\ V$, $I = 50\ pA$) STM image of a clean H:Si area. **(b)** KPFM grid taken of the same area. Two areas with similar contrast are marked with color coded X's for patterning of a DB (grid dimensions = 25 × 25 points, $z_{rel} = 0.0\ pm$, $V_{range} = -1.3 - 1.0\ V$). **(c)** Constant-current image once the two DBs were patterned at opposite corners. **(d)** $\Delta f(V)$ spectroscopy taken on top of the two DBs showing similar charge transition voltages ($z_{rel} = -350\ pm$). All scale bars are 2 nm.

Identity of the T2 Charge Feature

As mentioned earlier, the identity of T2s has been assigned inconclusively throughout the recent literature. Refs. [244] and [246] hypothesized them to be boron contamination due to their acceptor like behavior. Ref. [37] noted that this was unlikely because boron contamination at the concentrations reported is highly unlikely in commercial-grade wafers and instead proposed them to be negatively charged arsenic dopants. The corresponding two-electron state has been reported for both phosphorus [39, 249, 250] and arsenic donors [38, 251, 252], but that species is weakly bound with a binding energy only a few meV below the silicon conduction band edge for bulk donors. While this state exists at filled state biases and is observed as a peak in dI/dV spectroscopy [38], it cannot exist at large empty state biases [252] or elevated sample temperatures, as any electron potentially bound in that state would readily delocalize to the conduction band. Observations of T2 at room temperature as well as at empty state biases [247] are therefore inconsistent with the negative donor assignment.

We propose that the T2 features are more likely to originate from either negatively charged interstitial hydrogen atoms or a negative hydrogen-vacancy complex. We base our assignment on the sample fabrication process in a hydrogen-rich atmosphere and that the observed T2s are negatively charged. During preparation of the H:Si(100)-2 $\times$ 1 surface (see “Sample Preparation” in Methods Section 5.1.5), the silicon sample is rapidly heated to 1250° and then annealed at a temperature of 330°C for several minutes in an atmosphere of atomic hydrogen [117, 220]. The elevated temperature during our sample termination procedure is known to allow hydrogen atoms to readily enter the crystal [253–255], and secondary-ion mass spectrometry revealed that hydrogen is able to penetrate several microns into the silicon wafer, depending on parameters such as doping type, concentration, and growth method [253, 255]. In the very near surface region, the concentration of hydrogen atoms can be comparable [253, 255] to the doping level of the silicon crystal used in our present work [203, 220]. The hydrogen atoms can occupy various sites depending on their charge state [254]. They may be at defects [253–255], form complexes with

silicon [256–260] or with dopant atoms, or may reside interstitially [254].

The charge state of the suspected hydrogen atom or hydrogen-silicon complexes is determined by the Fermi-level of the bulk crystal, which in the present case is in a regime where such species would be negative [254, 256–258]. For hydrogen, the negative ions are reported to sit at the tetrahedral interstitial sites of the silicon lattice and exhibit a negative-U character [254], that is, the second bound electron is held more strongly than the first due to a repositioning of the hydrogen within the lattice after gaining a negative charge [254, 261]. Even lone hydrogen atoms that remain on the surface after the creation of a DB [136] can possess a negative charge. The Supporting Information in Section 5.1.7 shows how DBs are affected by the negative charge of a nearby hydrogen atom. While a direct comparison between the two forms, on-surface *vs.* bulk-trapped hydrogen, is impossible to be drawn due to the different local environments, the resemblance of their effect on DBs is striking. To determine conclusively whether the bulk-bound negative species are lone hydrogen atoms or a hydrogen-vacancy complex will require extensive high-level atomistic modeling of the various candidates. However, the stability of the negative charge state of hydrogen atoms and the abundance of hydrogen in the near surface region are strong indications for our proposal that the T2 features involve hydrogen atoms.

5.1.4 Conclusions

In this work, we used KPFM mapping to show surface electrostatic variation on a nm length scale caused by two oppositely charged near-surface species. We then went on to explore three charged species on the H:Si(100)-2 $\times$ 1 surface. In agreement with the literature, we assigned the T1 species to positively charged arsenic donors. The T2 species were shown to be conclusively negative in character, and we proposed that they may be negatively charged hydrogen atoms or negative hydrogen-vacancy complexes formed during sample preparation.

The quantum dot probe, reminiscent of scanning quantum dot microscopy, was realized through the sequential patterning and capping of a “moveable” DB. We showed that a charged species was able to shift the charge transition voltage of the

sensitive quantum dot probe DB with the expected reciprocal relation to absolute distance. Through analysis and fitting of the observed shifts of the charge transition levels in the on-surface DB point-probe, we were able to determine the dielectric constant, the screening length, and experimentally determine the depth of the species. The DB-DB analysis also allowed extraction of an experimentally determined distance where the DB pair occupation changes, confirming less direct measures and with important implications for DB-based device applications [19, 45, 49, 121].

Our approach of placing the single atom quantum dot directly on the surface of interest provides the highest spatial resolution of lateral potential variations as measured by scanning quantum dot microscopy to date. Direct comparison of our observations with complementary KPFM maps highlights the impact that charged species have on the electrostatic landscape of a surface. The various species studied and their different electrostatic impact over several nanometers underlines the necessity to carefully select areas for atom-scale device applications.

5.1.5 Methods

Measurement System Setup

Experiments were performed in a commercial ScientaOmicron qPlus AFM [73, 74] system operating at 4.5 K. Nanonis scanning probe control electronics and software (Specs) were used to acquire both the STM and AFM data. The recommended setup by ScientaOmicron where the tip is grounded and bias applied to the sample was employed to reduce crosstalk [78] between the Δf deflection signal and tunneling current signal (see the "Tip Preparation" section here in Methods for additional crosstalk reduction measures). For all constant-height images, $z_{rel} = 0$ pm corresponds to the relative tip elevation defined by the STM set points of $I = 50$ pA and $V = -1.8$ V on top of a bonded H atom. The tuning fork had a resonance frequency of 28.2 kHz, with a quality factor of $\sim 17,000$. An oscillation amplitude of 50 pm was used to aquire all presented AFM data. To minimize drift during the KPFM maps, the tip was left to settle for a minimum of 12 h before starting a map.

Sample Preparation

Highly arsenic-doped ($\sim 1.5 \times 10^{19}$ $atom\ cm^{-3}$) Si(100) was used. Overnight degassing in ultrahigh vacuum (UHV) was done at $\sim$ 600°C for 12 h to prepare the sample for flashing. Once degassed, a series of resistive flash anneals to 1250°C to remove oxide were done [117, 203, 220]. The series of resistive flash anneals has been shown to reduce surface dopant density, creating a region depleted of dopants ~ 70 nm below the sample surface with a donor concentration $\sim 10^{19}$ $atom\ cm^{-3}$ [203, 220]. The final step to terminate with hydrogen was done by holding the Si substrate at $\sim$ 330°C for 2 min, while molecular hydrogen (pressure $= 10^{-6}$ $Torr$) was cracked with a 1600°C tungsten filament [203, 220].

Tip Preparation

qPlus-style quartz tuning fork AFM sensors were used for all experiments [73, 74]. Once in UHV, tips were prepared by field evaporating the apex clean in a field ion microscope (FIM) [82]. Specifically, we use the third-generation Giessibl tuning forks with separate integrated tip-current electrode to reduce crosstalk between the AFM and STM signals [73]. The tip was then sharpened by a FIM nitrogen etching process [82]. Final *in situ* conditioning consisted of controlled contacts on patches of desorbed silicon [93].

Creating and Erasing Dangling Bonds

To create a DB, a sharp tip is positioned over the target atom at 1.3 V and 50 pA, and pulses of $2.0 - 2.5$ V for 10 ms are applied until the hydrogen is removed [134, 135, 200, 239]. Sometimes the removed hydrogen atom functionalizes the tip apex. A hydrogen atom terminated tip is immediately made obvious by enhanced topographic corrugations [134, 136]. Such a tip can then be used to erase a DB [136, 137]. This is done by bringing the functionalized tip at 0 V mechanically toward the DB to induce formation of a H:Si covalent bond and passivation of the DB [134, 136, 137].

KPFM Maps

The tip is left to settle overnight to minimize piezo creep during the experiment. Nanonis software supports a grid experiment feature, which is used to automate the acquisition of a $\Delta f(V)$ curve for every point in a defined grid. The presented map in Figure 5.3(n) took ∼2 h to acquire. Python code was used to fit a parabolic curve of the form $y = Ax^2 + Bx + C$ to each $\Delta f(V)$ and extract the maximum (V^*) of the fit parabola [124, 141]. An example of the fit for a single point in Figure 5.3(n) is shown in Supporting Information, Figure 5.9. These V^* maxima are extracted for every curve and then plotted as a KPFM map. Taking KPFM maps directly over DBs using the same voltage range as used for probing near-surface charges was avoided to prevent damage to the tip as a result of high tunneling current. KPFM maps can be taken over DBs but using more modest ranges or conservative heights. An example of a KPFM curve over a DB with parabolas fit to the negative and neutral charge states is shown in Supporting Information, Figure 5.10.

Tip-Induced Band Bending

During scanning probe imaging, a contact potential difference (CPD) exists between the tip and sample due to their different work functions. For the tungsten tip, the work function is estimated to be 4.5 eV, while for the n-doped silicon sample with a dopant depleted layer, concentration of $\sim 10^{18}$ $atom\ cm^{-3}$ (at low temperature) is estimated at 4.1 eV. This difference creates tip-induced band bending (TIBB) locally under the tip apex that can shift the charge transition levels of the DBs. While the contact potential difference is approximately constant, the TIBB predictably changes with varied tip-sample separation and applied bias. This has implications for the energy levels extracted in Supporting Information, Figure 5.12 from the $\Delta f(V)$ spectra. The energy level shifts extracted should have the TIBB factored in to give a band-bending free picture of the true shifts. The TIBB was calculated using a three-dimensional finite-element Poisson equation solver [49, 131]. For the calculation, a work function difference between tip and sample of 0.4 eV was assumed, a tip radius of 10 nm, a tip-sample height of $z_{rel} = -300\ or\ -350\ pm$ (see figure captions), and

a donor concentration of 10^{18} $atom\ cm^{-3}$ at the surface, monotonically increasing to 2×10^{19} $atom\ cm^{-3}$ in the bulk over a range of approximately 100 nm.

Fitting

The screened Coulomb eq (eq 5.5) was fit to the experimental data in a linearized form (eq 5.4, in the "Fitting Shifts of the Dangling Bond Probe" section) with an orthogonal distance regression method:

$$U(r) = \frac{e^2}{4\pi\epsilon_0\epsilon r} e^{\frac{-r}{L_{TF}}} \tag{5.5}$$

In the DB-DB experiment, the two free parameters of ϵ and L_{TF} were fit independently, and the estimated experimental read-out error ($\pm 10\ mV$) was factored in by using an orthogonal distance regression python algorithm. For the subsurface arsenic and T2, depth was incremented in steps of 0.1 nm from zero to an assumed maximum detectable depth of 5 nm [245]. For every depth increment, ϵ, L_{TF}, and the associated standard error for the two parameters were extracted. The values of depth, ϵ, and L_{TF} presented correspond to the parameters that minimized the combined standard errors.

5.1.6 Acknowledgments

We thank M. Cloutier and M. Salomons for their technical expertise. We thank W. Vine for helpful comments and critiques of the manuscript. We thank NRC-NRC, NSERC, QSi, Compute Canada, and Alberta Innovates for their financial support.

5.1.7 Supplementary Information: Electrostatic Landscape of a H-Silicon Surface Probed by a Moveable Quantum Dot

Negative Hydrogen

We show that a lone hydrogen on the H:Si(100)-2 $\times$ 1 surface is negatively charged. A hydrogen atom released by creating a DB sometimes appears to sit at metastable interstitial surface site and induces a lattice distortion of the adjacent dimer pairs as reported in Ref. [136] and shown again in Figure 5.13. Figure 5.14(a) shows a STM image of a DB pair with a physisorbed hydrogen in the upper left that landed near the pair after the tip was used to create the top DB. Figure 5.14(b,c) are nc-AFM Δf maps of the same area while the physisorbed hydrogen is present (dashed white circle), taken at two different heights. In both nc-AFM images, the top DB displays a less negative Δf shift than the lower one. Work done on DB pairs in another work [49] showed that a negative charge perturbation biasing a pair of DBs showed the same behavior; the one closer to the negative perturbative charge shows up with a less negative Δf shift. This biasing is confirmed by removing the physisorbed hydrogen. Figure 5.14(d) shows the STM image after removal, with Figure 5.14(e,f) being the nc-AFM images at the same two selected heights now showing the two DBs equal in Δf shift. $\Delta f(V)$ spectroscopy taken over the pairs before and after hydrogen removal are shown in Figure 5.14(g). In the presence of the hydrogen, the curves taken above the two DBs (dark and light purple curves) show a shift of the spectra. Two interesting features become apparent. First, the (0/-) charge transition step (marked by the vertical dashed lines), are offset for the two curves due to the slightly different distance from the negative hydrogen. Second, a small secondary dip or step is apparent at $-0.36 \pm 0.02\ V$ for both curves. This step has been reported to be the (+/0) charge transition level of the DB [201], which due to the perturbation of the hydrogen becomes accessible in the voltage range being probed. After hydrogen removal (orange and pink curves), the (0/-) transition steps return to more negative values and are no longer offset from each other. A common point was identified for

both before and after curves (vertical dashed lines). Using these points, analysis of the DB energy shift as a function of distance from the hydrogen was performed and plotted in Figure 5.5 of the main text as the two purple points.

We note here that unlike the $\Delta f(V)$ spectroscopy presented in the main text, these curves do not have a clean step for the charge transition. To obtain a measurable signal the spectroscopy was taken at a height of $z_{rel} = -350\ pm$, which can distort the shape of the curves due to non-linear interactions with the surface (See Supporting Information, Figure 5.15). Additionally, it is known that hydrogen's from a desorption event sit on a metastable surface site and can easily be moved with the field of a scanning tip [136]. The small tip-sample separation and the mechanical instability of the loosely-bound hydrogen atom as the bias is swept for the $\Delta f(V)$ spectroscopy account for the noisy appearance of the curves. A set of $\Delta f(V)$ curves taken at a larger tip-sample separation over the two DBs without the hydrogen present (blue curves) show a more typical charge transition step. With these technical limitations in mind, the extracted shifts from this experiment displayed in Figure 5.5 of the main text for the hydrogen-induced shifts are not as quantitatively rigorous as the other DB-probe experiments. However, the electrostatic energy shift is of a similar order of magnitude and of the same sign as a negative species. We fully acknowledge that while this evidence is compelling toward our assignment of the identity of the species T2, more work is required and we hope to stimulate further scientific discussion.

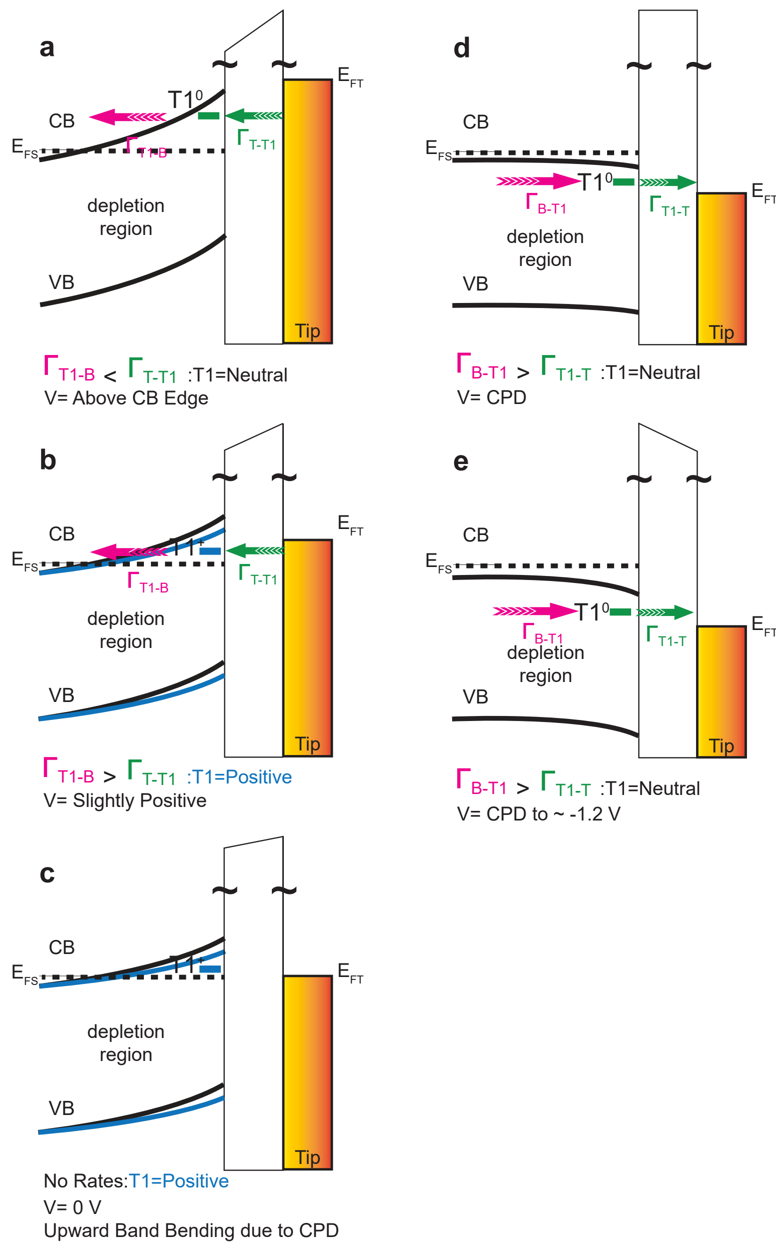

Figure 5.7: **Arsenic Dopant Energy Level Diagrams**. **(a-e)** Qualitative energy level diagrams of the arsenic dopant as it is swept through the voltage ranges listed underneath each panel. The dopant changes charge state depending on the tip-induced band bending conditions which tune the tunneling rates between tip and T1 (Γ_{T-T1}) and bulk and T1 (Γ_{B-T1}).

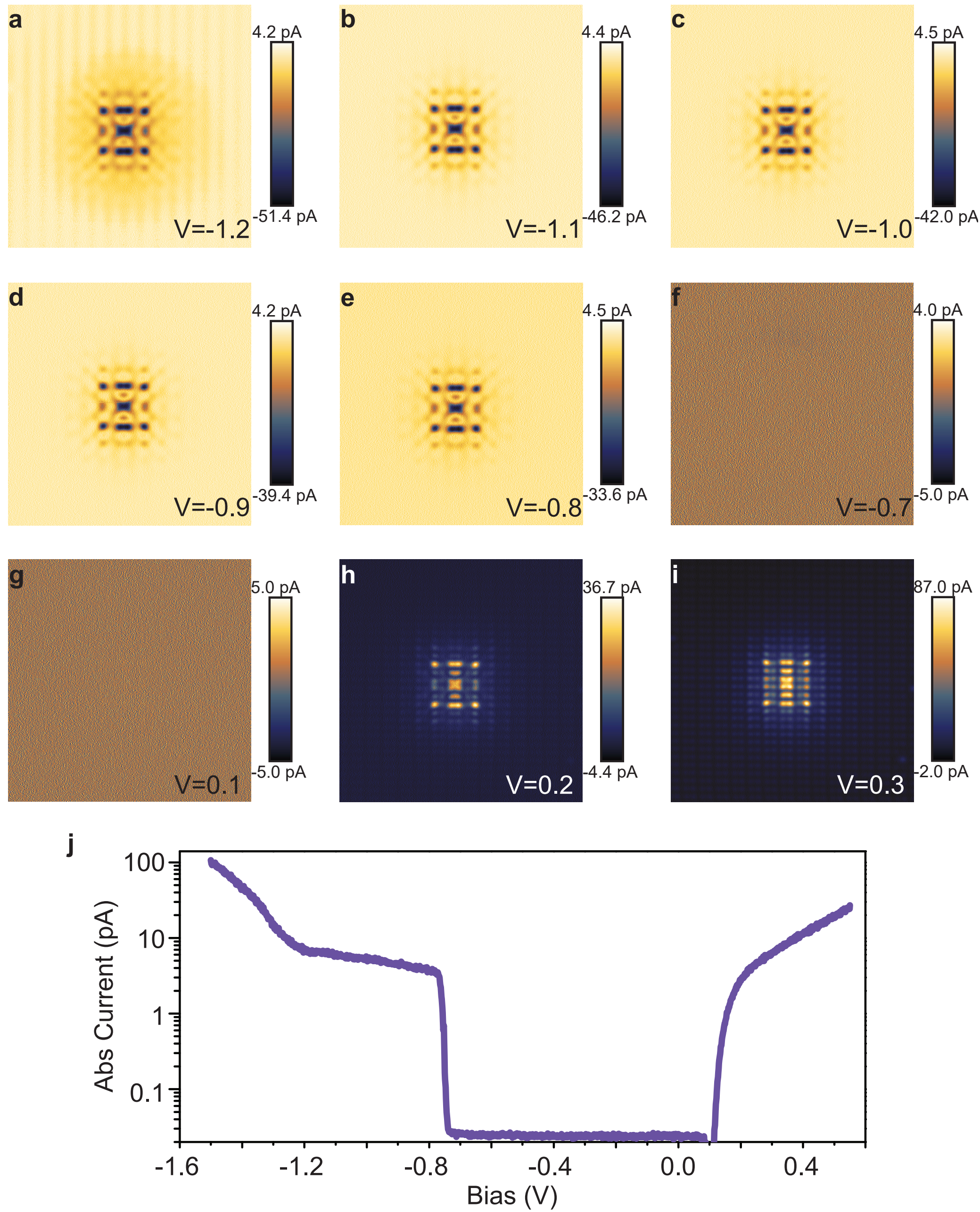

Figure 5.8: **Dopant at Different Biases**. **(a-i)** Constant-height STM images of the dopant from Figure 5.3(d,e) at additional bias's ($z_{rel} = -200\ pm$ and area$=$ $12 \times 12\ nm^2$). **(j)** $I(V)$ spectra taken above the center of the dopant at the same height as panels (a-i). The curve is plotted in log scale and absolute value, unlike (a-i). From the $I(V)$ curve, the bandgap runs from $\sim -0.7\ to\ 0.1\ V$, explaining the lack of features in panels (f,g).

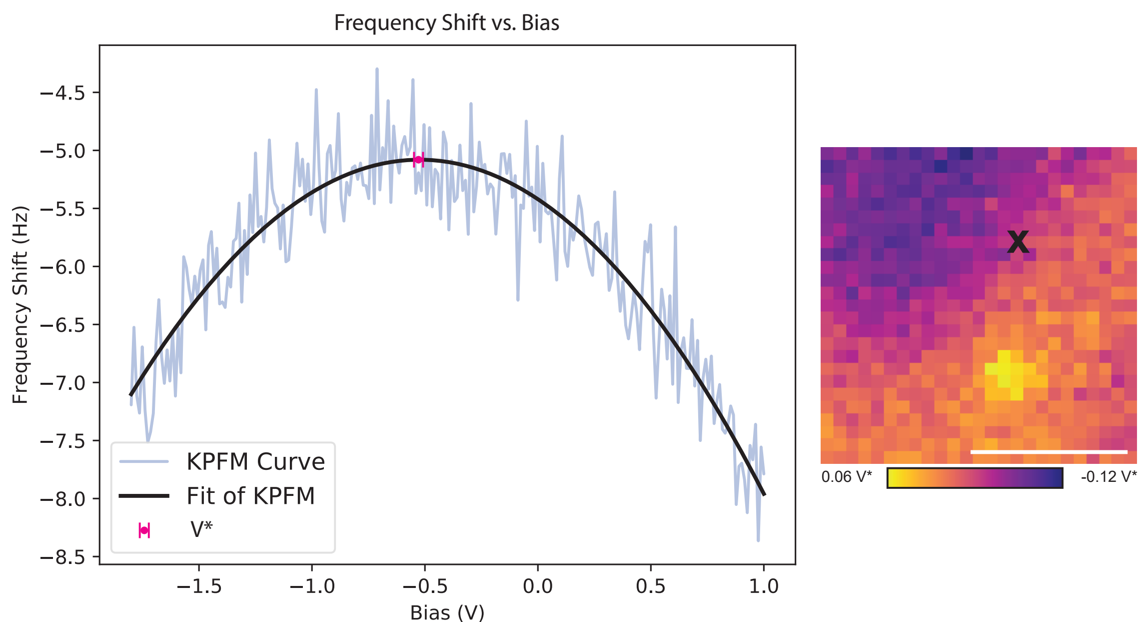

Figure 5.9: **Fitting a KPFM Curve**. Raw KPFM data from Figure 5.3(n) (reproduced on the right with location of spectroscopy marked with an X) fit with a parabolic function $z_{rel} = 0.0\ pm$, $V_{range} = -1.8\ to\ 1.0\ V$, and $Osc.\ Amp. = 50\ pm$). The maximum of the fit ($-0.53 \pm 0.02\ V$) is marked with the pink dot. Every point in a KPFM grid has this performed. The extracted maxima or V^*'s vary slightly for every point, generating a map of the electrostatic potential (*cf.* Figure 5.3(n)). The ± 0.02 on V^* represents the propagated uncertainty in the fit error.

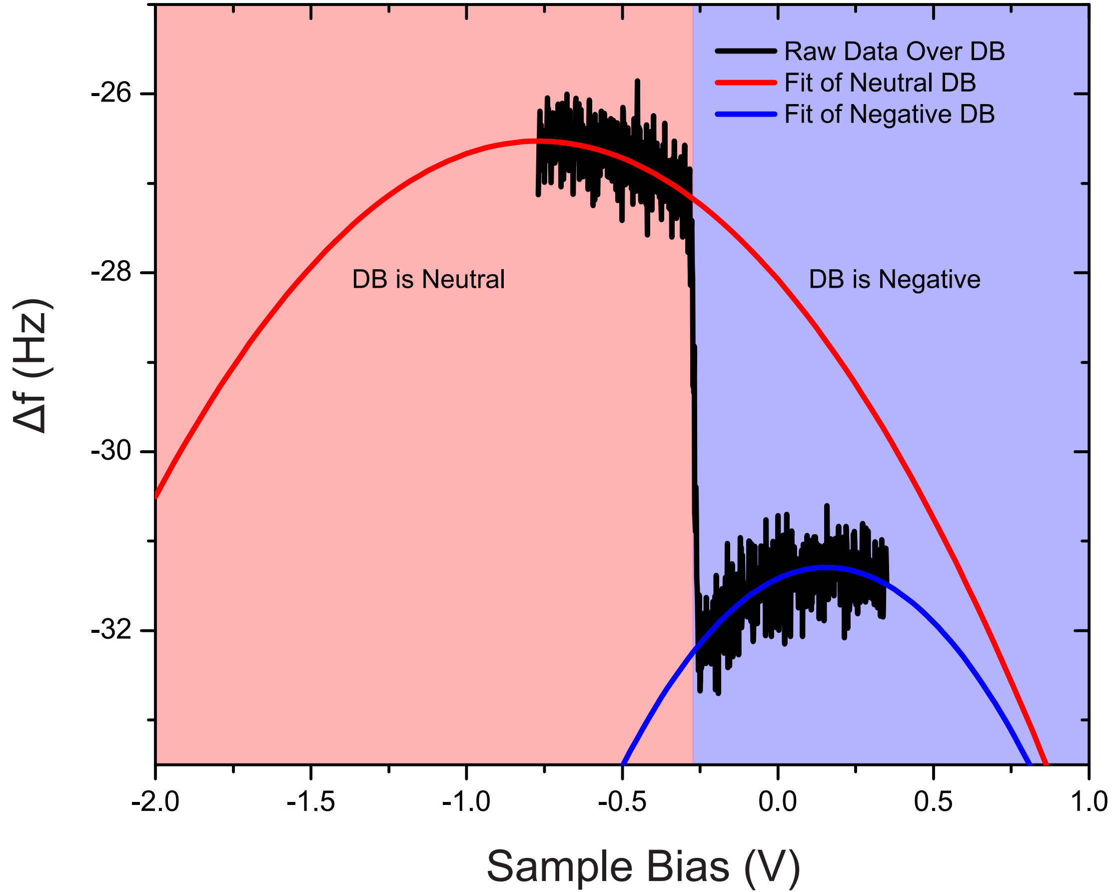

Figure 5.10: **Fitting a DB KPFM Curve**. Raw KPFM data (black curve) taken over a DB ($z_{rel} = -300\ pm$). For voltages in the red shaded area, the DB is neutral. For voltages in the blue shaded area, the DB is negative. The transition from neutral to negative, or the (0/-) charge transition step is seen at $V = -0.25 \pm 0.01\ V$. The parabolas were fit to both the neutral (red) and positive (blue) charge state of the DB. The LCPD could be extracted from the maximum value for each parabolic fit.

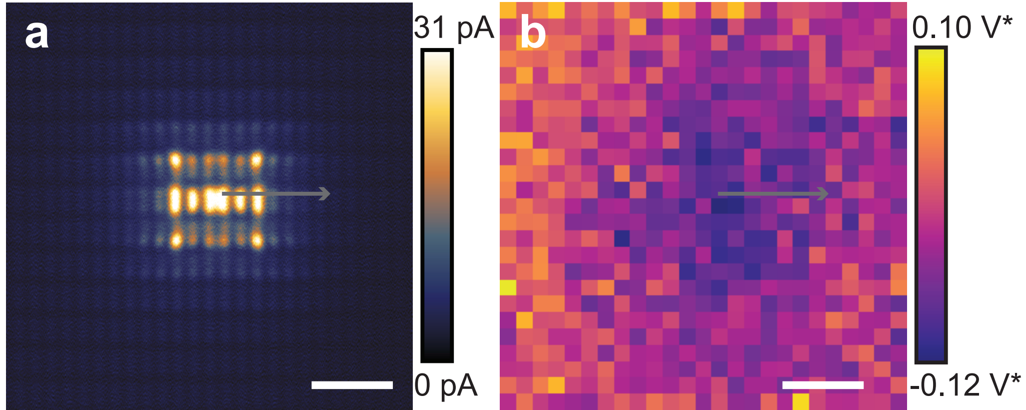

Figure 5.11: **KPFM Map of an Isolated Arsenic Dopant.**. **(a)** Larger area constant height frame of main text Figure 5.4(h). **(b)** KPFM map of the same area as (a) showing a local dark depression at the location of the dopant atom. (Grid Dimensions = 25 × 25 points, $z_{rel} = -200\ pm$, $V_{range} = -1.3\ to\ 600\ mV$). The contact potential difference of the surface background has been subtracted out from the map in (b).

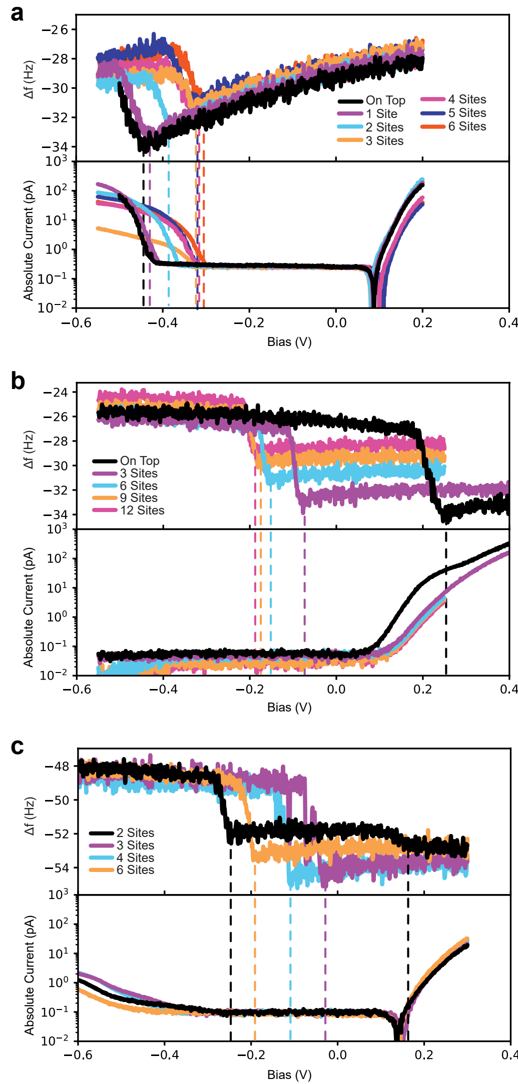

Figure 5.12: **I(V) and Extracted Shifts for $\Delta f(V)$ Spectroscopy**. **(a)** The $\Delta f(V)$ spectroscopy from main text Figure 5.4(i) for the DB-T1 case is reproduced in the top panel, with the simultaneously obtained I(V) spectrum at the bottom. As the DB probe is moved farther away, shifts also occur in the onset of the valence and conduction bands. **(b)** $\Delta f(V)$ spectroscopy from main text Figure 5.4(p) for the DB-T2 case, along with its $I(V)$ spectroscopy. **(c)** $\Delta f(V)$ spectroscopy from main text Figure 5.4(u) for the DB-DB case and its $I(V)$ spectroscopy. For all three cases their charge transition step onsets have been marked with a color-coded dashed line. These onsets were used as the common point of reference for extracting the electrostatic energy shifts plotted in Figure 5.5.

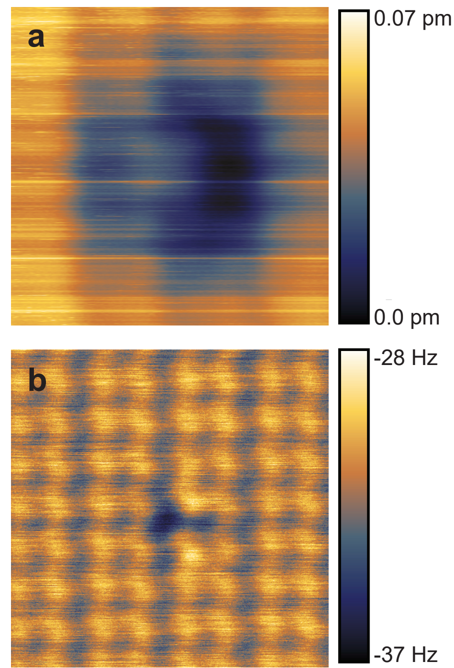

Figure 5.13: **Lattice Distortion from a Hydrogen Atom.**. **(a)** Constant-current empty states ($V = 1.3\ V$ and $I = 50\ pA$) STM image of a lone hydrogen atom on the H:Si surface. **(b)** Constant-height AFM image of the same area showing the hydrogen sits at an apparent surface hollow, distorting the upper hydrogen layer ($z_{rel} = -360\ pm$, $V = 0\ V$, and $Osc.\ Amp = 50\ pm$). Both images are $3 \times 3\ nm^2$.

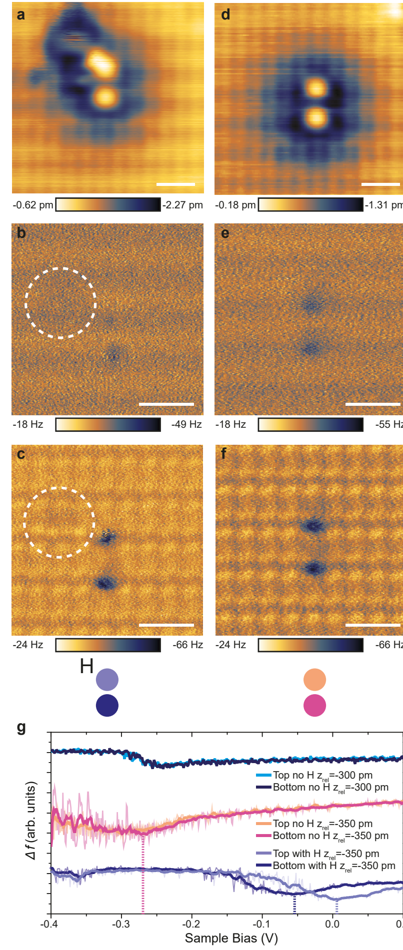

Figure 5.14: **Negative Hydrogen Atom Perturbing a Pair**. **(a)** Constant-current empty states ($V = 1.3\ V$ and $I = 50\ pA$) STM image of a DB pair with a physisorbed lone hydrogen visible in the upper left. Constant-height AFM images were taken at **(b)** $z_{rel} = -300\ pm$ and **(c)** $z_{rel} = -350\ pm$, of the same perturbed pair showing the upper DB lighter in contrast than the lower ($V = 0\ V$, and $Osc.\ Amp = 50\ pm$). The location of the hydrogen atom is marked by the dashed white circles. **(d)** Constant-current empty states ($V = 1.3\ V$ and $I = 50\ pA$) STM image of the pair after removal of the hydrogen. The constant-height AFM images were repeated at the same heights of **(e)** $z_{rel} = -300\ pm$ **(f)** $z_{rel} = -350\ pm$ ($V = 0\ V$, and $Osc.\ Amp = 50\ pm$). **(g)** $\Delta f(V)$ spectroscopy taken on top of the DBs both with the hydrogen present and without. Filtered curves are overlaid on the raw data. Color-coded models are provided above the panel. ($z_{rel} = -350\ pm$ and $Osc.\ Amp = 50\ pm$). Vertical color-coded dashed lines mark a common point of reference. All scale bars in images are 1 nm.

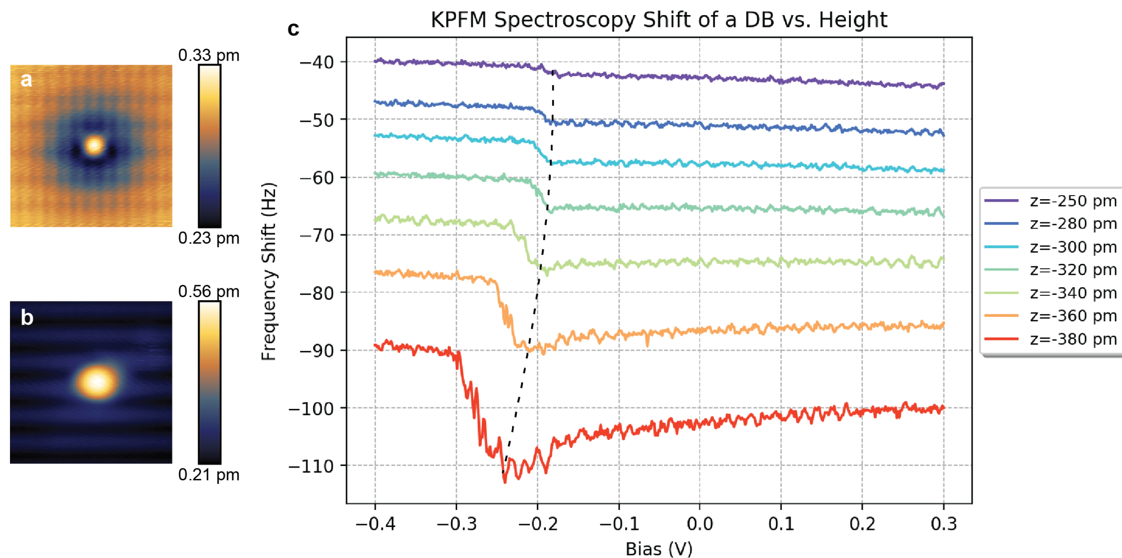

Figure 5.15: **KPFM Spectroscopy Shift with Height**. Constant-current **(a)** empty states ($V = 1.3\ V$ and $I = 50\ pA$) and **(b)** filled states ($V = -1.8\ V$ and $I = 50\ pA$) STM images of a lone DB. **(c)** KPFM spectroscopy performed over the same DB at different heights ($V_{range} = 0.3\ to\ -0.4\ V$ and $Osc.\ Amp = 50\ pm$), showing a shift of the neutral to negative charge transition level (0/-) as a function of height. Tip-induced band bending shifts the energetic position of the charge transition to more negative values with decreasing tip-sample separation. A black dashed line is provided as a guide to the eye.

5.2 Appendix: Not Published Additional Supplementary Results for Electrostatic Landscape of a H-Silicon Surface Probed by a Moveable Quantum Dot.

5.2.1 Spectroscopy over Arsenic Dopants

As discussed in the paper, an arsenic dopant is known to have three charge states: negative (D^-), neutral (D^0), and positive (D^+). In their respective studies of

dopants, both Voisin *et al.* [248] and Salfi *et al.* [38] found peaks in dI/dU spectroscopy that corresponded to these states, placing the dopant charge transition levels at $D(0/-) = -1.05\ V$ and the $D(+/0) = -0.77\ V$. Thus, it would be expected that two charge transition steps would be observed for the dopant atom at those values in $\Delta f(V)$ AFM probing, just as has been shown with DBs.

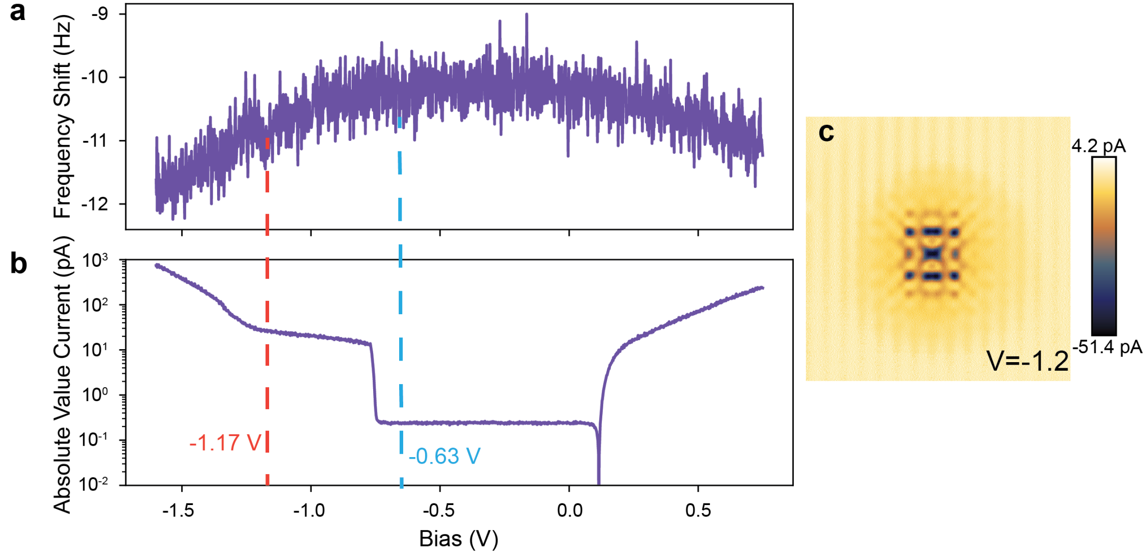

Figure 5.16: **Charge Transition Steps Over an Arsenic Dopant**. **(a)** $\Delta f(V)$ spectra taken over the center of an arsenic dopant (The same arsenic atom as in Figure 5.8 in Section 5.1). Two possible charge transition levels for the arsenic atom are marked with the vertical dashed orange and blue lines, potentially corresponding to the D(0/-) and D(0/+) levels ($z_{rel} = -150\ pm$ and $Osc.\ Amp. = 50\ pm$). **(b)** $I(V)$ spectra simultaneously acquired during the taking of the $\Delta f(V)$ in (a). Current is plotted in log scale and absolute value. **(c)** Constant-height STM image of the dopant at a similar bias ($V = -1.2\ V$) to the orange marked D(0/-) charge transition step. The arsenic atom displays a faint dark depression around its location, perhaps suggesting it is negatively charged ($z_{rel} = -200\ pm$, $V = -1.2\ V$, and $12.0 \times 12.0\ nm^2$). z_{rel} is referenced to a height defined by a STM tunneling current of $I = 50\ pA$ with $V = -1.8\ V$ applied, as taken over a surface hydrogen atom.

We present our best evidence toward observing these charge transitions in Figure 5.16(a). This was a $\Delta f(V)$ spectra taken directly over the dopant atom analyzed extensively as part of our paper (See Figure 5.8 in the Supplementary Information

of Section 5.1). This was not published as part of the manuscript because the size of the apparent steps in (a) in relation to our signal to noise ratio, we felt, did not meet the requirements for being academically rigorous. A better curve with more pronounced steps could not be obtained, despite $\Delta f(V)$ probing being attempted at different heights. In spite of this, if the curve in Figure 5.16(a) is examined closely near where the charge transitions for an arsenic atom are expected to be, two possible steps appear at $D(0/-) = -1.17\ V$ and $D(+/0) = -0.63\ V$, as marked with the orange and blue dashed lines, respectively. These values are in rough agreement with the above cited values from Voisin and Salfi [38, 248], adding some credibility to the experimental observations. As additional evidence, the constant-height STM image in (c) is taken at $V = -1.2\ V$, where the arsenic atom would be in a negative charge state. The STM image shows a faint dark depression surrounding the arsenic atom, which could be a Coulomb screening effect bending the bands locally around it.

There are several reasons why dopant charge transition steps could be absent or difficult to resolve. First, the arsenic charge transition states are possibly rate dependent. This could create a situation analogous to the one discussed for the DB(+/0) charge transition level earlier (See Section 4.2.4); if the arsenic atom's charge states are dependent on competing emptying and filling rates instead of a band-gap-insulated single-electron charge state change, the charge transition steps might appear as "dip-shaped", with the magnitudes of the competing rates determining how resolvable the dip is. The second reason they might not be easily resolvable is that the dopant atom is sub-surface. While a DB extends into vacuum as an sp^3 orbital allowing direct access for probing, a sub-surface arsenic atom's $\Delta f(V)$ signal is screened by the atomic layers above it. Better AFM sensors with a higher sensitivity or signal-to-noise ratio may have more success in measuring these charge state changes, necessitating future work to conclusively resolve this discussion.

5.2.2 Extracting Shifts

Fitting the DB(0/-) shifts to extract quantitative information about defect depth, dielectric constant, and screening length was a main result of the paper. To make this

technique more accessible, we now discuss details on how the raw shifts are extracted and TIBB processed, as well give details on how different TIBB subtractions can effect the final quantitative values obtained.

To extract values from the raw data, we use Supplementary Figure 5.12 (Section 5.1) as a case study. The location where the vertical color-coded dashed lines in all the panels intersect the x-axis are the extracted DB(0/-) shifts. The upturn of the charge transition step is chosen as our common reference instead of the middle, as this should be where the tip Fermi level first comes into resonance with the DB(0/-) level.

Once these values are obtained, they must be corrected for tip induced band bending (TIBB) to remove the influence of the tip on the system (See Section 2.4.1 for a review of TIBB). The spectroscopy for Figure 5.12(a) was taken at $z_{rel} = -350\ pm$, whereas the spectra in Figure 5.12(b,c) were taken at $z_{rel} = -300\ pm$. For both cases, height-dependent TIBB corrections were generated, with all other TIBB calculation inputs fixed as: donor concentration $= 10^{18} \frac{atoms}{cm^3}$ at the surface gradually increasing to $2 \times 10^{19} \frac{atoms}{cm^3}$ in the bulk over a range of 100 nm, work function = 0.4 eV, and tip radius = 10 nm. Slight variations on any of these parameters could effect the generated TIBB corrections, thus changing the extracted shifts and final fits. To motivate an intuitive understanding of how robust the fits are to minor TIBB variations, we explored the effect of how different reasonable tip radii alter the extracted values in Figure 5.17.

The generated TIBB corrections for each assumed tip radii were subtracted from the extracted DB(0/-) charge shifts discussed above, giving the estimated charge transition level shifts in the absence of a tip. These were then fit using the same methodology as in the paper, with the code used presented in Section 5.2.3. The 10 nm radius values match those given in the paper in Figure 5.5, but small variations can be seen for different tip radii. The extracted screening length L_{TF} seems relatively unvaried within this explored parameter space, but the calculated dielectric constant can vary by up to 15%. Similar variations on the extracted values would also be expected for TIBB corrections with a different work function or donor concentration, but these parameter spaces have not been explored yet and remain the

5 nm

Charge Defect	Dielectric ε	Depth (nm)	L_{TF} (nm)
T1 Arsenic	11.4 ± 2.5	0.7	2.6 ± 1.0
T2	10.2 ± 0.5	0.4	5.9 ± 0.6
DB	4.0 ± 0.2	0.0	1.8 ± 0.1

10 nm

Charge Defect	Dielectric ε	Depth (nm)	L_{TF} (nm)
T1 Arsenic	9.7 ± 2.5	0.8	2.1 ± 0.7
T2	10.6 ± 0.5	0.4	5.9 ± 0.6
DB	4.1 ± 0.2	0.0	1.8 ± 0.1

15 nm

Charge Defect	Dielectric ε	Depth (nm)	L_{TF} (nm)
T1 Arsenic	9.8 ± 2.5	0.8	2.1 ± 0.7
T2	10.8 ± 0.5	0.4	5.9 ± 0.6
DB	4.2 ± 0.2	0.0	1.8 ± 0.1

20 nm

Charge Defect	Dielectric ε	Depth (nm)	L_{TF} (nm)
T1 Arsenic	10.1 ± 2.5	0.8	2.1 ± 0.7
T2	11.0 ± 0.5	0.4	5.9 ± 0.6
DB	4.3 ± 0.2	0.0	1.8 ± 0.1

Figure 5.17: **Tip Radius Effect on TIBB and Final Extracted Parameters**. Fit-extracted values for the dielectric constant ϵ, defect depth, and screening length L_{TF}, after the application of different TIBB corrections generated for different tip radii. The TIBB corrections for a given radius were applied to the extracted DB(0/-) charge transition shifts from Figure 5.4(i,p,u) in the Electrostatic Probe paper (Section 5.1). The differently-TIBB-corrected shifts were then fit using the same code and methodology as given in both the paper and Section 5.2.3. The tip radii assumed are denoted above each table, with the extracted values from the fits below.

realm of future work.

One final thing that can be explored, however, is the importance of an attempt at TIBB corrections in general. In Figure 5.18 a comparison is made between TIBB corrected and non-TIBB corrected fits. Again, the screening length L_{TF} seem to be relatively invariant, however the dielectric constant ϵ has been reduced for all the charge defects in the case of no TIBB correction. Since our original extracted values already appeared to be underestimating the expected ones ($\epsilon = 11.7$ was expected for sub-surface defects and $\epsilon = 6.35$ for DB-DB interactions), reducing them further suggests a worse solution.

10 nm with TIBB Correction

Charge Defect	Dielectric ε	Depth (nm)	L_{TF} (nm)
T1 Arsenic	9.7 ± 2.5	0.8	2.1 ± 0.7
T2	10.6 ± 0.5	0.4	5.9 ± 0.6
DB	4.1 ± 0.2	0.0	1.8 ± 0.1

10 nm No TIBB Correction

Charge Defect	Dielectric ε	Depth (nm)	L_{TF} (nm)
T1 Arsenic	8.2 ± 1.8	0.7	2.6 ± 1.0
T2	7.5 ± 0.4	0.4	5.9 ± 0.6
DB	2.9 ± 0.1	0.0	1.8 ± 0.1

Figure 5.18: **Fit Effects for TIBB vs. No TIBB Correction**. Fits on the extracted DB(0/-) charge transition shifts from Figure 5.4(i,p,u) from the Electrostatic Probe paper (Section 5.1) performed with and without a TIBB correction applied.

In summary, this section attempted to motivate the importance of subtracting the perturbing effect of the tip from the acquired shift data and how the applied TIBB corrections effected the extracted parameters. While not a rigorous study, the fit values can be seen to shift by small amounts. More detailed work on these fits exploring a larger parameter space of variation, perhaps combined with statistics on more experimental data-sets, could refine the robustness of this methodology.

5.2.3 The Fitting Code

Here the source code for fits of the DB(0/-) charge transition levels when the DB is used as a point probe is presented. The Python code consists of three modules. The main module “MoveableProbeCode.py” imports the other two modules: “Skip-

Headerand1D.py" and "CoulombFits.py". "SkipHeaderand1D.py" reads in the shift data from the TIBB corrected .txt files as one dimensional arrays, and "CoulombFits.py" contains the definitions for the fit functions. While the code is commented to guide a user, we give a quick synopsis of the functionality here.

For each moving probe experiment the data should be put in a .txt source file. This file should contain the distances the probe DB was placed at when referenced to the the center of the charge defect (meters), the extracted TIBB-corrected DB(0/-) shifts when referenced to an unperturbed DB (milliVolts), and the estimated experimental read-out error for every measurement (milliVolts). Our estimates for readout error were calculated by sampling the onset of a charge transition shift many times, and looking at the variation observed in the sampling.

During a code run from the main module the raw data files are read in, passed to their own one dimensional arrays, and then forwarded to a fit with or without depth factored in (DB-DB experiments would be in the same height plane, sub-surface defects would have depth).

Starting with DB-DB interactions with no depth component, these are passed to an orthogonal distance regression fit of the linearized Coulomb equation (Equation 5.3) with dielectric constant and screening length the free parameters. Orthogonal distance regression was chosen as the fit algorithm because of its ability to factor in experimental error to the final outputted standard fit error easily. Orthogonal distance regression does require guess values for the free parameters to ensure convergence of the fit, with appropriate locations for these guess values marked in the code. The fit is performed on the data and the extracted parameters and error for the DB-DB experiment displayed in the terminal output.

For defects with a depth component, a similar methodology is applied as done for the DB-DB fitting except now the fit is tried for different user-iterated depths. In other words, depth is iterated and the fit is still performed on only two free parameters. This methodology was chosen instead of fitting on three free parameters to help with error minimization. It was found that fitting on three free parameters was either giving large error, unrealistic depths, or not converging at all. It is estimated that the maximum depth STM can see sub-surface charge defects is around

36 mono-layers [245], so the code iterates down to this reasonable maximum depth. Plots are generated for each depth, showing the best linear fit obtainable by the code. The fit with the smallest combined error (the sum of the error in both the free parameters) is selected and displayed along with its numerical values. As there might be more than one local minima for combined error, contour plots are also generated to easily visualize the error topography. Finally, the misfit of all three data types are calculated as a rough estimate of the goodness of fit. While this is not statistically rigorous due to the low sampling of points from the difficult nature of the experimental test, when combined with the individually generated plots showing the fit, it does give a rough measure on if a fit needs closer inspection.

File Read in Module: SkipHeaderand1D.py

```
"""
This Code has two definitions:
skipheader: Finds a particular keyword that precludes the data
                                your interested in. It returns the
                                 line number where this occurs.
create1Darraysofrafile: Once you know where the header is, it
                                reads in the header titles and
                                creates 1D arrays of the info so
                                it is easy to plot and process.
                                Returns these.
@author: Taleana
"""
import numpy as np

####DEFINITIONS####
def skipheader(keyword4skip,filedirec,filenumber): #finds out
                                where the data starts for output
                                file and skips the header
lookup = keyword4skip #Every header is pre-cluded by some keyword.
                                 Most often [DATA] in Nanonis.
                                looks for the the row number this
                                occurs at.
```

```
with open(filedirec+filenumber) as myFile:
for num, line in enumerate(myFile, 1):
if lookup in line:
headerskip=num+1 #want it to skip one line past [DATA] since the
                                    header is one line past it. No
                                    text. Only floats.
return headerskip #return appropriate row number


def create1Darraysforafile(headerskipnumber,filedirec,filenumber):
                                    #reads a Nanonis data file in and
                                    puts columns into 1D arrays

###READ IN NUMERICAL DATA###
data=np.loadtxt(filedirec+filenumber,skiprows=headerskipnumber,
                                    dtype=float) #read in the file
                                    using numpy's loadtxt. Auto skips
                                    header now and basically reads it
                                    into a giant array.Not great for
                                    large datasets but fine for ours.

###READ IN THE HEADER###
with open(filedirec+filenumber) as myFile:
for i, line in enumerate(myFile):
if i == headerskipnumber-1:
datatitles=line
datatitles=datatitles.split('\t') #split from a single string into
                                    a 1D array anywhere there is a
                                    tab
#print (datatitles)
upper=len(datatitles)

for i in range(0,upper):
datatitles[i]=data[0:,i]

return datatitles
```

Coulomb Fit Equation Module: CoulombFits.py

```
"""
This module contains definitions for the fitting of experimentally
                                obtained quantum dot probe data
                                with screened coulomb potentials.
Created on Tue Apr 16 14:42:20 2019
@author: Taleana
"""
import numpy as np
import scipy.constants as sp

###CONSTANTS###
convert=sp.e*(1/sp.electron_volt)/1e-3 #You multiply by elemcharge
                                again because you want to make it
                                an energy. 1 electron through 1V
                                =Joules. Then convert from Joules
                                to meV for plotting convenience.

def RMS_Error(observed,predicted,error,numberofpoints):
RMS=np.sqrt((1./numberofpoints)*sum(((observed-predicted)/error)**
                                2))
return RMS

def Screen_Coul_nodepth(B,r): #B is the fit array. If you have two
                                unknowns, it will be B[0], B[1].
                                If you have n things your a
                                fitting on, then B[0],B[1],B[2]...
                                B[n]
U=((sp.e/(4.0*sp.pi*sp.epsilon_0*B[0]*r))*np.exp(-r/B[1]))*convert
return U


def Screen_Coul_plot(b1,b3,r): #Screened Coulomb equation for
                                plotting.
U=((sp.e/(4.0*sp.pi*sp.epsilon_0*b1*r))*np.exp(-r/b3))*convert
return U
```

```
def Screen_Coul_depth(B,r): #Screened Coulomb Equation with depth
                                as an additional free parameter
U2=(sp.e/(4.0*sp.pi*sp.epsilon_0*B[0]*np.sqrt(r**2.0 +B[1]**2.0))*
                                np.exp(-np.sqrt(r**2.0 +B[1]**2.0)
                                /B[2]))*convert
return U2

def TrueR(depth, horzdist): #Actual distance of the defect is not
                                the horizontal distance or the
                                depth. Pythorean theorem those
                                values for the final plot of true
                                distance
r=np.sqrt(horzdist**2 +depth**2)
return r

def Screen_Coul_Log(B, r): #Linearized logarithmic form of the
                                screened Coulomb equation
lnUr = np.log(sp.e**2 /(4.*sp.pi* sp.epsilon_0 * B[0])) - r / B[1]
return lnUr

def Screen_Coul_Log_3f(B,horzdist): #Linearized logarithmic form
                                of the screened Coulomb equation
lnUr = np.log(sp.e**2 /(4.*sp.pi* sp.epsilon_0 * B[0])) - (np.sqrt
                                (horzdist**2 +B[2]**2) / B[1])-np.
                                log(np.sqrt(horzdist**2 +B[2]**2))
```

Moveable Probe Code: MoveableProbeCode.py

```
'''
'Fit A screened coulomb equation to electrostatic energy shifts
                                from a moving DB probe experiment.
                                 Use's a sum of squares Orthogonal
                                 Distance Regression
to fit on the free parameters. The DB-DB exeriment has no depth
                                component and has two free
```

```
                                    parameters. Any DB-Subsurface
                                    experiment will have an extra free
                                     one (3 total). For the three
                                    parameter fits
assume a depth of the sub-surface defect and fit the experimental
                                    U vs r for the other two. Do that
                                    iteratively over depth and
                                    minimize the error in the other
                                    free parameters. To make the fit
                                    more
robust (i.e fit something linear vs. Coulombic), use the derived
                                    log version of the screened
                                    Coulomb form:
ln(r* U(r)) = A(eps) - r / L_TF
where A(eps) = ln(e^2 / (4.* pi * vacperm * eps))
Optimize for eps and L_TF, looking for a minimized sum of the
                                    errors within experimentally
                                    expected values.

@author: Taleana
'''
import numpy as np
import matplotlib.pyplot as plt
import scipy.odr.odrpack as odr
import scipy.constants as sp
import SkipHeaderand1D as SH1D #Module I wrote to skip header and
                                    read in column titles. Return as
                                    1D arrays
import CoulombFits as CF #Module I wrote for fit equations
import matplotlib.tri as tri

plt.close('all') #closes any plots left up from a previous run.

#FILE PATH INFO#
filenames=["DB-T1_Shifts_20nm.txt","DB-T2_Shifts_20nm.txt","DB-
                                    DB_Shifts_20nm.txt"] #Files for
                                    read-in
```

```
filepath="C:\\Users\\Taleana\\Documents\\Python Code\\ODR Fit
                                Dopants Insight\\" #location

####READ IN DATA TO 1D ARRAYS####
xT1,U_DBT1,y_errT1=SH1D.create1Darraysforafile(SH1D.skipheader('[
                                DATA]',filepath,filenames[0]),
                                filepath,filenames[0]) #Make 1D
                                arrays for the x,y, and error
                                values for a desired fit on a
                                charge defect
xT2,U_DBT2,y_errT2=SH1D.create1Darraysforafile(SH1D.skipheader('[
                                DATA]',filepath,filenames[1]),
                                filepath,filenames[1])
xDB,U_DBDB,y_errDB=SH1D.create1Darraysforafile(SH1D.skipheader('[
                                DATA]',filepath,filenames[2]),
                                filepath,filenames[2])
U_DBT1=-1.0*U_DBT1 #opposite charge sign for this case to the
                                other charge defects.

###NICE PRINTING DEFINITIONS### #Could make this a module
                                eventually
def NF(x):
'''
nice format for printing floats
'''
return '%1.4g' %x

def fs(x):  # nice format for printing
# return '$%*.3f' %x
return '%1.2f' %x


### FITTING USING LOG-LINEAR SPACE###

### DB-DB CASE###
#depth increment in m.
```

```
d = 0. * 1e-9   #Zero for this case since they are in the same
                                plane
#Calculate actual distance
rDB = CF.TrueR(d, xDB)
# convert U to Joules
U_DBDB_J = U_DBDB * 1e-3 * sp.e
#Get y variable to log form of screened Coulomb from the
                                CoulombFits module
lnUr_DBDB = np.log(rDB * U_DBDB_J)

# Create a model for fitting.
log_model= odr.Model(CF.Screen_Coul_Log)
# Create a RealData object using our initiated data from above.
data_log_DB = odr.RealData(rDB, lnUr_DBDB, sy=y_errDB)
# Setup ODR with data and model
odrDB = odr.ODR(data_log_DB, log_model, beta0=[9., 1e-9], ifixb=[1
                                ,1], maxit=5000) #beta0 is guess
                                values for B[0] to B[n]. Otherwise
                                 it won't converge. ifixxb allows
                                you to fix a certain fit parameter
                                 if you want. 0 is fixed. 1 is
                                free
# Run ODR
outDB = odrDB.run()
comberrDB=NF(100.* outDB.sd_beta[0]/outDB.beta[0]+100.* outDB.
                                sd_beta[1]/outDB.beta[1])#Combined
                                 Error in both free variables for
                                the DB case.

#Print results
print ("For DB-DB, depth ="+str(d *1e9)+'nm')
print('The optimized values are: eps_rel=', NF(outDB.beta[0]),'
                                with std error: ', NF(outDB.
                                sd_beta[0]),'or', NF(100.* outDB.
                                sd_beta[0]/outDB.beta[0]), '%')
print('The optimized values are: L_TF=', NF(outDB.beta[1] *1e9),'
                                nm with std error: ', NF(outDB.
```

```
                                    sd_beta[1] *1e9),'or', NF(100.*
                                    outDB.sd_beta[1]/outDB.beta[1]), '
                                    %')

### T1-DB CASE###
#Unlike the DB case, we have three free parameters to fit. We have
                                     reasonable bounds for depth, so
                                    we will increment over depth,
#and look for a minimization in the error of the two other
                                    parameters. Need arrays to store
                                    our results in
Eps_T1=np.empty((20,1)) #Dielectric Constant
Eps_ErrT1=np.empty((20,1))
Screen_T1=np.empty((20,1)) #Screening length
Screen_ErrT1=np.empty((20,1))
CError_T1=np.empty((20,1)) #Combined Error in the two free
                                    parameters
depth_T1=np.empty((20,1)) #Depth increments

print ('\nT1-DB case:\n')
#For help with visualization, define a plot grid to look at the
                                    itterative results. Should make
                                    this more generalized in the
                                    future for arbitrary depth
                                    incrementations.
Nrow = 4
Ncol = 5
fig, axarr2 = plt.subplots(Nrow, Ncol, sharey='row',figsize=(20,10
                                    ))
dd = 0.1e-9    # depth increment. We know we can see between 0 to
                                    ~5nm deep, or 36 ML with 1ML = 0.
                                    135 nm.
d = 0.01e-9    # intial depth. Test a really shallow case for
                                    posterity since we know they can
                                    sometimes be quite shallow
id = 0 #counter for shallowest case of 0.01. Then we increment by
                                    0.1 after that.
```

```
cc= 0 #counter for array results

for ir in range(Nrow):
for ic in range(Ncol):
id += 1
rSS = CF.TrueR(d, xT1) #Since this has a lateral component (known)
                                 and an itterative depth component
                                , we have to calculate the true
                                direct distance to the probe
# convert U to Joules
U_DBT1_J = U_DBT1 * 1e-3 * sp.e
lnUr_DBT1 = np.log(rSS * U_DBT1_J) #ln(r* U(r)) = A(eps) - r /
                                L_TF where A(eps) = ln(e^2 / (4.*
                                pi * vacperm * eps)).
# Create a model for fitting.
log_model= odr.Model(CF.Screen_Coul_Log)
# Create a RealData object using our initiated data from above.
data_log_T1 = odr.RealData(rSS, lnUr_DBT1,sy=y_errT1)
# Setup ODR with data and model
odrT1 = odr.ODR(data_log_T1, log_model, beta0=[5., 1e-9], ifixb=[1
                                ,1], maxit=5000)
# Run ODR
outT1 = odrT1.run() #outputs array for the fit
#Print a quick tally of results
print ("\nFor DB-T1, depth ="+NF(d *1e9)+'nm')
print(' The optimized values are: eps_rel=', NF(outT1.beta[0]),',
                                with std error:', NF(outT1.sd_beta
                                [0]),'or' , NF(100.* outT1.sd_beta
                                [0]/outT1.beta[0]), '%')
print(' The optimized values are: L_TF=', NF(outT1.beta[1] *1e9),'
                                nm, with std error:', NF(outT1.
                                sd_beta[1] *1e9),'or', NF(100.*
                                outT1.sd_beta[1]/outT1.beta[1]), '
                                %')
print('The combined error is: ', NF(100.* outT1.sd_beta[0]/outT1.
                                beta[0]+100.* outT1.sd_beta[1]/
                                outT1.beta[1]),'%')
```

```
#Fill the arrays to work with later#
Eps_T1[cc]=outT1.beta[0]
Eps_ErrT1[cc]=outT1.sd_beta[0]
Screen_T1[cc]=outT1.beta[1]*1e9
comberrT1=NF(100.* outT1.sd_beta[0]/outT1.beta[0]+100.* outT1.
                                sd_beta[1]/outT1.beta[1])
Screen_ErrT1[cc]=NF(outT1.sd_beta[1] *1e9)
CError_T1[cc]=comberrT1
depth_T1[cc]=d
cc+= 1
#Plot results in the grid
axarr2[ir, ic].plot(rSS* 1e9, lnUr_DBT1, 'o')
axarr2[ir, ic].plot(rSS* 1e9, CF.Screen_Coul_Log(outT1.beta, rSS),
                                 '--')
axarr2[ir, ic].set_xlabel("distance, r (nm)", labelpad = 12)
axarr2[ir, ic].set_ylabel("ln(r U)")
axarr2[ir, ic].set_title('T1 case, depth='+NF(d *1e9)+'nm,'+'
                                Error= '+comberrT1+'%')
if id == 1: d = 0.  # reset to zero for next incrementations.
                                Allows us to test the really
                                shallow 0.01e-9 case.
d += dd #increments depth for rest of panels.

plt.tight_layout()


###CONTOUR PLOT OF ERROR T1### #Makes contour plots on a
                                triangular grid for the explored
                                screening lengths and dielectric
                                constants. Z height is the
                                combined percent error.
x = np.array(Eps_T1).squeeze() #countour package only accepts 1D
                                arrays. .squeeze makes it 1D.
                                Should probably just have 1D
                                arrays instead of having the .
                                squeeze. FIX
```

```
y = np.array(Screen_T1).squeeze()
z = np.array(CError_T1).squeeze()

triang=tri.Triangulation(x,y)
figc, (ax1,ax2) = plt.subplots(1,2, sharex=True, sharey=True)
tpc=ax1.tripcolor(triang,z, edgecolors='k',cmap="coolwarm") #
                                Countours
ax1.plot(x,y,'ko') #Original points being interpolated with
                                triangular grid
figc.colorbar(tpc, ax=ax1)
ax1.set_title('Combined % Error in Fits T1')
ax1.set_xlabel("Dielectric Constant")
ax1.set_ylabel("Screening Length (nm)")

ax2.tricontour(x, y, z, 20,linewidths=0.5, colors='k') #Same data,
                                slightly different visualization
cntr2=ax2.tricontourf(x,y,z, 50, cmap="coolwarm")
ax2.tricontourf(x,y,z, 50, cmap="coolwarm") # choose 20 contour
                                levels
figc.colorbar(cntr2, ax=ax2)
ax2.plot(x,y, 'ko ')
ax2.set_title('Combined % Error')
ax2.set_xlabel("Dielectric Constant")
ax2.set_ylabel("Screening Length (nm)")


### T2-DB CASE###
print ('\nT2-DB case:\n')

#Storage arrays
Eps_T2=np.empty((12,1))
Eps_ErrT2=np.empty((12,1))
Screen_T2=np.empty((12,1))
Screen_ErrT2=np.empty((12,1))
CError_T2=np.empty((12,1))
depth_T2=np.empty((12,1))
```

```
Nrow = 3
Ncol = 4
fig, axarr2 = plt.subplots(Nrow, Ncol, sharey='row',figsize=(20,10))
dd = 0.1e-9    # depth increment
d = 0.01e-9    # intial depth
cc = 0
id = 0
for ir in range(Nrow):
for ic in range(Ncol):
id += 1
rSS = CF.TrueR(d, xT2) #Since this has a lateral component (known) and an itterative depth component, we have to calculate the true direct distance to the probe
U_DBT2_J = U_DBT2 * 1e-3 * sp.e # convert U to Joules
#Get y variable to log form of screened Coulomb from the CoulombFits module
lnUr_DBT2 = np.log(rSS * U_DBT2_J)
# Create a model for fitting.
log_model= odr.Model(CF.Screen_Coul_Log)
# Create a RealData object using our initiated data from above.
data_log_T2 = odr.RealData(rSS, lnUr_DBT2, sy=y_errT2)
# Setup ODR with data and model
odrT2 = odr.ODR(data_log_T2, log_model, beta0=[5., 1e-9], ifixb=[1,1], maxit=5000)
# Run ODR
outT2 = odrT2.run()
#Print results
print ("\nFor DB-T2, depth ="+NF(d *1e9)+'nm')
print(' The optimized values are: eps_rel=', NF(outT2.beta[0]),', with std error:', NF(outT2.sd_beta[0]),'or' , NF(100.* outT2.sd_beta[0]/outT2.beta[0]), '%')
print(' The optimized values are: L_TF=', NF(outT2.beta[1] *1e9),' nm, with std error:', NF(outT2.sd_beta[1] *1e9),'or', NF(100.*
```

```
                                    outT2.sd_beta[1]/outT2.beta[1]), '
                                    %')
print('The combined error is: ', NF(100.* outT2.sd_beta[0]/outT2.
                                    beta[0])+NF(100.* outT2.sd_beta[1]
                                    /outT2.beta[1]),'%')
#Fill arrays
Eps_T2[cc]=outT2.beta[0]
Eps_ErrT2[cc]=NF(outT2.sd_beta[0])
Screen_T2[cc]=outT2.beta[1]*1e9
Screen_ErrT2[cc]=NF(outT2.sd_beta[1] *1e9)
comberrT2=NF(100.* outT2.sd_beta[0]/outT2.beta[0]+100.* outT2.
                                    sd_beta[1]/outT2.beta[1])
CError_T2[cc]=comberrT2
depth_T2[cc]=d
cc+= 1
comberrT2=NF(100.* outT2.sd_beta[0]/outT2.beta[0]+100.* outT2.
                                    sd_beta[1]/outT2.beta[1])
#Plot in Grid
axarr2[ir, ic].plot(rSS* 1e9, lnUr_DBT2, 'o')
axarr2[ir, ic].plot(rSS* 1e9, CF.Screen_Coul_Log(outT2.beta, rSS),
                                     '--')
axarr2[ir, ic].set_xlabel("distance, r (nm)", labelpad = 12)
axarr2[ir, ic].set_ylabel("ln(r U)")
axarr2[ir, ic].set_title('T2 case, depth='+NF(d *1e9)+'nm,'+'
                                    Error= '+comberrT2+'%')
if id == 1: d = 0.  # reset to zero for next incrementations
d += dd

plt.tight_layout()

###CONTOUR PLOT OF ERROR T2### #Makes contour plots on a
                                    triangular grid for the explored
                                    screening lengths and dielectric
                                    constants. Z height is the
                                    combined percent error.
x = np.array(Eps_T2).squeeze() #countour package only accepts 1D
                                    arrays. .squeeze makes it 1D.
```

```
y = np.array(Screen_T2).squeeze()
z = np.array(CError_T2).squeeze()

triang=tri.Triangulation(x,y)
fig, (ax1,ax2) = plt.subplots(1,2, sharex=True, sharey=True)
tpc=ax1.tripcolor(triang,z, edgecolors='k',cmap="coolwarm")
ax1.plot(x,y,'ko')
figc.colorbar(tpc, ax=ax1)
ax1.set_title('Combined % Error in Fits T2')
ax1.set_xlabel("Dielectric Constant")
ax1.set_ylabel("Screening Length (nm)")

ax2.tricontour(x, y, z, 20,linewidths=0.5, colors='k')
cntr2=ax2.tricontourf(x,y,z, 50, cmap="coolwarm")
ax2.tricontourf(x,y,z, 50, cmap="coolwarm") # choose 20 contour
                                levels, just to show how good its
                                interpolation is
figc.colorbar(cntr2, ax=ax2)
ax2.plot(x,y, 'ko ')
ax2.set_title('Combined % Error with Contours')
ax2.set_xlabel("Dielectric Constant")
ax2.set_ylabel("Screening Length (nm)")

###FIND THE INDEXES WHERE THE COMBINED ERROR IS MINIMIZED AND
                                PRINTS###
print('\nRESULTS')
print('\nThe minimized combined error for DB is', comberrDB, '%','
                                with epsilon =',NF(outDB.beta[0]),
                                '+/-', NF(outDB.sd_beta[0]), 'and
                                screening length =', NF(outDB.beta
                                [1]*1e9), '+/-', NF(outDB.sd_beta[
                                1] *1e9), 'nm')
print('\nThe minimized combined error for T1 is', min(CError_T1),'
                                %','with epsilon =',Eps_T1[
                                CError_T1.argmin()],'+/-',
                                Eps_ErrT1[CError_T1.argmin()], '
                                and screening length =', Screen_T1
```

```
                                [CError_T1.argmin()], '+/-',
                                Screen_ErrT1[CError_T1.argmin()],
                                'nm' , 'at a depth of', depth_T1[
                                CError_T1.argmin()]*1e9, 'nm')
print('\nThe minimized combined error for T2 is', min(CError_T2),
                                '%','with epsilon =',Eps_T2[
                                CError_T2.argmin()],'+/-',
                                Eps_ErrT2[CError_T2.argmin()], '
                                and screening length =',Screen_T2[
                                CError_T2.argmin()], '+/-',
                                Screen_ErrT2[CError_T2.argmin()],
                                'nm','at a depth of', depth_T2[
                                CError_T2.argmin()]*1e9, 'nm')



###PUT THE MINIMIZED ERROR FITS IN THEIR OWN PLOTS FOR A SANITY
                                CHECK###
minT1=[Eps_T1[CError_T1.argmin()], depth_T1[CError_T1.argmin()],
                                Screen_T1[CError_T1.argmin()]*1e-9
                                ]
minT2=[Eps_T2[CError_T2.argmin()], depth_T2[CError_T2.argmin()],
                                Screen_T2[CError_T2.argmin()]*1e-9
                                ]
#creat fit data from the optimized three parameters
x_fitDB = np.linspace(xDB[0], xDB[-1], 1000)
y_fitDB = CF.Screen_Coul_nodepth(outDB.beta, x_fitDB)

x_fitT1 = np.linspace(xT1[0],xT1[-1], 1000)
y_fitT1 = CF.Screen_Coul_depth(minT1,x_fitT1)
r_fitT1 = np.linspace(CF.TrueR(minT1[1],xT1[0]),CF.TrueR(minT1[1],
                                xT1[-1]), 1000)
yr_fitT1 = CF.Screen_Coul_plot(minT1[0],minT1[2],r_fitT1)

x_fitT2 = np.linspace(xT2[0],xT2[-1], 1000)
y_fitT2 = CF.Screen_Coul_depth(minT2,x_fitT2)
r_fitT2 = np.linspace(CF.TrueR(minT2[1],xT2[0]),CF.TrueR(minT2[1],
                                xT2[-1]), 1000)
```

```
yr_fitT2 = CF.Screen_Coul_plot(minT2[0],minT2[2],r_fitT2)

fig, ax = plt.subplots()
ax.errorbar(xDB/(10**-9), U_DBDB, yerr=y_errDB, linestyle='None',
                                  fmt='o',ecolor='g', capsize=4,
                                  capthick=2)
ax.plot(x_fitDB/(10**-9), y_fitDB)
ax.set_xlabel("Distance (nm)")
ax.set_ylabel("Energy Shift (meV)")
ax.set_title('DB-DB')

fig, ax2 = plt.subplots()
ax2.errorbar(xT1/(10**-9), U_DBT1, yerr=y_errT1, linestyle='None',
                                   fmt='o',ecolor='g', capsize=4,
                                  capthick=2)
ax2.plot(x_fitT1/(10**-9), y_fitT1)
ax2.set_xlabel("Distance (nm)")
ax2.set_ylabel("Energy Shift (meV)")
ax2.set_title('DB-T1')

fig, ax3 = plt.subplots()
ax3.errorbar(xT2/(10**-9), U_DBT2, yerr=y_errT2, linestyle='None',
                                   fmt='o',ecolor='g', capsize=4,
                                  capthick=2)
ax3.plot(x_fitT2/(10**-9), y_fitT2)
ax3.set_xlabel("Distance (nm)")
ax3.set_ylabel("Energy Shift (meV)")
ax3.set_title('DB-T2')

fig, ax4 =plt.subplots() #define figure params
plt.errorbar(1/(xDB/(10**-9)), U_DBDB, yerr=y_errDB, linestyle='
                                  None', fmt='o',ecolor='g', capsize
                                  =4, capthick=2)
plt.plot(1/(x_fitDB/(10**-9)), y_fitDB,'b',ls='--',label="Fit of
                                  DB")
```

```
plt.errorbar(1/(CF.TrueR(minT1[1],xT1)/(10**-9)), -1.0*U_DBT1,
                                yerr=y_errT1, linestyle='None',
                                fmt='o',ecolor='g', capsize=4,
                                capthick=2)
plt.plot(1/(r_fitT1/(10**-9)), -1.0*yr_fitT1,'r', ls='--', label="
                                Fit of T1")

plt.errorbar(1/(CF.TrueR(minT2[1],xT2)/(10**-9)), U_DBT2, yerr=
                                y_errT2, linestyle='None', fmt='o'
                                ,ecolor='g', capsize=4, capthick=2
                                )
plt.plot(1/(r_fitT2/(10**-9)), yr_fitT2,'k', ls='--', label="Fit
                                of T2")

plt.legend()
plt.title("Electrostatic Shift vs. Distance")
plt.xlabel("1/Distance(nm)")
plt.ylabel("Electrostatic Shift (meV)")
plt.savefig(filepath+"Finalplot"+".eps",format='pdf')

###CALCULATE MISFIT'S OF THE DATA TO TEST GOODNESS OF FIT###
ymodelDB=CF.Screen_Coul_nodepth(outDB.beta,xDB)
ymodelT1=CF.Screen_Coul_depth(minT1,xT1)
ymodelT2=CF.Screen_Coul_depth(minT2,xT2)

DBMis=CF.RMS_Error(U_DBDB,ymodelDB,y_errDB/2.,len(U_DBDB)) #Yerr
                                is divided by 2 because it should
                                be half of peak to peak error.
                                Make sure everything is in the
                                same units. I used meV
T1Mis=CF.RMS_Error(U_DBT1,ymodelT1,y_errT1/2.,len(U_DBT1))
T2Mis=CF.RMS_Error(U_DBT2,ymodelT2,y_errT2/2.,len(U_DBT2))

print('\nThe misfits are: ','\nDB =',DBMis,'\nT1 =', T1Mis,'\nT2 =
                                ', T2Mis)
#plt.close('all')
plt.show()
```

Chapter 6

Conclusion

6.1 Computation with Atom-Sized Quantum Dots: Revisiting the Requisites

In this work we have demonstrated the essential capabilities required to build all-silicon atom-scale electronics for binary computation. We called this approach BASiL, for Binary Atomic Silicon Logic. Our primary building block was the dangling bond on the hydrogen terminated silicon (100) surface, which we coupled to a partner DB to create paired binary electronic building blocks containing a moveable electron. Binary information was expressed as the spatial location of that electron in a given pair, with pairs geometrically arranged on the surface to electrostatically interact with each other in predictable ways. Perturbing local electrostatic inputs, for now represented by asymmetrically placed perturber DBs, were used to toggle the binary states. Higher order functionality was shown with the demonstration of reversible information transfer in wires and a logical OR gate made of many paired DBs. Reversibility of the logical states was accomplished by utilizing our newly developed "Atomic White-Out" error-correction abilities, were DB electrostatic perturbers were erased as needed through mechanical bonding to a single hydrogen atom sitting on the tip apex. Finally, a dedicated study was taken to examine electrostatic inhomogeneity in our DB-patterning surface from the effect of irregular doping and local

charge defects. These irregularities in the local electrostatic environment on length scales comparable to our DB devices had important implications for their correct operation, with our "Electrostatic Landscape" paper detailing how we could pre-screen areas for homogeneity using $\Delta f(V)$ (KPFM) mapping. Additionally, a new technique was developed that employed the sequential patterning and erasure of a DB in the vicinity of the electrostatic field from a given charge defect. This allowed the DB to act as an electrostatic point probe, with fits of its shifting DB(0/-) charge state transition level allowing us to extract the depth of the defect (if sub-surface), along with the local dielectric constant (ϵ) and screening length (L_{TF}) for the surface. With these three key results taken together, that of error-correction, atomic logic, and an examination of logic destabilization sources, we put forth BASiL as one of the most promising platforms for atom-based computing. To further that claim, we return to our seven key criteria listed in the introduction and discuss how DB-logic has met, or could meet, the requirements.

(1) *It should provide some existing or potential future benefit. For computing, this would be an increase in size density, processing speed, or power efficiency; optimally all three.*

DBs are atomically sized, can theoretically switch binary states at THz rates [50], and use only hundreds of meV of energy per binary bit switch (Section 4.2.3), hitting all three criteria. It will be important in the near future to more rigorously test the THz switching rate, which was calculated from theoretical modeling without lattice relaxation factored in. Measuring dynamics in the THz range is a challenging experimental test, but is of importance to both speed-up and energy dissipation claims. Our experimentally extracted bit energy is on order of hundreds of meV due to lattice relaxation within the DB pair, but lattice relaxation happens at a rate five orders of magnitude slower than THz speeds [50]. This suggests that if atomic circuits could be clocked at ultra-fast speeds, supposing simultaneous development of a way to perform the required rapid electrostatic gating without slow-down, lattice relaxation may not have time to come into effect lowering our power consumption even further. This may concurrently have other negative consequences, such as for thermal robustness, but all further speculation awaits future experimental testing.

(2) *One obvious disqualifier for a technology is it must not need cryogenic temperatures.*

DBs are well established to be structurally stable up to 200°C [53, 54]. In regard to operational stability where pairs localize charge, one prior STM example showed polarization at room temperature of DB structures [51], and results presented in this work suggest the bit energy of pairs is great enough to withstand thermal destabilization. For even the most clustered arrangements of pairs, such as in our OR gate, the smallest localization energy seen was $\sim 100\ meV$ (See Section 4.2.3). This value is still $4 \times$ the thermal background bath at room temperature ($k_B T = 25\ meV$), suggesting they should be robust to thermal destabilization (being excited out of their ground state). As with the purported THz speeds though, this claim too warrants additional future testing.

(3) *The patterned atoms or molecules need to be electrically distinct from the substrate.*

DBs are well known to possess gap-states, with their charge transition levels in the bandgap preventing them from substantially mixing properties with bulk states [47, 48]. This was additionally verified by the AFM calculation of the DB(0/-) and DB(0/+) charge transition levels in the bandgap, as shown in Section 4.2.5.

(4) *The atomic circuitry must not require mechanical or other reset processes, but be instantly reusable with toggle-able inputs from an outside source.*

In this work, we used asymmetrically placed perturber DBs to toggle the binary states of our examples. This is a slow mechanical reset process, as we must take the time to either make or erase a DB to alter the inputs. Despite failing this criteria now, we anticipate that these stand-in DBs can eventually be replaced with binary wires or metallic leads. This could be in the form of lithographically created wires of small feature size using conventional CMOS techniques, or even metallic DB wires as suggested in the research from Engelund *et al.* [186]. Regardless, macro-to-atom contacts are a necessity for the utility of future atomic devices. Addressing nm-sized patterns of atoms in a power-efficient, dynamic, and precise way will require a large dedicated effort.

(5) *Atomic patterns must have scalability.*

This thesis has presented several advances toward scalability of this platform. These include developed error-correction, new information about patterning efficiency for different tip-states [46], and an analysis of design considerations using quick modeling in the SiQAD simulation software. Currently, efforts are being made to develop an all-in-one machine learning software suite that will merge the already automated tip-sharpening [139] with a computer aided design tool. Thus, a user could input a DB pattern they want and the algorithm would find a clean electrostatically homogeneous area, pattern the structure, perform any necessary error correction, and notify the user upon completion, all without human intervention. It could be argued that even if this was implemented though, SPM's throughput capability is still a far cry from the billions of transistors required for a traditional chip. In the distant future, manufacturing will have to be sped up significantly for atom-scale devices to reach this metric. While no tools currently possess the ability, it is conceivable that further developments in a technology like ion-beam lithography could eventually get to atom-scale feature sizes. This would allow precise desorption to create DB circuits using beam writing, but for now this remains one of the more difficult problems in the realm of speculation. Regardless, there may be many interesting intermediary opportunities involving patterns of perhaps hundreds of atoms, a metric that is now achievable.

(6) *Information in atomic-logic structures must be robust, with a full accounting for noise and destabilization sources.*

Analysis performed as part of our "Electrostatic Landscape" paper began to address these destabilization sources. As part of this work, we have found that irregular doping and surface charge defects can be destabilizing to DB atomic-logic patterns. We think a two-level approach could help with these issues. First, to reduce the influence of irregular dopants we could flash the silicon wafers more. This would dopant-deplete the upper layers to a greater extent, hopefully ensuring most of the dopant atoms were far enough away to not disturb surface DB patterns. This may have adverse consequences, like changing the screening length, but more studies will have to be done to verify. The second level of addressing this is to refine our sample preparation to reduce the number of defects. A recent study was

undertaken to identify the nature of all the observed defects, which will hopefully inform better sample preparation methods (See "Atomic defects of the hydrogen-terminated silicon(100)-2x1 surface imaged with STM and nc-AFM" in Section 6.2 or [119]).

(7) *An ability to build on the silicon infrastructure that already exists.*

DBs are built on a fundamentally silicon base, allowing us to capitalize on the massive existing infrastructure already surrounding CMOS. Not only does this give us access to a wealth of already developed tools and knowledge, but the fundamental compatibility of patterning on Si may enable intermediary opportunities where atom-computing can be slowly phased in to optimize pieces of existing chips.

In summary, silicon DB-based devices are promising candidates for atom-scale computing. They are not only at the ultimate size limit, but offer up the possibility of also being incredibly fast and power efficient, while remaining robust at commercially friendly temperatures. Although this thesis presents but a small part of the broad effort toward atom-scale devices, it is hoped that it supports the case for DB devices strongly, encouraging future development of this interesting system. As our understanding continues to grow for this platform, there is no reason not to expect increasingly compelling demonstrations of higher order logic and interesting physics.

6.2 Publications Resulting from This Work

- Labidi, H., Kupsta, M., **Huff, T.**, Salomons, M., Vick, D., Taucer, M., Pitters, J., & Wolkow, R. A. (2015). New Fabrication Technique for Highly Sensitive qPlus Sensor with Well-Defined Spring Constant. Ultramicroscopy, 158, 33-37. [88]

- Labidi, H., Koleini, M., **Huff, T.**, Salomons, M., Cloutier, M., Pitters, J., & Wolkow, R. A. (2017). Indications of Chemical Bond Contrast in AFM Images of a Hydrogen-Terminated Silicon Surface. Nature Communications, 8, 14222. [93]

- **Huff, T. R.**, Labidi, H., Rashidi, M., Koleini, M., Achal, R., Salomons, M. H., & Wolkow, R. A. (2017). Atomic White-Out: Enabling Atomic Circuitry Through Mechanically Induced Bonding of Single Hydrogen Atoms to a Silicon Surface. ACS Nano, 11(9), 8636-8642. [136]

- Rashidi, M., Lloyd, E., **Huff, T. R.**, Achal, R., Taucer, M., Croshaw, J. J., & Wolkow, R. A. (2017). Resolving and Tuning Carrier Capture Rates at a Single Silicon Atom Gap State. ACS Nano, 11(11), 11732-11738. [201]

- Achal, R., Rashidi, M., Croshaw, J., Churchill, D., Taucer, M., **Huff, T.**, Cloutier, M., Pitters, J.,& Wolkow, R. A. (2018). Lithography for Robust and Editable Atomic-Scale Silicon Devices and Memories. Nature Communications, 9(1), 2778. [134]

- Rashidi, M., Vine, W., Dienel, T., Livadaru, L., Retallick, J., **Huff, T.**, Walus, K., & Wolkow, R. A. (2018). Initiating and Monitoring the Evolution of Single Electrons Within Atom-Defined Structures. Physical Review Letters, 121(16), 166801. [153]

- **Huff, T.**, Labidi, H., Rashidi, M., Livadaru, L., Dienel, T., Achal, R., Vine, W., Pitters, J., & Wolkow, R. A. (2018). Binary Atomic Silicon Logic. Nature Electronics, 1(12), 636. [49]

- **Huff, T. R.**, Dienel, T., Rashidi, M., Achal, R., Livadaru, L., Croshaw, J., & Wolkow, R. A. (2019). Electrostatic Landscape of a Hydrogen-Terminated Silicon Surface Probed by a Moveable Quantum Dot. ACS Nano. 13(9), 10566-10575. [52]

- Achal, R., Rashidi, M., Croshaw, J., **Huff, T.**, & Wolkow, R. A. (2020). Detecting and Directing Single Molecule Binding Events on H-Si(100) with Application to Ultra-Dense Data Storage. ACS Nano. 14(3), 2947-2955. [262]

- Ng, S.S.H., Retallick, J., Chiu, H.N., Lupoiu, R., Livadaru, L., **Huff, T.**, Rashidi, M., Vine, W., Dienel, T., Wolkow, R. A., & Walus, K. (2020) SiQAD:

A Design and Simulation Tool for Atomic Silicon Quantum Dot Circuits. IEEE Transactions on Nanotechnology, Vol. 19, 137-146 [215]

- Croshaw, J., Dienel, T., **Huff, T.**, & Wolkow, R. A. (2020). Atomic Defects of the Hydrogen-Terminated Silicon(100)-2x1 Surface Imaged with STM and nc-AFM. (In Preparation. arXiv preprint arXiv:2002.09138) [119]
- Rashidi, M., Lloyd, E., Croshaw, J., **Huff, T.**, & Wolkow, R. A. (2020). Linear Chains of Silicon Dangling Bonds. (In Preparation)

Bibliography

[1] G. C. Farrington, "ENIAC: The Birth of the Information Age," *Popular Science* **248** (1996) 74.

[2] U. Army, "ENIAC in BRL Building 328." https://en.wikipedia.org/wiki/ENIAC#/media/File:Eniac.jpg, 2005. Public Domain Image. (Accessed on 07/02/2019).

[3] R. Rojas and U. Hashagen, *The ENIAC: History, Operation and Reconstruction in VLSI*, pp. 121–178. MITP, 2002. https://ieeexplore.ieee.org/document/6302808.

[4] F. Macera, "Packaged ENIAC-on-a-Chip." https://www.seas.upenn.edu/~jan/pictures/eniacpictures/EniacChipPackaged.jpg, 1998. (Accessed on 21/11/2019) Reproduced with permission from principal investigator Dr. Jan Van der Spiegel.

[5] B. Hoefflinger, *ITRS 2028—International Roadmap of Semiconductors*, pp. 143–148. Springer International Publishing, Cham, 2016.

[6] S. K. Moore, "EUV Lithography Finally Ready for Fabs," *IEEE Spectrum* **55** (2018) 46–48.

[7] M. Horowitz, F. Labonte, O. Shacham, K. Olukotun, L. Hammond, C. Batten, and C. Moore, "40 Years of Microprocessor Trend Data." https://www.karlrupp.net/2015/06/40-years-of-microprocessor-trend-data/, 2018. (Accessed on 21/11/2019).

[8] J. Michael J. Ellsworth, "High Powered Chip Cooling – Air and Beyond Electronics Cooling." https://www.electronics-cooling.com/2005/08/high-powered-chip-cooling-air-and-beyond/, 2005. (Accessed on 07/02/2019).

[9] R. P. Feynman, "There's Plenty of Room at the Bottom," *Engineering and Science* **23** (1959) 22–36. https://resolver.caltech.edu/CaltechES:23.5.1960Bottom. Talk Presented to the American Physical Society in Pasadena.

[10] M. Jacoby, "30 Years of Moving Atoms: How Scanning Probe Microscopes Revolutionized Nanoscience." https://cen.acs.org/content/cen/articles/97/i44/30-years-moving-atoms-scanning.html?linkId=76835856, 2018. (Accessed on 11/30/2019).

[11] D. M. Eigler and E. K. Schweizer, "Positioning Single Atoms with a Scanning Tunnelling Microscope," *Nature* **344** (1990) 524–526.

[12] A. J. Heinrich, C. P. Lutz, J. A. Gupta, and D. M. Eigler, "Molecule Cascades," *Science* **298** (2002) 1381–1387.

[13] W. Soe, C. Manzano, A. De Sarkar, F. Ample, N. Chandrasekhar, N. Renaud, P. de Mendoza, A. M. Echavarren, M. Hliwa, and C. Joachim, "Demonstration of a NOR Logic Gate Using a Single Molecule and Two Surface Gold Atoms to Encode the Logical Input," *Physical Review B* **83** (2011) 155443.

[14] C. P. Collier, E. W. Wong, M. Belohradsk'y, F. M. Raymo, J. F. Stoddart, P. J. Kuekes, R. S. Williams, and J. R. Heath, "Electronically Configurable Molecular-Based Logic Gates," *Science* **285** (1999) 391–394.

[15] A. P. De Silva and S. Uchiyama, "Molecular Logic and Computing," *Nature Nanotechnology* **2** (2007) 399.

[16] C. Joachim, J. K. Gimzewski, and A. Aviram, "Electronics Using Hybrid-Molecular and Mono-Molecular Devices," *Nature* **408** (2000) 541.

[17] W.-H. Soe, C. Manzano, N. Renaud, P. de Mendoza, A. De Sarkar, F. Ample, M. Hliwa, A. M. Echavarren, N. Chandrasekhar, and C. Joachim, "Manipulating Molecular Quantum States with Classical Metal Atom Inputs: Demonstration of a Single Molecule NOR Logic Gate," *ACS Nano* **5** (2011) 1436–1440.

[18] A. A. Khajetoorians, J. Wiebe, B. Chilian, and R. Wiesendanger, "Realizing All-Spin-Based Logic Operations Atom by Atom," *Science* **332** (2011) 1062–1064.

[19] M. Yengui, E. Duverger, P. Sonnet, and D. Riedel, "A Two-Dimensional ON/OFF Switching Device Based on Anisotropic Interactions of Atomic Quantum Dots on Si (100):H," *Nature Communications* **8** (2017) 2211.

[20] B. Fresch, J. Bocquel, S. Rogge, R. D. Levine, and F. Remacle, "A Probabilistic Finite State Logic Machine Realized Experimentally on a Single Dopant Atom," *Nano Letters* **17** (2017) 1846–1852.

[21] M. Kolmer, R. Zuzak, G. Dridi, S. Godlewski, C. Joachim, and M. Szymonski, "Realization of a Quantum Hamiltonian Boolean Logic Gate on the Si (001): H Surface," *Nanoscale* **7** (2015) 12325–12330.

[22] A. Yazdani, D. M. Eigler, and N. D. Lang, "Off-Resonance Conduction Through Atomic Wires," *Science* **272** (1996) 1921–1924.

[23] C. Joachim, J. K. Gimzewski, R. R. Schlittler, and C. Chavy, "Electronic Transparence of a Single C_{60} Molecule," *Physical Review Letters* **74** (1995) 2102–2105.

[24] A. Bellec, F. Ample, D. Riedel, G. Dujardin, and C. Joachim, "Imaging Molecular Orbitals by Scanning Tunneling Microscopy on a Passivated Semiconductor," *Nano Letters* **9** (2009) 144–147.

[25] M. Sterrer, T. Risse, U. Martinez Pozzoni, L. Giordano, M. Heyde, H.-P. Rust, G. Pacchioni, and H.-J. Freund, "Control of the Charge State of Metal Atoms on Thin MgO Films," *Physical Review Letters* **98** (2007) 096107.

[26] M. Yulikov, M. Sterrer, M. Heyde, H.-P. Rust, T. Risse, H.-J. Freund, G. Pacchioni, and A. Scagnelli, "Binding of Single Gold Atoms on Thin MgO(001) Films," *Physical Review Letters* **96** (2006) 146804.

[27] W. Steurer, J. Repp, L. Gross, I. Scivetti, M. Persson, and G. Meyer, "Manipulation of the Charge State of Single Au Atoms on Insulating Multilayer Films," *Physical Review Letters* **114** (2015) 036801.

[28] J. Repp, G. Meyer, F. E. Olsson, and M. Persson, "Controlling the Charge State of Individual Gold Adatoms," *Science* **305** (2004) 493–495.

[29] I. Swart, T. Sonnleitner, and J. Repp, "Charge State Control of Molecules Reveals Modification of the Tunneling Barrier with Intramolecular Contrast," *Nano Letters* **11** (2011) 1580–1584.

[30] W. Steurer, S. Fatayer, L. Gross, and G. Meyer, "Probe-Based Measurement of Lateral Single-Electron Transfer Between Individual Molecules," *Nature Communications* **6** (2015) .

[31] F. E. Olsson, S. Paavilainen, M. Persson, J. Repp, and G. Meyer, "Multiple Charge States of Ag Atoms on Ultrathin NaCl Films," *Physical Review Letters* **98** (2007) 176803.

[32] C. S. Lent, P. D. Tougaw, W. Porod, and G. H. Bernstein, "Quantum Cellular Automata," *Nanotechnology* **4** (1993) 49.

[33] A. O. Orlov, I. Amlani, G. H. Bernstein, C. S. Lent, and G. L. Snider, "Realization of a Functional Cell for Quantum-Dot Cellular Automata," *Science* **277** (1997) 928–930.

[34] I. Amlani, A. O. Orlov, G. Toth, G. H. Bernstein, C. S. Lent, and G. L. Snider, "Digital Logic Gate Using Quantum-Dot Cellular Automata," *Science* **284** (1999) 289–291.

[35] A. O. Orlov, G. Toth, I. Amlani, R. Kummamuru, R. Ramasubramaniam, C. S. Lent, G. H. Bernstein, and G. L. Snider, "Experimental Studies of Clocked Quantum-Dot Cellular Automata Devices," in *58th DRC. Device Research Conference. Conference Digest (Cat. No.00TH8526)*, pp. 157–158. 2000.

[36] K. K. Yadavalli, A. O. Orlov, J. P. Timler, C. S. Lent, and G. L. Snider, "Fanout Gate in Quantum-Dot Cellular Automata," *Nanotechnology* **18** (2007) 375401.

[37] K. Sinthiptharakoon, S. R. Schofield, P. Studer, V. Brazdova, C. F. Hirjibehedin, D. R. Bowler, and N. J. Curson, "Investigating Individual Arsenic Dopant Atoms in Silicon Using Low-Temperature Scanning Tunnelling Microscopy," *Journal of Physics: Condensed Matter* **26** (2014) 012001.

[38] J. Salfi, J. Mol, R. Rahman, G. Klimeck, M. Simmons, L. Hollenberg, and S. Rogge, "Spatially Resolving Valley Quantum Interference of a Donor in Silicon," *Nature Materials* **13** (2014) 605.

[39] M. Fuechsle, J. A. Miwa, S. Mahapatra, H. Ryu, S. Lee, O. Warschkow, L. C. Hollenberg, G. Klimeck, and M. Y. Simmons, "A Single-Atom Transistor," *Nature Nanotechnology* **7** (2012) 242–246.

[40] T. C. Shen, C. Wang, G. C. Abeln, J. R. Tucker, J. W. Lyding, P. Avouris, and R. E. Walkup, "Atomic-Scale Desorption Through Electronic and Vibrational Excitation Mechanisms," *Science* **268** (1995) 1590–1592.

[41] E. T. Foley, A. F. Kam, J. W. Lyding, and P. Avouris, "Cryogenic UHV-STM Study of Hydrogen and Deuterium Desorption from Si(100)," *Physical Review Letters* **80** (1998) 1336–1339.

[42] L. Soukiassian, A. J. Mayne, M. Carbone, and G. Dujardin, "Atomic-Scale Desorption of H Atoms From the Si(100) - 2x1:H Surface: Inelastic Electron Interactions," *Physical Review B* **68** (2003) .

[43] M. A. Walsh and M. C. Hersam, "Atomic-Scale Templates Patterned by Ultrahigh Vacuum Scanning Tunneling Microscopy on Silicon," *Annual Review of Physical Chemistry* **60** (2009) 193–216.

[44] S. Schmucker, N. Kumar, J. Abelson, S. Daly, G. Girolami, M. Bischof, D. Jaeger, R. Reidy, B. Gorman, J. Alexander, J. Ballard, J. Randall, and J. Lyding, "Field-Directed Sputter Sharpening for Tailored Probe Materials and Atomic-Scale Lithography," *Nature Communications* **3** (2012) 935.

[45] S. R. Schofield, P. Studer, C. F. Hirjibehedin, N. J. Curson, G. Aeppli, and D. R. Bowler, "Quantum Engineering at the Silicon Surface Using Dangling Bonds," *Nature Communications* **4** (2013) 1649.

[46] M. Moller, S. P. Jarvis, L. Guerinet, P. Sharp, R. Woolley, P. Rahe, and P. Moriarty, "Automated Extraction of Single H Atoms with STM: Tip State Dependency," *Nanotechnology* **28** (2017) 075302.

[47] M. Rashidi, J. A. Burgess, M. Taucer, R. Achal, J. L. Pitters, S. Loth, and R. A. Wolkow, "Time-Resolved Single Dopant Charge Dynamics in Silicon," *Nature Communications* **7** (2016) .

[48] M. Taucer, L. Livadaru, P. G. Piva, R. Achal, H. Labidi, J. L. Pitters, and R. A. Wolkow, "Single-Electron Dynamics of an Atomic Silicon Quantum Dot on the H-Si(100) - (2x1)Surface," *Physical Review Letters* **112** (2014) 256801.

[49] T. Huff, H. Labidi, M. Rashidi, L. Livadaru, T. Dienel, R. Achal, W. Vine, J. Pitters, and R. A. Wolkow, "Binary Atomic Silicon Logic," *Nature Electronics* **1** (2018) 636.

[50] L. Livadaru, P. Xue, Z. Shaterzadeh-Yazdi, G. A. DiLabio, J. Mutus, J. L. Pitters, B. C. Sanders, and R. A. Wolkow, "Dangling-Bond Charge Qubit on a Silicon Surface," *New Journal of Physics* **12** (2010) 083018.

[51] M. B. Haider, J. L. Pitters, G. A. DiLabio, L. Livadaru, J. Y. Mutus, and R. A. Wolkow, "Controlled Coupling and Occupation of Silicon Atomic Quantum Dots at Room Temperature," *Physical Review Letters* **102** (2009) 046805.

[52] T. R. Huff, T. Dienel, M. Rashidi, R. Achal, L. Livadaru, J. Croshaw, and R. A. Wolkow, "Electrostatic Landscape of a Hydrogen-Terminated Silicon Surface Probed by a Moveable Quantum Dot," *ACS Nano* **13** (2019) 10566–10575.

[53] M. McEllistrem, M. Allgeier, and J. J. Boland, "Dangling Bond Dynamics on the Silicon (100)-2x1 Surface: Dissociation, Diffusion, and Recombination," *Science* **279** (1998) 545–548.

[54] C. H. Schwalb, M. Durr, and U. Hofer, "High-Temperature Investigation of Intradimer Diffusion of Hydrogen on Si(001)," *Physical Review B* **82** (2010) 193412.

[55] R. A. Wolkow, L. Livadaru, J. Pitters, M. Taucer, P. Piva, M. Salomons, M. Cloutier, and B. V. C. Martins, *Silicon Atomic Quantum Dots Enable Beyond-CMOS Electronics*, pp. 33–58. Springer Berlin Heidelberg, Berlin, Heidelberg, 2014.

[56] G. Binnig and H. Rohrer, "Scanning Tunneling Microscopy," *Surface Science* **126** (1983) 236–244.

[57] G. Binnig, H. Rohrer, C. Gerber, and E. Weibel, "Tunneling Through a Controllable Vacuum Gap," *Applied Physics Letters* **40** (1982) 178–180.

[58] G. Binnig, H. Rohrer, C. Gerber, and E. Weibel, "7x7 Reconstruction on Si(111) Resolved in Real Space," *Physical Review Letters* **50** (1983) 120–123.

[59] J. Tersoff and D. R. Hamann, "Theory of the Scanning Tunneling Microscope," *Physical Review B* **31** (1985) 805–813.

[60] G. Binnig, C. F. Quate, and C. Gerber, "Atomic Force Microscope," *Physical Review Letters* **56** (1986) 930–933.

[61] N. Jalili and K. Laxminarayana, "A Review of Atomic Force Microscopy Imaging Systems: Application to Molecular Metrology and Biological Sciences," *Mechatronics* **14** (2004) 907–945.

[62] F. J. Giessibl, "Atomic Resolution of the Silicon (111)-(7x7) Surface by Atomic Force Microscopy," *Science* **267** (1995) 68–71.

[63] J. Welker, E. Illek, and F. J. Giessibl, "Analysis of Force-Deconvolution Methods in Frequency-Modulation Atomic Force Microscopy," *Beilstein Journal of Nanotechnology* **3** (2012) 238.

[64] J. E. Sader and S. P. Jarvis, "Accurate Formulas for Interaction Force and Energy in Frequency Modulation Force Spectroscopy," *Applied Physics Letters* **84** (2004) 1801–1803.

[65] T. Huff, "Atomic Force Microscopy Characterization of Hydrogen Terminated Silicon (100) 2x1 Reconstruction," Master's thesis, University of Alberta, Edmonton, Alberta, Canada, 2015.

[66] J. Falter, M. Stiefermann, G. Langewisch, P. Schurig, H. Holscher, H. Fuchs, and A. Schirmeisen, "Calibration of Quartz Tuning Fork Spring Constants for Non-Contact Atomic Force Microscopy: Direct Mechanical Measurements and Simulations," *Beilstein Journal of Nanotechnology* **5** (2014) 507–516.

[67] F. J. Giessibl, "AFM's Path to Atomic Resolution," *Materials Today* **8** (2005) 32–41.

[68] T. R. Albrecht, P. Grutter, D. Horne, and D. Rugar, "Frequency Modulation Detection Using High Q Cantilevers for Enhanced Force Microscope Sensitivity," *Journal of Applied Physics* **69** (1991) 668–673.

[69] R. A. Wolkow, "Direct Observation of an Increase in Buckled Dimers on Si(001) at Low Temperature," *Physical Review Letters* **68** (1992) 2636–2639.

[70] A. Sweetman, S. Gangopadhyay, R. Danza, N. Berdunov, and P. Moriarty, "qPlus Atomic Force Microscopy of the Si(100) Surface: Buckled, Split-Off, and Added Dimers," *Applied Physics Letters* **95** (2009) 063112.

[71] R. Becker and R. Wolkow, "5.1. Silicon," in *Scanning Tunneling Microscopy*, vol. 27 of *Methods in Experimental Physics*, pp. 149 – 224. Academic Press, 1993.

[72] T. R. Albrecht, S. Akamine, T. E. Carver, and C. F. Quate, "Microfabrication of Cantilever Styli for the Atomic Force Microscope," *Journal of Vacuum Science and Technology A* **8** (1990) 3386–3396.

[73] F. J. Giessibl, "The qPlus Sensor, a Powerful Core for the Atomic Force Microscope," *Review of Scientific Instruments* **90** (2019) 011101.

[74] F. Giessibl, "High-Speed Force Sensor for Force Microscopy and Profilometry Utilizing a Quartz Tuning Fork," *Applied Physics Letters* **73** (1998) 3956.

[75] J. C. Brice, "Crystals for Quartz Resonators," *Review of Modern Physics* **57** (1985) 105–146.

[76] F. J. Giessibl, "Principles and Applications of the qPlus Sensor," in *Noncontact Atomic Force Microscopy*, NanoScience and Technology, pp. 121–142. Springer Berlin Heidelberg, 2009.

[77] F. J. Giessibl, H. Bielefeldt, S. Hembacher, and J. Mannhart, "Calculation of the Optimal Imaging Parameters for Frequency Modulation Atomic Force Microscopy," *Applied Surface Science* **140** (1999) 352–357.

[78] Z. Majzik, M. Setvin, A. Bettac, A. Feltz, V. Chab, and P. Jelinek, "Simultaneous Current, Force and Dissipation Measurements on the Si (111) 7x7 Surface with an Optimized qPlus AFM/STM Technique," *Beilstein Journal of Nanotechnology* **3** (2012) 249–259.

[79] B. J. Albers, M. Liebmann, T. C. Schwendemann, M. Z. Baykara, M. Heyde, M. Salmeron, E. I. Altman, and U. D. Schwarz, "Combined Low-Temperature Scanning Tunneling/Atomic Force Microscope for Atomic Resolution Imaging and Site-Specific Force Spectroscopy," *Review of Scientific Instruments* **79** (2008) 033704.

[80] J. Berger, M. Svec, M. Muller, M. Ledinsky, A. Fejfar, P. Jelinek, and Z. Majzik, "Characterization of the Mechanical Properties of qPlus Sensors," *Beilstein Journal of Nanotechnology* **4** (2013) 1–9.

[81] C. Tan, K. Zhou, W. Ma, B. Attard, P. Zhang, and T. Kuang, "Selective Laser Melting of High-Performance Pure Tungsten: Parameter Design, Densification Behavior and Mechanical Properties," *Science and Technology of Advanced Materials* **19** (2018) 370–380.

[82] M. Rezeq, J. Pitters, and R. Wolkow, "Tungsten Nanotip Fabrication by Spatially Controlled Field-Assisted Reaction with Nitrogen," *The Journal of Chemical Physics* **124** (2006) 204716.

[83] R. Urban, J. L. Pitters, and R. A. Wolkow, "Gas Field Ion Source Current Stability for Trimer and Single Atom Terminated W(111) Tips," *Applied Physics Letters* **100** (2012) 263105.

[84] O. L. Guise, J. W. Ahner, M.-C. Jung, P. C. Goughnour, and J. T. Yates, "Reproducible Electrochemical Etching of Tungsten Probe Tips," *Nano Letters* **2** (2002) 191–193.

[85] B.-F. Ju, Y.-L. Chen, and Y. Ge, "The Art of Electrochemical Etching for Preparing Tungsten Probes with Controllable Tip Profile and Characteristic Parameters," *Review of Scientific Instruments* **82** (2011) 013707.

[86] A.-S. Lucier, *Preparation and Characterization of Tungsten Tips Suitable for Molecular Electronics Studies.* PhD thesis, McGill University, 2004.

[87] S. Toh, H. Tan, J. Lam, L. Hsia, and Z. Mai, “Optimization of AC Electrochemical Etching for Fabricating Tungsten Nanotips with Controlled Tip Profile,” *Journal of The Electrochemical Society* **157** (2010) E6–E11.

[88] H. Labidi, M. Kupsta, T. Huff, M. Salomons, D. Vick, M. Taucer, J. Pitters, and R. A. Wolkow, “New Fabrication Technique for Highly Sensitive qPlus Sensor with Well-Defined Spring Constant,” *Ultramicroscopy* **158** (2015) 33–37.

[89] E. W. Muller and K. Bahadur, “Field Ionization of Gases at a Metal Surface and the Resolution of the Field Ion Microscope,” *Physical Review* **102** (1956) 624–631.

[90] R. G. Forbes, “Field Electron and Ion Emission From Charged Surfaces: A Strategic Historical Review of Theoretical Concepts,” *Ultramicroscopy* **95** (2003) 1–18.

[91] G. Binnig and H. Rohrer, “Scanning Tunneling Microscopy—From Birth to Adolescence (Nobel Lecture),” *Angewandte Chemie International Edition in English* **26** (1987) 606–614.

[92] S.-W. Hla, “Scanning Tunneling Microscopy Single Atom/Molecule Manipulation and its Application to Nanoscience and Technology,” *Journal of Vacuum Science and Technology B* **23** (2005) 1351–1360.

[93] H. Labidi, M. Koleini, T. Huff, M. Salomons, M. Cloutier, J. Pitters, and R. A. Wolkow, “Indications of Chemical Bond Contrast in AFM Images of a Hydrogen-Terminated Silicon Surface,” *Nature Communications* **8** (2017) 14222.

[94] R. Perez, M. C. Payne, I. Stich, and K. Terakura, “Role of Covalent Tip-Surface Interactions in Noncontact Atomic Force Microscopy on Reactive Surfaces,” *Physical Review Letters* **78** (1997) 678–681.

[95] P. Dieska, I. Stich, and R. Perez, "Covalent and Reversible Short-Range Electrostatic Imaging in Noncontact Atomic Force Microscopy," *Physical Review Letters* **91** (2003) 216401.

[96] L. Gross, F. Mohn, N. Moll, P. Liljeroth, and G. Meyer, "The Chemical Structure of a Molecule Resolved by Atomic Force Microscopy," *Science* **325** (2009) 1110–1114.

[97] L. Gross, F. Mohn, N. Moll, B. Schuler, A. Criado, E. Guitian, D. Pena, A. Gourdon, and G. Meyer, "Bond-Order Discrimination by Atomic Force Microscopy," *Science* **337** (2012) 1326–1329.

[98] G. Teobaldi, K. Lammle, T. Trevethan, M. Watkins, A. Schwarz, R. Wiesendanger, and A. L. Shluger, "Chemical Resolution at Ionic Crystal Surfaces Using Dynamic Atomic Force Microscopy with Metallic Tips," *Physical Review Letters* **106** (2011) 216102.

[99] T. Trevethan, M. Watkins, and A. L. Shluger, "Models of the Interaction of Metal Tips with Insulating Surfaces," *Beilstein Journal of Nanotechnology* **3** (2012) 329–335.

[100] R. Smoluchowski, "Anisotropy of the Electronic Work Function of Metals," *Physical Review* **60** (1941) 661–674.

[101] T. Chutora, B. de la Torre, P. Mutombo, J. Hellerstedt, J. Kopecek, P. Jelinek, and M. Svec, "Nitrous Oxide as an Effective AFM Tip Functionalization: a Comparative Study," *Beilstein Journal of Nanotechnology* **10** (2019) 315–321.

[102] H. Monig, S. Amirjalayer, A. Timmer, Z. Hu, L. Liu, O. D. Arado, M. Cnudde, C. A. Strassert, W. Ji, M. Rohlfing, *et al.*, "Quantitative Assessment of Intermolecular Interactions by Atomic Force Microscopy Imaging Using Copper Oxide Tips," *Nature Nanotechnology* **13** (2018) 371.

[103] L. Gross, B. Schuler, F. Mohn, N. Moll, N. Pavilcek, W. Steurer, I. Scivetti, K. Kotsis, M. Persson, and G. Meyer, "Investigating Atomic Contrast in Atomic Force Microscopy and Kelvin Probe Force Microscopy on Ionic Systems Using Functionalized Tips," *Physical Review Letters* **90** (2014) 155455.

[104] P. Sharp, S. Jarvis, R. Woolley, A. Sweetman, L. Kantorovich, C. Pakes, and P. Moriarty, "Identifying Passivated Dynamic Force Microscopy Tips on H:Si (100)," *Applied Physics Letters* **100** (2012) 233120.

[105] A. Sweetman, S. Jarvis, R. Danza, and P. Moriarty, "Effect of the Tip State During qPlus Noncontact Atomic Force Microscopy of Si (100) at 5 K: Probing the Probe," *Beilstein Journal of Nanotechnology* **3** (2012) 25–32.

[106] V. Ukraintsev and J. T. Yate Jr, "The Role of Nickel in Si(001) Roughening," *Surface Science* **346** (1996) 31–39.

[107] M. Yoshimura, T. An, I. Ono, and K. Ueda, "Nickel-Induced Surface Reconstructions on Si(110) Studied by Scanning Tunneling Microscopy," *Surface Science* **433** (1999) 470–474.

[108] A. Sherman, "In Situ Removal of Native Oxide From Silicon Wafers," *Journal of Vacuum Science and Technology B* **8** (1990) 656–657.

[109] K. Hata, T. Kimura, S. Ozawa, and H. Shigekawa, "How to Fabricate a Defect Free Si (001) Surface," *Journal of Vacuum Science and Technology A* **18** (2000) 1933–1936.

[110] J. L. Pitters, P. G. Piva, and R. A. Wolkow, "Dopant Depletion in the Near Surface Region of Thermally Prepared Silicon (100) in UHV," *Journal of Vacuum Science and Technology B* **30** (2012) 021806.

[111] H. Labidi, M. Taucer, M. Rashidi, M. Koleini, L. Livadaru, J. Pitters, M. Cloutier, M. Salomons, and R. A. Wolkow, "Scanning Tunneling

Spectroscopy Reveals a Silicon Dangling Bond Charge State Transition," *New Journal of Physics* **17** (2015) 073023.

[112] H. Bender, S. Verhaverbeke, M. Caymax, O. Vatel, and M. Heyns, "Surface Reconstruction of Hydrogen Annealed (100) Silicon," *Journal of Applied Physics* **75** (1994) 1207–1209.

[113] G. Cerofolini, C. Galati, S. Reina, L. Renna, N. Spinella, D. Jones, and V. Palermo, "Formation of Terraced, Nearly Flat, Hydrogen-Terminated, (100) Si Surfaces After High-Temperature Treatment in H-2 of Single-Crystalline Silicon," *Physical Review B* **72** (2005) 125431.

[114] Y. J. Chabal and K. Raghavachari, "New Ordered Structure for the H-Saturated Si(100) Surface," *Physical Review Letters* **54** (1985) 1055–1058.

[115] J. J. Boland, "Role of Bond-Strain in the Chemistry of Hydrogen on the Si(100) Surface," *Surface Science* **261** (1992) 17–28.

[116] C. C. Cheng and J. T. Yates, "H-Induced Surface Restructuring on Si(100): Formation of Higher Hydrides," *Physical Review B* **43** (1991) 4041–4045.

[117] J. J. Boland, "Scanning Tunnelling Microscopy of the Interaction of Hydrogen with Silicon Surfaces," *Advances in Physics* **42** (1993) 129–171.

[118] A. Sutoh, Y. Okada, S. Ohta, and M. Kawabe, "Cracking Efficiency of Hydrogen with Tungsten Filament in Molecular Beam Epitaxy," *Japanese Journal of Applied Physics* **34** (1995) L1379.

[119] J. Croshaw, T. Dienel, T. Huff, and R. A. Wolkow, "Atomic Defects of the Hydrogen-Terminated Silicon (100)-2x1 Surface Imaged with STM and nc-AFM," *arXiv preprint arXiv:2002.09138* (2020) .

[120] M. Rashidi, M. Taucer, I. Ozfidan, E. Lloyd, M. Koleini, H. Labidi, J. L. Pitters, J. Maciejko, and R. A. Wolkow, "Time-Resolved Imaging of Negative Differential Resistance on the Atomic Scale," *Physical Review Letters* **117** (2016) 276805.

[121] J. Wyrick, X. Wang, P. Namboodiri, S. W. Schmucker, R. V. Kashid, and R. M. Silver, "Atom-by-Atom Construction of a Cyclic Artificial Molecule in Silicon," *Nano Letters* **18** (2018) 7502–7508.

[122] J. A. Wood, M. Rashidi, M. Koleini, J. L. Pitters, and R. A. Wolkow, "Multiple Silicon Atom Artificial Molecules," *arXiv preprint arXiv:1607.06050* (2016) .

[123] L. Livadaru, J. Pitters, M. Taucer, and R. A. Wolkow, "Theory of Nonequilibrium Single-Electron Dynamics in STM Imaging of Dangling Bonds on a Hydrogenated Silicon Surface," *Physical Review B* **84** (2011) 205416.

[124] F. Mohn, L. Gross, N. Moll, and G. Meyer, "Imaging the Charge Distribution Within a Single Molecule," *Nature Nanotechnology* **7** (2012) 227–231.

[125] M. Taucer, *Silicon Dangling Bonds Non-equilibrium Dynamics and Applications*. PhD thesis, University of Alberta, 2015.

[126] R. M. Feenstra, "Electrostatic Potential for a Hyperbolic Probe Tip Near a Semiconductor," *Journal of Vacuum Science and Technology B* **21** (2003) 2080–2088.

[127] K. Teichmann, M. Wenderoth, S. Loth, R. Ulbrich, J. Garleff, A. Wijnheijmer, and P. Koenraad, "Controlled Charge Switching on a Single Donor with a Scanning Tunneling Microscope," *Physical Review Letters* **101** (2008) 076103.

[128] M. McEllistrem, G. Haase, D. Chen, and R. Hamers, "Electrostatic Sample-Tip Interactions in the Scanning Tunneling Microscope," *Physical Review Letters* **70** (1993) 2471.

[129] R. M. Feenstra, "Electrostatic Potential for a Hyperbolic Probe Tip Near a Semiconductor," *Journal of Vacuum Science and Technology B* **21** (2003) 2080–2088.

[130] R. M. Feenstra, Y. Dong, M. P. Semtsiv, and W. T. Masselink, "Influence of tip-induced band bending on tunnelling spectra of semiconductor surfaces," *Nanotechnology* **18** (2006) 044015.

[131] P. M. Ryan, L. Livadaru, G. A. DiLabio, and R. A. Wolkow, "Organic Nanostructures on Hydrogen-Terminated Silicon Report on Electric Field Modulation of Dangling Bond Charge State," *Journal of the American Chemical Society* **134** (2012) 12054–12063.

[132] M. Moller, S. P. Jarvis, L. Guerinet, P. Sharp, R. Woolley, P. Rahe, and P. Moriarty, "Automated Extraction of Single H Atoms with STM: Tip State Dependency," *Nanotechnology* **28** (2017) 075302.

[133] M. Ternes, C. P. Lutz, C. F. Hirjibehedin, F. J. Giessibl, and A. J. Heinrich, "The Force Needed to Move an Atom on a Surface," *Science* **319** (2008) 1066–1069.

[134] R. Achal, M. Rashidi, J. Croshaw, D. Churchill, M. Taucer, T. Huff, M. Cloutier, J. Pitters, and R. A. Wolkow, "Lithography for Robust and Editable Atomic-Scale Silicon Devices and Memories," *Nature Communications* **9** (2018) 2778.

[135] T. C. Shen, C. Wang, G. C. Abeln, J. R. Tucker, J. W. Lyding, P. Avouris, and R. E. Walkup, "Atomic-Scale Desorption Through Electronic and Vibrational Excitation Mechanisms," *Science* **268** (1995) 1590–1592.

[136] T. R. Huff, H. Labidi, M. Rashidi, M. Koleini, R. Achal, M. H. Salomons, and R. A. Wolkow, "Atomic White-Out: Enabling Atomic Circuitry through Mechanically Induced Bonding of Single Hydrogen Atoms to a Silicon Surface," *ACS Nano* **11** (2017) 8636–8642.

[137] N. Pavlicek, Z. Majzik, G. Meyer, and L. Gross, "Tip-Induced Passivation of Dangling Bonds on Hydrogenated Si(100)-2×1," *Applied Physics Letters* **111** (2017) 053104.

[138] S. Chen, H. Xu, K. Goh, L. Liu, and J. Randall, “Patterning of Sub-1 nm Dangling-Bond Lines with Atomic Precision Alignment on H: Si (100) Surface at Room Temperature,” *Nanotechnology* **23** (2012) 275301.

[139] M. Rashidi and R. A. Wolkow, “Autonomous Scanning Probe Microscopy In Situ Tip Conditioning Through Machine Learning,” *ACS Nano* **12** (2018) 5185–5189.

[140] C. Schonenberger and S. F. Alvarado, “Observation of Single Charge Carriers by Force Microscopy,” *Physical Review Letters* **65** (1990) 3162–3164.

[141] L. Gross, F. Mohn, P. Liljeroth, J. Repp, F. J. Giessibl, and G. Meyer, “Measuring the Charge State of an Adatom with Noncontact Atomic Force Microscopy,” *Science* **324** (2009) 1428–1431.

[142] H. Jacobs, P. Leuchtmann, O. Homan, and A. Stemmer, “Resolution and Contrast in Kelvin Probe Force Microscopy,” *Journal of Applied Physics* **84** (1998) 1168–1173.

[143] A. Bettac, J. Koeble, K. Winkler, B. Uder, M. Maier, and A. Feltz, “qPlus: Atomic Force Microscopy on Single-Crystal Insulators with Small Oscillation Amplitudes at 5 K,” *Nanotechnology* **20** (2009) 264009.

[144] N. LI, X. Chen, and Q.-K. Xue, “Contribution of Chemical Bonding to the Force in Atomic Force Microscopy,” *Acta Physico-Chimica Sinica* **30** (2014) 205–209.

[145] F. Pielmeier and F. J. Giessibl, “Spin Resolution and Evidence for Superexchange on NiO(001) Observed by Force Microscopy,” *Physical Review Letters* **110** (2013) 266101.

[146] A. J. Weymouth, T. Wutscher, J. Welker, T. Hofmann, and F. J. Giessibl, “Phantom Force Induced by Tunneling Current: A Characterization on Si(111),” *Physical Review Letters* **106** (2011) 226801.

[147] T. Wutscher, A. J. Weymouth, and F. J. Giessibl, "Localization of the Phantom Force Induced by the Tunneling Current," *Physical Review B* **85** (2012) 195426.

[148] A. J. Weymouth and F. J. Giessibl, "The Effect of Sample Resistivity on Kelvin Probe Force Microscopy," *Applied Physics Letters* **101** (2012) 213105.

[149] R. Stomp, Y. Miyahara, S. Schaer, Q. Sun, H. Guo, P. Grutter, S. Studenikin, P. Poole, and A. Sachrajda, "Detection of Single-Electron Charging in an Individual InAs Quantum Dot by Noncontact Atomic-Force Microscopy," *Physical Review Letters* **94** (2005) 056802.

[150] R. Stomp, Y. Miyahara, S. Schaer, Q. Sun, H. Guo, P. Grutter, S. Studenikin, P. Poole, and A. Sachrajda, "Detection of Single-Electron Charging in an Individual InAs Quantum Dot by Noncontact Atomic-Force Microscopy," *Physical Review Letters* **94** (2005) 056802.

[151] Y. Miyahara, A. Roy-Gobeil, and P. Grutter, "Quantum State Readout of Individual Quantum Dots by Electrostatic Force Detection," *Nanotechnology* **28** (2017) 064001.

[152] J. L. Pitters, L. Livadaru, M. B. Haider, and R. A. Wolkow, "Tunnel Coupled Dangling Bond Structures on Hydrogen Terminated Silicon Surfaces," *The Journal of Chemical Physics* **134** (2011) 064712.

[153] M. Rashidi, W. Vine, T. Dienel, L. Livadaru, J. Retallick, T. Huff, K. Walus, and R. A. Wolkow, "Initiating and Monitoring the Evolution of Single Electrons Within Atom-Defined Structures," *Physical Review Letters* **121** (2018) 166801.

[154] J. A. Dagata, J. Schneir, H. H. Harary, J. Bennett, and W. Tseng, "Pattern Generation on Semiconductor Surfaces by a Scanning Tunneling Microscope Operating in Air," *Journal of Vacuum Science and Technology B* **9** (1991) 1384–1388.

[155] E. S. Snow, P. M. Campbell, and P. J. McMarr, “Fabrication of Silicon Nanostructures with a Scanning Tunneling Microscope,” *Applied Physics Letters* **63** (1993) 749–751.

[156] S. M, C. Thirstrup, and M. Aono, “Nanoscale Growth of Silver on Prepatterned Hydrogen-Terminated Si (001) Surfaces,” *Physical Review B* **62** (2000) 16167.

[157] B. Naydenov and J. J. Boland, “Engineering the Electronic Structure of Surface Dangling Bond Nanowires of Different Size and Dimensionality,” *Nanotechnology* **24** (2013) 275202.

[158] I. Dogel, S. Dogel, J. Pitters, G. DiLabio, and R. Wolkow, “Chemical Methods for the Hydrogen Termination of Silicon Dangling Bonds,” *Chemical Physics Letters* **448** (2007) 237–242.

[159] H. Labidi, L. Kantorovich, and D. Riedel, “Atomic-Scale Control of Hydrogen Bonding on a Bare Si (100)-2x1 surface,” *Physical Review B* **86** (2012) 165441.

[160] M. K. Beyer and H. Clausen-Schaumann, “Mechanochemistry: The Mechanical Activation of Covalent Bonds,” *Chemical Reviews* **105** (2005) 2921–2948.

[161] O. Custance, R. Perez, and S. Morita, “Atomic Force Microscopy as a Tool for Atom Manipulation,” *Nature Nanotechnology* **4** (2009) 803.

[162] A. Sweetman, S. Jarvis, R. Danza, J. Bamidele, S. Gangopadhyay, G. A. Shaw, L. Kantorovich, and P. Moriarty, “Toggling Bistable Atoms via Mechanical Switching of Bond Angle,” *Physical Review Letters* **106** (2011) 136101.

[163] G. Langewisch, J. Falter, H. Fuchs, and A. Schirmeisen, “Forces During the Controlled Displacement of Organic Molecules,” *Physical Review Letters* **110** (2013) 036101.

[164] S. P. Jarvis, S. Taylor, J. D. Baran, N. R. Champness, J. A. Larsson, and P. Moriarty, "Measuring the Mechanical Properties of Molecular Conformers," *Nature Communications* **6** (2015) 8338.

[165] J. N. Ladenthin, T. Frederiksen, M. Persson, J. C. Sharp, S. Gawinkowski, J. Waluk, and T. Kumagai, "Force-Induced Tautomerization in a Single Molecule," *Nature Chemistry* **8** (2016) 935–940.

[166] G. Dujardin, A. Mayne, O. Robert, F. Rose, C. Joachim, and H. Tang, "Vertical Manipulation of Individual Atoms by a Direct STM Tip-Surface Contact on Ge(111)," *Physical Review Letters* **80** (1998) 3085–3088.

[167] N. Oyabu, Ó. Custance, I. Yi, Y. Sugawara, and S. Morita, "Mechanical Vertical Manipulation of Selected Single Atoms by Soft Nanoindentation Using Near Contact Atomic Force Microscopy," *Physical Review Letters* **90** (2003) 176102.

[168] Y. Sugimoto, M. Abe, S. Hirayama, N. Oyabu, Ó. Custance, and S. Morita, "Atom Inlays Performed at Room Temperature Using Atomic Force Microscopy," *Nature Materials* **4** (2005) 156.

[169] M. A. Lantz, H. J. Hug, R. Hoffmann, P. J. A. van Schendel, P. Kappenberger, S. Martin, A. Baratoff, and H.-J. Guntherodt, "Quantitative Measurement of Short-Range Chemical Bonding Forces," *Science* **291** (2001) 2580–2583.

[170] Y. Sugimoto, P. Pou, M. Abe, P. Jelinek, R. Perez, S. Morita, and O. Custance, "Chemical Identification of Individual Surface Atoms by Atomic Force Microscopy," *Nature* **446** (2007) 64–67.

[171] F. Mohn, L. Gross, and G. Meyer, "Measuring the Short-Range Force Field Above a Single Molecule with Atomic Resolution," *Applied Physics Letters* **99** (2011) 053106.

[172] J. B. Ballard, J. H. G. Owen, J. D. Alexander, W. R. Owen, E. Fuchs, J. N. Randall, R. C. Longo, and K. Cho, "Spurious Dangling Bond Formation During Atomically Precise Hydrogen Depassivation Lithography on Si(100): The Role of Liberated Hydrogen," *Journal of Vacuum Science and Technology B* **32** (2014) 021805.

[173] L. Bartels, G. Meyer, K.-H. Rieder, D. Velic, E. Knoesel, A. Hotzel, M. Wolf, and G. Ertl, "Dynamics of Electron-Induced Manipulation of Individual CO Molecules on Cu (111)," *Physical Review Letters* **80** (1998) 2004.

[174] F. Mohn, B. Schuler, L. Gross, and G. Meyer, "Different Tips for High-Resolution Atomic Force Microscopy and Scanning Tunneling Microscopy of Single Molecules," *Applied Physics Letters* **102** (2013) 073109.

[175] A. Yurtsever, Y. Sugimoto, H. Tanaka, M. Abe, S. Morita, M. Ondravcek, P. Pou, R. Perez, and P. Jelinek, "Force Mapping on a Partially H-Covered Si(111)-(7x7) Surface: Influence of Tip and Surface Reactivity," *Physical Review B* **87** (2013) 155403.

[176] Y. Sugimoto, P. Pou, O. Custance, P. Jelinek, M. Abe, R. Perez, and S. Morita, "Complex Patterning by Vertical Interchange Atom Manipulation Using Atomic Force Microscopy," *Science* **322** (2008) 413–417.

[177] J. Berger, E. J. Spadafora, P. Mutombo, P. Jelínek, and M. Švec, "Force-Driven Single-Atom Manipulation on a Low-Reactive Si Surface for Tip Sharpening," *Small* **11** (2015) 3686–3693.

[178] B. Such, M. Kolmer, S. Godlewski, J. Lis, J. Budzioch, M. Wojtaszek, and M. Szymonski, "Imaging of Defects on Ge(001):H by Non-Contact Atomic Force Microscopy," in *Imaging and Manipulation of Adsorbates Using Dynamic Force Microscopy*, P. Moriarty and S. Gauthier, eds., Advances in Atom and Single Molecule Machines, pp. 111–118. Springer International Publishing, 2015.

[179] P. G. Piva, G. A. DiLabio, J. L. Pitters, J. Zikovsky, M. Rezeq, S. Dogel, W. A. Hofer, and R. A. Wolkow, "Field Regulation of Single-Molecule Conductivity by a Charged Surface Atom," *Nature* **435** (2005) 658–661.

[180] S. Godlewski, M. Kolmer, H. Kawai, B. Such, R. Zuzak, M. Saeys, P. de Mendoza, A. M. Echavarren, C. Joachim, and M. Szymonski, "Contacting a Conjugated Molecule with a Surface Dangling Bond Dimer on a Hydrogenated Ge(001) Surface Allows Imaging of the Hidden Ground Electronic State," *ACS Nano* **7** (2013) 10105–10111.

[181] F. Bocquet, L. Nony, and C. Loppacher, "Polarization Effects in Noncontact Atomic Force Microscopy: A Key to Model the Tip-Sample Interaction Above Charged Adatoms," *Physical Review B* **83** (2011) 035411.

[182] T. Hitosugi, S. Heike, T. Onogi, T. Hashizume, S. Watanabe, Z.-Q. Li, K. Ohno, Y. Kawazoe, T. Hasegawa, and K. Kitazawa, "Jahn-Teller Distortion in Dangling-Bond Linear Chains Fabricated on a Hydrogen-Terminated Si (100)-2x1 Surface," *Physical Review Letters* **82** (1999) 4034.

[183] L. Nony, F. Bocquet, F. Para, and C. Loppacher, "Frequency Shift, Damping, and Tunneling Current Coupling with Quartz Tuning Forks in Noncontact Atomic Force Microscopy," *Physical Review B* **94** (2016) 115421.

[184] S. Jarvis, A. Sweetman, J. Bamidele, L. Kantorovich, and P. Moriarty, "Role of Orbital Overlap in Atomic Manipulation," *Physical Review B* **85** (2012) 235305.

[185] M. Ratner, "A Brief History of Molecular Electronics," *Nature Nanotechnology* **8** (2013) 378.

[186] M. Engelund, N. Papior, P. Brandimarte, T. Frederiksen, A. Garcia-Lekue, and D. Sanchez-Portal, "Search for a Metallic Dangling-Bond Wire on n-Doped H-Passivated Semiconductor Surfaces," *The Journal of Physical Chemistry C* **120** (2016) 20303–20309.

[187] E. Bussmann and C. C. Williams, "Single-Electron Tunneling Force Spectroscopy of an Individual Electronic State in a Nonconducting Surface," *Applied Physics Letters* **88** (2006) 263108.

[188] T. Konig, G. H. Simon, H.-P. Rust, G. Pacchioni, M. Heyde, and H.-J. Freund, "Measuring the Charge State of Point Defects on MgO/Ag(001)," *Journal of the American Chemical Society* **131** (2009) 17544–17545.

[189] A. P. [de Silva], S. Uchiyama, T. P. Vance, and B. Wannalerse, "A Supramolecular Chemistry Basis for Molecular Logic and Computation," *Coordination Chemistry Reviews* **251** (2007) 1623–1632.

[190] R. Robles, M. Kepenekian, C. Joachim, R. Rurali, and N. Lorente, *Band Engineering of Dangling-Bond Wires on the Si(100)H Surface*, pp. 83–93. Springer International Publishing, Cham, 2017.

[191] A. Imre, G. Csaba, L. Ji, A. Orlov, G. H. Bernstein, and W. Porod, "Majority Logic Gate for Magnetic Quantum-Dot Cellular Automata," *Science* **311** (2006) 205–208.

[192] C. S. Lent and P. D. Tougaw, "A Device Architecture for Computing with Quantum Dots," *Proceedings of the IEEE* **85** (1997) 541–557.

[193] J. Gorman, D. Hasko, and D. Williams, "Charge-Qubit Operation of an Isolated Double Quantum Dot," *Physical Review Letters* **95** (2005) 090502.

[194] D. Kim, Z. Shi, C. Simmons, D. Ward, J. Prance, T. S. Koh, J. K. Gamble, D. Savage, M. Lagally, M. Friesen, *et al.*, "Quantum Control and Process Tomography of a Semiconductor Quantum Dot Hybrid Qubit," *Nature* **511** (2014) 70–74.

[195] G. Schedelbeck, W. Wegscheider, M. Bichler, and G. Abstreiter, "Coupled Quantum Dots Fabricated by Cleaved Edge Overgrowth: From Artificial Atoms to Molecules," *Science* **278** (1997) 1792–1795.

[196] M. Bayer, P. Hawrylak, K. Hinzer, S. Fafard, M. Korkusinski, Z. Wasilewski, O. Stern, and A. Forchel, "Coupling and Entangling of Quantum States in Quantum Dot Molecules," *Science* **291** (2001) 451–453.

[197] R. Landauer, "Minimal Energy Requirements in Communication," *Science* **272** (1996) 1914–1918.

[198] N. Mathur, "Beyond the Silicon Roadmap," *Nature* **419** (2002) 573–575.

[199] K. Shibata, H. Yuan, Y. Iwasa, and K. Hirakawa, "Large Modulation of Zero-Dimensional Electronic States in Quantum Dots by Electric-Double-Layer Gating," *Nature Communications* **4** (2013) 2664.

[200] J. W. Lyding, T. Shen, G. Abeln, C. Wang, and J. Tucker, "Nanoscale Patterning and Selective Chemistry of Silicon Surfaces by Ultrahigh-Vacuum Scanning Tunneling Microscopy," *Nanotechnology* **7** (1996) 128.

[201] M. Rashidi, E. Lloyd, T. R. Huff, R. Achal, M. Taucer, J. J. Croshaw, and R. A. Wolkow, "Resolving and Tuning Carrier Capture Rates at a Single Silicon Atom Gap State," *ACS Nano* **11** (2017) 11732–11738.

[202] P. Scherpelz and G. Galli, "Optimizing Surface Defects for Atomic-Scale Electronics: Si Dangling Bonds," *Physical Review Materials* **1** (2017) 021602.

[203] H. Labidi, M. Taucer, M. Rashidi, M. Koleini, L. Livadaru, J. Pitters, M. Cloutier, M. Salomons, and R. A. Wolkow, "Scanning Tunneling Spectroscopy Reveals a Silicon Dangling Bond Charge State Transition," *New Journal of Physics* **17** (2015) 073023.

[204] M. Kolmer, S. Godlewski, R. Zuzak, M. Wojtaszek, C. Rauer, A. Thuaire, J.-M. Hartmann, H. Moriceau, C. Joachim, and M. Szymonski, "Atomic Scale Fabrication of Dangling Bond Structures on Hydrogen Passivated Si(001) Wafers Processed and Nanopackaged in a Clean Room Environment," *Applied Surface Science* **288** (2014) 83–89.

[205] B. Hesson and R. Wolkow, "Three-Dimensional Rendered Cartoon Animation Demonstrating the Functionality of Silicon Dangling Bond Structures." https://static-content.springer.com/esm/art%3A10.1038%2Fs41928-018-0180-3/MediaObjects/41928_2018_180_MOESM2_ESM.mpg.

[206] C. Wagner, M. F. Green, P. Leinen, T. Deilmann, P. Kruger, M. Rohlfing, R. Temirov, and F. S. Tautz, "Scanning Quantum Dot Microscopy," *Physical Review Letters* **115** (2015) 026101.

[207] Z. Shaterzadeh-Yazdi, B. C. Sanders, and G. A. DiLabio, "Ab Initio Characterization of Coupling Strength for All Types of Dangling-Bond Pairs on the Hydrogen-Terminated Si (100)-2x1 Surface," *The Journal of Chemical Physics* **148** (2018) 154701.

[208] A. Bellec, L. Chaput, G. Dujardin, D. Riedel, L. Stauffer, and P. Sonnet, "Reversible Charge Storage in a Single Silicon Atom," *Physical Review B* **88** (2013) 241406.

[209] H. Kawai, O. Neucheva, T. L. Yap, C. Joachim, and M. Saeys, "Electronic Characterization of a Single Dangling Bond on n- and p-Type Si(001)-(2×1):H," *Surface Science* **645** (2016) 88 – 92.

[210] J. E. Northrup, "Effective Correlation Energy of a Si Dangling Bond Calculated with the Local-Spin-Density Approximation," *Physical Review B* **40** (1989) 5875–5878.

[211] G. J. Gerardi, E. H. Poindexter, P. J. Caplan, and N. M. Johnson, "Interface Traps and Pb Centers in Oxidized (100) Silicon Wafers," *Applied Physics Letters* **49** (1986) 348–350.

[212] T. Blomquist and G. Kirczenow, "Controlling the Charge of a Specific Surface Atom by the Addition of a Non-Site-Specific Single Impurity in a Si Nanocrystal," *Nano Letters* **6** (2006) 61–65.

[213] A. Bellec, D. Riedel, G. Dujardin, O. Boudrioua, L. Chaput, L. Stauffer, and P. Sonnet, "Electronic Properties of the n-Doped Hydrogenated Silicon (100) Surface and Dehydrogenated Structures at 5 K," *Physical Review B* **80** (2009) 245434.

[214] E. F. Schubert, *Doping in III-V semiconductors.* Cambridge University Press, Cambridge, 2015.

[215] S. S. H. Ng, J. Retallick, H. N. Chiu, R. Lupoiu, L. Livadaru, T. Huff, M. Rashidi, W. Vine, T. Dienel, R. A. Wolkow, and K. Walus, "SiQAD: A Design and Simulation Tool for Atomic Silicon Quantum Dot Circuits," *IEEE Transactions on Nanotechnology* **19** (2020) 137–146.

[216] C. Barthel, M. Kaergaard, J. Medford, M. Stopa, C. M. Marcus, M. Hanson, and A. C. Gossard, "Fast Sensing of Double-Dot Charge Arrangement and Spin State with a Radio-Frequency Sensor Quantum Dot," *Physical Review B* **81** (2010) 161308.

[217] A. A. Prager, A. O. Orlov, and G. L. Snider, "Integration of CMOS, Single Electron Transistors, and Quantum Dot Cellular Automata," in *2009 IEEE Nanotechnology Materials and Devices Conference*, pp. 54–58, IEEE. 2009.

[218] H.-S. Goan, G. J. Milburn, H. M. Wiseman, and H. B. Sun, "Continuous Quantum Measurement of Two Coupled Quantum Dots Using a Point Contact: A Quantum Trajectory Approach," *Physical Review B* **63** (2001) 125326.

[219] K. Eng, R. McFarland, and B. Kane, "High Mobility Two-Dimensional Electron System on Hydrogen-Passivated Silicon (111) Surfaces," *Applied Physics Letters* **87** (2005) 052106.

[220] J. L. Pitters, P. G. Piva, and R. A. Wolkow, "Dopant Depletion in the Near Surface Region of Thermally Prepared Silicon (100) in UHV," *Journal of Vacuum Science and Technology B* **30** (2012) 021806.

[221] M. Ellner, P. Pou, and R. Perez, *The Electrostatic Field of CO Functionalized Metal Tips*, pp. 465–497. Springer International Publishing, Cham, 2018.

[222] S. P. Jarvis, "Resolving Intra-and Inter-Molecular Structure with Non-Contact Atomic Force Microscopy," *International Journal of Molecular Sciences* **16** (2015) 19936–19959.

[223] J. Wood, "The Emergent Electronic Structure and Charging Configurations of Silicon Dangling Bond Chains," Master's thesis, University of Alberta, Alberta, Canada, 2016.

[224] H. M. Tutuncu, S. J. Jenkins, and G. P. Srivastava, "Theoretical Studies of Atomic Vibrations on the Si(001)(2x1) Surface," *Physical Review B* **56** (1997) 4656–4664.

[225] N. Kocic, S. Decurtins, S.-X. Liu, and J. Repp, "Forces From Periodic Charging of Adsorbed Molecules," *The Journal of Chemical Physics* **146** (2017) 092327.

[226] N. Kocic, P. Weiderer, S. Keller, S. Decurtins, S.-X. Liu, and J. Repp, "Periodic Charging of Individual Molecules Coupled to the Motion of an Atomic Force Microscopy Tip," *Nano Letters* **15** (2015) 4406–4411.

[227] E. H. Poindexter, G. J. Gerardi, M. Rueckel, P. J. Caplan, N. M. Johnson, and D. K. Biegelsen, "Electronic Traps and Pb Centers at the Si/SiO2 Interface: Band-Gap Energy Distribution," *Journal of Applied Physics* **56** (1984) 2844–2849.

[228] P. Broqvist, A. Alkauskas, and A. Pasquarello, "Defect Levels of Dangling Bonds in Silicon and Germanium Through Hybrid Functionals," *Physical Review B* **78** (2008) 075203.

[229] G. Pica and B. W. Lovett, "Quantum Gates with Donors in Germanium," *Physical Review B* **94** (2016) 205309.

[230] L. C. L. Hollenberg, A. S. Dzurak, C. Wellard, A. R. Hamilton, D. J. Reilly, G. J. Milburn, and R. G. Clark, "Charge-Based Quantum Computing Using Single Donors in Semiconductors," *Physical Review B* **69** (2004) 113301.

[231] A. J. Sigillito, A. M. Tyryshkin, T. Schenkel, A. A. Houck, and S. A. Lyon, "All-Electric Control of Donor Nuclear Spin Qubits in Silicon," *Nature Nanotechnology* **12** (2017) 958.

[232] D. Gohlke, R. Mishra, O. D. Restrepo, D. Lee, W. Windl, and J. Gupta, "Atomic-Scale Engineering of the Electrostatic Landscape of Semiconductor Surfaces," *Nano Letters* **13** (2013) 2418–2422.

[233] F. Albrecht, J. Repp, M. Fleischmann, M. Scheer, M. Ondráček, and P. Jelínek, "Probing Charges on the Atomic Scale by Means of Atomic Force Microscopy," *Physical Review Letters* **115** (2015) 076101.

[234] B. Schuler, S.-X. Liu, Y. Geng, S. Decurtins, G. Meyer, and L. Gross, "Contrast Formation in Kelvin Probe Force Microscopy of Single π-Conjugated Molecules," *Nano Letters* **14** (2014) 3342–3346.

[235] C. Barth and C. R. Henry, "Surface Double Layer on (001) Surfaces of Alkali Halide Crystals: A Scanning Force Microscopy Study," *Physical Review Letters* **98** (2007) 136804.

[236] C. Barth, A. S. Foster, C. R. Henry, and A. L. Shluger, "Recent Trends in Surface Characterization and Chemistry with High-Resolution Scanning Force Methods," *Advanced Materials* **23** (2011) 477–501.

[237] M. Ondráček, P. Hapala, M. Švec, and P. Jelínek, "Imaging Charge Distribution Within Molecules by Scanning Probe Microscopy," in *Kelvin Probe Force Microscopy*, pp. 499–518. Springer, 2018.

[238] C. Wagner, M. F. Green, M. Maiworm, P. Leinen, T. Esat, N. Ferri, N. Friedrich, R. Findeisen, A. Tkatchenko, R. Temirov, *et al.*, "Quantitative

Imaging of Electric Surface Potentials with Single-Atom Sensitivity," *Nature Materials* **18** (2019) 853–859.

[239] J. W. Lyding, T. Shen, J. S. Hubacek, J. R. Tucker, and G. C. Abeln, "Nanoscale Patterning and Oxidation of H-Passivated Si(100)-2×1 Surfaces with an Ultrahigh Vacuum Scanning Tunneling Microscope," *Applied Physics Letters* **64** (1994) 2010–2012.

[240] L. Gross, F. Mohn, N. Moll, P. Liljeroth, and G. Meyer, "The Chemical Structure of a Molecule Resolved by Atomic Force Microscopy," *Science* **325** (2009) 1110–1114.

[241] E. Spadafora, J. Berger, P. Mutombo, M. Telychko, M. Svec, Z. Majzik, A. McLean, and P. Jelínek, "Identification of Surface Defects and Subsurface Dopants in a Delta-Doped System Using Simultaneous nc-AFM/STM and DFT," *The Journal of Physical Chemistry C* **118** (2014) 15744–15753.

[242] T. Yap, H. Kawai, O. Neucheva, A. Wee, C. Troadec, M. Saeys, and C. Joachim, "Si (100)-2× 1-H dimer rows contrast inversion in low-temperature scanning tunneling microscope images," *Surface Science* **632** (2015) L13–L17.

[243] J. J. Boland, "Structure of the H-saturated Si(100) surface," *Physical Review Letters* **65** (1990) 3325–3328.

[244] L. Liu, J. Yu, and J. W. Lyding, "Subsurface Dopant-Induced Features on the Si (100) 2/spl times/1: H Surface: Fundamental Study and Applications," *IEEE Transactions on Nanotechnology* **1** (2002) 176–183.

[245] M. Usman, J. Bocquel, J. Salfi, B. Voisin, A. Tankasala, R. Rahman, M. Y. Simmons, S. Rogge, and L. Hollenberg, "Spatial Metrology of Dopants in Silicon with Exact Lattice Site Precision," *Nature Nanotechnology* **11** (2016) 763.

[246] L. Liu, J. Yu, and J. W. Lyding, "Atom-Resolved Three-Dimensional Mapping of Boron Dopants in Si (100) by Scanning Tunneling Microscopy," *Applied Physics Letters* **78** (2001) 386–388.

[247] P. G. Piva, G. A. DiLabio, L. Livadaru, and R. A. Wolkow, "Atom-Scale Surface Reactivity Mediated by Long-Ranged Equilibrium Charge Transfer," *Physical Review B* **90** (2014) 155422.

[248] B. Voisin, J. Salfi, J. Bocquel, R. Rahman, and S. Rogge, "Spatially Resolved Resonant Tunneling on Single Atoms in Silicon," *Journal of Physics: Condensed Matter* **27** (2015) 154203.

[249] A. Ramdas and S. Rodriguez, "Spectroscopy of the Solid-State Analogues of the Hydrogen Atom: Donors and Acceptors in Semiconductors," *Reports on Progress in Physics* **44** (1981) 1297.

[250] A. Tankasala, J. Salfi, J. Bocquel, B. Voisin, M. Usman, G. Klimeck, M. Y. Simmons, L. C. L. Hollenberg, S. Rogge, and R. Rahman, "Two-Electron States of a Group-V Donor in Silicon from Atomistic Full Configuration Interactions," *Physical Review B* **97** (2018) 195301.

[251] R. Rahman, G. P. Lansbergen, J. Verduijn, G. C. Tettamanzi, S. H. Park, N. Collaert, S. Biesemans, G. Klimeck, L. C. L. Hollenberg, and S. Rogge, "Electric Field Reduced Charging Energies and Two-Electron Bound Excited States of Single Donors in Silicon," *Physical Review B* **84** (2011) 115428.

[252] J. Salfi, B. Voisin, A. Tankasala, J. Bocquel, M. Usman, M. Y. Simmons, L. C. L. Hollenberg, R. Rahman, and S. Rogge, "Valley Filtering in Spatial Maps of Coupling between Silicon Donors and Quantum Dots," *Physical Review X* **8** (2018) 031049.

[253] B. Sopori, X. Deng, J. Benner, A. Rohatgi, P. Sana, S. Estreicher, Y. Park, and M. Roberson, "Hydrogen in Silicon: A Discussion of Diffusion and Passivation Mechanisms," *Solar Energy Materials and Solar Cells* **41-42** (1996) 159 – 169.

[254] C. Herring, N. M. Johnson, and C. G. Van de Walle, "Energy Levels of Isolated Interstitial Hydrogen in Silicon," *Physical Review B* **64** (2001) 125209.

[255] N. M. Johnson, C. Herring, and D. J. Chadi, "Interstitial Hydrogen and Neutralization of Shallow-Donor Impurities in Single-Crystal Silicon," *Physical Review Letters* **56** (1986) 769–772.

[256] M. A. Roberson and S. K. Estreicher, "Vacancy and Vacancy-Hydrogen Complexes in Silicon," *Physical Review B* **49** (1994) 17040–17049.

[257] Y. K. Park, S. K. Estreicher, C. W. Myles, and P. A. Fedders, "Molecular-Dynamics Study of the Vacancy and Vacancy-Hydrogen Interactions in Silicon," *Physical Review B* **52** (1995) 1718–1723.

[258] P. Deák, M. Heinrich, L. Snyder, and J. Corbett, "Hydrogen-Related Vibrations in Crystalline Silicon," *Materials Science and Engineering: B* **4** (1989) 57–62.

[259] P. Deák, L. Snyder, M. Heinrich, C. Ortiz, and J. Corbett, "Hydrogen Complexes and Their Vibrations in Undoped Crystalline Silicon," *Physica B: Condensed Matter* **170** (1991) 253–258.

[260] J. Corbett, J. Lindström, and S. Pearton, "Hydrogen in Silicon," *MRS Online Proceedings Library Archive* **104** (1987) .

[261] G. D. Watkins, "Negative-U Properties for Point Defects in Silicon," *MRS Proceedings* **2** (1980) 21.

[262] R. Achal, M. Rashidi, J. Croshaw, T. R. Huff, and R. A. Wolkow, "Detecting and Directing Single Molecule Binding Events on H-Si (100) with Application to Ultradense Data Storage," *ACS Nano* **14** (2020) 2947–2955.